Pós-Graduação em Ciência da Computação

DUSAN STOSIC

NUMERICAL SIMULATIONS OF MAGNETIC SKYRMIONS IN ATOMICALLY-THIN FERROMAGNETIC FILMS

Universidade Federal de Pernambuco
posgraduacao@cin.ufpe.br
www.cin.ufpe.br/~posgraduacao

Recife
2018

Dusan Stosic

Numerical simulations of magnetic skyrmions in atomically-thin ferromagnetic films

Thesis presented to the Programa de Pós-graduação em Ciência da Computação of Centro de Informática of Universidade Federal de Pernambuco and the Doctoral Study Program of University of Antwerp as partial requirement to award the joint degree of Doctor in Computer Science and Physics.

Advisor: Teresa Bernarda Ludermir
Joint Advisor: Milorad Vlado Milošević

Recife
2018

Catalogação na fonte
Bibliotecária Monick Raquel Silvestre da S. Portes, CRB4-1217

S888n Stosic, Dusan
Numerical simulations of magnetic skyrmions in atomically-thin ferromagnetic films / Dusan Stosic. – 2018.
149 f.: il., fig.

Orientadora: Teresa Bernarda Ludermir.
Tese (Doutorado) – Universidade Federal de Pernambuco. CIn, Ciência da Computação, Recife, 2018.
Inclui referências e apêndice.

1. Inteligência artificial. 2. Filmes ferromagnéticos. I. Ludermir, Teresa Bernarda (orientadora). II. Título.

006.3 CDD (23. ed.) UFPE- MEI 2018-105

Dusan Stosic

“Numerical Simulations of Magnetic Skyrmions in Atomically-thin Ferromagnetic Films'”

Tese de Doutorado apresentada ao Programa de Pós-Graduação em Ciência da Computação da Universidade Federal de Pernambuco, como requisito parcial para a obtenção do título de Doutora em Ciência da Computação

Aprovado em: 02/05/2018.

_____

Orientadora: Profa. Dra. Teresa Bernarda Ludermir

BANCA EXAMINADORA

_____

Prof. Dr. Tsang Ing Ren
Centro de Informática /UFPE

_____

Prof. Dr. Paulo Salgado Gomes de Mattos Neto
Centro de Informática / UFPE

_____

Prof. Dr. Milan Lalic
Departamento de Física / UFS

_____

Profa. Dra. Viviane Moraes de Oliveira
Departamento de Física / UFRPE

_____

Prof. Dr. Pedro Hugo de Figueirêdo
Departamento de Física / UFRPE

ACKNOWLEDGEMENTS

I would like to express sincere gratitude to my advisers Prof. Teresa Ludermir and Prof. Milorad Milošević for their continuous and unconditional support throughout my doctoral studies. I also gratefully acknowledge funding from the Conselho National de Desenvolvimento Científico e Tecnológico (CNPq, No. 140840/2016-8) received towards the doctoral work.

ABSTRACT

Moore's Law has driven the electronics industry for the past half century. However, the doubling of transistors about every two years is beginning to break down, owing to fundamental limits that arise as they approach the atomic length. As a result, the search for new pathways for electronics has become crucial. Among potential candidates, the discovery of magnetic textures known as skyrmions has attracted considerable interest and attention in spintronic technology, which relies on both the electron charge and its spin. The unusual topological and particle-like behavior launched skyrmions into the spotlight of scientific research. Topological protected stability, nanoscale size, and low driving currents needed to move them make skyrmions promising candidates for future consumer nanoelectronics. Recent advances in the field have provided all of the basic functions needed for carrying and processing information. In this thesis, we look to advance the current understanding of skyrmion physics, and explore their potential to replace conventional electronics technology. First, the fundamental properties and lifetimes of racetrack skyrmions at room temperature are investigated. We discover that skyrmions can easily collapse at the boundary in laterally finite systems, and propose ways to improve their stability for constrained geometries. Then, pinning of single skyrmions on atomic defects of distinct origins are studied. We reveal that the preferred pinning positions depend on the skyrmion size and type of defect being considered, and discuss applications where control of skyrmions by defects is of particular interest. Next, we explore other magnetic configurations that can compete with skyrmions when considering new materials, and describe a previously unseen mechanism for collapse of skyrmions into cycloidal spin backgrounds. Finally, switching and interactions between skyrmions with distinct topologies are reported. We find that skyrmions transition to higher or lower topologies by absorbing a unit spin texture. The interactions between skyrmions of different topological charges can be attractive or repulsive, leading to the formation of arranged clusters. We conclude with a numerical library for simulating magnetic skyrmions in various scenarios.

Keywords: Ferromagnetic films. Skyrmions. Atomistic spin simulations.

RESUMO

A Lei de Moore tem impulsionado a indústria eletrônica no último meio século. No entanto, a duplicação de transistores a cada dois anos está começando a quebrar, devido aos limites fundamentais que surgem à medida que se aproximam a largura atômica. Como resultado a busca por novos caminhos para a eletrônica se tornou crucial. Entre os potenciais candidatos, a descoberta de texturas magnéticas conhecidas como *skyrmions* atraiu muito interesse e atenção na tecnologia spintrônica, que depende ambos da carga e do spin de elétrons. O comportamento topológico e de partículas lançou skyrmions no centro de atenção da pesquisa científica. Skyrmions são candidatos promissores para a futura nano eletrônica do consumidor devido a sua estabilidade topológica, tamanho em nano escala e baixas correntes necessárias para movê-los. Avanços recentes fornecem todas as funções básicas necessárias para transportar e processar informação baseada em skyrmions. Nesta tese, procuramos avançar o conhecimento atual da física de skyrmions e explorar seu potencial para substituir a tecnologia eletrônica convencional. Primeiro investigamos propriedades fundamentais de skyrmions e sua estabilidade em temperatura ambiente. Descobrimos que skyrmions podem escapar pela borda em sistemas finitos e propomos maneiras de melhorar sua estabilidade para geometrias restritas. Depois estudamos como skyrmions ficam presos em defeitos atômicos de origens distintas. Mostramos que as suas posições dependem do tamanho e do tipo de defeito a ser considerado, e também discutimos aplicações em que o controle de skyrmions por defeitos é de interesse. Em seguida, exploramos outras configurações magnéticas que podem competir com os skyrmions quando novos materiais são considerados, e descrevemos um mecanismo inédito para o colapso de skyrmions em fundos de spin ciclóides. Finalmente, relatamos as comutações e interações entre skyrmions de topologias distintas. Descobrimos que skyrmions transacionam para topologias mais altas ou mais baixas pela absorção de uma textura de spin unitária. As interações entre skyrmions de diferentes cargas topológicas podem ser atrativas ou repulsivas, formando agrupamentos arranjados. Concluímos com uma biblioteca numérica para simular skyrmions magnéticos em vários cenários.

Palavras-chaves: Filmes ferromagnéticos. Skyrmions. Simulações atomísticas de spin.

SAMENVATTING

De wet van Moore heeft de elektronica-industrie de afgelopen halve eeuw gedreven. De verdubbeling van transistors om de twee jaar begint echter af te nemen, vanwege de fundamentele limieten die ontstaan als ze de atoomlengte naderen. Als gevolg hiervan is het zoeken naar nieuwe wegen voor elektronica cruciaal geworden. Onder potentiële kandidaten heeft de ontdekking van magnetische texturen die bekend staan als skyrmions veel belangstelling en aandacht getrokken in spintronische technologie, die berust op zowel de elektronenlading als de spin. Het ongewone topologische en deeltjesachtige gedrag introduceerde skyrmions in de schijnwerpers van wetenschappelijk onderzoek. Topologisch beschermde stabiliteit, nanoschaalgrootte en laagstromende stromingen die nodig zijn om ze te verplaatsen, maken skyrmions veelbelovend voor toekomstige nano-elektronica voor de consument. Recente ontwikkelingen in het veld hebben alle basisfuncties opgeleverd die nodig zijn voor het dragen en verwerken van informatie. In dit proefschrift doen we ons best om het huidige inzicht in de skyrmion-fysica te verbeteren en hun potentieel te verkennen om de conventionele elektronische technologie te vervangen. Eerst worden de fundamentele eigenschappen en levensduren van racetrack skyrmions bij kamertemperatuur onderzocht. We ontdekken dat skyrmionen gemakkelijk kunnen instorten aan de grens in zijdelings eindige systemen, en manieren kunnen voorstellen om hun stabiliteit voor beperkte geometrieën te verbeteren. Vervolgens pinning van enkele skyrmionen op atomaire defecten van verschillende oorsprong worden bestudeerd. We onthullen dat de voorkeurspinposities afhankelijk zijn van de skyrmiongrootte en het type defect dat wordt overwogen, en bespreken toepassingen waarbij de beheersing van skyrmionen door defecten van bijzonder belang is. Vervolgens verkennen we andere magnetische configuraties die kunnen concurreren met skyrmionen bij het overwegen van nieuwe materialen en beschrijven een tot nu toe onzichtbaar mechanisme voor het instorten van skyrmionen in cycloïdale spin-achtergronden. Ten slotte worden overschakeling en interacties tussen skyrmionen met verschillende topologieën gerapporteerd. We vinden dat skyrmionen overgaan naar hogere of lagere topologieën door een spinstructuur van een eenheid te absorberen. De interacties tussen skyrmionen van verschillende topologische ladingen kunnen aantrekkelijk of afstotend zijn, wat leidt tot de vorming van geordende clusters. We sluiten af met een numerieke bibliotheek voor het simuleren van magnetische skyrmionen in verschillende scenario's.

Trefwoorden: Ferromagnetische films. Skyrmions. Atomistische spin-simulaties.

LIST OF ABBREVIATIONS

2D	Two-dimensional
AFM	Antiferromagnetic
Co	Cobalt
CPU	Central Processing Unit
DFT	Density Functional Theory
DM	Dzyaloshinsky-Moriya
DMI	Dzyaloshinsky-Moriya Interaction
DW	Domain Wall
eV	Electron Volt
Fe	Iron
FM	Ferromagnetic
GNEB	Geodesic Nudged Elastic Band
GPU	Graphics Processing Unit
Ir	Iridium
LL	Landau-Lifshitz
LLG	Landau-Lifshitz Gilbert
MC	Monte Carlo
MEP	Minimum Energy Path
ML	Monolayer
MgO	Magnesium Oxide
NEB	Nudged Elastic Band
Pd	Palladium
Pt	Platinum
QM	Quick-Min
SCy	Spin Cycloid
SD	Steepest Descent

Sk	Skyrmion
SkX	Skyrmion Lattice
SOC	Spin-Orbit Coupling
SP	Saddle Point
SP-STM	Spin-Polarized Scanning Tunneling Microscopy
STM	Scanning Tunneling Microscopy

CONTENTS

1 INTRODUCTION

Since the era of electronics began with the invention of the transistor in 1947 and silicon-based semiconductor technology, companies were trying to make their products smaller. Transistors are widely used in modern electronics as building blocks of electronic circuits. As transistors get smaller, more of them can be packed on a chip, they also get faster and consume less electricity. For the past four decades, the electronics industry has been driven by Moore's Law [1], which effectively suggests that electronic devices double in speed and capability about every two years. Indeed, every two years companies come up with new chips that have double the number of transistors for processing [2] or for memory [3] (see Fig. 1.1). However, the exponential growth envisioned by Moore does not come without a cost. From a feature size of 90 nm around 2004 to one of 10 nm today, considerable progress was made in processing and patterning technologies, as well as in nanotechnology. Modern chips are manufactured with billions of transistors, making it extremely challenging to keep up with the exponential scaling. The doubling has already started to slow down due to heat that is inevitably generated when more silicon circuitry is packed into a small area [4]. Moreover, some even more fundamental limits on the physics await. As the size of a transistor reaches to the 2-3 nanometer limit, where features are just 10 atoms across, quantum mechanical effects begin to take place due to the wavelike behavior of particles [5, 6]. Precisely, at that scale particles behave in strange ways, taking on more than one state at the same time and interacting with other particles that are very far away, that will make transistors hopelessly unreliable [2]. These issues appear both on the processing and memory side, with little chances for solutions using current technology.

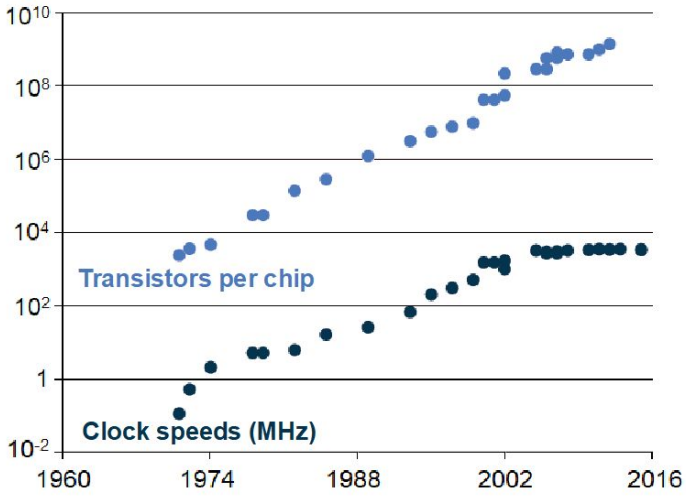

Figure 1.1 – Increase of the number of transistors per chip together with the increase of their clock speed, adapted from Ref. [2].

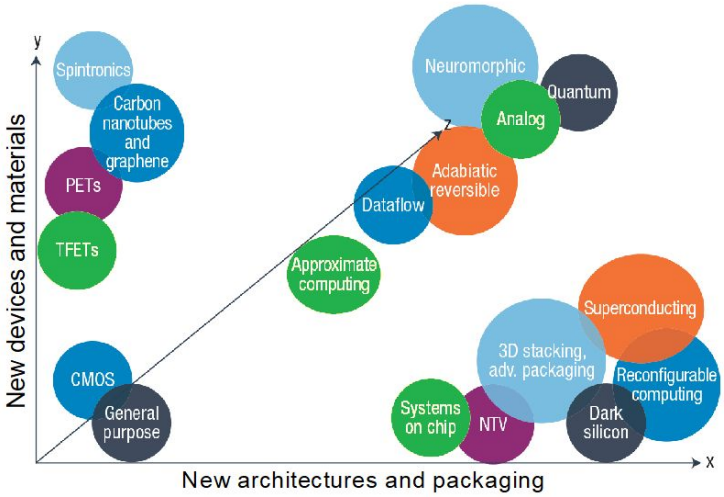

Figure 1.2 – Technology scaling options based on new paradigms and materials, adapted from Ref. [7].

For many years silicon was the only option for electronics. However, recent developments in material-engineering and nanotechnology, as well as in other fields of science, have introduced new pathways for electronics (see Fig. 1.2). One possibility is to embrace a completely new paradigm like quantum computing [8,9], which harnesses quantum phenomena to process information in a novel and promising way, or neuromorphic computing [10,11], which aims to mimic neurons in the brain, or even photonic computing [12], which use light instead of electricity for processing. But none of these alternative paradigms has left the laboratory, and many are believed to offer advantages only for specific applications, rather than for the everyday tasks of digital computing. A different approach is to stick with silicon, but configure it in entirely new ways. One popular option is to expand vertically by stacking many thin layers of silicon circuitry [2]. While this works for memory chips that consume power only when a memory element is accessed, which is not that often, microprocessor chips are more challenging as stacking layer after layer of hot circuits only makes the heat problem worse. Finally, one can stay in the digital realm, but look for materials that could be used for electronics as fast as their silicon counterparts while generating much less heat. There are many candidates, ranging from graphene [13] and other near 2D-like compounds [14], to organic electronic materials [15], based on organic molecules or polymers using chemical synthesis, to memristors [16], which couples the electrons with electrically charged atoms called ions.

Among the various potential candidates, spintronic materials [17], that rely not only on the electron charge but also on its spin to carry and process information, have attracted considerable interest and attention. The spotlight of this technology are skyrmions, topological spin textures that were recently discovered in magnetic materials. Skyrmions are promising candidates for future consumer nanoelectronics due to their topological protected stability, nanoscale size, and low driving currents needed to move them. Recent advances in the field have provided all of the basic functions needed for storing and processing information, which further highlights

their potential for future electronic applications [18]. In this thesis, we procure to advance the theoretical understanding of magnetic skyrmions in various situations, and explore their potential to replace conventional electronics technology.

1.1 Timeline

Since the 1950s, the problem of how to explain the presence of countable particles in continuous fields has been of interest [19]. Stable localized field configurations were searched to form a general field theory of elementary particles, but the majority of nonlinear field models were unable to predict them. As an exception, in 1961 Skyrme was able to describe nuclear particles as localized states called 'skyrmions' [20]. In quantum field theory, particles are wave-like excitations with finite lifetimes. Skyrme proposed to describe their stability by treating the particles as topological defects in a quantum vector field. These defects are characterized by a topological integer that cannot be changed through continuous deformation of the field, leading to the notion of "topological protection". Interestingly, they have turned out to be relevant in condensed matter systems such as the quantum Hall system [21], liquid crystals [22], and Bose condensate [23]. Indeed, it was found that topologically protected particles can also appear in chiral magnets in the form of stable spin textures [24], referred to as magnetic skyrmions, the protagonist of this thesis.

For over a decade, theoretical predictions [27–30] of skyrmion excitations in condensed matter systems with chiral interactions were made. Following these pioneering theoretical works, a set of experiments in 2009 [26,31,32] established the existence of skyrmion phases in magnets. A key ingredient to their existence is the Dzyaloshinsky–Moriya (DM) interaction [33, 34], which results from spin-orbit coupling (SOC) in a structure without inversion symmetry, for example, a chiral crystal structure or a surface. Extended lattices of magnetic skyrmions, as shown in Fig. 1.3, were first observed in B20-type bulk and thin film chiral magnets [35], such as MnSi [26], $Fe_{1-x}Co_xSi$ [36], FeGe [37, 38], or $Mn_{1-x}Fe_xGe$ [39]. In B20 magnets, the chiral inter-

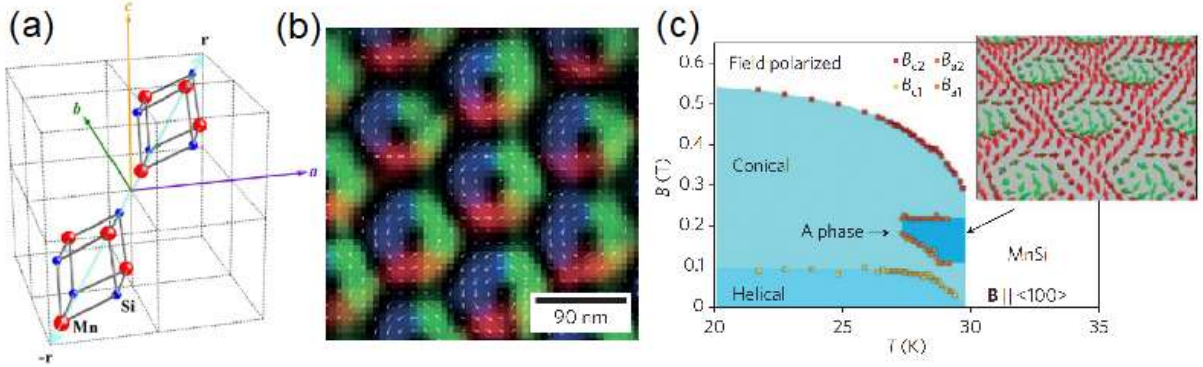

Figure 1.3 – (a) Crystal structure of MnSi with B20 cubic symmetry, retrieved from Ref. [25]. (b) Skyrmion crystal state imaged by Lorentz TEM with the superimposed spin orientation. (c) Phase diagram of MnSi as a function of temperature T and field B. Inset: Schematic of the skyrmion "A" phase, retrieved from Ref. [26].

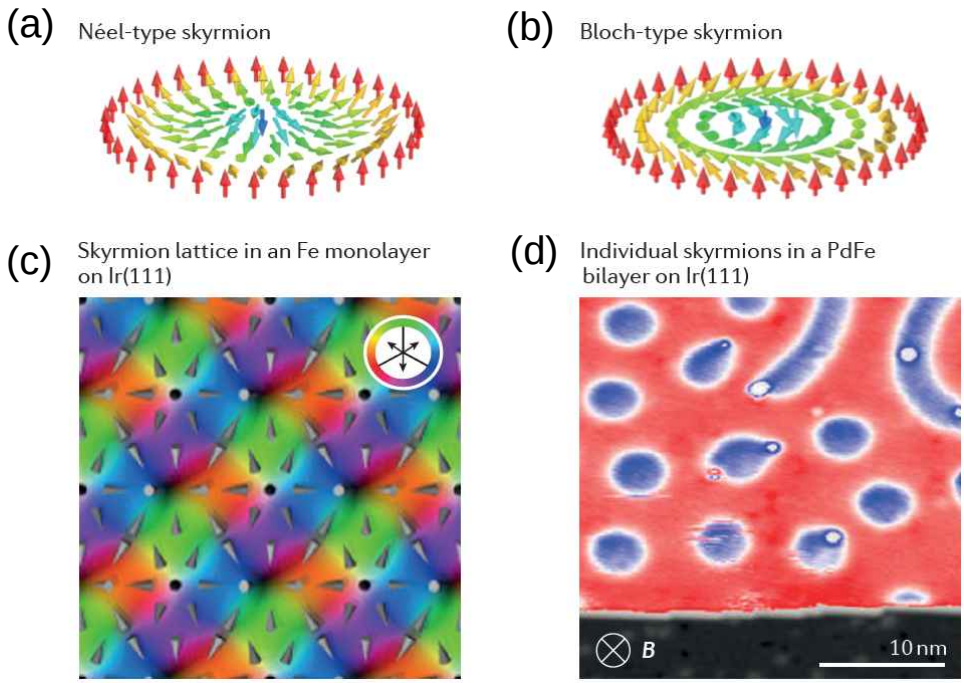

Figure 1.4 – (a) Néel-type and (b) Bloch-type skyrmions, retrieved from Ref. [44]. (c) Lattice of skyrmions as observed by SP-STM in a monolayer of Fe grown on Ir(111). Colors indicate in-plane magnetization, retrieved from Ref. [45]. (d) Individual skyrmions observed by the same technique in a PdFe bilayer on Ir(111), where out-of-plane magnetization is color-coded from red for 'up' to blue for 'down' magnetization, retrieved from Ref. [46].

actions are induced from the lack of space-inversion symmetry in the atomic crystal, seen in Fig. 1.3(a), which creates weak SOC in the form of DM interactions. These interactions are ultimately responsible for the existence of skyrmion states. The skyrmion lattices can be moved by very small electrical currents and simulations have shown they are less hindered by defects [40]. However, this state only exists in a finite and narrow temperature region, labeled as the "A" phase in Fig. 1.3(c), which indicates that it can only be observed below room temperatures and in the presence of an external magnetic field. Fortunately, recent experiments have shown that robust skyrmion states can be achieved near or beyond room temperatures [41,42] and for a wide range of fields [43].

Until then, skyrmion phases were restricted to bulk magnets with a particular chiral crystal symmetry, namely B20 compounds, greatly limiting the available systems that can be considered. Starting from 2011, skyrmions were also observed in ultrathin magnetic films epitaxially grown on heavy metals, which are subject to large DM interactions (DMIs) induced by the breaking of inversion symmetry at the interface and to the strong SOC of the neighboring heavy metal. The Néel-like skyrmion states observed in ultrathin metallic films differ substantially from the Bloch-like skyrmions found in bulk materials, as illustrated in Fig. 1.4. The first investigated systems in this class were Fe monolayers on Ir(111), where a nanoscale skyrmion lattice was found to form the magnetic ground state by scanning tunnelling microscopy (STM) [47].

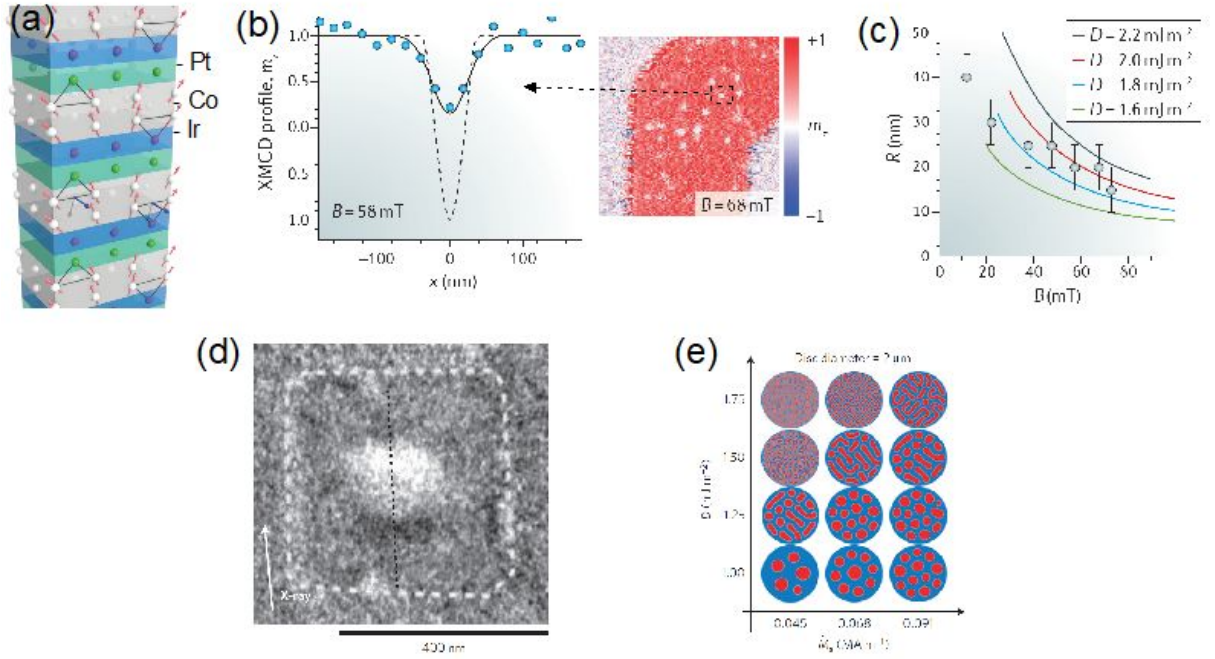

Figure 1.5 – (a) Asymmetric metallic multilayer made of several repetitions of a trilayer composed of a Co layer (grey) sandwiched between two different heavy metals, Pt (green) and Ir (blue). (b) Scanning transmission X-ray microscopy (STXM) of skyrmions with sizes below 100 nm in Ir/Co/Pt multilayers. (c) Skyrmion radius R plotted against the magnetic field B for different DM couplings D. Figures are retrieved from Ref. [49]. (d) XMCD-photoemission electron microscopy image of a skyrmion in a square dot patterned in a Pt/Co/MgO trilayer, indicated by the white dashed line, retrieved from Ref. [50]. (e) Examples of stable spin structures for 2 μm discs close to the Pt/Co/Ta sample used in experiments, retrieved from Ref. [51].

The large DM and weak exchange interactions for the Ir/Fe interface leads to Néel skyrmions which are forced on a square lattice with a period of only 1 nm by the four-spin interaction (see Fig. 1.4(c)), formed spontaneously even in zero external magnetic field. However, this skyrmion lattice cannot be driven into a different topological state, and as result does not seem suited for exploring single skyrmions. Instead, Romming [48] showed that adding an atomic Pd overlayer can push the system into a regime where skyrmion phases are observed at low field, but an applied field on the order of 1 T induces a transition to a ferromagnetic state embedding individual metastable skyrmions, shown in Fig. 1.4(d), that can be manipulated by spin-polarized currents in STM. For further increases of the magnetic field, the system undergoes a second transition into the saturated ferromagnetic phase.

So far, the nanoscale skyrmions in Fe monolayers and PdFe bilayers on Ir(111) could only be observed at low temperatures, typically 4 K, and high magnetic fields, typically 1.5 T. However, a prerequisite for their practical use is the ability to stabilize small individual skyrmions at room temperature and in near-zero applied fields. A promising path towards this goal can be achieved by increasing the thickness of the

transition metal film, by making use of interlayer exchange coupling, or by designing asymmetric multilayer structures [45]. This has been well demonstrated in series of publications in early 2016 for multilayer structures formed by stacking layers of magnetic and non-magnetic heavy thin metallic films [49–51]. For example, Ref. [49] showed that in metallic multilayers with Co layers sandwiched between two different heavy-metal layers, such as Ir and Pt illustrated in Fig. 1.5(a), the additive interfacial DM interactions are large enough to stabilize skyrmions below 100 nm in size at room temperature and in external fields of only a few tens of millitesla (see Fig. 1.5(b-c)). This results from a coupling of the skyrmions in successive Co layers, combined with the increase of the effective magnetic volume obtained by repeating the magnetic layer vertically. Refs. [50] and [51] achieved similar sub-100 nm skyrmions at room temperature, shown in Fig. 1.5(d-e), by employing multilayers of Pt/Co/MgO and Pt/Co/Ta, respectively. Importantly, this type of multilayer can be fabricated by sputter deposition, which are standard technologies for industrial production [44].

Lastly, there is increasing interest in new classes of nanoscale topological spin textures in magnets, since they are expect to provide new means for electric control of magnetism. The relevant literature has been mostly focused on skyrmion textures that arise in materials with chiral interactions of the DM type. However, besides the DM interaction, chiral interactions can also arise from the four-spin interactions [47], which occurs due to electron hopping between four adjacent sites, and frustration in the isotropic exchange interactions [52]. The latter is particularly useful for the creation of various distinct skyrmion-like structures in magnets. Recently, it was discovered experimentally that a phase consisting of skyrmion and anti-skyrmion lattices can be stabilized in the triangular spin model with competing interactions [52]. Then, a rich phase diagram of an anisotropic frustrated magnet with frustrated skyrmions of arbitrary vorticity and helicity was investigated [53]. Simultaneously, a new form of particle-like state, composed of a smooth magnetization vector field and a magnetic singularity, was found on the surface of bulk chiral magnets. Ref. [54] revealed a new class of skyrmion crystals, while Ref. [55] analyzed skyrmion and anti-skyrmion pair creation by spin-polarized currents. Other variants of skyrmion-like structures in frustrated magnetic materials have also been studied theoretically [56–58].

1.2 Technologies

Skyrmionics refers to the emerging technologies based on magnetic skyrmions in the fields of spintronics and nanoelectronics. Skyrmions can be used as information carriers in the next-generation information-processing devices due to their remarkable stability, extremely small size (down to a few nanometers), and very small current densities needed to displace them in nanostructures [40,59,60]. To realize the eventual commercialization of skyrmionics for future electronics, various challenges need to be solved such as creation and annihilation, detection, and manipulation of skyrmions. Here we discuss the technological advancements made in this context.

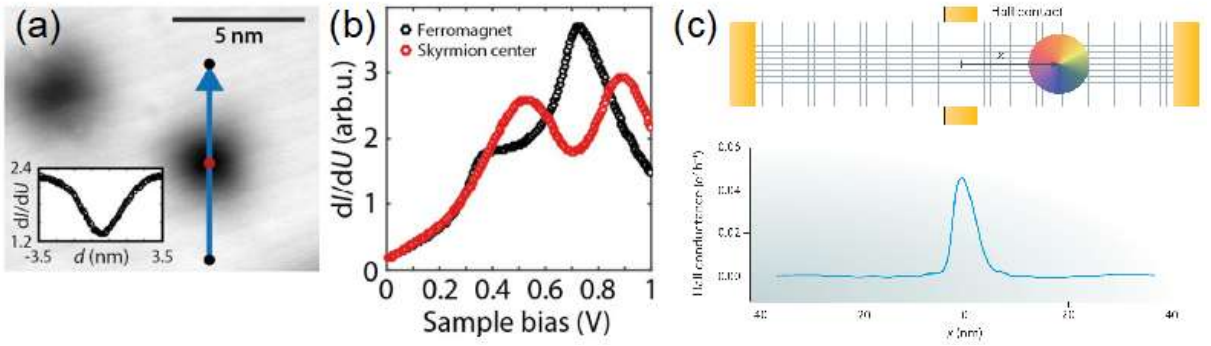

Figure 1.6 – (a) Differential tunnel conductance, dI/dU, map of two skyrmions with a profile along the arrow in inset. (b) dI/dU tunnel spectra in the skyrmion center (red) and in the FM background (black). Figures are adapted from Ref. [61]. (c) Schematic illustration of setup to measure topological Hall effect (top). Calculated topological Hall effect conductance as a function of distance between skyrmion and Hall contacts (bottom), retrieved from [44, 62].

1.2.1 Detection

In view of future skyrmionics, a key issue is the detection of individual nanoscale skyrmions. Several magneto-electric phenomena can be used towards this end. Operating a spin-polarized scanning tunneling microscopy (SP-STM) allows for direct real-space observation of complex non-collinear spin configurations. Specifically, individual skyrmions were observed with atomic-scale spatial resolution using SP-STM imaging [46,48], where low tunneling currents and low bias voltages are typically chosen. Ref. [61] proposed a detection scheme that takes advantage of the non collinear magnetoresistance that arises. This magnetoresistance effect, called NCMR, is associated with the large magnetization gradient observed in the presence of a skyrmion, illustrated in Fig. 1.6(a-b), and was used to detect skyrmions on a one-by-one basis. However, the NCMR depends on the highly non-collinear spin structure rather than on the topological properties of the skyrmion. A similar consideration holds for the longitudinal anisotropic magnetoresistance, or the anomalous Hall effect [63]. Another approach for the efficient detection of skyrmions relies on the topological Hall effect [62], and is directly related to the topological properties of skyrmions. This effect arises from the accumulated Berry phase which is proportional to the skyrmion number and creates an emergent magnetic field. Produced by the skyrmion, this emergent field leads to a measurable Hall voltage that allows a purely electrical detection of skyrmions [62], as shown in Fig. 1.6(c). While the topological Hall effect has been observed in bulk magnets, it remains to be reported at room temperature for metallic multilayers [44].

1.2.2 Writing and deleting

Any application of future skyrmionics will require the ability to write and delete individual skyrmions. One possible route to achieve these goals is through current-induced effects. For example, Ref. [64] proposed creating skyrmions around an ar-

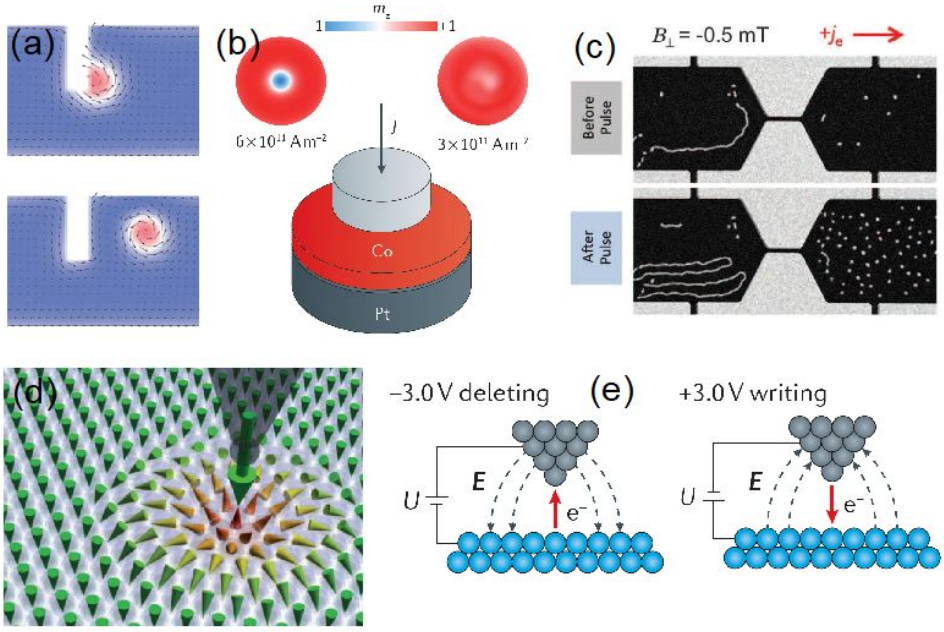

Figure 1.7 – (a) Snapshots of the creation of a skyrmion around a notch by current-induced spin transfer torque, adapted from Ref. [64]. (b) Schematic representation of a device for vertical spin injection through a magnetic tunnel junction, retrieved from Ref. [65]. (c) Nucleation of skyrmion bubbles by current-induced expansion of domains at the exit of a constriction, retrieved from Ref. [66]. (d) Concept of skyrmion manipulation with local currents from an SP-STM probe tip, retrieved from Ref. [48]. (e) Deleting (left) and writing (right) skyrmions by local electric fields, retrieved from Ref. [67].

tificial notch by the action of the current-induced spin transfer torque, as shown in Fig. 1.7. To avoid the introduction of local defects, one can instead inject the spin-polarized current vertically through a magnetic tunnel junction (see Fig. 1.7), where the spin torques under the injection contact lead to the formation of a magnetic skyrmion [65]. This nucleation process was experimentally observed by injecting a current through a SP-STM in an FePd bilayer [48]. While originally introduced for the real-space observation of individual nanoscale skyrmions, by increasing the tunneling current and the applied bias voltage the SP-STM can be used write and delete nanoscale skyrmions in a reproducible manner by local injection of spin-polarized electrons, as shown in Fig. 1.7. The energy of the injected electrons dictates the switching between the skyrmion and ferromagnetic states, and the exerted spin-transfer torque provides a means to control the direction of switching [45]. An alternative approach involves the current-induced expansion of domains at the exit of a constriction, seen in Fig. 1.7, which leads to the formation of micrometer-sized magnetic skyrmion bubbles [66]. Lastly, it has been demonstrated that nanoscale skyrmions can also be created and deleted by local electric fields [67], generated from a non-magnetic tip as shown in Fig. 1.7, where the polarity of the applied bias voltage provides a means to control the directionality of the switching, or skyrmion writing and deleting processes. This offers an interesting all-electric alternative to the spin-transfer-torque-

based switching by local spin-polarized current injection [45].

1.2.3 Motion by currents

Skyrmions will be used for spintronic devices only if they can be moved or excited at low enough energy costs. Therefore, the motion of skyrmions is an active area of research, and its effect from currents has been studied since early experiments of bulk crystals. In 2010, Jonietz [59] first detected a current-induced rotation of the skyrmion lattice in the B20 MnSi crystal, while a direct observation of its current-induced motion in the flow regime in FeGe was reported later in 2012 [68]. Meanwhile, Schultz [69] established a means to estimate the skyrmion velocity from the correlation between the current-induced motion of skyrmion lattices and the deviation of the Hall resistivity. Particularly, it was found that the current densities required to move skyrmion lattices are very small, a few 10^6 Am^{-2}, which is five or six orders of magnitude smaller than those needed to move domain walls (DWs), of the order 10^{12} Am^{-2} [60]. This is due both because skyrmion lattices couple efficiently to the current, and because they remain relatively unaffected by disorder [40, 59]. Furthermore, the efficient current-driven motion can result from the skyrmion interaction with the edges of a nanostructure. In general, the motion of skyrmions consists of a longitudinal motion, along the direction of the current, and a transverse motion, often dubbed the skyrmion Hall effect, generated by gyrotropic forces that are related to the topology of the skyrmion [60]. As shown in Fig. 1.8(a), the skyrmion has both longitudinal and transverse velocities under an applied current, but the transverse disappears close to the edge due to its repulsive interaction. Moreover, the direction of the longitudinal motion depends both on the chirality of the skyrmion and on the sign of the spin Hall angle, while the deflection along the transverse direction depends on the polarization at the center of the skyrmion, up or down. At sufficiently high current densities, the skyrmion will collapse by going over the edge.

For the theory of current-induced motion of skyrmions, the Thiele equation [70] for describing the dynamics of magnetic solitons can be used:

$$\boldsymbol{F} + \boldsymbol{G} \times \boldsymbol{v} + \alpha D \boldsymbol{v} = 0, \tag{1.1}$$

where $\boldsymbol{F}$ is the sum of the force exerted by the skyrmion Hall effect and the repulsive force from the track edges, $\boldsymbol{G}$ is a gyrovector oriented along the out-of-plane direction, D is the dissipative tensor, $\boldsymbol{v}$ is the skyrmion velocity, and α is the Gilbert damping coefficient. Everschor [71] used the Thiele equation to describe the skyrmion dynamics induced by spin torque. Iwasaki [40] then compared predictions from the Thiele equation with numerical simulations of a skyrmion lattice and a spin helix, or a series of DWs. They found that the depinning currents are practically zero for skyrmions, the Magnus force and the flexibility of skyrmions to avoid pinning centers induce a weak influence from defects, and the skyrmion velocity increases linearly with the current according to a universal slope, as seen in Fig. 1.8(b-c).

1.2.4 Towards devices

Bringing skyrmionics into electronic devices offers unique opportunities for information and communications technologies. For example, the concept of racetrack mem-

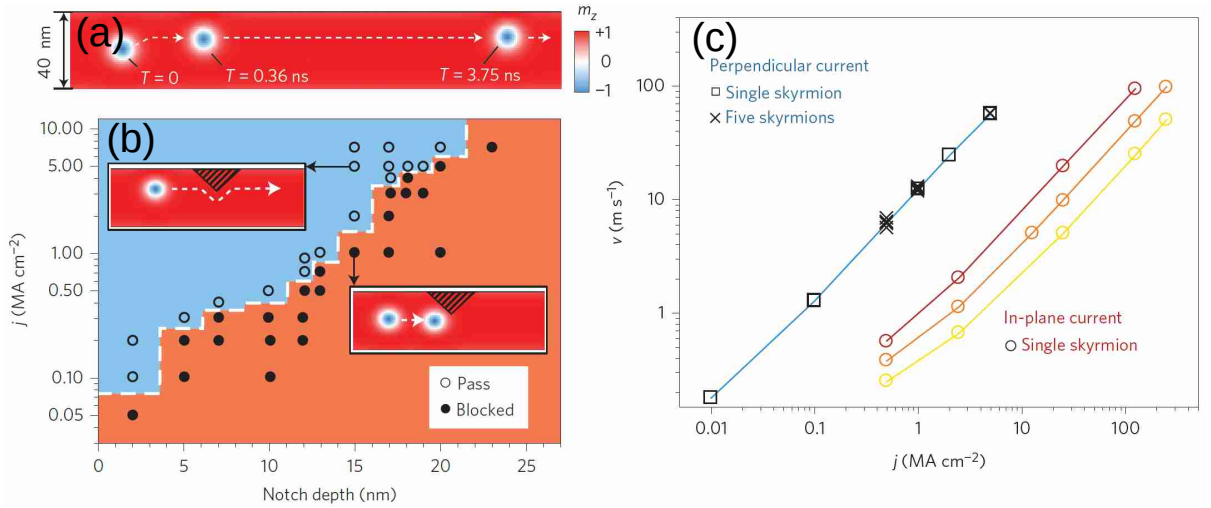

Figure 1.8 – (a) Motion of a skyrmion in a track as it bends the trajectory owing to repulsion by the edge and finally propagates along the edge. (b) Pinning of the current-induced motion of skyrmions by defects (triangular region of higher perpendicular anisotropy) in a 40-nm-wide nanotrack for different notch depths and current densities. (c) Skyrmion velocity v as a function of current density j for in-plane currents. Figures are adapted from Ref. [65].

ory [72], in which a train of up and down magnetic domains is moved electrically along a magnetic track, could be extended to skyrmionics. Specifically, Refs. [65,73,74] showed that exploiting the solitonic character of skyrmions, the information can be encoded by a sequence of individual skyrmions in a magnetic track, illustrated in Fig. 1.9(a). Such tracks for skyrmions may be realized using lithographic techniques to fabricate magnetic stripes which are put in contact with high SOC materials, or they may be aligned by spatial modulations of strain fields, magnetic anisotropies or relevant magnetic interactions [45]. Their diameters can be reduced by decreasing the width of the track, as shown in Fig. 1.9(b). The spacing between neighboring skyrmions in a track can be of the order of magnitude of the skyrmion diameter (down to a few nanometers) [65,75], and many such tracks can be stacked close together. This means that a much higher information density can be expected with skyrmions as compared with domain walls in a racetrack memory [60,76]. Moreover, because their motion is induced by spin torques, skyrmions can be guided in straight and curved tracks alike. Interestingly, the concept of skyrmion racetrack can be easily transformed and adapted to produce a nanoscale skyrmion transistor [77] by adding a field-induced gate in a given part of the track that allows or forbids the passage of a skyrmion, creating the equivalent of the on-off switch of a transistor.

The fact that a skyrmion behaves like a particle has motivated the application of skyrmionics to logic devices. Most of them rely on the conversion between a single skyrmion and a pair of DWs. This allows one to perform basic logic operations by duplicating or merging skyrmions through the design of specific nanostructures. Ref. [78] proposed logic gates AND and OR based on these concepts, which can be used as a first step to realize a complete logical architecture that replaces existing spin

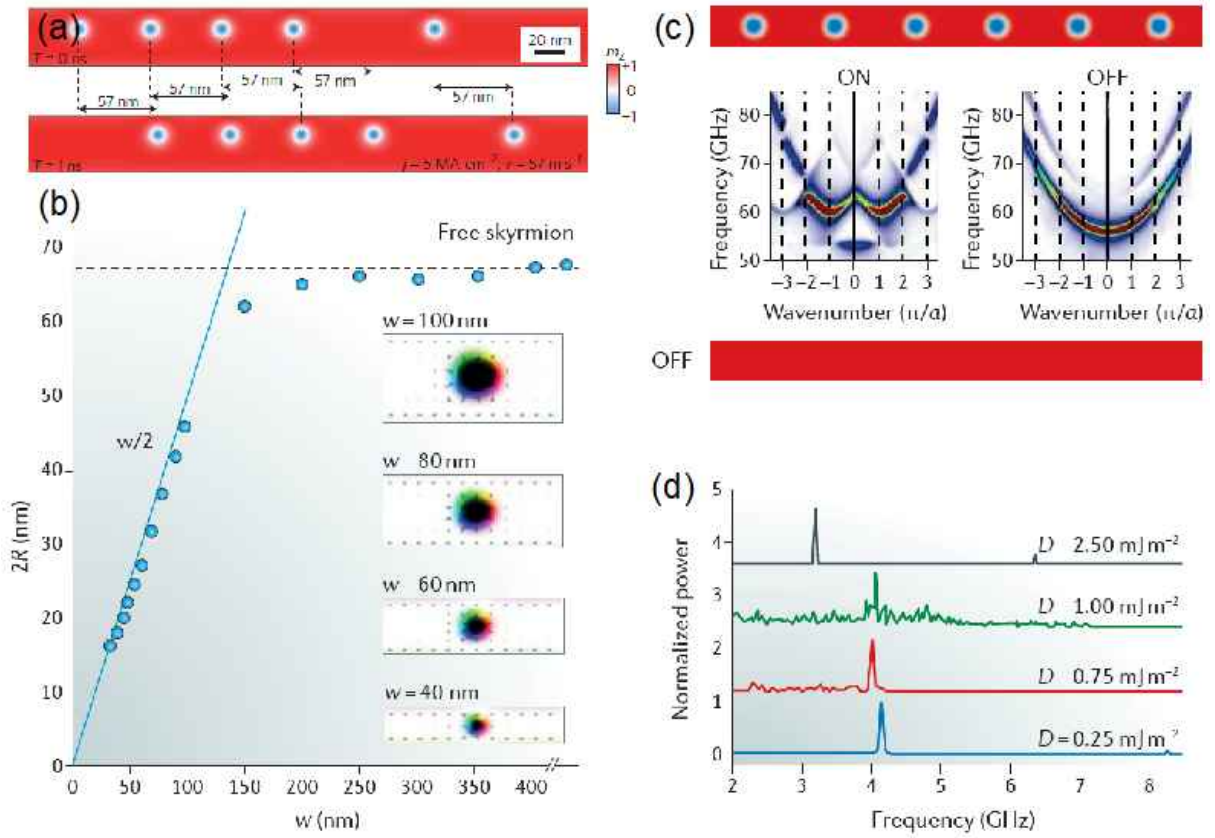

Figure 1.9 – (a) Individual and train of skyrmions in a racetrack, retrieved from Ref. [65]. (b) Micromagnetic simulations showing that skyrmions are compressed in a track. (c) Dispersion relation for spin-wave propagation along a magnonic waveguide with and without skyrmions, with gaps in frequency due to periodicity of the skyrmion lattice. (d) Frequency spectra of skyrmions excitation modes for different DM interaction constants, D. Figures are adapted from Ref. [44].

logic devices [44]. The ability to create artificial periodic arrangements of skyrmions in one- or two-dimensional nanostructures can be used for skyrmionic magnonic crystals. The artificial lattices are used to periodically modulate the magnetization and hence control the propagation of spin waves inside them. Skyrmionic crystals on the nanoscale can then be envisaged, which is unthinkable for conventional magnonic crystals. Such crystals can be dynamically reconfigured simply by changing the diameter of the skyrmions, or the periodicity of the lattice, or even by erasing it [79,80], see in Fig. 1.9(c). Another class of components for which skyrmionics can be used are nanoscale radio-frequency devices. For example, Ref. [81] proposed the skyrmion breathing modes of a skyrmion, induced by spin torques, can be used to generate a radio-frequency signal, as illustrated in Fig. 1.9(d). Being a localized soliton, the skyrmion is less sensitive to external perturbations and the resulting spin torque oscillator will exhibit a more coherent dynamic. Finally, a skyrmionic microwave detector was investigated in Ref. [82], which relies on the conversion of the resonant excitation of the breathing mode into a d.c. mixed voltage. For an extensive review of

skyrmionic devices, see Ref. [18].

1.2.5 Lifetimes

An important and often overlooked concept for the eventual commercialization of skyrmionics is the lifetime of a skyrmion state, which is one of the focuses of this thesis. Since skyrmions represent metastable states, they have finite energy barriers that can be overcome by thermal fluctuations. The lifetime describes the length of time a skyrmion exists before an excitation in energy induces its collapse to another available magnetic spin texture. The study on lifetimes of topological spin textures began when Bessarab [83] proposed a new method for characterizing their transitions in magnetic systems, based on minimum energy paths shown in Fig. 1.10(a). Rohart [84] was the first to study the stability of a single Néel skyrmion, revealing two distinct mechanisms for its collapse. However, it was later shown [85] and proven [86] that in fact only an isotropic shrinking of the skyrmion, or rotation of magnetic spins in the radial direction, represents a correct transition mechanism for Co monolayers on Pt. Moreover, the energy barriers for such transitions were found to be very small, on the order of tens of mili-electronvolts, meaning that single skyrmions can exist only for very short time scales, of nanoseconds, in ultrathin films. To make matters worse, Ref. [87] found that their stability drops drastically near the edges of a racetrack memory, as illustrated in Fig. 1.10(b). However, it was later demonstrated [88], as part of the results of this thesis, that the lifetime of skyrmions at room temperatures can be extended from nanoseconds to seconds by increasing the DMI and designing nontrivial atomic structures along the edges, making skyrmions much more favorable for future racetrack memories. Similar findings for the FePd bilayer on Pt were made in Ref. [89]. Other works on racetrack memories studied their energy surfaces [90] and confinement effects [91].

The lifetimes of skyrmions can also be considered in other contexts. Ref. [92] identified a new particle-like state, the chiral "bobber" shown in Fig. 1.10(c), and studied its stability in chiral magnets. Recently, the pinning of magnetic skyrmions on ever present material defects was analyzed, and their geometries exploited for the realization of practical devices [93]. The skyrmion stability was also analyzed against competing spin configurations [94]; both works are results of this thesis. Interestingly, von Malottki [95] demonstrated that exchange frustration can greatly enhance skyrmion stability, based on parameters from first-principles calculations. Wild [96], however, used Lorentz transmission electron microscopy to study the lifetime of skyrmions and found a substantial reduction by entropic effects, an extreme case of enthalpy-entropy compensation. Another contribution to the area is the study of other topological spin textures. Bessarab [97] recently characterized the stability and lifetime of anti-ferromagnetic skyrmions, and found them to be feasible to observe in experiments. Skyrmions with topological numbers other than unity were first investigated in Ref. [95], where the collapse of an anti-skyrmion was analyzed. This was extended to transition mechanisms and interactions between skyrmions of different topological orders [98], as a result of this thesis.

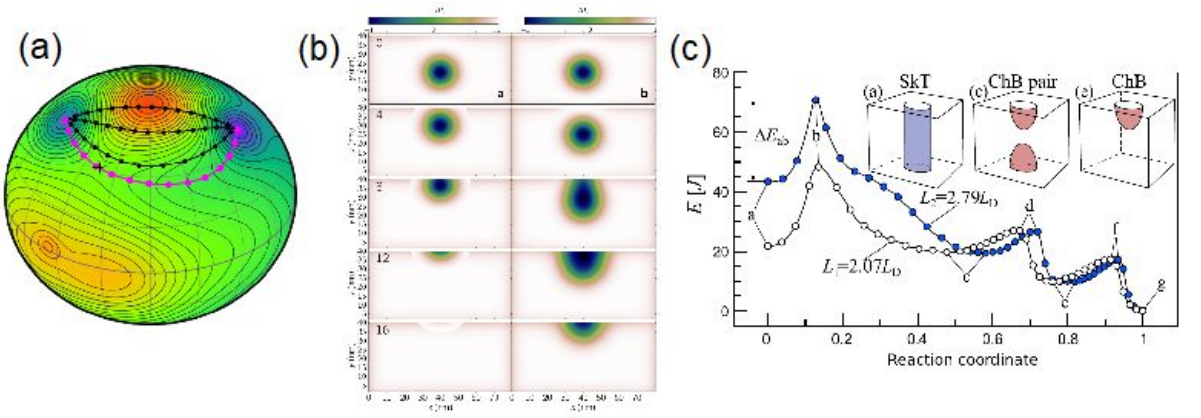

Figure 1.10 – (a) Minimum energy path for a single spin system with initial path chosen to lie near a maximum (red) between the energy minima (blue), while converged path is shown in pink. Figure is retrieved from Ref. [83]. (b) Initial path (left) and minimum energy path (right) for collapse of a skyrmion at the edge of a racetrack, adapted from Ref. [87]. (c) Minimum energy path from a Bloch skyrmion to a pair of chiral bubbles to a single chiral bubble for two thicknesses, L_1 and L_2, retrieved from Ref. [92].

1.3 Motivation

Skyrmions exhibit fascinating new properties that distinguish the spin texture from others. Their behavior mimics that of particles, which along with their topology, makes them useful objects in which to encode information. Even though concepts of topology are ubiquitous in several of the most exciting recent advances in condensed matter physics, such as high-temperature interfacial superconductivity, quantum Hall effect, or topological insulators, magnetic skyrmions remain the most promising candidates for consumer nanoelectronics. Amazing advances have been made in the field, providing all the basic function needed for information storage and processing: writing (nucleation of individual skyrmions), processing (current-induced motion), and reading the information (electrical detection of single skyrmions). However, many of the findings are obtained only at low temperature and for skyrmion lattices, rather than for single skyrmions at room temperature. Another issue is the misuse of numerical simulations for describing certain physics involving magnetic skyrmions. For example, the thermal stability (or lifetime) of single skyrmions, which is vital for their practical use in devices, cannot be quantified using the continuous description of magnetization assumed in micromagnetics, by far the most popular numerical choice in magnetism. Similar arguments hold true in regards to the behavior and stability of skyrmions around defects, as well as their interactions with one another. Possibly, the overarching problem involves either processes that take too long for direct simulations, such as magnetic transitions that are rare events on the time scale of spin oscillations, or twisting of the spin texture in a way that cannot be described continuously. In these situations, one must resort to another set of numerical approaches to accurately describe the desired physics. One viable candidate is minimum en-

ergy paths combined with atomistic models of magnetism (this will be discussed in more detail in Chapter 2). Therefore, the purpose of this thesis is to advance the current understanding of skyrmion physics, as well as provide possible applications for skyrmionics, using the discussed methods. The present work is very important for the experimental realization of nanoelectronic devices based on skyrmions and can be divided into the following categories:

I. Skyrmions in multilayers: To date, DMI has been found in few bulk materials, but can also be induced in atomically thin magnetic films in contact with surfaces with large SOC interactions. Recent experiments have reported that isolated magnetic skyrmions can be stabilized even near room temperature in few-atom thick magnetic layers sandwiched between materials that provide asymmetric SOC. However, a proper analysis of the lifetimes of single skyrmions in such multilayers remains lacking. *We therefore study the thermal stability of isolated skyrmions in ultrathin chiral magnetic structures composed of few monolayers, and try to find ways to improve their stability for constrained geometries.* This will be the topic of Chapter 3.

II. Pinning on defects: Pinning due to ever present material imperfections crucially affects the mobility of skyrmions. Therefore, a proper understanding of how magnetic skyrmions pin to defects is necessary for the development and performance of skyrmionic devices. Existing works assume a phenomenological model for pinning (effective parabolic potentials) rather than a microscopically justified one. *We revisit the pinning of a magnetic skyrmion by considering the minimum energy paths for transition from pinned to unpinned states, exploring linear and planar defect geometries that can be exploited to develop practical devices.* The results are presented in Chapter 4.

III. Competing spin backgrounds: The stability of isolated skyrmions was thoroughly studied in ferromagnetic cobalt or iron based structures. However, other spin configurations can compete with skyrmions when considering novel magnetic materials and substrates, and a proper understanding of how magnetic skyrmions transit to alternative non-trivial spin structures becomes crucial, both from a theoretical perspective and for applications in devices. *We explore transitions between skyrmion lattices and spin cycloids, and provide reflections on their thermal stability against competing transition mechanisms.* This will be discussed in Chapter 5.

IV. Manipulations in topology: The discovery of nontrivial topological particles has brought about much innovation in modern matter physics. A great deal of attention is being placed on metastable states characterized by high thermodynamic stability, which are able to persist for long periods of time. Among them, magnetic skyrmions have been of particular interest since they are expected to provide the means for electric control of magnetism. Such nontrivial topological particles are rather desirable as they can bring richer physics, and may allow for more involved practical applications. Recently, skyrmions with topological numbers other than unity have been studied theoretically, but their stability and mechanisms for transition remain elusive both in theory and in experiments. *We therefore report on the theoretical discovery of switching mechanisms and interactions between skyrmions with distinct topological charges.* This will be the topic of Chapter 6.

1.4 Organization

The thesis is organized as follows:

In **Chapter 2**, we introduce theoretical concepts of magnetic skyrmions. We also introduce the numerical approaches for simulating the considered magnetic textures. The concepts put forth will be used in the rest of the thesis.

In **Chapter 3**, we investigate the behavior of isolated skyrmions in ultrathin chiral magnetic films composed of few-monolayers. The structures considered are similar to those used for multilayers at room-temperature, and an approach to improve their stability in racetrack memories is proposed. The results of this Chapter are published in Ref. [88].

In **Chapter 4**, the effect of defects on pinning of magnetic skyrmions is investigated. We show that different material inhomogeneities have different effects on the skyrmion. Linear and planar defect geometries that can be used in practical applications are also explored. The results of this Chapter are published in Ref. [93].

In **Chapter 5**, we reveal that other spin configurations can compete with skyrmions when considering new materials. We put forth a previously unknown transition mechanism from skyrmion lattices to spin cycloids. Furthermore, we show that the effective stability of single skyrmions is lowered when all possible spin configurations are considered. The results of this Chapter are published in Ref. [94].

In **Chapter 6**, the underlying switching mechanisms between skyrmions with different topological numbers is investigated. We find that skyrmions with higher topological charges are more likely to transition into other topologies. The interactions between skyrmions of different topological charges can be attractive or repulsive, leading to the formation of arranged clusters or a sea of isolated spin textures. The results of this Chapter are published in Ref. [98].

In **Chapter 7**, we present an overview of the numerical library which was developed along with this thesis. The library represents a culmination of the computational effort made in each of the previous chapters. The focus is placed on the numerical approaches that were used, and examples on how to simulate some of the discussed problems. The results of this Chapter are published in Ref. [99].

In **Chapter 8**, we briefly summarize the results of this thesis and give closing remarks and discuss future outlook.

2 THEORY AND NUMERICAL CONCEPTS

The unusual topology and particle-like behavior launched skyrmions into the spotlight of scientific research. In this Chapter we will detail some of the theory behind magnetic skyrmions. We start by introducing their spin structure and the atomistic spin model, which proves to be an extremely useful tool for their description. We then discuss the multi-scale approach that allows us to simulate systems closer to experiment. We are interested in inhomogeneous material systems, which we model with spatially varying material parameters and beyond nearest neighbor interactions. Working with skyrmions requires special numerical techniques, so we present three popular approaches that deal with magnetic systems on the atomic scale.

2.1 Skyrmions

2.1.1 Spin structure

Skyrmions can be either of the Néel-type or the Bloch-type, which correspond to different symmetries of the interaction between spins, resulting in different directions of rotation [44]. For example, this can be due to the underlying crystal lattice [26,32,100] for Bloch skyrmion, or due to the presence of an interface [47,48] for Néel skyrmions. In most systems, the spin structure of skyrmions is determined by the competition between chiral interactions of the isotropic exchange and Dzyaloshinskii–Moriya (DM) type. Other possible candidates for stabilizing magnetic skyrmions include frustration of isotropic exchange interactions [52], four-spin interactions [47], and dipole-

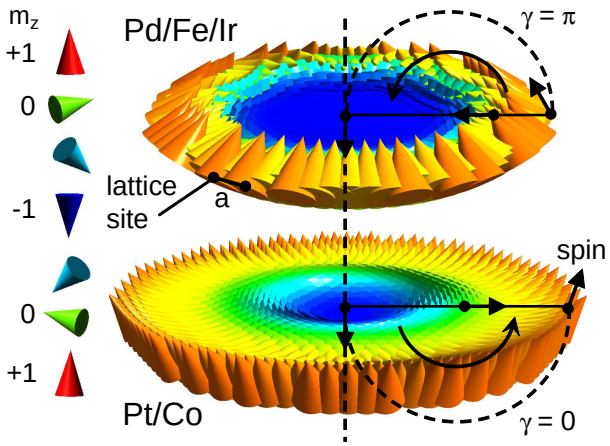

Figure 2.1 – Single Néel skyrmion in a Pd/Fe/Ir (top) and a Pt/Co (bottom) nanostructure. The spins are represented by cones which are centered on lattice sites, separated by the atomic distance a. The resulting skyrmions have opposite helicities of $\gamma = 0$ and $\gamma = \pi$ in the two materials.

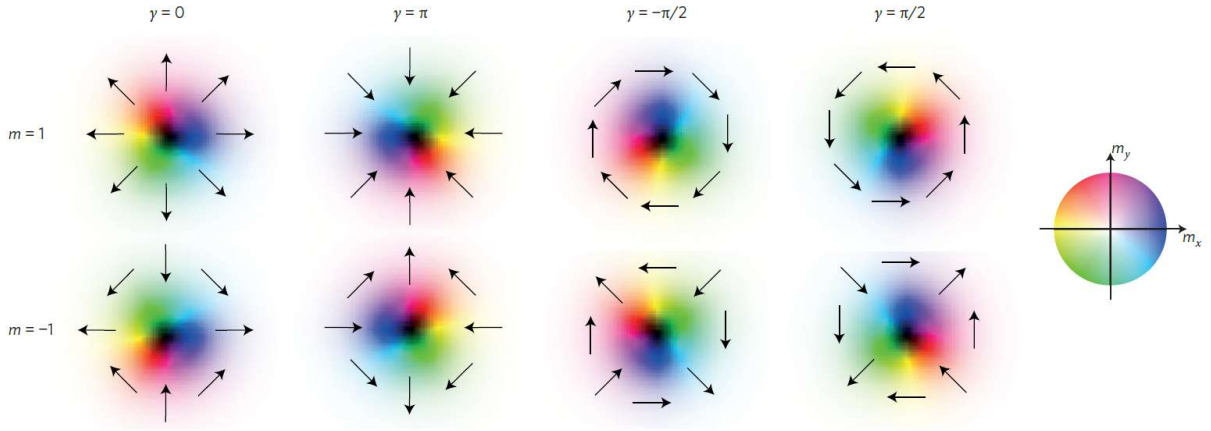

Figure 2.2 – Skyrmion structures with varying m and γ. The arrows indicate the direction of the in-plane spin component, and the brightness indicates the normal component to the plane, with white denoting the up direction and black the down direction. Figure retrieved from Ref. [35].

dipole interactions. The latter is responsible for magnetic bubbles, but they would not have the defined chirality found in skyrmions [24, 60]. The size and shape of the skyrmion can be manipulated by the geometry of the system and external magnetic fields [76, 101].

The focus of this thesis is on Néel skyrmions, which consist of atomic spins arranged in near two-dimensional magnetic structures, as illustrated in Fig. 2.1. On the atomic level, the structure contains spin orientations localized on atomic sites, separated by the lattice constant a. The lattice constant is the distance between atoms and depends on the magnetic material being considered. The spin at the skyrmion center (or core) points along an out-of-plane direction, while spins at the perimeter point in the opposite direction. The magnetization rotates radially from the skyrmion center to the perimeter, where the sense of rotation is set by the chirality (or equivalently, the helicity) of the skyrmion. We can determine the direction of the skyrmion by the orientation of the center spin, and the size from the spin orientations in the same half-plane as its direction.

2.1.2 Helicity and vorticity

Skyrmions can be defined by the Pontryagin number Q (or topological number), which is a measure of the winding of the normalized local magnetization, $\hat{\boldsymbol{m}}(\boldsymbol{r})$. In two dimensions, the topological number can be mathematically described by

$$Q = \frac{1}{4\pi} \int \hat{\boldsymbol{m}}(\boldsymbol{r}) \cdot \left(\frac{\partial \hat{\boldsymbol{m}}(\boldsymbol{r})}{\partial x} \times \frac{\partial \hat{\boldsymbol{m}}(\boldsymbol{r})}{\partial y} \right) dxdy, \tag{2.1}$$

as the integral of the solid angle, 4π, and counts how many times $\hat{\boldsymbol{m}}(\boldsymbol{r}) = \hat{\boldsymbol{m}}(x, y)$ wraps the unit sphere [35, 102, 103]. Using the symmetry of the skyrmion, we can represent the spins in the spherical variables Θ and Φ as

$$\hat{\boldsymbol{m}}(\boldsymbol{r}) = \hat{\boldsymbol{m}}(\Theta, \Phi) = (\sin\Theta\cos\Phi, \sin\Theta\sin\Phi, \cos\Theta), \tag{2.2}$$

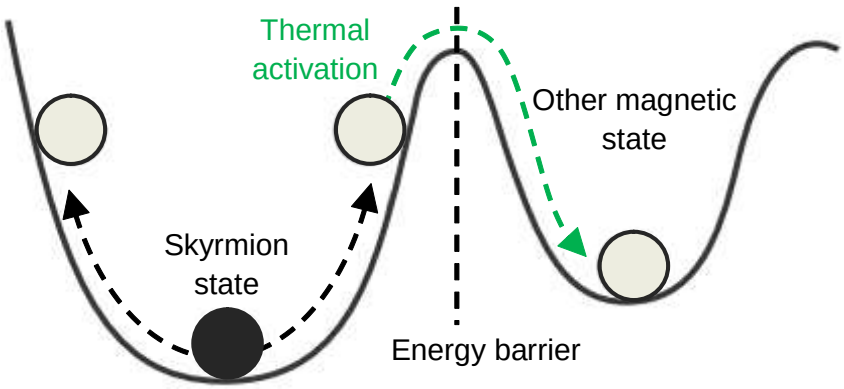

Figure 2.3 – Artistic sketch of a metastable skyrmion being thermally activated and collapsing into another magnetic state.

with

$$\Phi = m\phi + \gamma, \tag{2.3}$$

where ϕ is the azimuthal angle ($0 \leq \phi \leq 2\pi$) and γ is the helicity. The vorticity m determines the skyrmion number as $Q = m$. Special values of the helicity ($\gamma = 0, \pi/2, \pi, 3\pi/2$) play important roles [56], they also determine the chirality of the skyrmion. For Néel skyrmions the helicity is either $\gamma = 0$ or $\gamma = \pi$ and determines whether the in-plane spins are oriented inward or outward (see Fig. 2.1), while Bloch skyrmions have helicity of $\gamma \pm \pi/2$ which defines a clockwise or counterclockwise rotation of the in-plane spins. Different helicities are obtained for different DM interactions. We may index a skyrmion as (Q, γ) with the use of the topological number and the helicity. Fig. 2.2 illustrates various skyrmion structures corresponding to vorticity $m = \pm 1$, and helicity $\gamma = 0, \pm\pi/2, \pi$. Note that Q reverses sign when all the directions of the magnetic moments are reversed, $\hat{\boldsymbol{m}} \to -\hat{\boldsymbol{m}}$, and the configuration can be called an "anti-skyrmion".

2.1.3 Topological protection

A question studied in many fields of science is the lifetime of metastable states. Thermal activation across energy barriers governs the lifetime of memory elements in electronics and the transport of ions and electrons in disordered media [96]. Often, these processes are controlled by the activation energy. Special attention is drawn to systems which are able to persist in a particular metastable state for an unbounded or noticeably long time. One prominent example, and the focus of these thesis, are skyrmions induced in magnetic materials with chiral interactions. Particularly, the non-trivial topology of skyrmions plays a crucial role in their stability [35, 84]. In the continuous limit, the topology gives rise to a topological barrier that protects the skyrmion from other competing spin configurations, such as ferromagnetic (FM) and cycloidal (helical or conical) orders [43], as the spin configuration cannot be twisted continuously to result in a magnetic configuration with a different topology. This can also be interpreted as the fact that a Bloch point has to appear, resulting in an infinite exchange energy contribution. However, in real materials the system is discrete with

magnetic moments localized on atoms, which results in finite energy or topological barriers that can be surpassed by thermal fluctuations, as illustrated in Fig. 2.3.

Owing to their topological protection, skyrmions are highly stable [104], but only in applied field and at low temperature, which limits their use as individual particles in devices. Therefore, understanding the extent of topological protection in magnetic skyrmions, as well as finding ways to preserve their stability, remains crucial. These concepts are addressed in this thesis.

2.2 Atomistic spin model

While quantum mechanical in nature, magnetic materials are heavily influenced by thermal effects that are often difficult to describe using standard approaches from quantum theory. Therefore, models of magnetic materials should combine their quantum mechanical characteristics with thermodynamic formalism, for example, using atomistic spin models. The physical basis of atomistic spin models is the localization of unpaired electrons to atomic sites, where atoms are treated as possessing localized magnetic moments. This assumption has been proven valid for ferromagnets based on first-principles calculations [105]. Atomistic models of magnetic materials originated with Ising in 1925, as the first model of the behavior in a ferromagnet [106]. However, the forced quantization of atomic moments to one of two allowed states limits the uses of the Ising model in real materials, e.g., the anisotropy is infinite. A natural extension is to take a continuous description of the spin direction in three dimensions [107], which corresponds to the Heisenberg model. Stanley further generalized the dimensionality of spins in the n-vector model [108], which reduces to the Heisenberg model for $n = 3$. In some ways the classical spin model is analogous to Molecular Dynamics, where the energy of the system is determined from quantum mechanics, but the time evolution and thermodynamics are treated classically [109].

The extended Heisenberg spin model describes the essential physics of a magnetic material at the atomic level, and is formed from a summation of energy contributions given by a Hamiltonian of the form

$$\mathcal{H} = \mathcal{H}_{exc} + \mathcal{H}_{ani} + \mathcal{H}_{app} + \mathcal{H}_{dip}, \tag{2.4}$$

each of which describes the interaction between an atomic spin moment, $\boldsymbol{\mu}_i$, and neighboring moments or external magnetic fields. Note that one can introduce a three dimensional unit vector, $\hat{\boldsymbol{m}}_i = \boldsymbol{\mu}_i/|\boldsymbol{\mu}_i|$, describing the direction of the effective magnetic moment, $\boldsymbol{\mu}_i$, localized on atomic sites. Each of the individual contributions to the Hamiltonian $\mathcal{H}$ are described in detail below.

2.2.1 Exchange interactions

As two identical particles are localized close to each other, their wavefunctions can overlap yielding the exchange interaction. The effect is due to the wavefunction of indistinguishable particles being subject to exchange symmetry, and the Pauli exclusion principle [110], which governs the orientation of electron spins in overlapping orbitals. The dominant contribution to $\mathcal{H}$ in ferromagnetic materials comes from the

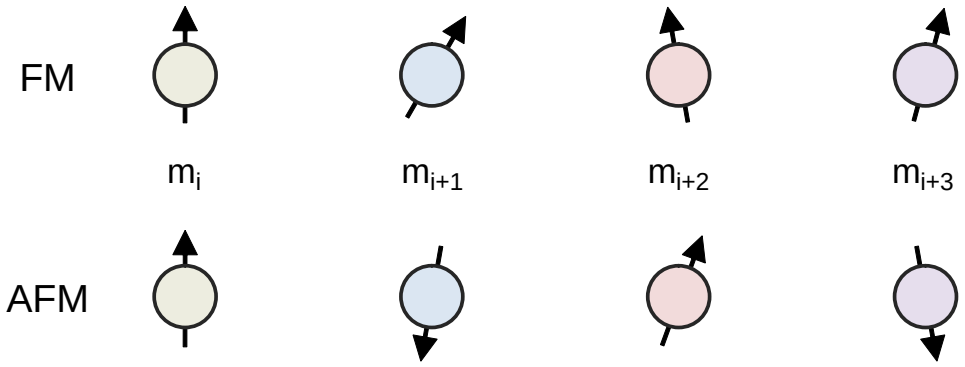

Figure 2.4 – One-dimensional sketch to illustrate the effect of nearest neighbor isotropic and antisymmetric exchange interactions in FM (upper panel) and AFM (lower panel) materials.

exchange Hamiltonian

$$\mathcal{H}_{exc} = -\frac{1}{2}\sum_{ij} \hat{\boldsymbol{m}}_i \mathcal{J}_{ij} \hat{\boldsymbol{m}}_j, \tag{2.5}$$

in which the sum is taken over the exchange Hamiltonians for all the i, j pairs of the system of interacting atomic moments. The tensorial exchange coupling, $\mathcal{J}_{ij}$, is a 3×3 matrix of the form

$$\mathcal{J}_{ij} = \begin{bmatrix} J_{ij}^{xx} & J_{ij}^{xy} & J_{ij}^{xz} \\ J_{ij}^{yx} & J_{ij}^{yy} & J_{ij}^{yz} \\ J_{ij}^{zx} & J_{ij}^{zy} & J_{ij}^{zz} \end{bmatrix}, \tag{2.6}$$

where its elements can be denoted by $J_{ij}^{\alpha\beta}$ and $\alpha, \beta = x, y, z$. The matrix describes the exchange interaction between atomic sites i and j, and can be decomposed into three terms [111]:

$$\mathcal{J}_{ij} = J_{ij}\mathcal{I} + \mathcal{J}_{ij}^{S} + \mathcal{J}_{ij}^{A}. \tag{2.7}$$

$\mathcal{I}$ is the identity matrix and J_{ij} represents the isotropic exchange interaction

$$J_{ij} = \frac{1}{3}\mathrm{Tr}(\mathcal{J}_{ij}), \tag{2.8}$$

which corresponds to the classical Heisenberg exchange. For ferromagnetic (FM) materials the exchange energy favors neighboring spins that align in parallel, or $J_{ij} > 0$, and for antiferromagnetic (AFM) materials the interaction prefers the spins to align anti-parallel, or $J_{ij} < 0$, as shown in Fig. 2.4. This is by far the dominating term in the Hamiltonian, and can be an order of magnitude larger than the next largest contribution. The second term, $\mathcal{J}_{ij}^{S}$, corresponds to the traceless symmetric anisotropic exchange coupling [112, 113]

$$\mathcal{J}_{ij}^{S} = \frac{1}{2}(\mathcal{J}_{ij} + \mathcal{J}_{ij}^{T}) - J_{ij}\mathcal{I}, \tag{2.9}$$

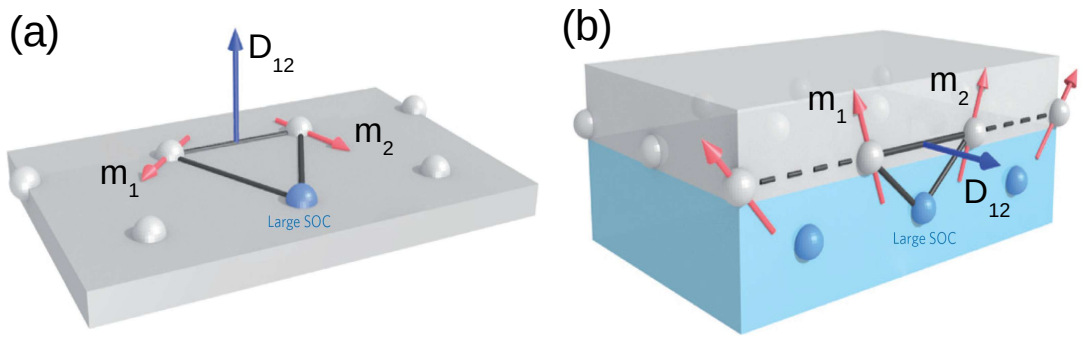

Figure 2.5 – Schematic of DM interaction, $\boldsymbol{D}_{12}$, induced by (a) the indirect exchange of the triangle composed of two atomic spins, $\hat{\boldsymbol{m}}_1$ and $\hat{\boldsymbol{m}}_2$, and an atom with a strong SOC, and (b) at the interface between a ferromagnetic metal (grey) and a metal with a strong SOC (blue) (right panel). Figure was adapted from Ref. [60].

where $\mathcal{J}_{ij}^T$ is the transpose of the exchange tensor. This is also known as the anisotropic exchange or two-site magnetic anisotropy. Lastly, the third term is the antisymmetric exchange interaction

$$\mathcal{J}_{ij}^A = \frac{1}{2}(\mathcal{J}_{ij} - \mathcal{J}_{ij}^T). \tag{2.10}$$

The antisymmetric part represents the Dzyaloshinsky-Moriya interaction (DMI) [33, 34]

$$\hat{\boldsymbol{m}}_i \mathcal{J}_{ij}^A \hat{\boldsymbol{m}}_j = \boldsymbol{D}_{ij} \cdot (\hat{\boldsymbol{m}}_i \times \hat{\boldsymbol{m}}_j), \tag{2.11}$$

where $\boldsymbol{D}_{ij}$ is the Dzyaloshinsky-Moriya (DM) vector defined as

$$D_{ij}^x = \frac{1}{2}(J_{ij}^{yz} - J_{ij}^{zy}), \quad D_{ij}^y = \frac{1}{2}(J_{ij}^{xz} - J_{ij}^{zx}), \quad D_{ij}^z = \frac{1}{2}(J_{ij}^{xy} - J_{ij}^{yx}), \tag{2.12}$$

arising from a three-site indirect exchange mechanism that couples two atomic spins to a neighbor atom with large spin-orbit coupling [114] (see Fig. 2.5). For atomically-thin ferromagnetic films considered in this thesis, the DMI is interfacial and can be written as $\boldsymbol{D}_{ij} = D_{ij} \cdot (\hat{\boldsymbol{z}} \times \hat{\boldsymbol{u}}_{ij})$ [48], where $\hat{\boldsymbol{z}}$ and $\hat{\boldsymbol{u}}_{ij}$ are unit vectors perpendicular to the interface in the direction of the magnetic layer and pointing from site i to site j, respectively. The DM interaction lowers or increases the energy of the spins depending on whether the rotation from $\hat{\boldsymbol{m}}_i$ to $\hat{\boldsymbol{m}}_j$ around $\boldsymbol{D}_{ij}$ is in the clockwise or in the anticlockwise direction. For $D_{ij} > 0$ the DMI favors anticlockwise rotations from $\hat{\boldsymbol{m}}_i$ to $\hat{\boldsymbol{m}}_j$, while for $D_{ij} < 0$ the interaction prefers clockwise rotations [47, 48]. If $\hat{\boldsymbol{m}}_i$ and $\hat{\boldsymbol{m}}_j$ are initially parallel, a strong DMI compared with the symmetric exchange interaction, J_{ij}, will introduce a relative tilt around $\boldsymbol{D}_{ij}$. This tilt is responsible for the formation of magnetic skyrmions. We can then rewrite the exchange Hamiltonian as a function of the isotropic, symmetric anisotropic, and antisymmetric (or DM) exchanges as

follows:

$$\mathcal{H}_{exc} = -\frac{1}{2}\sum_{ij} \hat{\boldsymbol{m}}_i (J_{ij}\mathcal{I} + \mathcal{J}_{ij}^S + \mathcal{J}_{ij}^A)\hat{\boldsymbol{m}}_j \tag{2.13}$$

$$= -\frac{1}{2}\sum_{ij} J_{ij}(\hat{\boldsymbol{m}}_i \cdot \hat{\boldsymbol{m}}_j) - \frac{1}{2}\sum_{ij} \hat{\boldsymbol{m}}_i \mathcal{J}_{ij}^S \hat{\boldsymbol{m}}_j - \frac{1}{2}\sum_{ij} \boldsymbol{D}_{ij} \cdot (\hat{\boldsymbol{m}}_i \times \hat{\boldsymbol{m}}_j) \tag{2.14}$$

$$= \mathcal{H}_{iso} + \mathcal{H}_{sym} + \mathcal{H}_{DM}. \tag{2.15}$$

2.2.2 Magneto-crystalline anisotropy

The thermal stability of a magnetic material is dictated by the anisotropy, or the tendency for atomic moments to align along a preferred spatial direction. While there are different physical origins for anisotropy, the most important is the magneto-crystalline anisotropy arising from the interaction of atomic spin orbitals with the local crystal environment [115]. The simplest form of anisotropy is uniaxial, where the magnetic moments prefer to align along a single axis, $\hat{\boldsymbol{e}}$. Uniaxial anisotropy exists where the crystal lattice is distorted along a single axis. For example, in ultrathin magnetic films the anisotropy is normal to the surface. The uniaxial anisotropy Hamiltonian is given by

$$\mathcal{H}_{ani} = -\sum_i K_i (\hat{\boldsymbol{m}}_i \cdot \hat{\boldsymbol{e}})^2, \tag{2.16}$$

where K_i is the anisotropic energy per atom i. Other forms of anisotropy include the cubic anisotropy which appears in materials with cubic crystal structures, and the two-site anisotropy which originates from the interaction of neighboring spins.

2.2.3 Externally applied fields

Many magnetic problems consist of interactions with external applied fields, $\boldsymbol{H}_{app}$. External fields can arise in many ways, such as from an electric current or a nearby magnetic material. They play a crucial role in stabilizing nanoscale skyrmions in near two dimensional magnetic films. In an external field, magnetic moments will experience a torque proportional to the angle between the field and the spin direction, as well as the field strength. The applied field energy is given by

$$\mathcal{H}_{app} = -\sum_i \boldsymbol{\mu}_i \cdot \boldsymbol{H}_{app}, \tag{2.17}$$

where $\boldsymbol{\mu}_i$ is the effective magnetic moment localized on atomic site i, as defined earlier. This term favors a parallel alignment of the spins along the field direction, moving the system towards a ferromagnetic state for increasing values of the field.

2.2.4 Dipole-dipole interactions

From electrodynamics, magnetostatic (or dipolar) interactions refer to the direct interaction between magnetic dipoles, or atomic spin moments. Thus, the magnetized body will have a certain dipolar field opposing the overall magnetization. This dipolar

field depends on the size and shape of the magnetic body, and on the separation of individual moments. In the point-dipole approximation, the Hamiltonian for dipole-dipole interactions is given by

$$\mathcal{H}_{dip} = -\frac{\mu_0}{8\pi} \sum_{ij} \frac{3(\boldsymbol{\mu}_i \cdot \hat{\mathbf{r}}_{ij})(\boldsymbol{\mu}_j \cdot \hat{\mathbf{r}}_{ij}) - \boldsymbol{\mu}_i \cdot \boldsymbol{\mu}_j}{r_{ij}^3}, \tag{2.18}$$

which sums over all moment pairs, where μ_0 is the permeability of free space, $\hat{\mathbf{r}}_{ij}$ is the unit position vector between sites i and j, and r_{ij} is the distance between sites i and j.

2.3 Features in the numerics

2.3.1 Multi-scale modeling

Magnetism has a quantum origin with systems characterized by atomic magnetic moments, the exchange interaction, and spin-orbit coupling, to name a few. These are the province of ab initio models, but long simulation times limits the problem size to several hundred atoms, making a study of macroscopic systems from first principles intractable. In addition, magnetic materials are heavily influenced by thermal effects which are typically difficult to incorporate into standard density functional theory approaches. Therefore, models of magnetic materials should combine quantum mechanical properties with a robust thermodynamic formalism [109].

Density functional theory (DFT) calculations rely on the Hohenberg–Kohn–Sham theory [116], which states that the total energy of a system can be described by the electron density, ρ. In practice, both the electron and spin density are used in the total energy expression for spin polarized systems [117]. DFT can calculate a wide range of properties including lattice constants, localized spin moments, magnetic ground states and effective anisotropy. Standard software packages such as VASP [118] and FLEUR [119] make such calculations readily accessible. They provide detailed insight into magnetic properties that can be used as input into atomistic models.

In this situation, multiscale modeling can provide a proper description by using the results from ab initio calculations (on a system with a small size) to provide the magnetic parameters which will be included in the atomistic simulations. A significant capability of the atomistic spin model is that magnetic properties calculated at the electronic level can often be mapped onto a Heisenberg spin model with effective local moments. This multiscale electronic and atomistic approach treats magnetic materials at the natural atomic scale and avoids the continuum approximations of micromagnetics. However, one can also calculate effective parameters for larger scale micromagnetic simulations [120, 121]. The atomistic model can interface directly with micromagnetism by calculating interface properties at the atomic level, while treating the bulk of the material with a micromagnetic description [122]. Such approaches have become popular in simulating magnetic skyrmions [123, 124].

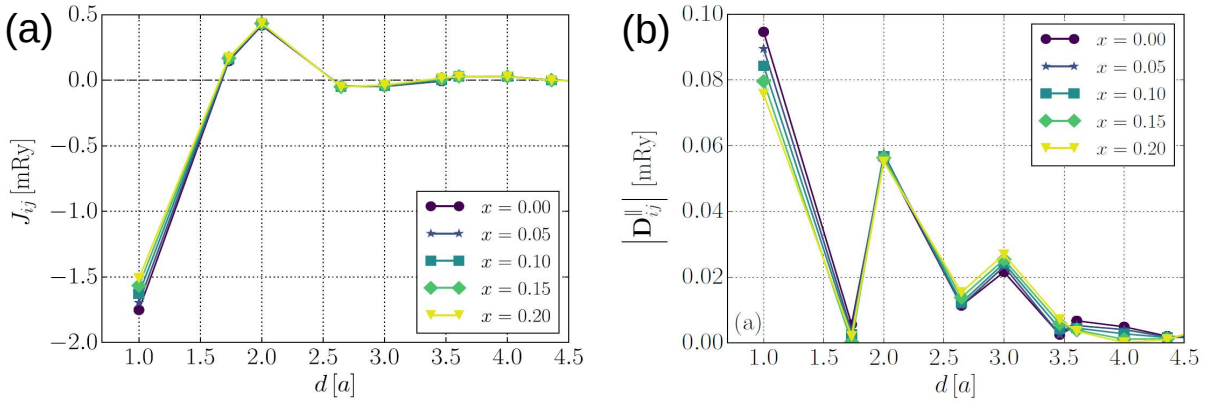

Figure 2.6 – (a) Isotropic exchange interactions, J_{ij}, and (b) in-plane DM vector components, $\boldsymbol{D}_{ij}^{||}$, in a $(Pt_{1-x}Ir_x)Fe$ bilayer on Pd(111), as a function of the distance d between the Fe atoms, for different Ir concentrations x in the overlayer. Figure adapted from Ref. [125].

2.3.2 Beyond nearest neighbors

The exchange Hamiltonian can be approximated to include only nearest neighbors of the exchange interactions, due to their strong distance dependence. However, in many materials the exchange interactions can extend to several atomic spacings [126], with the presence of FM and AFM contributions. For example, Fig. 2.6 shows that in a $(Pt_{1-x}Ir_x)Fe$ bilayer on Pd(111) the isotropic exchange and DM interactions have non-zero contributions up to $d \sim 4a$. The change in sign of J_{ij} results in exchange frustration which has been recently found responsible for attractive magnetic skyrmions [125], further discussed in Chapter 6. This leads to complex behaviors of the magnetic body that cannot be described using an effective exchange coupling. Neighbor-resolved exchange interactions can greatly enhance the stability of magnetic skyrmions [95]. Meanwhile, exchange frustration plays a crucial role in constructing skyrmion structures of different topologies [53, 58]. One can easily incorporate long-range exchange interactions by including pair terms that are beyond nearest neighbors in Eq. (2.13). The exchange coupling coefficients, J_{ij} and D_{ij}, are typically retrieved either from experiments [127] or from ab initio calculations [53, 125, 128, 129].

2.3.3 Material inhomogeneities

Inhomogeneities in the material parameters can have a large effect on the magnetic system. They typically arise from distinct origins and appear in any of the terms in Eq. (2.4). These inhomogeneous terms can be viewed as naturally occurring imperfections in the magnetic material such as impurity atoms, lattice defects, and geometrical constrictions. However, they can also result from artificial engineering of the material for desired behavior. Physically, the local minima of exchange strength can be realized by engineering the density of itinerant electrons in the material [130, 131]. One can alter DMI locally by increasing the interfacial spin-orbit coupling with two different materials below and above the film [49, 50], and using lithographic techniques to change or remove the heavy-metal layer on top, see Chapter 3 for examples. The

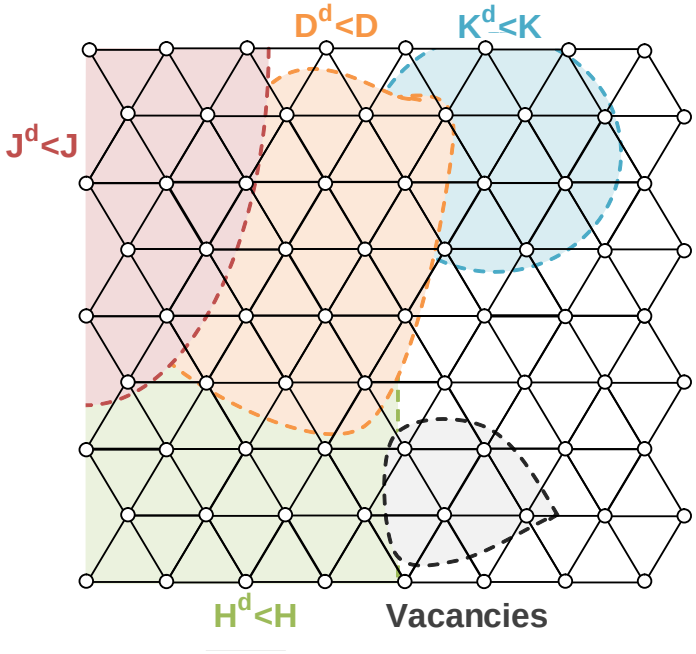

Figure 2.7 – Schematic of hexagonal lattice with inhomogeneities in the isotropic exchange interactions ($J^d < J$), DM interactions ($D^d < D$), anisotropy ($K^D < K$), and applied fields ($H^d < H$), located in colored regions with dashed boundaries. Atomic vacancies in the magnetic material are also present.

strength of the magnetic anisotropy can be varied by distortions in the underlying atomic lattice and from impurity sites [69,71]. Lastly, the ever present atomistic vacancies in ultrathin magnetic layers can be strategically introduced and patterned to provide particular collective or individual manipulation of skyrmions [46]. Therefore, these inhomogeneities act as pinning sites and can result in an effective slow-down or even capturing of magnetic skyrmion [51,132], which is the focus of Chapter 4.

Numerically, material inhomogeneities are introduced by changing the material parameters, possibly obtained from ab initio calculations, for specific atomic sites. While the anisotropy and field can be easily changed at a given atomic position, for the exchange interactions we must identify the coupling coefficients that correspond to a given pair of atomic spins. For example, Fig. 2.7 illustrates how different inhomogeneities are mapped to the atomic lattice. Lastly, inhomogeneities of distinct material parameters can be combined to construct more realistic situations, or to model atomic vacancies in the magnetic material.

2.4 Spin dynamics

2.4.1 Landau-Lifshitz-Gilbert equations

While the Hamiltonian describes the energetics of the magnetic system, it provides no information regarding its time evolution. The first understanding of spin dynamics came from experiments on ferromagnetic crystals, where the time dependent behavior

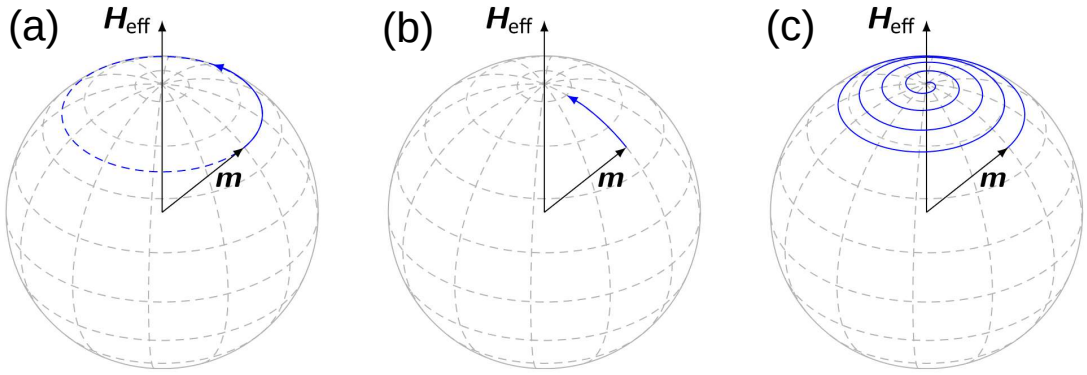

Figure 2.8 – Time evolution of a single magnetic moment as described by the Landau-Lifshitz-Gilbert equation. The motion can be divided into (a) a precessional motion around the effective field and (b) a damped motion that relaxes the magnetization towards the effective field. (c) The resulting motion including precession and damping. Figure retrieved from Ref. [133].

of the magnetic moments was described by the phenomenological equation derived by Lifshitz and Landau [134], with the effect of relativistic interactions also included as a damping term. The Landau-Lifshitz (LL) equation is given in the modern form by

$$\frac{\partial \hat{\boldsymbol{m}}}{\partial t} = -\gamma \left[\hat{\boldsymbol{m}} \times \boldsymbol{H} + \alpha \hat{\boldsymbol{m}} \times (\hat{\boldsymbol{m}} \times \boldsymbol{H}) \right], \tag{2.19}$$

where $\hat{\boldsymbol{m}}$ is a unit vector describing the direction of magnetization, $\boldsymbol{H}$ is the effective field acting on the material, γ is the gyromagnetic ratio, and α is a phenomenological damping constant that is specific to the material. This contains two terms, the first describing the precession of the spin, and the second providing a damping of the precessional motion, as illustrated in Fig. 2.8. They also possess distinct physical origins. While the precession of magnetization arises due to the interaction of the atomic spin with an applied field, the relaxation term represents the coupling of the magnetization to a heat bath which aligns the magnetization along the field direction, with a coupling strength of α [109]. As the magnetic system is excited the precession is damped, eventually leading the spin to align with the field direction. The damping comes from a range of different physical phenomena, meaning that no first principles derivations exist and the constant can only be measured from experiments. In 1955, Gilbert [135,136] introduced a more convincing form for the damping term, based on a Lagrangian approach, and the combined form is now called the Landau–Lifshitz–Gilbert (LLG) equation, which is the standard approach for describing dynamics in magnetism [137–139]. The same equation of motion can also be applied at the atomistic level given by

$$\frac{\partial \hat{\boldsymbol{m}}_i}{\partial t} = -\frac{\gamma}{1+\alpha^2} \left[\hat{\boldsymbol{m}}_i \times \boldsymbol{H}_i^{\text{eff}} + \alpha \hat{\boldsymbol{m}}_i \times (\hat{\boldsymbol{m}}_i \times \boldsymbol{H}_i^{\text{eff}}) \right], \tag{2.20}$$

where $\hat{\boldsymbol{m}}_i$ is the unit vector representing the direction of the magnetic spin moment at site i. The dimensionless Gilbert damping coefficient is denoted by α, while γ stands

for the gyromagnetic ratio. The atomistic LLG equation describes the interaction of an atomic spin moment i with an effective magnetic field, $\boldsymbol{H}_i^{\text{eff}}$. All interactions of the Hamiltonian $\mathcal{H}$ describing the system, or Eq. (2.4), are contained in the effective field

$$\boldsymbol{H}_i^{\text{eff}} = -\frac{1}{\mu_s}\frac{\partial \mathcal{H}}{\partial \hat{\boldsymbol{m}}_i}, \tag{2.21}$$

which represents the net magnetic field on each spin i, where $\mu_s = |\boldsymbol{\mu}_i|$ and $\frac{\partial}{\hat{\boldsymbol{m}}_i} = (\frac{\partial}{\partial \hat{m}_i^x}, \frac{\partial}{\partial \hat{m}_i^y}, \frac{\partial}{\partial \hat{m}_i^z})$.

2.4.2 Langevin dynamics

The LLG equation of motion is restricted to simulations at zero temperature. However, thermal effects often play an important role in magnetic transitions, which are caused by thermodynamic fluctuations of the spin moments at sufficiently high temperatures. Therefore, effects of temperature must be taken into account, for example, using Langevin dynamics [140, 141]. The basic idea is to follow an approach similar to molecular dynamics, in which a thermal heat bath acts on the system through the thermal field

$$\boldsymbol{H}_i^{\text{the}} = \eta_i(t)\sqrt{\frac{2\alpha k_B T}{\gamma \mu_s \Delta t}}, \tag{2.22}$$

where T is the temperature, k_B is the Boltzmann constant, α is the Gilbert damping, γ is the gyromagnetic ratio, Δt is the integration time step, and thermal fluctuations on each atomic site i can be represented by Gaussian white noise, $\eta_i(t)$. The thermal field, $\boldsymbol{H}_i^{\text{the}}$, is added as a contribution to the effective field term in both the precession and damping term,

$$\boldsymbol{H}_i^{\text{eff}} = -\frac{1}{\mu_s}\frac{\partial \mathcal{H}}{\partial \hat{\boldsymbol{m}}_i} + \boldsymbol{H}_i^{\text{the}}, \tag{2.23}$$

which leads to a stochastic equation of motion for LLG.

2.4.3 Time integration

The stochastic LLG equation has to be solved numerically in order to describe the time evolution of a magnetic system. However, the numerical choices are limited due to the stochastic nature of the equations. Particularly, one must ensure conservation of the magnitude of the spin, either implicitly or by renormalization [142]. The simplest integration scheme is the Euler method [143], which updates the spin direction in a single discretized time step, Δt. An improved integration scheme is the Heun method [141], which allows for larger time steps because of its predictor–corrector approach. In the Heun method, the predictor step calculates the new spin direction, $\hat{\boldsymbol{m}}_i'$, by Euler integration

$$\hat{\boldsymbol{m}}_i' = \hat{\boldsymbol{m}}_i^t + \Delta t \Delta \hat{\boldsymbol{m}}_i^t, \tag{2.24}$$

for every spin i on the system, where $\Delta\hat{\boldsymbol{m}}_i^t \equiv \frac{\partial \hat{\boldsymbol{m}}_i^t}{\partial t}$. The corrector step then uses $\hat{\boldsymbol{m}}_i'$ to calculate the revised spin position

$$\hat{\boldsymbol{m}}_i^{t+\Delta t} = \hat{\boldsymbol{m}}_i^t + \frac{\Delta t}{2}(\Delta\hat{\boldsymbol{m}}_i^t + \Delta\hat{\boldsymbol{m}}_i'), \tag{2.25}$$

where $\Delta\hat{\boldsymbol{m}}_i' \equiv \frac{\partial \hat{\boldsymbol{m}}_i'}{\partial t}$ and the revised effective field is reevaluated based on $\hat{\boldsymbol{m}}_i'$. The thermal field does not change between the predictor and corrector steps, and can be calculated using the Ziggurat method [144] for generating the random noise term η_i. For the low temperatures used in this work, time steps of $\Delta t \propto 10^{-15}$ give correct solutions to the stochastic LLG equations [109]. However, the time steps are also sensitive to material parameters and so will depend on the system being considered (see Chapter 7).

2.5 Minimum energy paths

2.5.1 The case of magnetic transitions

The stability of magnetic states is an important problem in the theory of magnetism. The preparation of a magnetic system in a particular state can be destroyed by thermal activation to other available states. These transitions are typically rare events on the time scale of oscillations of magnetic moments (or spin switching), which makes direct simulations of spin dynamics an impractical way to characterize them. Instead, one can determine the activation energy, the primary quantity determining thermal stability, by the energy difference between the initial state and the highest first-order saddle point (SP) located on a path that characterizes the transition [83]. The description of thermal stability of the magnetic states then essentially becomes a problem of locating the relevant SPs on the energy surface. While different approaches for identifying SPs of a transition exist [145], they often do not work for magnetic systems with many degrees of freedom.

Transitions between magnetic states can instead be described by minimum energy paths (MEPs). A MEP between two minima is the path in configuration space which lies lowest on the energy surface. Since the MEP is a path of highest statistical weight connecting the initial and final states, one can say it represents a particular mechanism of the transition. Following a MEP means advancing the system during the transition from the initial state to the final state. There can be more than one MEP between any given pair of states, each path corresponding to a specific mechanism of transition. Any maximum on a MEP is a SP on the energy surface, but only the highest maximum gives an estimate of the activation energy for the corresponding transition mechanism. In atomic systems, the nudged elastic band (NEB) [146] and variations thereof [147–149] are often used to find MEPs of transitions involving atomic rearrangements. They have also been extended to address problems in magnetism, both on the atomic scale and on a mesoscopic scale described by micromagnetics [150–153]. However, in many cases the magnetic systems considered are rather simple with vectors rotating mainly along one direction. The situation becomes more complicated for complex systems involving non-trivial rotations of the magnetic vectors, since one must account for the curvature (due to the fact that the magnitude of the magnetic

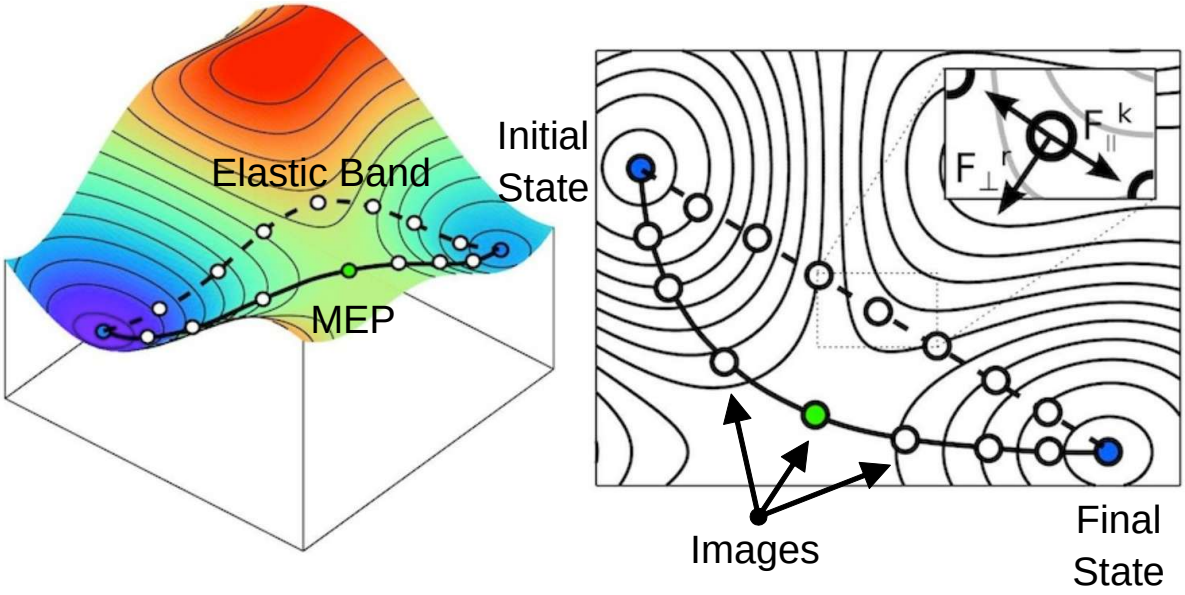

Figure 2.9 – Schematic of the geodesic nudged elastic band. An initial guess of the path is chosen (dashed lines), which is moved using the energy gradient, $F^r_\perp$ and spring force, $F^k_{||}$. After applying the GNEB, the configurations lie along the MEP (continuous line). The blue circles represent the initial and final magnetic states, and the green circle corresponds to the transition state (or saddle point). Figure is adapted from Ref. [154].

vectors is assumed constant) of the configuration space. Instead, the geodesic nudged elastic band (GNEB) [83] has been proposed for tackling these situations.

2.5.2 Geodesic nudged elastic band

The geodesic nudged elastic band builds on the NEB for magnetic systems. The method involves a discretization of the path between two minima, and then using an iterative procedure to bring the discrete points to the nearest MEP. They represent specific configurations, or the full set of magnetic vectors, and are often referred to as "images" of the system. Adjacent images are connected with springs in order to ensure continuity of the path, forming an "elastic band". At each image, the force guiding the images towards the nearest MEP is defined as the sum of the negative energy gradient and the spring force. An illustration of the forces acting on the elastic band is shown in Fig. 2.9. These forces are then used to move images on the energy surface, after projection to the tangent of the path in a process termed "nudging". The images provide a discrete approximation to a continuous path, which describes the mechanism of transition when converges to the MEP. For magnetic systems, the curved manifold is taken into account by use of geodesic distances and projection of path tangents and forces on the tangent space of the manifold of magnetic configurations. GNEB has become the standard for dealing with complex magnetic transitions, and widely employed in the study of skyrmions [83–89, 91, 95, 97]. Particularly, this is the main method of choice in the thesis for analyzing nucleation and collapse of individual skyrmions, their pinning on defects, topological charge switching, and

skyrmion interactions.

The state of a magnetic system of N spins is described by $3N$ parameters, or components of the magnetic vectors in three-dimensional space. However, one usually considers only the orientation of the magnetic vectors, as changes in their magnitudes are in most materials much faster than changes in orientation [155]. This is analogous to the Born–Oppenheimer approximation in atomic systems where the electronic degrees of freedom are assumed to be fast compared with the slowly varying positions of the nuclei [83]. The configuration of a system of N magnetic moments then contains N constraints on the magnitude of the vectors, which are expressed in terms of the slow degrees of freedom. For magnetic systems, instead of solving a constrained problem one can consider the two-dimensional Riemannian manifold

$$\mathcal{R} = \prod_{i=1}^{N} S_i^2, \tag{2.26}$$

which corresponds to the direct product of N two-dimensional unit spheres $(S_1^2, \ldots, S_N^2)$ associated with the N magnetic moment vectors [83]. This results in an unconstrained problem within the $\mathcal{R}$-manifold. An important aspect to consider is the projection of the tangent on the curved space of the Riemannian manifold, $\mathcal{T}_{\hat{\boldsymbol{m}}}$. For a single spin system, the state can be described by a unit vector $\hat{\boldsymbol{m}}$ corresponding to a point on a 2D unit sphere, S^2. The tangent space to S^2 at a point $\hat{\boldsymbol{m}} \in S^2$ is then defined as the span of all vectors $\boldsymbol{X}$ perpendicular to $\hat{\boldsymbol{m}}$:

$$\mathcal{T}_{\hat{\boldsymbol{m}}} S^2 = \{\boldsymbol{X} : \boldsymbol{X} \cdot \hat{\boldsymbol{m}} = 0\}. \tag{2.27}$$

For a system of N spins, the tangent space $\mathcal{T}_{\hat{\boldsymbol{M}}}\mathcal{R}$ at a point $\hat{\boldsymbol{M}} = (\hat{\boldsymbol{m}}_1, \ldots, \hat{\boldsymbol{m}}_N)$ generalizes to a direct product of tangent spaces to the unit spheres S_i^2 associated with each unit vector $\hat{\boldsymbol{m}}_i$,

$$\mathcal{T}_{\hat{\boldsymbol{M}}}\mathcal{R} = \prod_{i=1}^{N} \mathcal{T}_{\hat{\boldsymbol{m}}_i} S_i^2, \tag{2.28}$$

where $\hat{\boldsymbol{m}}_i$ represents the orientation of the ith magnetic moment. Therefore, any vector $\boldsymbol{A} = (\boldsymbol{A}_1, \ldots, \boldsymbol{A}_N)$ in $3N$ dimensions can be projected on the tangent space $\mathcal{T}_{\hat{\boldsymbol{M}}}\mathcal{R}$,

$$\mathcal{P}_{\mathcal{T}}\boldsymbol{A} = \left(\boldsymbol{A}_1^{\mathcal{T}}, \ldots, \boldsymbol{A}_N^{\mathcal{T}}\right), \tag{2.29}$$

by subtracting out the component parallel to $\hat{\boldsymbol{m}}_i$ from each three-dimensional vector $\boldsymbol{A}_i$:

$$\boldsymbol{A}_i^{\mathcal{T}} = \boldsymbol{A}_i - (\boldsymbol{A}_i \cdot \hat{\boldsymbol{m}}_i)\hat{\boldsymbol{m}}_i, \tag{2.30}$$

following the prescription in Ref. [83].

The GNEB involves taking some initial guess of the path represented by a discrete chain of Q images of the system, $\left[\boldsymbol{M}^1, \ldots, \boldsymbol{M}^Q\right]$, where $\boldsymbol{M}^v = \left(\hat{\boldsymbol{m}}_1^v, \hat{\boldsymbol{m}}_2^v, \ldots, \hat{\boldsymbol{m}}_N^v\right)$ represents the configuration of the vth image of a system of N spins and $\hat{\boldsymbol{m}}_i$ specifies the orientation of the ith magnetic moment (see Fig. 2.9 for an example). First, the tangent

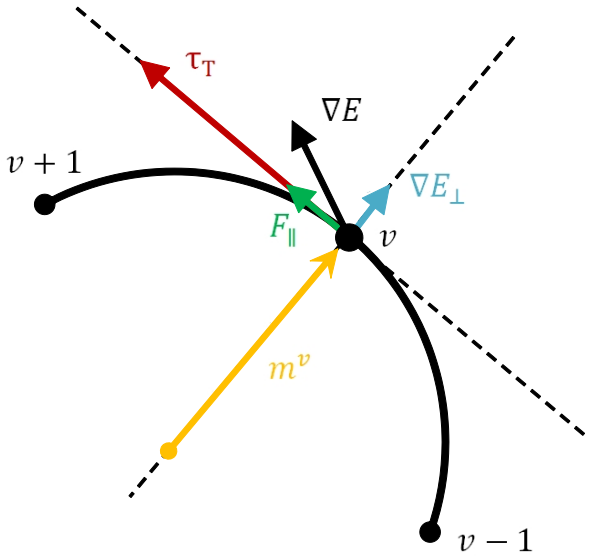

Figure 2.10 – Illustration of the force projection used in GNEB for the image v located on the geodesic path. The tangent projected on the tangent space, $\hat{\boldsymbol{\tau}}_{\mathcal{T}}$, is used to obtain the perpendicular component of the gradient, $\nabla E_\perp$, and the parallel component of the spring force, $\boldsymbol{F}_{||}$, for image v.

to the path at image v, $\hat{\boldsymbol{\tau}}^v$, is estimated using the forward or backward difference of the two adjacent images [147]

$$\hat{\boldsymbol{\tau}}^v = \begin{cases} \hat{\boldsymbol{\tau}}^v_+, & \text{if } E^{v+1} > E^v > E^{v-1}, \\ \hat{\boldsymbol{\tau}}^v_-, & \text{if } E^{v+1} < E^v < E^{v-1}, \end{cases} \tag{2.31}$$

where $\hat{\boldsymbol{\tau}}^v_+ = \boldsymbol{M}^{v+1} - \boldsymbol{M}^v$, $\hat{\boldsymbol{\tau}}^v_- = \boldsymbol{M}^v - \boldsymbol{M}^{v-1}$, and E^v is the Hamiltonian energy for the vth magnetic configuration. If image v is close to an energy minimum, $E^{v+1} > E^v < E^{v-1}$, or to an energy maximim, $E^{v+1} < E^v > E^{v-1}$, then the tangent is taken to be a weighted average of $\hat{\boldsymbol{\tau}}^v_+$ and $\hat{\boldsymbol{\tau}}^v_-$:

$$\hat{\boldsymbol{\tau}}^v = \begin{cases} \hat{\boldsymbol{\tau}}^v_+ \Delta E^v_{max} + \hat{\boldsymbol{\tau}}^v_- \Delta E^v_{min}, & \text{if } E^{v+1} > E^{v-1}, \\ \hat{\boldsymbol{\tau}}^v_+ \Delta E^v_{min} + \hat{\boldsymbol{\tau}}^v_- \Delta E^v_{max}, & \text{if } E^{v+1} < E^{v-1}, \end{cases} \tag{2.32}$$

where the energy differences are $\Delta E^v_{max} = \max(|E^{v+1} - E^v|, |E^{v-1} - E^v|)$ and $\Delta E^v_{min} = \min(|E^{v+1} - E^v|, |E^{v-1} - E^v|)$. The tangent can then be projected on the tangent space

$$\hat{\boldsymbol{\tau}}^v_{\mathcal{T}} = \frac{\mathcal{P}_{\mathcal{T}} \hat{\boldsymbol{\tau}}^v}{|\mathcal{P}_{\mathcal{T}} \hat{\boldsymbol{\tau}}^v|}, \tag{2.33}$$

as illustrated in Fig. 2.10. The position of the individual images needs to be adjusted so as to zero the acting force in order to converge on the MEP. This can be accomplished by displacing the images along the component of the force, or negative of the energy gradient, $\boldsymbol{F} = -\nabla E$, that is perpendicular to the path and obtained by subtracting out the parallel component:

$$\nabla E\left(\boldsymbol{M}^v\right)|_\perp = \nabla E\left(\boldsymbol{M}^v\right) - \left(\nabla E\left(\boldsymbol{M}^v\right) \cdot \hat{\boldsymbol{\tau}}^v_{\mathcal{T}}\right) \hat{\boldsymbol{\tau}}^v_{\mathcal{T}}. \tag{2.34}$$

Adjacent images are connected with springs in order to ensure the images are distributed evenly along the path. Therefore, the acting force also takes into account the component of the spring force along the tangent, so as not to interfere with the displacement of images, which is evaluated using geodesic distances:

$$\boldsymbol{F}_s^v|_{\parallel} = \kappa \left[D(\boldsymbol{M}^{v+1}, \boldsymbol{M}^v) - D(\boldsymbol{M}^v, \boldsymbol{M}^{v-1}) \right] \hat{\boldsymbol{\tau}}_{\mathcal{T}}^v, \tag{2.35}$$

where κ is a spring constant and $D(\boldsymbol{M}^{v+1}, \boldsymbol{M}^v)$ denotes the geodesic distance between adjacent images $v+1$ and v on the $\mathcal{R}$-manifold. In particular, the distance between images u and v is given by

$$D(\boldsymbol{M}^u, \boldsymbol{M}^v) = \sqrt{(d_1^{u,v})^2 + \cdots + (d_N^{u,v})^2}. \tag{2.36}$$

$d_i^{u,v}$ is the geodesic distance between points u and v and can be expressed in terms of the great-circle distance on the unit sphere S_i^2, given by the spherical law of cosines [156]

$$d_i^{u,v} = \arccos(\hat{\boldsymbol{m}}_i^u \cdot \hat{\boldsymbol{m}}_i^v), \tag{2.37}$$

or other formulas for geodesic distances as described in Ref. [83]. The acting force is then defined as the sum of the perpendicular component of the negative energy gradient, $\nabla E\left(\boldsymbol{M}^v\right)|_{\perp}$, and the component of the spring force along the tangent, $\boldsymbol{F}_s^v|_{\parallel}$:

$$\boldsymbol{F}_{act}^v = \mathcal{P}_{\mathcal{T}} \left(-\nabla E(\boldsymbol{M}^v)|_{\perp} + \boldsymbol{F}_s^v|_{\parallel} \right), \tag{2.38}$$

which is projected on the tangent space with $\mathcal{P}_{\mathcal{T}}$ once more in order to satisfy the magnetic constraints. Fig. 2.10 illustrates the force projections for a simple example. $\boldsymbol{F}_{act}^v$ defines the direction of motion of images and must be coupled with an optimization procedure for their displacement towards the nearest MEP.

2.5.3 Optimization procedure

The magnitude and exact direction of motion depend on the particular optimization being applied to the GNEB. A trivial approach involves replacing the usual effective fields in Eq. (2.20) with the acting forces, $\boldsymbol{F}_{act}^v$, where the precession term is removed and the equations are iterated until convergence to the MEP [83]. However, one can also employ standard iterative procedures [157], where the search direction is defined by the force along the tangent of the curved manifold. The simplest of these is the steepest descent (SD), which follows the force vector until a zero in the acting force. The SD moves to the location of an image v at step n with

$$\boldsymbol{M}_{n+1}^v = \boldsymbol{M}_n^v + \alpha \boldsymbol{F}_n^v, \tag{2.39}$$

where α is an adjustable parameter and $\boldsymbol{F}_n^v \equiv \boldsymbol{F}_{act}^v$ at step n. It follows that $\boldsymbol{M}_{n+1}^v \leq \boldsymbol{M}_m^v$ for small enough values of α. The SD is known to converge slowly in stiff systems [158], but can be improved on by accelerating the system in the direction of the force, which makes the optimization more aggressive [157]. For example, Quickmin (QM) damps the velocity by including only the component in the direction of

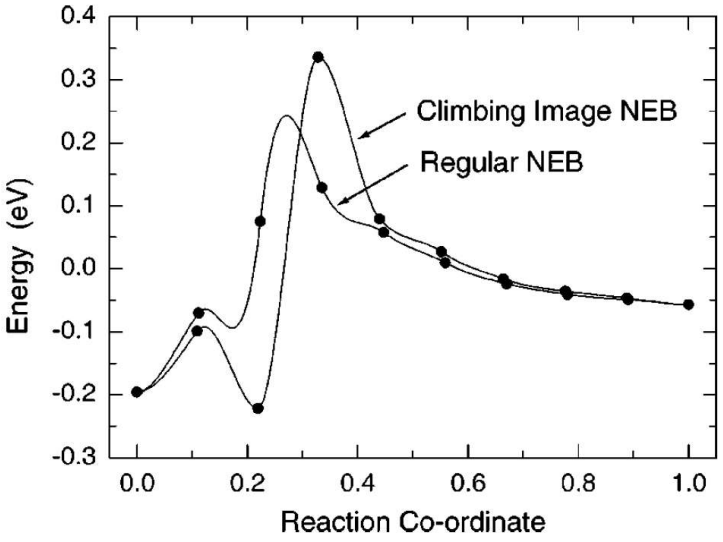

Figure 2.11 – Example of the minimum energy paths obtained with and without the climbing image, where the latter clearly gives a better approximation of the activation energy (peak). Figure retrieved from Ref. [160].

the force. The optimization can be coupled with Verlet integration [159] based on fictitious equations of motion, or with an Euler integrator as described here. First, the velocity of an image v is projected in the direction of the acting force, $\boldsymbol{F}_n^v$:

$$\boldsymbol{V}_n^v = \begin{cases} (\boldsymbol{V}_n^v \cdot \boldsymbol{F}_n^v)\boldsymbol{F}_n^v / |\boldsymbol{F}_n^v|^2, & \text{if } \boldsymbol{V}_n^v \cdot \boldsymbol{F}_n^v > 0, \\ 0, & \text{if } \boldsymbol{V}_n^v \cdot \boldsymbol{F}_n^v \leq 0, \end{cases} \tag{2.40}$$

where the velocity is zeroed (or damped) if anti-parallel to the force. Then, an integration step (in this case Euler) of the form

$$\begin{aligned} \boldsymbol{M}_{n+1}^v &= \boldsymbol{M}_n^v + \Delta t \boldsymbol{V}_n^v \\ \boldsymbol{V}_{n+1}^v &= \boldsymbol{V}_n^v + \Delta t \boldsymbol{F}_n^v, \end{aligned} \tag{2.41}$$

is taken on image v, where Δt is the time step, $\boldsymbol{M}_{n+1}^v$ and $\boldsymbol{V}_{n+1}^v$ are the revised state and velocity vectors, respectively. This procedure is applied simultaneously to all Q images and repeated until $\boldsymbol{F}_n^v$ reaches zero, within numerical precision.

2.5.4 Climbing image

The stability of a localized state is dictated by the highest SP located on a path that characterizes the transition. Since the elastic band provides a discrete representation of the MEP, the energy of saddle points needs to be obtained through interpolation. However, when the resolution of the MEP near the saddle point is poor (e.g., when the energy barrier is narrow and sharp compared with the length of the path), then estimates of the activation energy from the interpolation can be inaccurate. An example of such situation is shown in Fig. 2.11. Instead, one can choose an image c with highest energy and move it up the energy surface along the tangent of the path towards the SP [160]. This image is denoted the "climbing image" and the acting force

on it is only the component of the energy gradient, ∇E, that is parallel to the path

$$\boldsymbol{F}_{act}^{c} = \mathcal{P}(-\nabla E(\boldsymbol{M}^{c}) + 2(\nabla E(\boldsymbol{M}^{c}) \cdot \hat{\boldsymbol{\tau}}_{\mathcal{T}}^{c})\hat{\boldsymbol{\tau}}_{\mathcal{T}}^{c}). \tag{2.42}$$

The climbing image is not affected by the spring forces, while the other images define the degree of freedom along which the energy is maximized [160]. The localized optimization guarantees that the climbing image will converge to the saddle point, as shown in Fig. 2.11.

2.6 Monte Carlo

While spin dynamics are particularly useful for obtaining dynamic information about a magnetic system and minimum energy paths for characterizing their transitions, they are often not useful for determining the equilibrium properties. Instead, Monte Carlo methods [161, 162] provide a natural way to simulate temperature effects and study the energetics of a physical system under equilibrium conditions. The Buffon needle can be seen as an early variant of Monte Carlo, where π is estimated by randomly dropping needles on parallel and equidistant strips. However, Enrico Fermi was the first to invent the method when he was experimenting with neutron diffusion in the 1930s. Monte Carlo was introduced as a Markov Chain in the late 1940s, when Stanislaw Ulam was working on nuclear weapons projects at Los Alamos National Laboratory [163]. The method was first applied to simulations of equilibrium systems composed of many interacting particles, through their equations of state based on

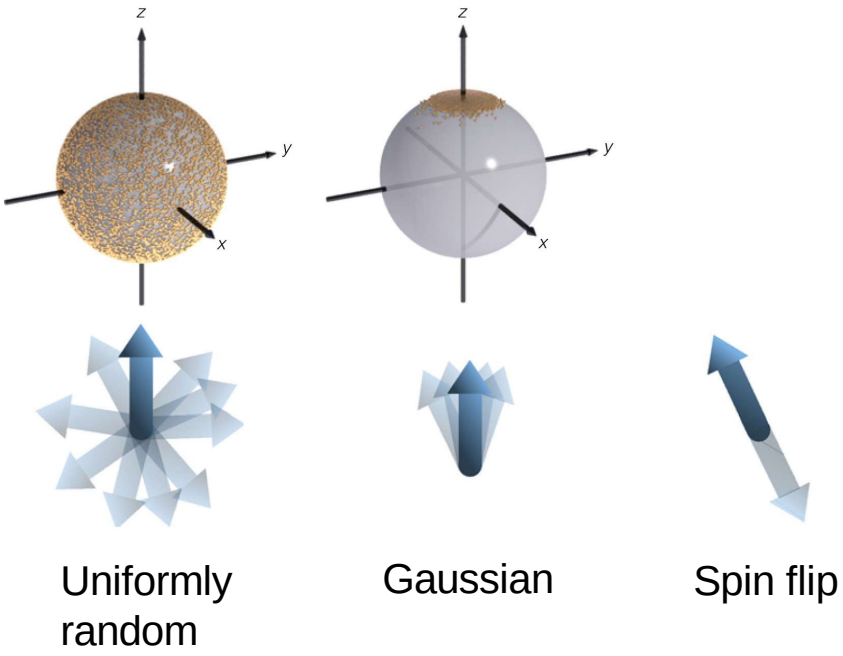

Figure 2.12 – Schematic showing the three Monte Carlo moves: random, Gaussian, and spin flip, from left to right (lower panel). Illustration of Monte Carlo sampling on the unit sphere for random and Gaussian moves (upper panel). Figure adapted from Ref. [109].

two dimensional motion of solid spheres, which was termed the Metropolis Monte Carlo [164].

The basic idea is to make a small change to the system and calculate the difference in energy, ΔE. This change is then accepted or rejected based on the Boltzmann distribution at a given temperature. In the case of classical spin models the Metropolis Monte Carlo can be used as follows: First, a single spin i is randomly chosen and its spin direction, $\hat{\boldsymbol{m}}_i$, is displaced randomly to a new candidate position, $\hat{\boldsymbol{m}}_i'$. The difference in energy, $\Delta E = E(\hat{\boldsymbol{m}}_i') - E(\hat{\boldsymbol{m}}_i)$, is then evaluated and the move is accepted with probability $\mathcal{P}$ given by the Metropolis choice [164]:

$$\mathcal{P} = \min\left[1, \exp\left(-\frac{\Delta E}{k_B T}\right)\right], \tag{2.43}$$

where k_B is the Boltzmann constant and T is the temperature. Note that the second argument corresponds to the Boltzmann factor, $P_B = e^{-\Delta E/k_B T}$, and that values greater than unity are accepted unconditionally, as they represent a decrease in energy. The procedure is then repeated until N trial moves have been attempted, where N is the number of spins in the system. Each set of N moves comprises a single Monte Carlo step. Repeating this procedure many times allows us to simulate the thermal motion of spins when the system is in equilibrium.

The nature of the trial move is important since it must satisfy the detailed balance principle [165]:

$$P_B(\hat{\boldsymbol{m}}_i)\mathcal{P}(\hat{\boldsymbol{m}}_i \to \hat{\boldsymbol{m}}_i') = P_B(\hat{\boldsymbol{m}}_i')\mathcal{P}(\hat{\boldsymbol{m}}_i' \to \hat{\boldsymbol{m}}_i), \tag{2.44}$$

which requires that a process is both reversible and ergodic. While reversibility is already satisfied in Eq. (2.43), ergodicity can be satisfied by moving the spin to random positions along the surface of a unit sphere [166], as illustrated in Fig. 2.12. However, for low temperatures deviations of spins from the collinear direction result in significant changes in energy due to the strength of the exchange interactions. This means that a series of trial moves on the unit sphere will lead to most moves being rejected, and long simulations are required to reach thermal equilibrium. Instead, one can consider only moves of small angles given by

$$\hat{\boldsymbol{m}}_i' = \frac{\hat{\boldsymbol{m}}_i + \sigma\boldsymbol{\eta}}{|\hat{\boldsymbol{m}}_i + \sigma\boldsymbol{\eta}|}, \tag{2.45}$$

where $\boldsymbol{\eta}$ is a Gaussian distributed random vector and σ is the width of a cone around the spin $\hat{\boldsymbol{m}}_i$, as shown in Fig. 2.12. After normalization, the choice of a Gaussian distribution leads to a uniform sampling of trial moves over the cone, thus satisfying the ergodic property. The width of the cone can be chosen to depend on temperature and of the form

$$\sigma = \frac{2}{25}\left(\frac{k_B T}{\mu_B}\right)^{1/5}, \tag{2.46}$$

where μ_B is the Bohr magneton. Therefore, the Gaussian trial move [109] favors small angular changes in spin direction at low temperatures and results in good acceptance rates for most temperatures. Lastly, one can consider a spin flip, $\hat{\boldsymbol{m}}_i = -\hat{\boldsymbol{m}}_i$, which

reverses the direction of the spin (see Fig. 2.12). This move corresponds to that in Ising spin models, and includes explicit nucleation and switching events. Choosing one of these three moves at random for each trial step allows for a robust search over the configuration space, including finding stable magnetic skyrmion textures.

3 SKYRMIONS IN FEW-MONOLAYER FERROMAGNETIC FILMS

In this Chapter[1] we investigate the thermal stability of an isolated skyrmion in ultra-thin chiral magnetic structures composed of few monolayers. We present three distinct mechanisms for skyrmion collapse on a racetrack memory, based on ab initio input and the performed atomic-spin simulations. We focus on the stability of a skyrmion in three atomic layers of Co, either epitaxial on the Pt(111) surface, or within a hybrid multilayer where DMI nontrivially varies per monolayer due to competition between different symmetry-breaking from two sides of the Co film. In laterally finite systems, their constrained geometry causes poor thermal stability of the skyrmion toward collapse at the boundary, which we show to be resolved by designing the high-DMI structure within an extended film with lower or no DMI.

3.1 Introduction

Single magnetic skyrmions have already been extensively studied both in theory [65, 104] and in experiments [46,48]. Very recently Refs. [84,85] reported detailed descriptions of the mechanisms for skyrmion collapse in a single atomic layer of magnetic material with interfacially-induced DM interaction [167]. However, these restricted conditions can severely limit the use of skyrmions in practical applications because (a) creating large-area monolayers requires specialized preparation which will make commercial production hard to achieve and (b) isolated skyrmions in magnetic monolayers have only been observed at very low temperatures. For realistic applications, room-temperature skyrmions can be achieved by increasing the thickness of the magnetic film to few monolayers and increasing the interfacial spin-orbit coupling by using two different materials below and above the film [49,50]. In view of the emergent importance of such multilayer hybrid structures, a deep investigation of the behavior of isolated magnetic skyrmions within few-atom thick ferromagnets with monolayer-resolved DMI is crucial for the design of future spintronic devices.

In this Chapter we consider a 0.6 nm thick cobalt (Co) film with perpendicular magnetic anisotropy on a platinum (Pt) substrate, without or with a capping layer of a different material (MgO, Ir, or other). Realistically, the DM interaction is diluted from one Co monolayer to another, correspondingly to related ab initio calculations in the literature [50,168]. The magnetic layer is composed of three atomic monolayers (MLs), as shown in Fig. 3.1, with an fcc stacking sequence and a lattice constant of $a = 2.51$, similar to values found in Refs. [169,170]. We describe the magnetic material by Eq. (2.4), where $\boldsymbol{\mu}_i = 2.1\mu_B$ and similar values for the spin moment are found in thin films of Co on Pt(111) [171]. Since the dipolar coupling mainly acts as a shape

[1] The results of this Chapter are published in Ref. [88].

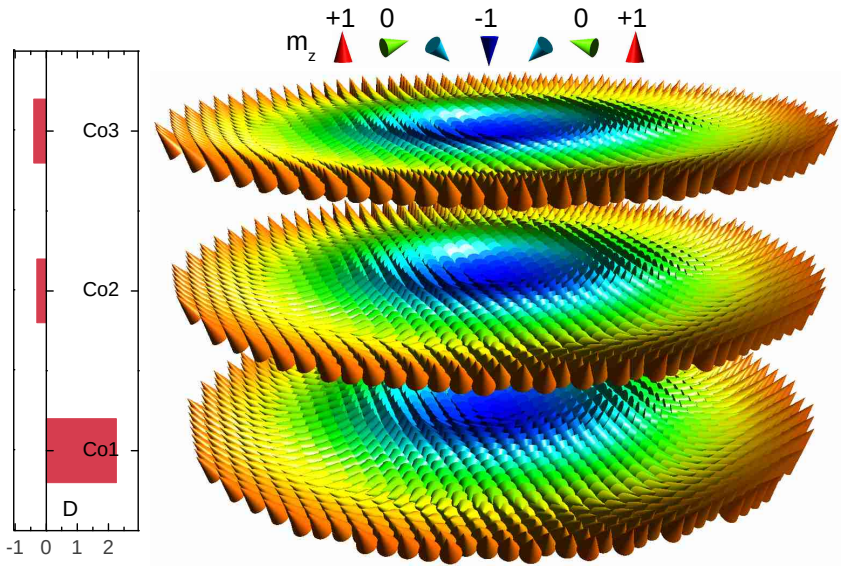

Figure 3.1 – Oblique view of the 3ML skyrmion structure, with color-coded spin directions. The monolayer-resolved DMI (shown in the left) corresponds to 3ML Co on Pt. The remaining parameters are taken to be $J = 10$ meV per bond and $K = 0.1$ meV per atom. An fcc stacking sequence is used, where interlayer distances are not drawn to scale.

anisotropy [28], it is possible to include its effect by reducing the anisotropy constant in the Hamiltonian [84, 85]. This has been carefully examined in the current work for few-atom thick films by directly calculating the dipolar interactions in the full neighborhood (i.e. all spin pairs). The massive computational effort involved, with over one billion atomic spin pairs, is tackled by graphics processing units (GPUs) for this part of the calculations (see Section 7.9). Similarity in the obtained results point to the same conclusions as in the monolayer case, so we consider a reduced anisotropy constant which effectively mimics the inclusion of dipolar interactions, much like in Refs. [84, 85]. References to anisotropy in the text are in terms of the effective anisotropy, where the dipolar term is implicitly included. This assumption is made for the rest of the thesis.

The considered sample is delimited by open (or free) boundary conditions and the size is chosen to roughly match the width of skyrmion-based racetrack memories proposed to date [60]. In this context, open boundary conditions means that the exchange and DM bonds are ignored between a boundary atom and anything that is outside of the finite geometry. This approach leads to similar magnetization profiles (canting of spins along the boundary) as those found in Refs. [172, 173], which have included explicit corrections in the boundary conditions to account for DM interactions. A lattice of $130 \times 130 \times 3$ spins is used, which roughly corresponds to a $32 \times 28 \times 0.6$ nm nanostructure. Simulations are performed at zero temperature and in absence of magnetic fields. The exchange stiffness ($J = 29$ meV per bond), DM interaction ($D = 1.5$ meV per bond), and effective anisotropy ($K = 0.276$ meV per atom) are taken from experimental works on Co/Pt samples, as listed in Ref. [84]. For particular cases considered in this work, the monolayer-resolved DMI is retrieved from ab initio calculations [50, 168] (see Fig. 3.1), and can exhibit fairly nontrivial dis-

tribution depending on the chosen capping layer on top of Co. For the anisotropy and exchange interaction, however, we kept the parameter values constant throughout the magnetic material. This is mainly caused by the lack of available information on layer-resolved interactions, but it also facilitates the understanding of our results (since we avoid competing interactions between the known monolayer-resolved DMI and the arbitrary variation of other parameters). Note that different J and K are necessary for stabilizing skyrmions with monolayer-dependent DMI, compared to the case of uniform (average) D from Ref. [84]. In our simulations, both interlayer and intralayer bonds are considered for the exchange and DM interactions using only the nearest neighbors.

3.2 Stability of a skyrmion

3.2.1 Three monolayers Co on Pt

We start the analysis by considering the case of constant (uniform) DM interaction (DMI) in the 3ML Co film on Pt. The skyrmion found is similar to the one in a Co monolayer with same DMI [84,85], where its energy of 1580 meV roughly matches the 500 meV for a monolayer skyrmion considering there are three times more atoms in an 3ML fcc structure than in a two dimensional triangular lattice, albeit with a slightly larger diameter of 6.4 nm instead of 4.6 nm in the monolayer case. The diameter is calculated as the sum of inter-atomic distance between spins with $\boldsymbol{S}_i \cdot \hat{\boldsymbol{z}} \leq 0$. However, assuming a constant effective DMI for few monolayers is highly unrealistic since the DMI strength, D, should be inversely proportional to the thickness of the magnetic layer [174,175]. A more accurate approach is to obtain the monolayer-resolved D from first principles [50,168] and incorporate it in our atomistic spin model. Here D takes a large positive value in the first monolayer (2.25 meV per bond) and weakly proliferates away from the Co/Pt interface (-0.3 and -0.4 meV per bond for the middle and top layers, respectively) [see Fig. 3.1]. Although Ref. [168] neglects interlayer contributions as being too small, we include them in our calculations as the average between DMIs in successive monolayers. In this approach we find that the skyrmion is no longer stable for the conditions defined earlier [84]. Instead, a full sweep of the relevant parameters is needed to find a parametric domain where skyrmions are stable.

For the case of monolayer-resolved DMI in a 3ML Co film, we constructed a magnetic state diagram as a function of magnetic anisotropy, K, and exchange coupling, J. Fig. 3.2 shows that metastable skyrmions can form in a significant portion of the parameter space, albeit at zero temperature. The rest of the diagram corresponds to the uniform (FM) ground state, except at very low exchange couplings where the system remains in a mixed (noncollinear or multidomain) state. We find that skyrmions can only exist for anisotropies that are much lower than expected. In particular, the Sk state survives when K is almost an order of magnitude smaller than in the usual case of constant DMI ($K = 0.276$ meV per atom). A plausible explanation is that vertical dilution of DMI in Co monolayers reduces the ability for a skyrmion to form through the entire depth of the magnetic material. Atomic layers further from the Pt substrate will have weak DMI that cannot sustain a stable skyrmion structure, which then propagates into the lower layers through the exchange coupling. Strong

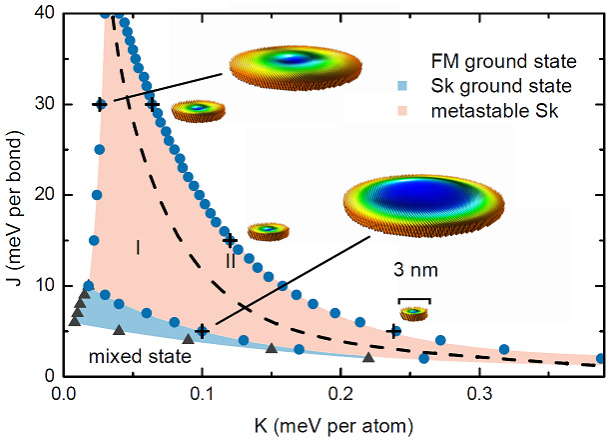

Figure 3.2 – Magnetic state diagram at zero temperature and in absence of magnetic field, as a function of anisotropy and exchange interaction, for DMI taken as in Fig. 3.1. Data points (circles and triangles) are retrieved from numerical simulations. The transition boundaries separate regions of metastable skyrmions (shaded in red) from the uniform (FM) ground state (white), and the skyrmion ground state (shaded in blue). Skyrmions are shown for different locations in the parameter space, denoted by crosses. Dashed line separating the region where stability of the skyrmion is dictated by boundary collapse (I) from the region where the isotropic collapse dominates (II). The discrimination between collapse mechanisms is obtained on energy grounds, and does not take into account the skyrmion lifetime.

ferromagnetic ordering therefore takes over, whereas a low exchange coupling would restore the stability of skyrmions. We also note the inverse relation between the effects of anisotropy and the exchange interaction on skyrmion stability, well characterized by the transition lines and the shape of the stability domain of the skyrmion in Fig. 3.2.

Fig. 3.3(a) shows that the Sk energy (calculated as the energy difference between the Sk and FM state) is higher for stronger exchange interactions and increases with increasing magnetic anisotropy. For strong exchange ($J = 30$ meV per bond) the skyrmion has an average energy of 2.2 eV compared to 0.5 eV for weak exchange ($J = 10$ meV per bond). It can also be seen that the variation of energy as a function of K difference is only 80 meV in the former case but as high as 202 meV in the latter. This demonstrates that the anisotropy has a more pronounced effect on the skyrmion energy for weak exchange interactions. Energetically favorable configurations, that are closer to the ground state, can thus be obtained by decreasing either of the two parameters. The size (diameter) of the skyrmion core is inversely proportional to the anisotropy, which lies in correspondence with its energy [Fig. 3.3(b)]. As anisotropy decreases the skyrmion grows in size until the remaining outer spins are flipped to the uniform ground state (all spins down), or until the skyrmion slides outside from the boundary. For large K and lower J the skyrmion shrinks in size and its energy increases until it overcomes the energy barrier and collapses to the uniform ground state with all spins up. It is worth noting that the skyrmions found here can be as small as $1 - 2$ nm in diameter or as large as ~ 18 nm for low exchange constants.

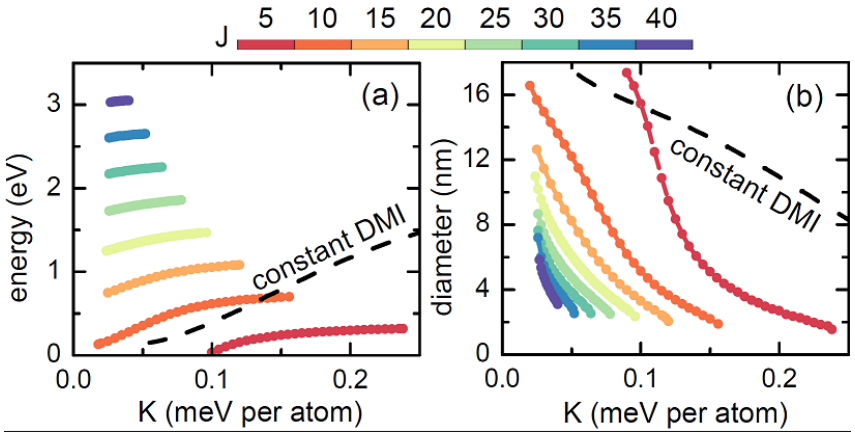

Figure 3.3 – (a) Skyrmion energy and (b) skyrmion size as a function of magnetic anisotropy for fixed values of the exchange coupling, J. Dotted line corresponds to the case of constant DMI, with parameter values taken from Ref. [84].

For high J, the skyrmions never surpass 10 nm in diameter [see exemplified cases in Fig. 3.2]. This implies that the constraining geometry of finite systems can have a strong effect on skyrmion size and energy, especially in the presence of strong exchange coupling [176].

It is informative to compare the skyrmion structure in our approach to that in the case of constant DMI. The skyrmion energy in the latter case is 1.59 eV, and skyrmion core has a diameter of 6.4 nm in all three monolayers. In Fig. 3.1 we have shown that for a 3ML sample with monolayer-resolved DMI, the Sk structure persists through the entire magnetic material. The skyrmion core, however, can shrink for monolayers far from the Co/Pt interface, since the DMI strength decreases vertically in the magnetic material. In Fig. 3.4 we observe for what range of parameters are there significant variations in skyrmion size between individual monolayers. The figure shows

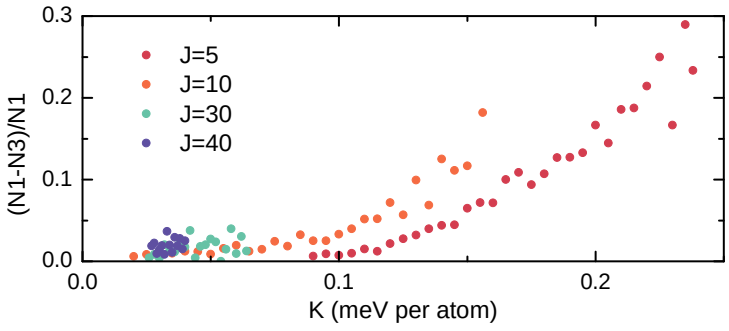

Figure 3.4 – Relative difference between the number of core spins in the first and the third monolayer $[(N1 - N3)/N1)]$ as a function of magnetic anisotropy for weak and strong exchange interactions. Oscillations in values result from the lattice discretization, where the $\hat{\boldsymbol{m}}_z$ spin component switches sign for a given set of spins at different values of the anisotropy in the first and third monolayer.

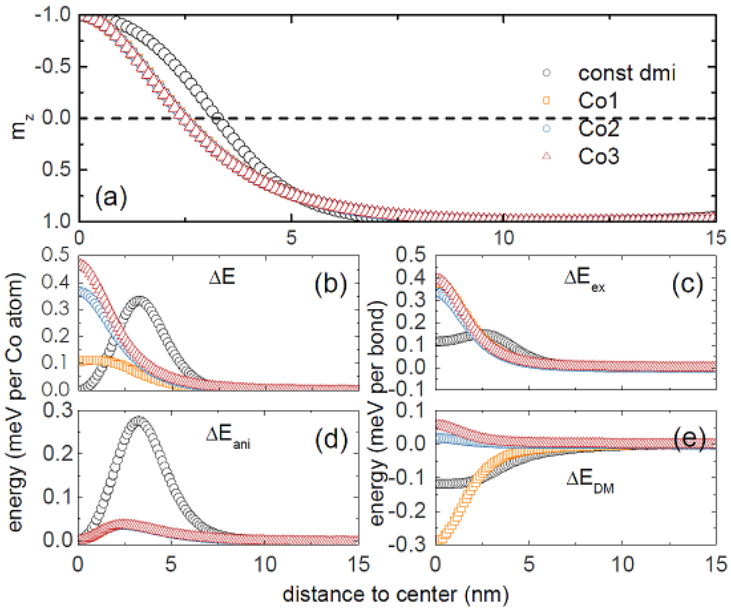

Figure 3.5 – (a) Line profile of an individual skyrmion for constant DMI and for monolayer-resolved DMI [see Fig. 3.1]. Strong exchange coupling is assumed ($J = 30$ meV per bond) and the anisotropy is chosen to be $K = 0.036$ meV per atom. The labels refer to the individual Co monolayers that are closest (Co1), in between (Co2), and furthest (Co3) from the Pt substrate. (b) Total energy difference (exchange, DM, and anisotropy) per Co atom with respect to the uniform FM state as a function of distance from the skyrmion center. (c-e) Energy difference due to exchange interaction, magnetic anisotropy and DM interaction, respectively.

that the skyrmion diameter depends heavily on the strength of exchange interactions. While fluctuations in skyrmion size between monolayers are negligible for strong exchange (less than 5% regardless of the anisotropy, which amounts to only a few spins), for weak J they vary from small to large as we increase the anisotropy. A plausible explanation for this behavior is that strong exchange interactions prevent distortion of the skyrmion structure across different monolayers. We can therefore expect that interlayer variations are not important in the few ML Co on Pt system considered here.

Fig. 3.5(a) reveals a change in skyrmion profile compared with that for constant DMI. In particular, the skyrmion is more extended in the sense that spins rotate to the uniform FM state at a slower spatial rate while the core spins ($\hat{\boldsymbol{m}}_z \leq 0$) have smaller magnitudes. However, this could be a result of the different anisotropies used in the two cases which induce different skyrmion sizes. The fact that the profile is identical throughout all three Co monolayers matches our previous results regarding skyrmion diameter throughout the magnetic structure for strong exchange couplings [see Fig. 3.4]. The total energy contribution per Co atom appears to be significantly different. For the constant DMI case the energy profile (energy difference per Co atom or bond as a function of distance from skyrmion center) has a maximum ($E > 0$) followed by a minimum ($E < 0$) as expected from literature [167,177]. In our approach there are three distinct energy profiles for different monolayers, which correspond to

the different DMIs in the three layers. The monolayer closest to the surface has an energy profile similar to one found in the constant case, but the energy profiles of the two monolayers further above follow a monotonic decrease.

These energy profiles can be understood by analyzing individual contributions of different magnetic interactions, plotted in Fig. 3.5(c-e). The two curves in Fig. 3.5(c) distinguish the stronger local variation of the exchange energy in the central monolayer compared to the top and bottom ones. There is a peak in exchange energy for the constant case as the spins rotate from the skyrmion core to ferromagnetic ordering. This is not observed for the monolayer-resolved DMI because the core is already too small to have spins aligned in the center. In that case the DM energy takes three different profiles which correspond to the dilution of DMI in three Co monolayers [according to Fig. 3.1]. The difference in total energy profiles arises from the cancellation of contributions of exchange and DM interactions in the first monolayer, but not in the other two due to low DM energy there. In the constant case the anisotropy energy has a significantly stronger effect on the total energy per Co atom compared to the monolayer-resolved DMI [see Fig. 3.5(d)]. This can be explained by the higher K needed to stabilize a skyrmion with constant DMI [see Fig. 3.3].

3.2.2 Three monolayers Co in a spin-orbit sandwich

In what follows, we consider samples where the magnetic film is sandwiched between materials that provide (a)symmetric spin-orbit coupling (Pt-Co-MgO [50], Pt-Co-Ir [49, 168], and Pt-Co-Pt [168]). The choice of materials is guided by recent ex-

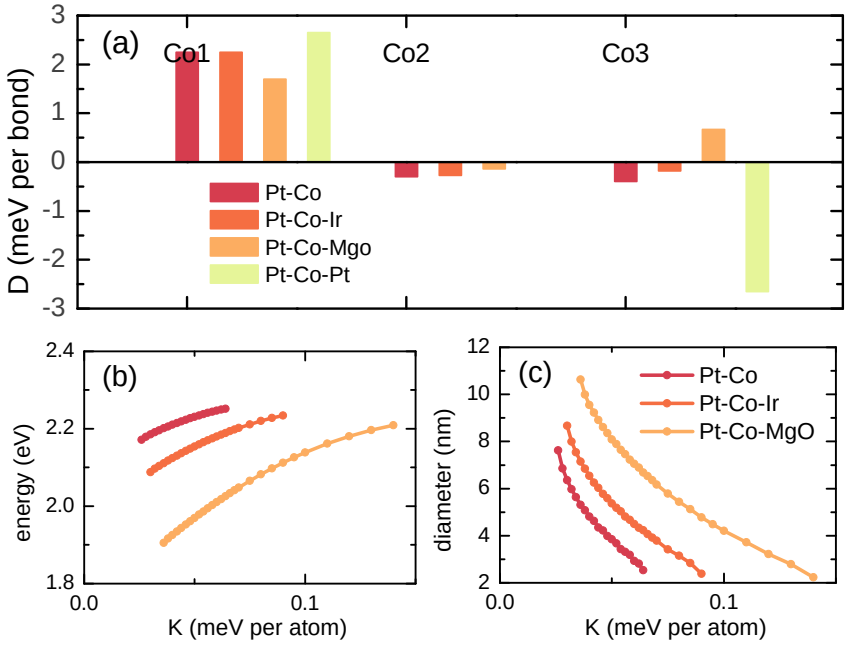

Figure 3.6 – (a) Layer resolved DMI strength for the 3ML Co in considered sandwich multilayers, compared to the case of epitaxial 3ML Co on Pt, retrieved from ab initio calculations [50,168]. (b) Skyrmion energy and (c) skyrmion size (diameter) as a function of magnetic anisotropy for strong exchange coupling ($J = 30$ meV per bond).

periments where skyrmions were stabilized at room-temperature [49, 50] and by ab initio predictions for DMI in ferromagnetic/heavy metal bilayers [168]. This class of samples allows for relatively large DMI to be achieved, which is clearly favorable for skyrmions. In Fig. 3.6(a), we show the comparative analysis of monolayer-resolved DMI in sandwiched 3ML Co samples and the previously considered 3ML Co on Pt. DMI remains largest in the first Co monolayer, mainly stemming from the Pt-Co interface [50]. In a Pt-Co-Ir sandwich, the DMI for Co-Ir interface is weaker than for the third Co monolayer for 3ML Co on Pt, which reduces the negative value of DMI in the central Co monolayer and increases the total DMI. In a Pt-Co-MgO case, DMI at the Co-MgO interface has the same sign as that of Pt-Co, which enhances the total DMI and further reduces the negative DMI in the central monolayer. Pt-Co-Pt samples would ideally have symmetric interfaces, which leads to no DMI in the central monolayer and (in practice nearly) zero overall DMI [168].

With this input for monolayer-resolved DMI, we present the properties of isolated skyrmions in the discussed hybrid multilayer structures, retrieved from atomic-spin simulations. Fig. 3.6(b) shows that Sk energies have similar (monotonically) increasing profiles as a function of anisotropy as found in the 3ML Co on Pt case. For the assumed identical exchange coupling, skyrmions in Pt-Co-MgO samples have lower energies than those found in Pt-Co-Ir, which are in turn lower than in Pt-Co case. No skyrmion states were found in Pt-Co-Pt, for either strong or weak exchange interactions, because of the specific self-canceling DMI in that case. We also note that in multilayers the skyrmion stability is extended to higher anisotropy values, as expected from the increase in total DMI seen in Fig. 3.6(a). In particular, the energy profile of Pt-Co-MgO extends significantly more to higher anisotropy since the DMI strength is positive in the last Co ML, contrary to negative values found in Co-Pt-Ir and Pt-Co cases. The range of possible skyrmion sizes also increases in multilayer structures [see Fig. 3.6(c)]. For strong exchange coupling, the largest found skyrmions are 7 nm in diameter for Pt-Co, 8 nm for Pt-Co-Ir, and 10 nm for Pt-Co-MgO, whereas the smallest ones are 2.3 nm, 2 nm and 1.8 nm, respectively.

In Fig. 3.7, the total energy per Co atom is shown for the individual monolayers. In the Pt-Co-Ir case the energy profiles closely resemble those discussed for Pt-Co. In Pt-Co-MgO, however, the energy profiles differ significantly from latter two cases, as peaks in the energy profiles are shifted outward to about 5 nm from the skyrmion core. The energy profiles of the three monolayers are much closer in magnitude than those found in Pt-Co and Pt-Co-Ir, mostly because the DMI has the same sign in the first and third monolayers which results in more stable skyrmion structures. This suggests that the spatial profile of the skyrmion core is significantly different compared to other cases.

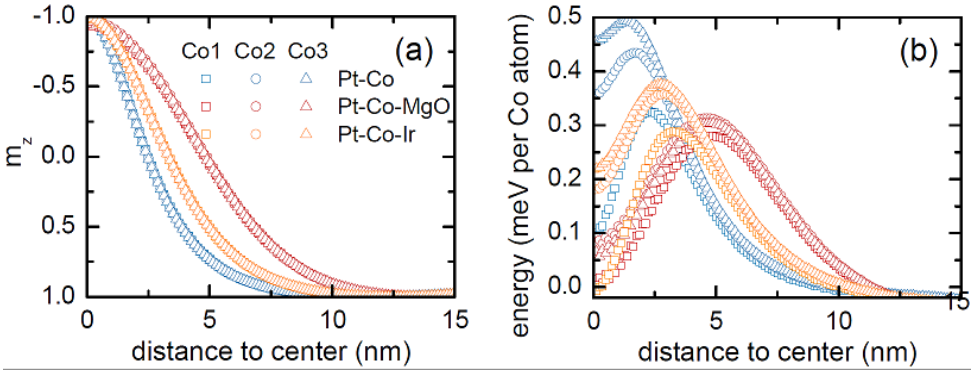

Figure 3.7 – (a) Line profile of an individual skyrmion for the 3ML Co in considered sandwich multilayers and the case of epitaxial 3ML Co on Pt. (b) The energy difference per Co atom with respect to the FM ground state as a function of distance from the skyrmion core. Strong exchange coupling is assumed ($J = 30$ meV per bond) and the anisotropy is taken as $K = 0.036$ meV per atom. The symbols correspond to the individual Co monolayers that are closest (squares), in between (circles), and farthest (triangles) from the Pt substrate.

3.3 Energy paths for skyrmion collapse

The thermal stability of magnetic skyrmions can be assessed by studying the mechanisms for collapse and associated energy barriers using minimum energy path calculations, as discussed in Section 2.5. Refs. [84,85] have used minimum energy paths to describe the collapse of isolated skyrmions. However, they restricted to a single atomic layer of magnetic material, and considered solely the isotropic (on itself) collapse of a skyrmion. Here we extend the material system to a more realistic few-monolayer case, sandwiched or not, laterally finite in size with either physical end of the ferromagnetic film or an interface where DMI vanishes (due to e.g. laterally finite heavy-metal layer). We consider two evolution paths the system can take in the process of skyrmion nucleation or annihilation: an isotropic transition where a symmetric rotation of the spins in the radial direction takes place [84,85] and collapse at the boundary [87]. We make use of GNEB with the climbing image (see Section 2.5.4) to calculate minimum energy paths for an isolated skyrmion. The convergence to a first-order staddle point is verified by ensuring that the energy gradient is sufficiently close to zero. Given the complexity of the energy surface, different stable paths can be obtained depending on the initial guess.

3.3.1 Isotropic vs. boundary collapse

First, we consider the case of an isotropic collapse in a 3ML Co film on Pt. The initial path is constructed by rotating each atomic spin from its initial orientation to the final one using Rodrigues' rotation formula [83]. Fig. 3.8(a-e) shows that the converged path is characterized by a progressive reduction of the skyrmion diameter down to zero [84,85]. Once the skyrmion core disappears [see Fig. 3.8(e)], the central spins are flipped due to ferromagnetic ordering (shown in red) which leaves a ring of spins

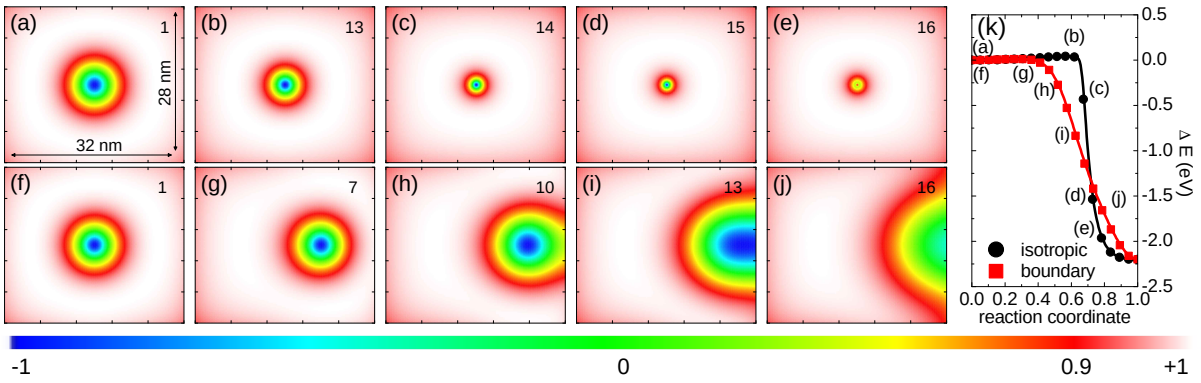

Figure 3.8 – Top view of magnetization ($\hat{\boldsymbol{m}}_z$) distribution for (a-e) isotropic and (f-j) boundary collapse paths of a skyrmion in 3ML Co on Pt, with monolayer resolved DMI. The skyrmion is initially 4.7 nm in diameter, for taken $J = 30$ meV per bond and $K = 0.036$ meV per atom. $\hat{\boldsymbol{m}}_z$ is shown color coded from white to red to green to blue (shown above). The initial images (a, f) are followed by saddle points (b, g), and remaining images show configurations on the subsequent energy decline towards the FM ground state (not shown). Numbers on top right correspond to ordering of images in minimum-energy path curves for the isotropic and boundary collapse (k). The reaction coordinate is defined as the normalized (geodesic) displacement along the minimum energy path.

pointing in the plane (shown in yellow). While the observed behavior coincides with the magnetization profiles in Ref. [85], this was not found in Ref. [84] where the paths failed to converge to a minimum-energy path.

The second considered situation is the skyrmion collapse at the sample boundary, i.e. the physical end of the ferromagnetic film [87]. In this case, an initial path is made by sliding a window containing the skyrmion from the center to the boundary of the sample. In the final transition path [shown in Fig. 3.8(f-j)], the skyrmion core is distorted towards the boundary, before opening into a half circle, after which the spins gradually relax into the FM state. The saddle point in energy is found when the approaching skyrmion causes the boundary spins to cant outwards, such that their angle with the substrate (further denoted as θ) is greater than $\pi/2$. The exact distance at which this happens can be described by the exchange interaction length $l_{ex} = \sqrt{J/K}$, which is the length below which atomic exchange interactions dominate anisotropy or magnetostatic fields, and governs the width of the transition between magnetic domains [178]. In the considered few-monolayer ferromagnetic films, we find that Néel domain walls can have widths of around $3\sqrt{J/K}$, as was suggested in literature for the case of very thin films [178,179].

Fig. 3.9(a) shows that energy barriers for the isotropic collapse of a skyrmion increase for lower magnetic anisotropy, surpassing 100 meV for $J < 30$ meV per bond. The monotonic decrease in energy barriers for increasing values of J follows the decrease in skyrmion size, since fewer core spins are required to flip into the FM state along the path. We note however that the exact shape and maximum of the energy curve will depend on the geometry and size of the finite system. Fig. 3.9(b) shows that the energy barriers in a boundary collapse are significantly different than those

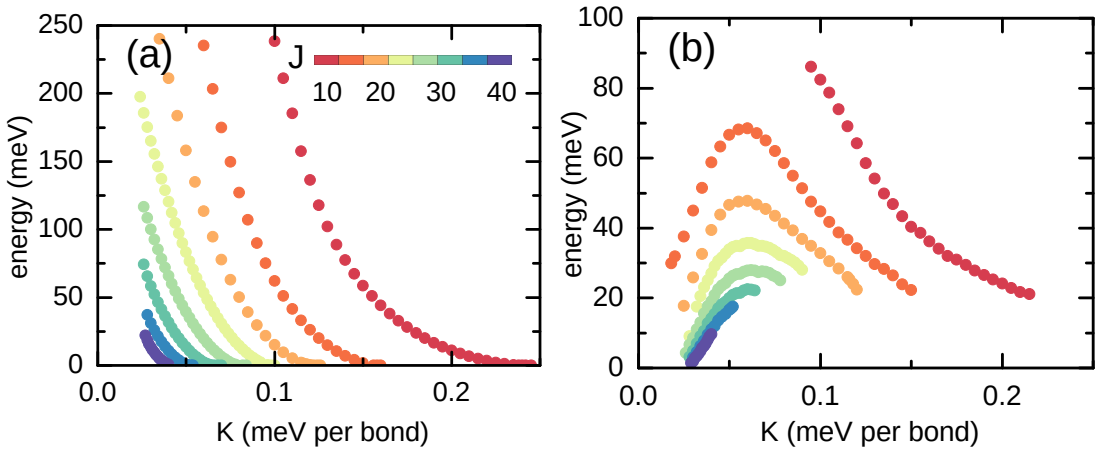

Figure 3.9 – Energy barriers for (a) isotropic and (b) boundary collapse of a skyrmion as a function of magnetic anisotropy. Each point corresponds to a unique energy barrier retrieved from the maximum (saddle point) in a minimum-energy path.

found for the isotropic collapse [Fig. 3.9(a)], presenting a maximum for intermediate anisotropy instead of the monotonic decrease with anisotropy. Further investigation reveals that the observed maxima in barriers is in fact the boundary effect due the confined geometry of the sample. Due to open boundary conditions, one finds a spontaneous inward canting of the boundary spins [172] even for the FM ground

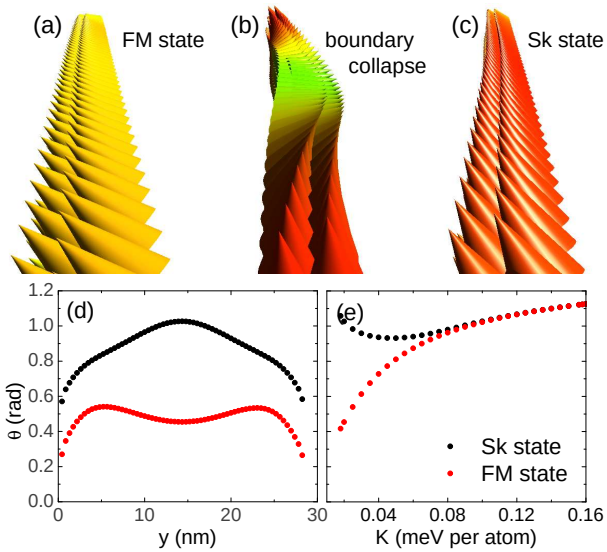

Figure 3.10 – (a) Side view of atomic spins along the right boundary of the system for the FM ground state, during boundary collapse, and the Sk state left to right respectively. The variation of the angle that boundary spins make with the substrate is shown in panel (d) as a function of position along the boundary and in panel (e) as a function of magnetic anisotropy, for the central spin on the boundary. Calculations are performed for low exchange coupling ($J = 10$ meV per bond).

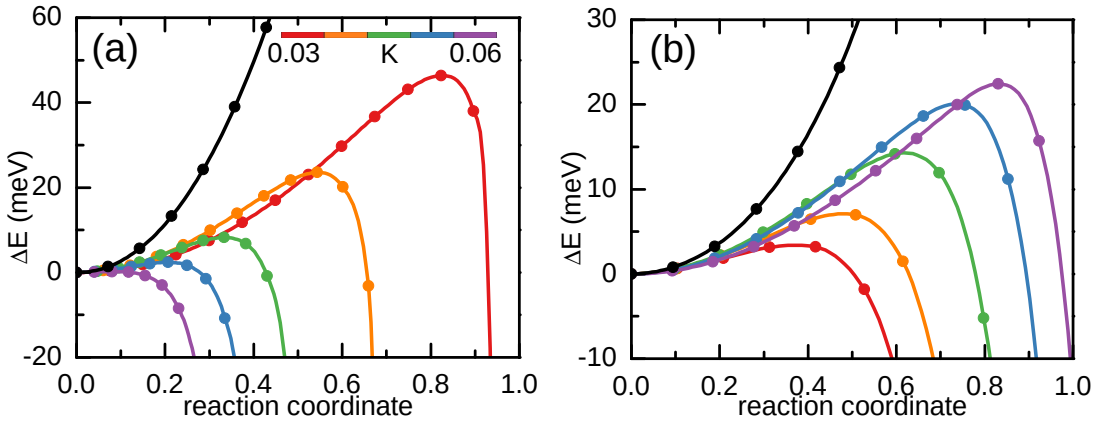

Figure 3.11 – Minimum-energy paths for (a) isotropic and (b) boundary skyrmion collapse in case of strong exchange coupling ($J = 30$ meV per bond). Paths are shown for different magnetic anisotropies with respect to the FM ground state. Solid lines are cubic polynomial interpolations [83] of the discrete images (dots). Black lines correspond to the case of constant DMI.

state [shown in Fig. 3.10(a)]. However, the presence of a large skyrmion (for example for weak exchange interaction) can affect the boundary spins in such a way that the tilt angle increases [i.e. θ approaches $\pi/2$, see Fig. 3.10(b)] and the energy required to collapse the skyrmion (or equivalently, to surpass the canting of boundary spins) is reduced. For given size of the system, the skyrmion size for which the latter canting occurs will depend on l_{ex}. For example, the peak energy barrier occurs at skyrmion diameter of 12 nm for low exchange interactions ($J < 15$ meV per bond), whereas for high exchange couplings skyrmions of only a few nanometers in size can already affect the boundary spins in our samples.

The obtained minimum energy paths [Fig. 3.11(a)] indicate that the isotropic collapse exhibits a similar transition to the monolayer case [84,85]. For a skyrmion with diameter of 4.7 nm the energy barrier is 41 meV compared to the 37 meV found in Ref. [85]. The low energy barrier can be explained by the competition between the destabilizing DMI which dilutes in monolayers away from the substrate and the thickness of the magnetic layer which increases skyrmion stability. This suggests that the energy barriers in the considered case are going to be similar to those in 1ML Co on Pt. Minimum energy paths for skyrmion collapse at the boundary are shown in Figs. 3.11(b) and 3.12(b), for strong and weak exchange respectively. For strong J the paths have a similar behavior to the paths found for the isotropic collapse. On the other hand, paths for weak J are characterized by two stages corresponding to the (i) skyrmion reaching the boundary, and (ii) skyrmion fully exiting on the boundary. This step is found when the exchange length is smaller than the skyrmion diameter, thus becomes less pronounced for stronger exchange couplings or anisotropies (where l_{ex} exceeds the skyrmion size).

The calculated energy barriers for the isolated and boundary collapse enable us to determine the preferential collapse mechanism of a skyrmion in a 3ML Co on Pt, in the presence of e.g. thermal fluctuations. The found preferential collapse mecha-

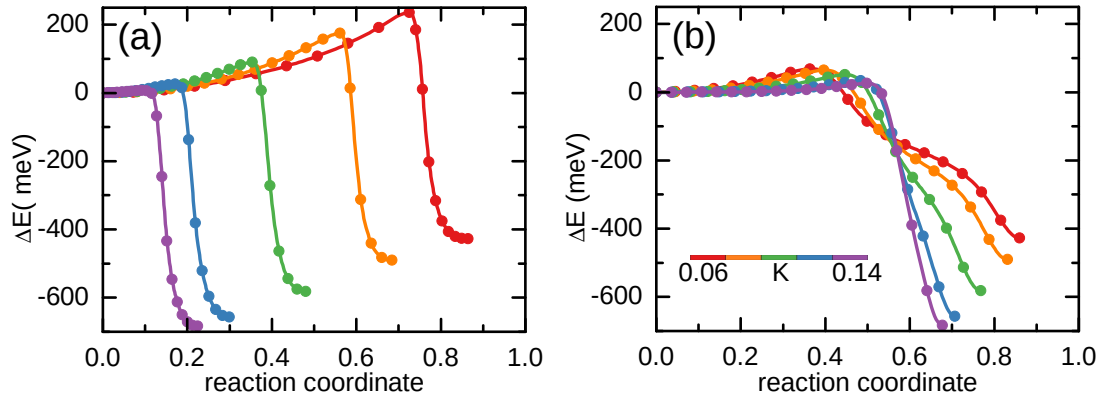

Figure 3.12 – Minimum-energy paths for (a) isotropic and (b) boundary skyrmion collapse in case of weak exchange coupling ($J = 10$ meV per bond). Paths are shown for different magnetic anisotropies with respect to the FM ground state. Solid lines are cubic polynomial interpolations of the discrete images (dots).

nisms, superimposed on the parametric range of stability for a skyrmion are indicated in Fig. 3.2. For skyrmions near the upper bound of their stability area in the magnetic state diagram of Fig. 3.2, the isotropic collapse has a smaller energy barrier compared to the collapse at the boundary. Therefore we expect the isotropic collapse to be deterministic for the stability of skyrmions in that parametric range and not the boundary collapse as suggested in Ref. [87]. The energy barriers for the isotropic collapse can be increased by lowering the anisotropy, i.e. increasing the skyrmion size, which would however strongly decrease the barrier for the boundary collapse. However, the width of the racetrack also plays a crucial role since a skyrmion in the center of a large sample is unlikely to travel and escape through the boundary. We can then conclude that for large skyrmions [region I in Fig. 3.2] the boundary collapse limits their stability, whereas for small skyrmions [region II in Fig. 3.2] their stability is dictated by the isotropic collapse, but the exact collapse mechanism the skyrmion undertakes will also depend on its distance from the boundary of the finite sample [see Sec. 3.3.2 for more details].

Finally we discuss the comparison to the minimum energy paths for skyrmions in case of constant DMI for all three Co monolayers, given by black lines in Fig. 3.11. The collapse behavior for isotropic and boundary transitions is seemingly similar to those obtained in the monolayer-resolved case for 3ML Co on Pt. This is expected since we found earlier that the skyrmion persists through all three monolayers, with nearly equal size and energy as for monolayer resolved DMI. However, the energy barriers are significantly different. The isotropic collapse has an energy barrier of 336 meV for constant DMI compared to the maximum of 74 meV found for monolayer-resolved DMI, whereas the boundary collapse occurs at 172 meV compared to 22 meV respectively. This is another manifestation of the fact that the increased cumulative DMI of 4.5 meV per bond (1.5 meV for each monolayer) induces more stable Sk states, since in the layer-resolved case DMI is diluted in monolayers away from the interface with Pt.

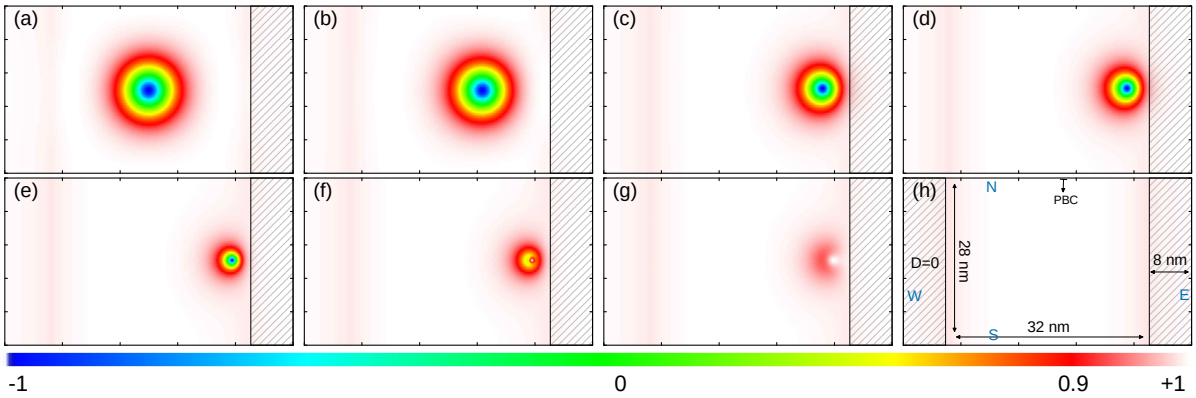

Figure 3.13 – Top view of spatial magnetization distribution $[\hat{\boldsymbol{m}}_z(x,y)]$ in a 3ML Co on Pt, for skyrmion collapse at the interface with boundary region (of width 8 nm, see inset) where DMI vanishes. The parameters used are $J = 30$ meV per bond for exchange and $K = 0.050$ meV per atom for anisotropy. Individual images correspond to the initial Sk state (a), path towards the saddle point (b-d), and subsequent stages (e,g) towards the FM ground state (h).

3.3.2 Collapse at lateral DM interfaces

It is clear that skyrmions have poor thermal stability in finite systems due to proximity of the boundaries, which complicates their practical applications in e.g. racetrack memories. For skyrmions to be usable in desirable situations, such as near room temperature and in nanostructured circuits, one needs to increase the energy barrier for the collapse of the Sk state. One recently reported way to achieve this is by lateral heterostructuring of the DMI [180], so that the confining system is not determined by the finite size of the ferromagnetic film but rather by vanishing DMI (due to e.g. patterned heavy-metal layer(s)). In what follows, we consider the same system (3ML Co on Pt) with monolayer resolved DMI inside, surrounded by an outer region with no DMI, where then an open boundary is placed. We thus study the stability of a skyrmion towards collapse at the interface between regions with different DMI. In Fig. 3.13 we illustrate the considered system, where we extended the previous sample by a surrounding band of width 8 nm where DMI vanishes (so system now contains a total of 75660 spins). We considered several initial paths: sliding a window containing the skyrmion from the center to the boundary, relaxing each image by fixing the core spin, and using the boundary transition as input. As shown in Fig. 3.13(a-g), the converged path involves a skyrmion translation towards the interface and a rotation of the spins into the FM state. The rotation is similar to that of the isotropic collapse and occurs right before the interface.

Fig. 3.14(a) reveals that the energy barrier for collapse of the skyrmion at the interface where DMI vanishes (East/West side, see sample in Fig. 3.13), is significantly larger than the barrier for a transition at the open boundary. The barrier for collapse at the DMI interface is actually rather similar to the one for the isotropic collapse, since the spin-flipping sequence along the minimal energy path is essentially the same in those two cases. This implies that the the favorable collapse mechanisms in the (J, K)

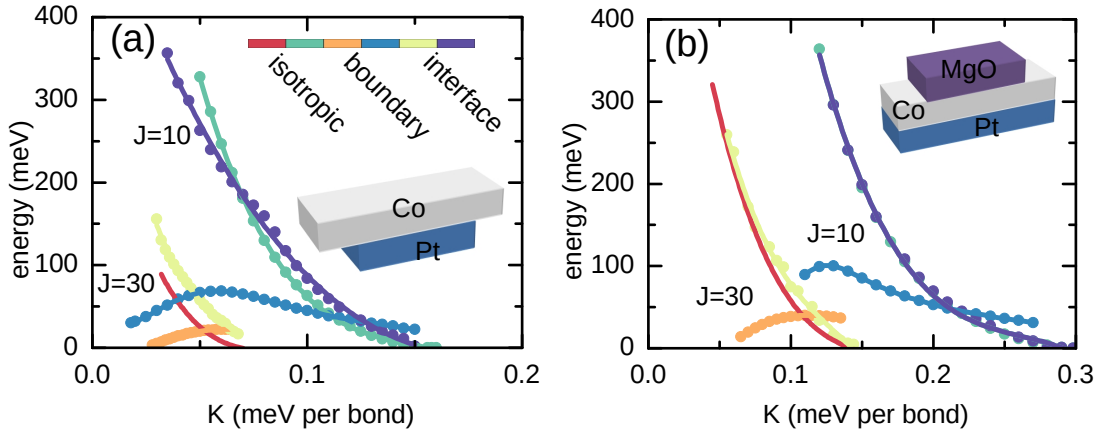

Figure 3.14 – (a) Energy barriers for the collapse of a skyrmion in the sample shown in Fig. 3.13(h) (3ML Co on Pt, with monolayer resolved DMI), at a lateral (East/West) interface where DMI vanishes, at North/South open boundary of the film, and for the isotropic collapse, as a function of magnetic anisotropy. Each point corresponds to a unique energy barrier retrieved from the maximum (saddle point) in a minimum energy path. (b) Same as (a), but for the Pt-3ML Co-MgO sandwich, with monolayer resolved DMI, and removed MgO on lateral sides of the sample (thus lower DMI, particularly in the top Co monolayer). In either sample, stability of the skyrmion is dictated by boundary collapse at low anisotropy and isotropic collapse otherwise. The barrier for collapse at DMI interface greatly exceeds the one for boundary collapse at all (J, K).

diagram for the considered system with supressed DMI on the two sides will be nearly the same as for the sample without any DMI interface. However, our results also mean that if we were to completely surround the inner region by a region with low DMI, or elongate the sample vertically, the boundary collapse will be suppressed and the barrier for skyrmion collapse for all (J, K) combinations will be increased. This is very beneficial for future design of e.g. skyrmion racetracks, by having an extended Co film on a track defined by the pre-patterned Pt substrate.

Arguably, it is more convenient to use the extended Pt substrate and Co film on it, but then pattern the MgO capping layer to form a racetrack. In Fig. 3.14(b) we show the barriers for different types of skyrmion collapse for this case, for the sample size identical to one of Fig. 3.14(a). The interior of the sample now has MgO on top, with corresponding layer-resolved DMI (high in the top Co monolayer, see Fig. 3.6), while the outer region is bare 3ML Co on Pt - with significantly lower DMI in the top Co monolayer. In this case, the stability of the skyrmion is improved as energy barriers for the skyrmion collapse are higher [shown in Fig. 3.14(b)], but the relationships between different mechanisms for collapse remain similar to the previously considered sample [in Fig. 3.14(a)].

The fact that we do not observe an escape through the interface like in the boundary case can be explained by the inclusion of the magnetic layer instead of a vacuum. While at the boundary with a vacuum only canting of the boundary spins provides the force keeping the skyrmion inside the track, at the interface the force is dominated

by ferromagnetic ordering between spins near the interface and by the anisotropy. The energy barrier required to overcome this ordering (due to exchange interactions and anisotropy) is greater than energy contributions arising from the DMI, which leads to an isotropic collapse of the skyrmion near the interface where the DMI contributions are stronger. Therefore, we attribute the absence of the boundary escape mechanism to the lack of (or reduced) DM interactions which are needed to overcome the exchange and anisotropy energies [see Fig. 3.5], and to facilitate the motion of the skyrmion through the interface. To quantify the possible energy barrier for an escape through the interface and the boundary, we took images from the boundary escape mechanism and then calculated the corresponding energies after having removed MgO on lateral sides of the sample. The energy barrier exceeds 200 meV, which is roughly twice higher than the barrier for the skyrmion to collapse on the interface [as in Fig. 3.14(b)].

We note that thus far we assumed spatially homogeneous material parameters, which lead to stable skyrmions on one side of the interface, but stable ones on the other side. In the case a magnetic layer is present in the extended region, it is important to allow the anisotropy to vary so that the skyrmion remains stable on both sides of the interface. We therefore choose exchange and anisotropy values on the two sides of the interface which result in skyrmions of similar diameters. Our simulations indicate that an escape mechanism at the boundary is indeed possible in this configuration, as expected since the skyrmion can exist in both regions with different DMI. The stability and energy barrier of the skyrmion, however, demonstrate complex dependence on the exchange and anisotropy parameters, and other possibilities for skyrmion collapse may occur. For example, for interfaces that are far away from the boundary one can expect that the boundary escape will only be observed when the skyrmion is stable on both sides of the interface, since the skyrmion is unlikely to remain in an unfavorable configuration as it travels towards the boundary. On the other hand, for relatively narrow heterogeneous structures such as the ones considered in this work, one can expect that the skyrmion can indeed enter a region where it is not stable and collapse without an energy barrier. Due to lacking information on particular exchange and anisotropy values to be used, detailed investigations in this direction remain outside the scope of the present work.

Therefore, as an optimized design of the skyrmion racetrack at room temperature we discuss the case of the same geometry of the sample as in Fig. 3.13, but with periodic boundary conditions on North/South edges. The behavior of the barriers for skyrmion collapse, now that there is no open boundary, are shown in Fig. 3.15(a,b), for the materials considered in Fig. 3.14(a,b) respectively. We indeed confirm that the barriers for collapse are significantly higher, particularly in the low-anisotropy regime where boundary collapse usually dominates. Next, from these optimized energy barriers in Fig. 3.15(a,b), it is interesting to quantify the lifetime of skyrmions using the Arrhenius law

$$\tau = \tau_0 \exp\left(\frac{\Delta E}{k_B T}\right), \tag{3.1}$$

where τ_0 is related to the attempt frequency $f_0 = 1/\tau_0$, ΔE is the energy barrier, k_B is the Boltzmann constant, and T is the temperature. Since the attempt frequencies are hard to obtain and can vary in magnitude, we assume $f_0 = 10^9$ Hz as suggested in

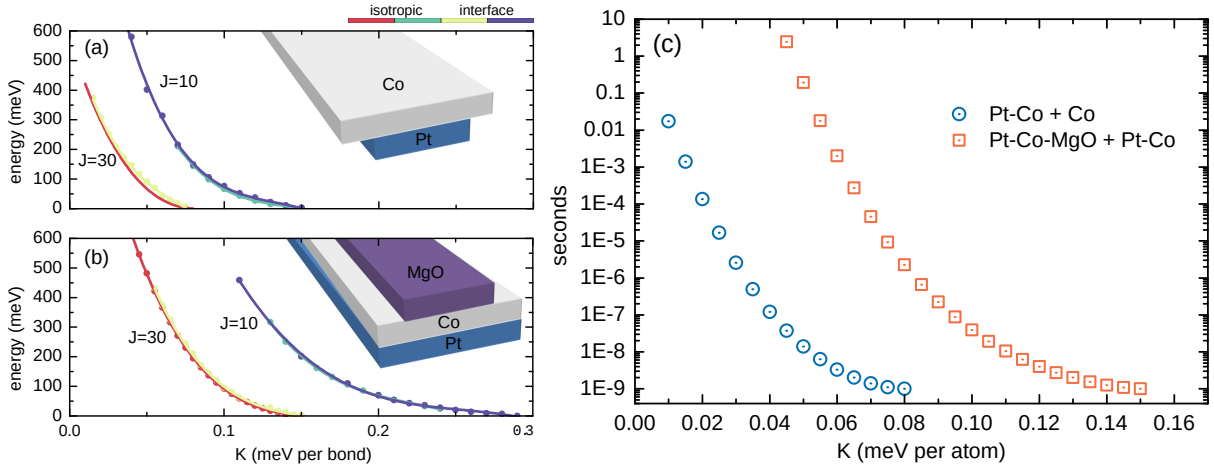

Figure 3.15 – (a,b) Same as Fig. 3.14(a,b) respectively, but for periodic boundary conditions used at North/South edges of the sample, so that effectively an elongated track with laterally suppressed DMI is considered. (c) The lifespan of an isolated skyrmion [given by Eq. (3.1)] calculated for the most favorable mechanism of collapse in (a,b), for standard exchange coupling for Co ($J = 30$ meV per bond), as a function of anisotropy, at room temperature.

literature [84, 87]. We focus on the skyrmion lifetime for the considered systems (see Figs. 3.14 and 3.15) and scan the lowest energy barrier for skyrmion collapse as the effective anisotropy is varied. Fig. 3.15(c) shows that the lifespan of the skyrmion at room temperature spans a wide range of magnitudes, from the order of seconds to just a few nanoseconds, but we can determine the relevant values based on parameters retrieved from experimental works [49, 50]. The exchange constant for the Co layer is roughly 30 meV per bond. The effective anisotropy varies between 0.019 meV per atom for Pt-Co-MgO sandwich [50] and 0.015 meV per atom for Pt-Co-Ir multilayers [49] (conversion relations between micromagnetic and atomistic parameters can be found in Ref. [87]). For such parameter values the skyrmion lifetime can reach few seconds, based on isotropic or interfacial collapse discussed in Fig. 3.15. The boundary escape is not a realizable collapse mechanism in the considered system, which has interfaces with regions of no DMI in East/West direction the skyrmion cannot surpass (see previous discussions), and is taken periodic in North/South direction so there is no boundary there. However, for systems with open boundary conditions in the North/South direction, the boundary collapse has lifetimes that can reach maximum of few nanoseconds, as seen from the energy barriers in Fig. 3.14.

A proper analysis of skyrmion lifetimes is difficult as the exact collapse mechanism which the skyrmion will undertake depends on its distance from the boundary or interface. For example, a skyrmion positioned at the center of a very large sample will naturally be limited by the isotropic collapse, whereas a skyrmion near the edge might escape at the boundary instead. Ref. [51] has indeed observed long-lived skyrmions near room-temperatures, albeit on racetracks that are 20 times wider than the skyrmion diameter, where escape at the boundary is very unlikely to occur. In nanometer-wide racetracks which are suitable for ultradense magnetic storage de-

vices, however, the diameter of the skyrmion is only two to five times smaller than the width of the racetrack, and we can therefore expect that collapse at the boundary is inevitable and will dictate skyrmion stability. We therefore believe that our analysis on skyrmion lifetimes matches the behavior of room-temerature skyrmions observed in experiments. These results indicate that lifetime of a skyrmion can reach seconds in the considered samples, compared to maximum few nanoseconds in same geometries with open boundary. This confirms again that the DM interface as proposed here could be a very convenient solution to the weak stability of skyrmions in finite systems.

4 PINNING OF MAGNETIC SKYRMIONS

In this Chapter[1] we investigate the interactions of single skyrmions with atomic defects of distinctly different origins. We first report the preferred pinning loci of the skyrmion as a function of its nominal size and the type of defect being considered, to further reveal the manipulation and "breathing" of skyrmion core in the vicinity of a defect. We also show the behavior of skyrmions in presence of an extended defect of particular geometry, that can lead to ratcheted skyrmion motion or a facilitated guidance on a defect "trail". We close off the study by reflections on the expected thermal stability of the skyrmion against collapse on itself for a given nature of the defect, and discuss the applications where control of skyrmions by defects is of particular interest.

4.1 Introduction

Pinning plays a very important role in the mobility of skyrmions: imperfections in the magnetic material (such as impurity atoms, lattice defects, and geometrical constrictions) act as pinning sites and can result in an effective slow-down or even capturing of the skyrmion [51, 132]. This could lead to artificial placement of pinning centers within the material for precise positioning of individual skyrmions, as was previously done for magnetic domain walls [72]. However, overly strong pinning is detrimental for the intentional movement of magnetic skyrmions, such as in racetrack memories. Skyrmion lattices have been moved through materials with defects by laterally applied currents [59, 68, 69], and it was found that they can be pinned below a critical current density but remain undisturbed for larger currents [40]. For individual magnetic skyrmions several pinning mechanisms have been studied theoretically: local maxima in magnetic exchange [130, 181], vacancies in the magnetic material [182], areas with higher magnetic anisotropy [40, 65], and more recently magnetic grains with varying anisotropy or DMI [183, 184]. Recent experiments [185] have also considered interactions with atomic scale defects and have identified preferred pinning positions for the skyrmion.

While crucial for the development of future spintronic applications, a proper understanding of how magnetic skyrmions pin to defects remains lacking. Ref. [185] discusses the pinning positions for individual skyrmions, but neglects to provide an exact description and only considers the static situation. Other theoretical works [40, 65, 130, 181, 182] have studied the dynamical behavior of skyrmions around a defect, but could not quantify the exact transition from a pinned to an unpinned state. There are also a number of works in the literature that have considered skyrmion behavior in periodic [80, 186] and random [187–189] pinning arrays, ratchet geometries [190], and linear defects [191–194]. However, these works typically assume a phenomeno-

[1] The results of this Chapter are published in Ref. [93].

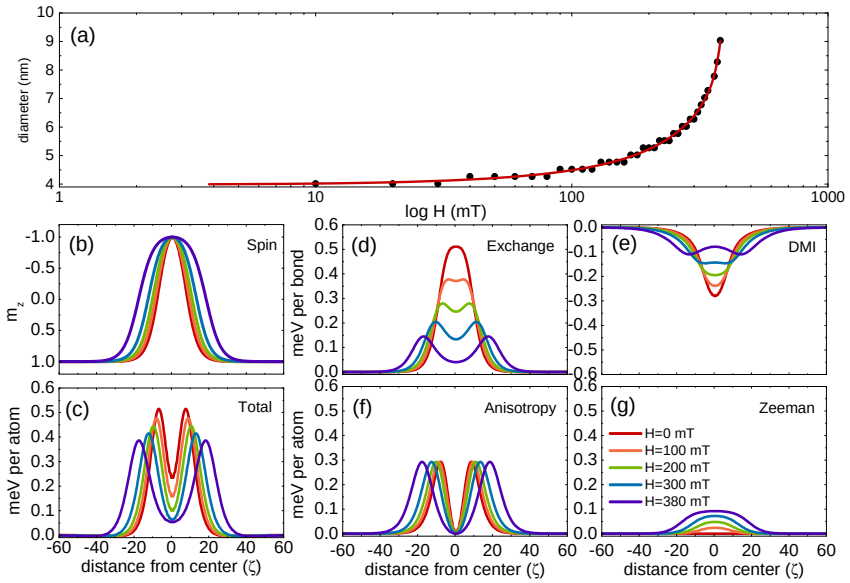

Figure 4.1 – (a) Core diameter in different external magnetic fields, and (b) line profile of magnetization S_z, for an individual skyrmion. Energy difference per Co atom or bond with respect to the uniform state for (c) total, (d) exchange, (e) DMI, (f) anisotropy, and (g) Zeeman contributions.

logical model for pinning (effective parabolic potentials) rather than a microscopically justified one.

To obtain the proper description of the interaction of a skyrmion with a defect, an energetic consideration of the depinning is needed in the microscopic framework. Transitions from complex magnetic states such as pinned skyrmions are slow events on the time scale of spin switching, which makes direct dynamical spin simulations an impractical way to characterize pinning. Instead, the maximum along the minimum energy path, which provides an estimate of the activation energy of a depinning transition, can be used to quantify the stability of a pinned magnetic state. In that way, the description of single-spin-resolved transitions from pinned skyrmion state essentially becomes a problem of finding the path of minimum energy on the energy surface, and the corresponding evolution of the magnetic spin texture.

With this in mind, the pinning of a magnetic skyrmion is revisited in this Chapter by considering the minimum energy paths for transition from a pinned state, where the skyrmion is trapped in a potential well induced by the given defect, to an unpinned state, where the pinning forces are negligible and the skyrmion is free to move through the material. For the magnetic system to consider, a single atomic layer of Co grown epitaxially on the Pt(111) surface is considered which can be modeled using Eq. (2.4). The material parameters for Co/Pt samples are listed in Chapter 3. An external magnetic field $\boldsymbol{H}$ is applied in the $-\hat{\boldsymbol{z}}$ direction (parallel to the skyrmion core) and used to control the size of the skyrmion. As shown in Fig. 4.1(a), the skyrmion can grow up to roughly 9 nm in diameter at a field of $H = 380$ mT before it collapses to the uniform state. Fig. 4.1(b-g) reveal substantial variations in the various components of the energy across different applied magnetic fields.

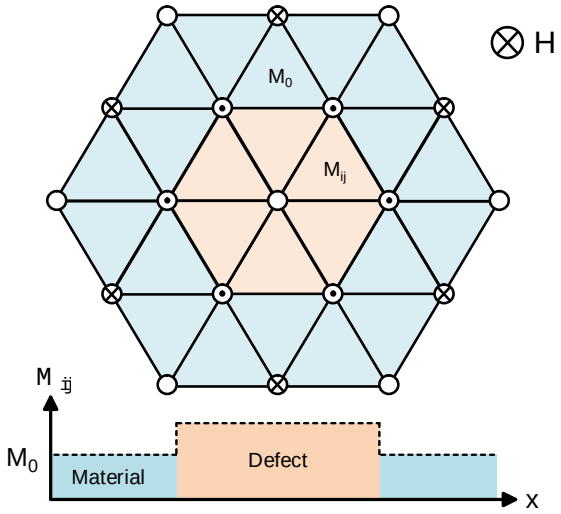

Figure 4.2 – Schematic illustration of the considered defects, having hexagonal geometry on a triangular lattice. Defects are represented by atoms (circles) and bonds (lines) inside the inner region (in red), while bonds intersecting the outer region (in blue) are removed in the case of hole defects (where atoms are absent). Bottom graph shows the line profile of the material parameter M_{ij} (denoting either exchange, DMI, or anisotropy), being higher or lower inside the defect with respect to the rest of the sample where $M_{ij} = M_0$. Circles with dots correspond to nearest neighbors of the central lattice point, whereas circles with crosses represent next-nearest neighbors.

4.2 Pinning fundamentals

Pinning at a defect can have different origins, and a theoretical analysis on the different ways to pin a skyrmion is needed. We therefore begin the discussion by considering pinning that arises from four different defects: local minimum of the exchange strength, increase of DMI, areas with lower magnetic anisotropy, and atomistic vacancies in the magnetic material. Details on their physical origins are summarized in Section 2.3.3.

4.2.1 Pinning on material defects

Defects due to spatial variations in material parameters (magnetic exchange, DM interaction, and anisotropy) are modeled by step functions (with hexagonal geometry) as shown in Fig. 4.2, where a set of lattice points is chosen to have different material parameter M_{ij} from the rest of the sample that has $M_{ij} = M_0$. Fig. 4.3 reveals that three distinct pinning positions can be effectuated depending on the properties of the considered defect. For anisotropy defects, the skyrmion pins at the domain wall when a lower anisotropy is considered ($K_i < K_0$). A similar pinning behavior is found for inlayer defects with reduced exchange interaction ($J_{ij} < J_0$), where the parallel alignment of spins at the domain wall is favorable. Defects with increased DM interactions ($D_{ij} > D_0$) favor canting of the magnetic spins and will therefore pin the skyrmion

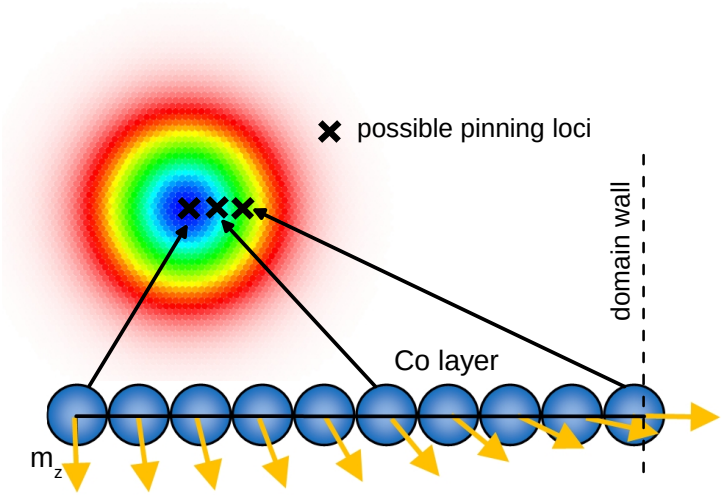

Figure 4.3 – Possible pinning positions for an individual skyrmion considering different kinds of defects. Spheres correspond to individual Co atoms. Skyrmions can pin either at the center (in blue), at the domain wall (in green), or between the two (in cyan) depending on the energy landscape in the vicinity of the defect.

between the center and the domain wall where the angle between spins is the largest. Note that the pinning positions can be explained by individual energy contributions for a magnetic skyrmion (see Fig. 4.1). Defects with opposite material parameters to ones discussed above will have their energy difference due to interaction with the skyrmion inverted, and will pin the skyrmion at its center. Table 4.1 summarizes the pinning positions of skyrmions at the considered material defects, with similar results to Refs. [61,130]. In the remainder of this Chapter we will consider defects with either $K_i = 0.5K_0$, $J_{ij} = 0.9J_0$, or $D_{ij} = 2D_0$, unless stated otherwise.

Table 4.1 – Pinning position of a skyrmion at different kinds of material defects.

Defect	$M_{ij} > M_0$	$M_{ij} < M_0$	Description
Anisotropy	At the center of the core	Off-center, at domain wall	Favors spins normal to the plane
Exchange	At the center of the core	Off-center, at domain wall	Favors parallel alignment of the spins
DMI	Between center and domain wall	At the center of the core	Favors canting of the spins

The preferred pinning position can also depend on the size of the defect with respect to the diameter of the skyrmion core. One might intuitively expect that a skyrmion with a large core will pin at a different location than a skyrmion with a

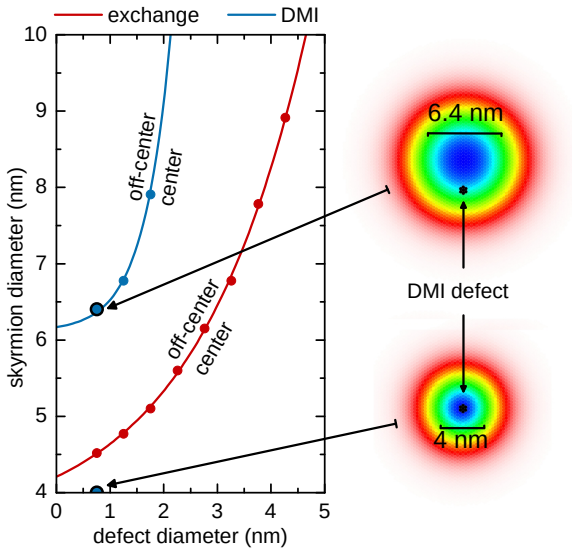

Figure 4.4 – Pinning regimes (centered or off-centered) of an individual skyrmion at defects induced by variations in either exchange or DMI. Images on the right illustrate skyrmion pinning for considered DMI defects (in black) for $H = 0$ mT (bottom) and $H = 300$ mT (top).

small number of core spins. Fig. 4.4 reveals that an inlayer defect induced by variation in exchange or DM interaction would pin the skyrmion at its center for low magnetic fields (small skyrmions), but off-center for higher field values (large skyrmions). The off-center pinning occurs at the domain wall of the skyrmion core for exchange defects, and between the domain wall and the center of the skyrmion for DMI defects. The transition from center to off-center pinning can be explained by the alignment of magnetic spins in the skyrmion core. For large skyrmions with proper alignment of the core spins, a defect in the center of the skyrmion which reduces exchange or increases DMI will be unfavorable, whereas for small skyrmions such a defect is preferred precisely because it reduces the energy contributions due to canting of the spins. Fig. 4.4 shows that the transition (ratio of skyrmion to defect size) is not linear and depends strongly on the character of the defect. DMI defects are far less likely to pin skyrmions off-center when compared to exchange defects, while both favor pinning at the center for larger defects.

Next we study the mechanism by which an isolated skyrmion transits from a pinned to an unpinned state. Fig. 4.5 plots the minimum energy paths of pinning a skyrmion with and without an applied magnetic field at different material defects. The observed behavior of the total energy confirms our previous findings that pinning (position of the energy minimum) occurs at the center for small skyrmions and off-center for large skyrmions, except for anisotropy defects where pinning is always off-center. From the individual energy contributions we find that the transition mechanisms are similar across different material defects and pinning positions. As the skyrmion approaches the defect from a distant point, the exchange and anisotropy energies increase (i.e. become less favorable than when the skyrmion is in an unpinned state), contrary to the behavior of the DMI and Zeeman energies. The individual energy contributions reach a maximum (or minimum) when the defect is close to the

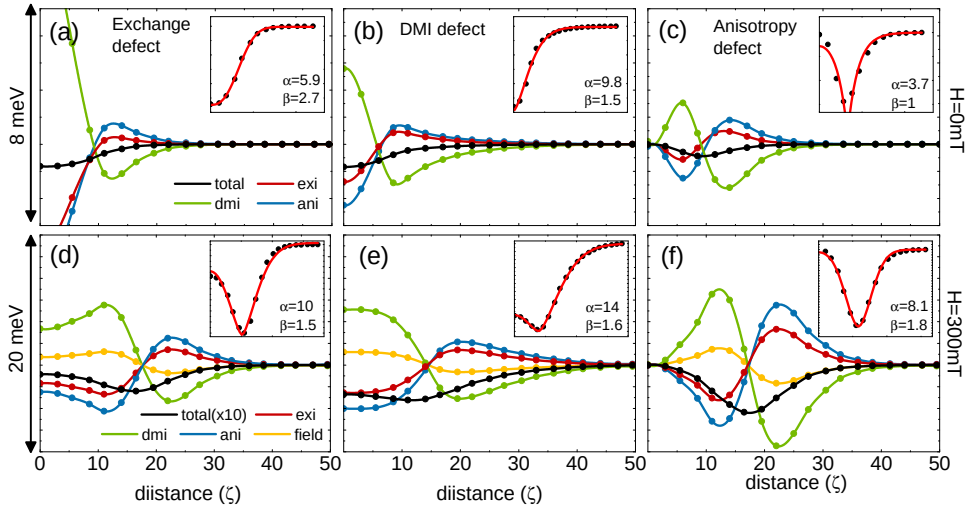

Figure 4.5 – Separate components of the energy [exchange (exi), Dzyaloshinskii-Moriya (dmi), anisotropy (ani), Zeeman (field)] and the total energy, plotted along the minimum energy paths for skyrmion escape from three kinds of material defects, at $H = 0$ mT (a-c), and $H = 300$ mT (d-f). Distances (in units of the lattice constant ζ) are calculated between the center of the skyrmion core and the center of the defect (placed in the center of the system). Insets plot functional forms of the total energy landscape (i.e. the effective pinning potential) fitted using exponential power function [see Eqs. (4.1)-(4.2)].

domain wall and decrease (or increase) as the skyrmion engulfs the defect. In the case of centered pinning, the described behavior of energy components persists up to the minimum in total energy at the center, whereas for off-center pinning the individual energy terms will peak somewhere between the center and the actual pinning location. This can be summarized as follows: while in terms of exchange and anisotropy energy the defect acts as an obstacle, adding to the skyrmion energy once it is overcome, the total energy remains a potential well due to the apparent dominance of DMI.

The effective pinning potential is often assumed to be parabolic in phenomenological models [130, 181, 182]. As seen in Fig. 4.5, the situation is much more complex, with pinning potentials that either capture the skyrmion in a well centered in the defect, or those that lead to off-center pinning locations. The insets in Fig. 4.5 reveal that potentials for centered pinning are well represented by an exponential power function (or generalized Gaussian) of the form

$$\mathcal{G}(\rho) \propto -e^{-\left(\frac{\rho}{\alpha}\right)^{\beta}}, \tag{4.1}$$

where ρ is the distance of the center of the skyrmion to the center of the defect (in units of ζ), and α and β are the scale and the shape parameter, respectively. The shape of the potential can be possibly related to the power law distribution of avalanches in driven magnetic skyrmions [188], and at least very useful for phenomenological models of pinning. The off-center pinning potentials are reasonably well described by the same function, shifted by the radial coordinate R at which the skyrmion is pinned

(exactly at, or near the domain wall of the skyrmion, cf. Table 4.1):

$$\mathcal{G}(\rho) \propto -e^{-\left(\frac{|\rho-R|}{\alpha}\right)^{\beta}}. \tag{4.2}$$

The coefficients best describing the pinning potentials for variations in material parameters that induce inlayer defects in Fig. 4.5 are listed in the corresponding insets. We note that the functional dependence of Eqs. (4.1-4.2) is preserved even in the presence of the magnetic field. It is obvious that coefficients α and β depend on all involved parameters, but the detailed description of that dependence is beyond the scope of this work.

4.2.2 Pinning in holes

As the last type of possible defects in a monolayer Co on Pt(111), we consider the physical hole due to vacancies in the magnetic layer. Such a defect can be modeled by removing a set of lattice sites and the corresponding bonds (see Fig. 4.2). In this case, any bond involving a missing atom must be excluded, as opposed to the case of material defects where only bonds between pairs of defect atoms were affected. Minimum energy paths in Fig. 4.6(a,b) indicate that the total energy is characterized by a weak energy barrier when transitioning from an unpinned to a pinned state as skyrmion spins are pressed against the edge of the hole before the skyrmion engulfs the pinning center, while individual energy contributions behave in a similar fashion to previously discussed cases of material defects. Furthermore, Fig. 4.6(c) shows that the preferable position of the skyrmion can be either at the center or at the domain wall (off-center), depending on the ratio of skyrmion to hole size.

Therefore, the effective pinning potential for skyrmions in the case of holes in the magnetic material is somewhat more complex as described by Eqs. (4.1-4.2), and needs to be expanded by a decaying exponential in order to describe the energy barrier that skyrmion needs to overcome before resting into the potential well at the pinning site:

$$\mathcal{G}(\rho) \propto -e^{-\left(\frac{|\rho-R|}{\alpha}\right)^{\beta}} + Ae^{-\frac{\rho}{\gamma}}. \tag{4.3}$$

Here ρ is the distance of the center of the skyrmion to the center of the defect (in units of ζ), α and β are the scale and the shape parameter [as in Eq. (4.2)], R is either zero or equal to the radius of the domain wall of the skyrmion, and γ is the exponential decay constant for the relaxation of the skyrmion far away from the hole. The coefficients best describing the pinning potentials in the presence of a hole in Fig. 4.6(a,b) are listed in the corresponding insets. Fig. 4.6(c) shows that the functional form in Eq. (4.3) accurately describes the pinning potentials for different values of the magnetic field, i.e. different size of the skyrmion, with coefficients depending on all involved parameters (including the size of the hole and the magnetic field).

However, the presence of a hole can also be detrimental for the skyrmions, as the skyrmion may isotropically collapse (magnetic spins undergo collective rotation in the radial direction towards the uniform FM state) for sufficiently large defects. Fig. 4.6(d) reveals that small vacancies in the magnetic material, which make up only one percent of the skyrmion core, can already induce a collapse of the skyrmion. This is likely due to the low activation barriers needed to stabilize individual skyrmions

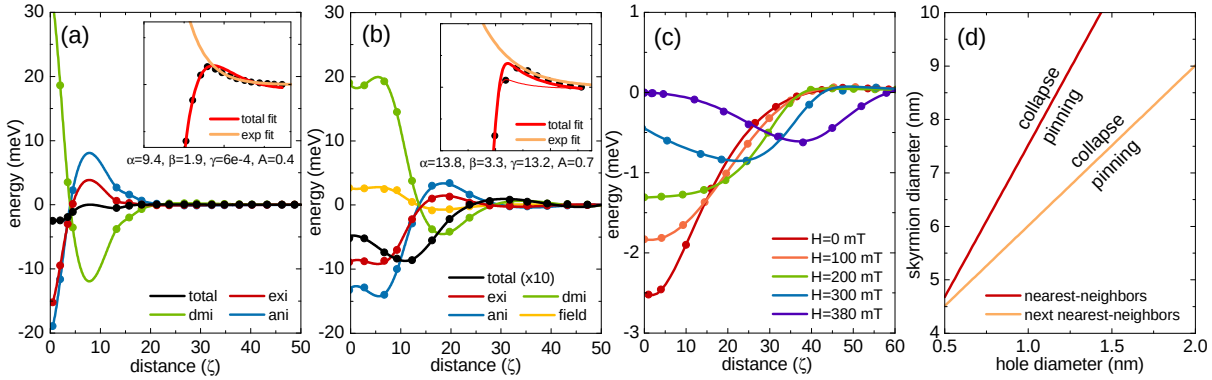

Figure 4.6 – Pinning of a skyrmion at a hole in Co monolayer on Pt. Separate components and the total energy are plotted along the minimum energy paths of the skyrmion pinned to a hole, for (a) $H = 0$ mT, and (b) $H = 300$ mT. Distances (in units of the lattice constant ζ) are calculated between the center of the skyrmion core and the center of the hole. Insets plot the effective pinning potential fitted using Eq. (4.3). (c) Evolution of the pinning potential of a hole with diameter 0.5nm, for different applied magnetic field. (d) The boundary between regimes of skyrmion pinning and skyrmion collapse at $H = 0$, as a function of skyrmion and defect size, for nearest and next-nearest neighbor approximations of the exchange interaction.

in Co monolayer on Pt. For example, a defect with three atomic vacancies (24 missing bonds) will induce a collapse of the 4 nm skyrmion, since the amount of energy lost in the defect essentially removes the energy barrier for isotropic collapse, of mere 36 meV. Therefore, the collapse of an isolated skyrmion is facilitated by the presence of magnetic vacancies, which makes its stability much more sensitive than previously anticipated. Similar findings of poor skyrmion stability were reported by Ref. [91], and were found to be in agreement with experimental measurements involving skyrmion nucleation near structural defects [48].

Since this poor stability around the defect in our simulations could be an artifact of nearest-neighbor approximations, we also tested the influence of the next-nearest neighbor exchange interactions ($J_1 = 29$ meV per bond and $J_2 = -0.6$ meV per bond). Similar results are obtained [see Fig. 4.6(d)], albeit with somewhat weaker scaling since the anti-ferromagnetic exchange improves skyrmion stability. While monolayer skyrmions (typically less than 10 nm in diameter) will annihilate for defects larger than 1.5 nm, room-temperature skyrmions that have been recently observed, with size between 30 and 100 nm [49–51], will pin and survive for up to 5 nm and 8.5 nm large holes, respectively. Although Ref. [182] reported stable skyrmions near holes in the magnetic layer, only a single missing spin was considered there, and micromagnetic simulations could not properly capture the skyrmion annihilation arising from a Bloch point.

A possible way to improve skyrmion stability in the presence of a hole involves adding a heavy-metal capping layer, i.e. increasing DMI in the vicinity of the hole, as illustrated in inset of Fig. 4.7. By increasing the DMI around the hole, the chiral interactions are strengthened and the size of the skyrmion increases, which permits

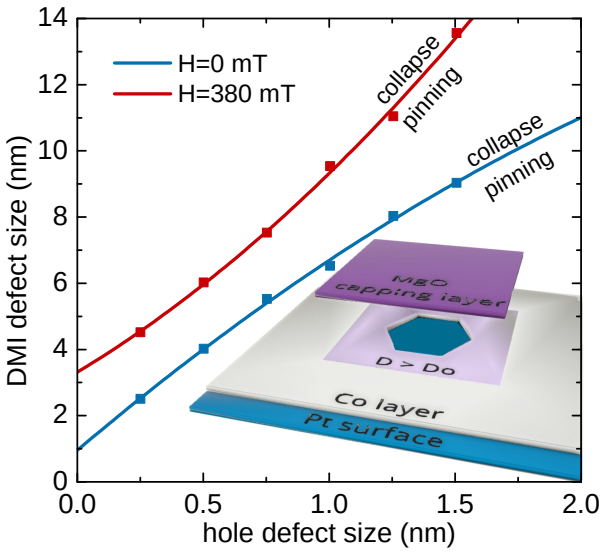

Figure 4.7 – Skyrmion pinning at a hole in Co monolayer on Pt, surrounded by region with higher DMI due to MgO capping layer. Regimes of skyrmion pinning and collapse as described in Fig. 4.6, using the next-nearest-neighbor exchange approximation, in absence and presence of external magnetic field. Inset: Artistic illustration of the considered structure.

for the presence of larger holes in the material without harming the skyrmion stability. Fig. 4.7 shows that individual skyrmions can pin near few-nanometer large holes when using a MgO capping patch on the Co film on Pt ($D_{ij} = 2.23$ meV per bond). The patch needed to prevent skyrmion annihilation in the present case is more than an order of magnitude larger than the hole, but can be designed smaller by using a heavy metal that induces a stronger DMI in the film than MgO does.

4.3 Employing the defects

Defects were shown to exert pinning and thus affect dynamics of magnetic skyrmions. It is therefore of interest to envisage possible use of defects in existing and emergent spintronic devices. In this section we consider three distinct defect geometries which can be exploited to induce particular behavior of skyrmions. Needed defects (or periodic [80, 186] and random [187–189] arrays thereof) can be constructed by spatial engineering of relevant parameters by e.g. patterning an additional (e.g. heavy-metal) layer (MgO, Ir, or other) on top of the Co/Pt system in the desired geometry of the defect.

4.3.1 Controlled breathing of a skyrmion

The interaction of an isolated skyrmion with a defect can affect skyrmion motion [130, 182], in a non-trivial fashion and in a plethora of ways. One can also expect that variations in size and other skyrmion properties should arise due to the spatially inhomogeneous pinning forces. Fig. 4.8 reveals that defects induce a breathing behavior on skyrmions: the skyrmion expands as it approaches a defect and then shrinks back

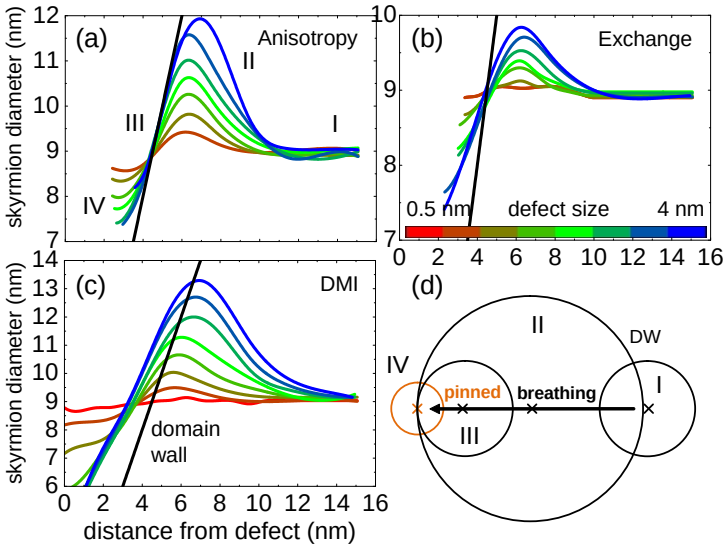

Figure 4.8 – Breathing of the skyrmion in the vicinity of a defect [for a defect arising from variations in anisotropy (a), exchange (b), and DMI (c)]. Defect diameter is varied between 0.5 nm and 4 nm (see color bar) and the applied field was held at $H = 380$ mT. In each panel the solid black line denotes the position where the domain wall of the skyrmion reaches the defect. (d) Schematic illustration explaining the observed breathing behavior (solid line depicts the domain wall of the skyrmion): (I) initial skyrmion near a defect, (II) skyrmion expansion, (III) skyrmion shrinking, and (IV) pinned skyrmion.

to its original size at the pinning position. While the maximal bloat of a skyrmion depends on the defect size, the pinning position and size recovery point will instead rely on the type of the defect. For example, one can see from Fig. 4.8 that the skyrmion diameter recovers its unpinned value when the domain wall sits on the defect for anisotropic and exchange defects, but for the defect between the domain wall and the center of the skyrmion for defects arising from DMI inhomogeneity. Fig. 4.8(d) depicts a schematic explanation for this breathing behavior. At a given distance from the defect (I) the skyrmion favors energetically that its domain wall [shown by solid line in Fig. 4.8(d)] sits at the pinning center, and thus expands to reach such configuration (II), to subsequently shrink once approaching the defect (III). For the case of an off-center pinning, the skyrmion recovers its unpinned size after stage III, whereas in the case of centered pinning the diameter of the skyrmion is further reduced when its core occupies the pinning site (IV). Note that the skyrmion can easily experience substantial variations in diameter (by as much as 50%) for relatively large defects.

Clearly, the pinning influence of material defects on isolated skyrmions can be used to control the skyrmion diameter. To obtain such manipulation, we consider defects formed as rings matching the shape of the skyrmion. Such defects can be induced through variations in DMI, where a heavy metal is patterned in the desired shape on top of the magnetic layer. Fig. 4.9 shows that when a skyrmion is placed inside the ring defect it can either translate so that it remains centered on the ring, or expand until the domain wall reaches the preferred position by coinciding with the

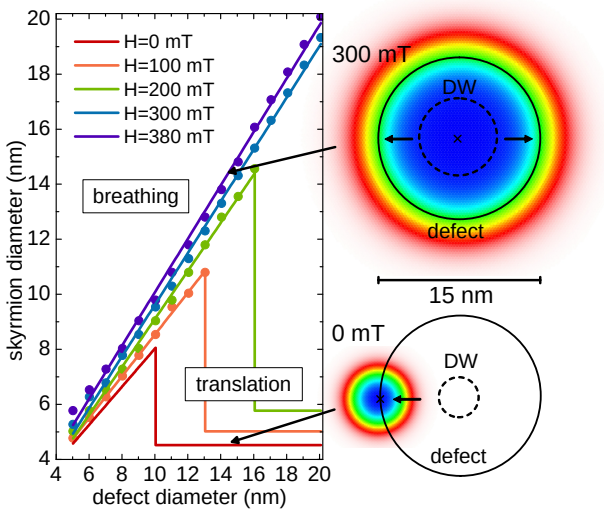

Figure 4.9 – Skyrmion behavior in a defect with inhomogeneous DMI shaped as a ring, as a function of ring diameter and for different applied magnetic field. Illustration on the right depicts a skyrmion either expanding to overlap its domain wall with the ring defect (top) or translating so that its core locates at the defect (bottom). The defect is shown by a solid line, while the dotted line corresponds to the domain wall (DW) of the initial skyrmion.

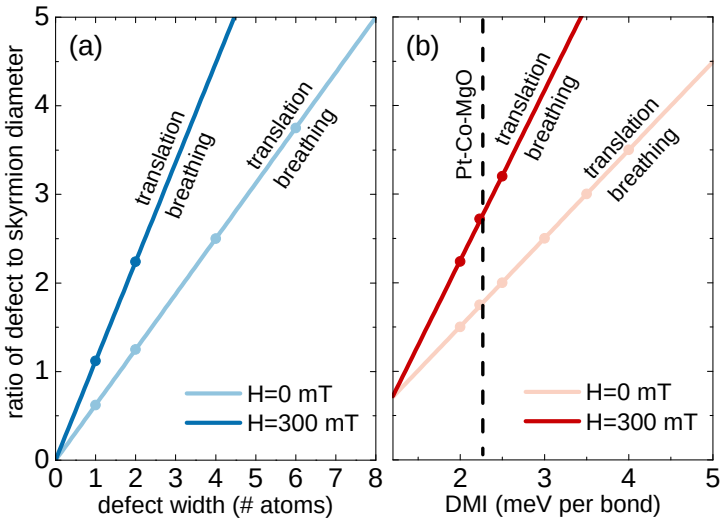

Figure 4.10 – Pinning regimes (either skyrmion expansion or translation) in the case of a ring defect, for different ratios of defect to skyrmion diameters, as a function of (a) the width of the defect, and (b) DMI strength.

ring defect. For centered pinning the skyrmion retains its original diameter, whereas in the case of off-center pinning the skyrmion diameter will match that of the defect. Fig. 4.9 also shows that the dynamics of the skyrmion (translation or expansion) depends on the ratio of the size of the unpinned skyrmion (dotted line) to the defect size. Breathing of the skyrmion only occurs for small defects (< 10 nm) when no magnetic field is applied, but remains present in larger defects (even above 20 nm)

for higher external fields. Fig. 4.10 shows that the transition line scales with both the width of the defect ring and the DMI strength. Increasing the width of the ring enables skyrmions to grow two to four times their size in order to reach more stable configurations. For known parameters of realistic material defects, such as a MgO capping layer patterned in the desired shape on Co film on Pt, we have realized the expansion of the skyrmion by defects that are *several times* the original size of the skyrmion, depending on the external magnetic field. This efficient manipulation of the skyrmion size suggests particular applications, for example in optics, based on the interaction of polarized light [195] with preformed periodic spin structures such as pinned skyrmion arrays, or in skyrmion-based magnonic crystals [79] tailored at will by the nanoengineered pinning.

4.3.2 Skyrmion ratchet

Ratcheting of particles in asymmetric potentials, and thereby creating a net motion in one direction despite a symmetric drive, is of pertinent interest in biological systems and pharmaceutical applications. Similar principle has already been employed to other, seemingly very remote systems, such as vortices in superconductors. There, vortices are carriers of dissipation in the presence of applied current, and asymmetric pinning potentials have been employed to either remove vortices from the sample in the presence of an *ac* drive, or to broadly manipulate the vortex motion and engineer fluxonic devices. For possible spintronic devices based on skyrmions one therefore also wonders to which extent the analogy to above systems can be applied.

For example, for a row of triangular holes in the superconducting film and an

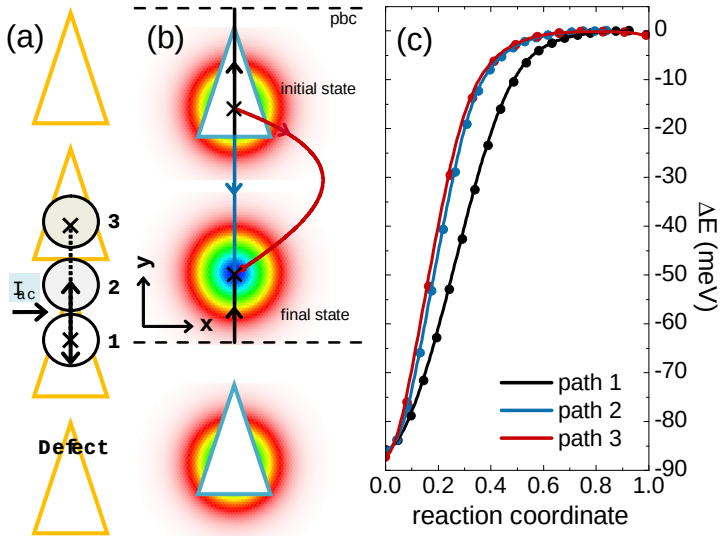

Figure 4.11 – Skyrmion motion along a linear row of planar triangular defects induced by changes in DMI. (a) Schematic illustration of the considered defect geometry. (b) Spatially resolved paths for escape of the skyrmion from the defect: along the upper apex (in black), across the base (in blue), and over the side edge (in red). (c) Energy differences of the three paths in (b) with respect to the initial (pinned) state.

applied *ac* current as shown in Fig. 4.11(a), the vortex will oscillate perpendicular to the direction of the current, but will experience an asymmetric depinning force in up/down directions due to the triangular shape of the pinning site. This results in a net vertical movement of the vortex (dotted line) along the nanostructured pinning. A similar process could be devised to control the motion of magnetic skyrmions, as an *ac* current-based method for controlling skyrmion positions and motion for spintronic applications.

To examine this, we calculated the interaction of a skyrmion with the triangular defect created by stronger DMI, $D = 2D_0$, as seen in Fig. 4.11(b). Fig. 4.11(b) shows three possible paths the skyrmion can take in order to escape from such a triangular defect: over its protruded apex, on the lateral side, or over the base of the triangular defect. Minimum energy paths reveal that the path towards the top apex of the triangle is in fact much lower in energy than the remaining two paths [see Fig. 4.11(c)], with the barrier for skyrmion depinning being higher on the side of the triangle, and highest at its base. As a result, for a prepatterned line of triangular defects as shown in Fig. 4.11(a), in the presence of an *ac* drive for skyrmions, or even for sufficiently large thermal fluctuations, a skyrmion will exhibit a net motion in the bottom-to-top direction, due to the asymmetry in the depinning potential seen in Fig. 4.11(c). Our simulations thereby prove the ratchet concept for skyrmions in the presence of asymmetric defects, but more detailed dynamic simulations are needed to optimize the performance of such a ratchet and skyrmion guidance, bearing in mind the peculiarities of the Magnus force and the resulting skyrmion orbits [196]. Due to such differences from other previously considered ratcheting systems, it is of fundamental value to further examine a possible variety of skyrmion ratchet behaviors in nanoengineered heterochiral systems, the use of asymmetric *ac* driving [190], as well as the novel collective effects due to competition of skyrmion-skyrmion interactions (possibly even nonmonotonic [125]) with a given geometry of a preformed pinning lattice.

4.3.3 Skyrmion on the rails

Since we have focused most of our analysis so far on point-localized defects, we next discuss the pinning behavior of skyrmions on extended defects where material properties are changed. We first consider the motion of an isolated skyrmion along a linear defect [191–194] (a narrow strip with a varied material parameter) to be used in e.g. racetrack memories [see Fig. 4.12(a-c)]. Fig. 4.12 reveals that exchange defect supports either center or off-center pinning of skyrmions, while anisotropy defects only pin off-center, as expected from our earlier findings. On the other hand, linear defects induced by varied DMI can only pin skyrmion at its center, which differs from point defects where pinning could occur either at the center or at an off-center locus. These results suggest that for linear defects, variations in DMI will produce more stable pinning, being at the center of the skyrmion core, and with significantly higher energy barrier than for off-center pinning. Fig. 4.13(a) shows that the energy barriers for depinning a skyrmion scale linearly with the width of the linear DMI defect, while the slope of that scaled behavior increases with the DMI strength inside the defect. For the case of MgO capping layer patterned on monolayer Co on Pt substrate, we find that the energy required to depin the skyrmion surpasses that

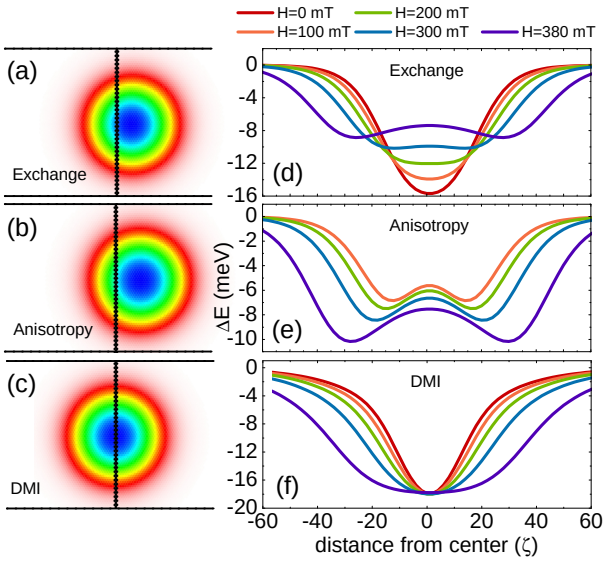

Figure 4.12 – Skyrmion pinning at a linear defect, to be used in racetrack memories. (a-c) Preferential pinning positions on the considered defects (with variations in either exchange, anisotropy, or DMI). (d-f) Energy difference as a function of the position of the skyrmion w.r.t. the defect, obtained by minimum energy path calculations.

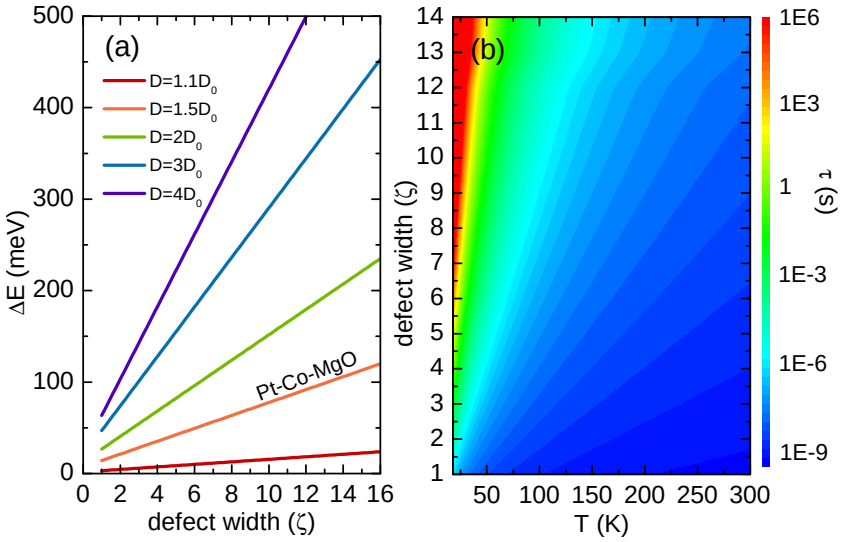

Figure 4.13 – Depinning a skyrmion from a linear defect with stronger DMI. (a) Energy barrier for depinning as a function of defect width and DMI strength there. (b) Skyrmion "lifetime" in the racetrack for various temperatures and widths of the nanoengineered pinning trail, ranging from nanoseconds (blue) to days (red).

needed for the skyrmion to self collapse, which was found to be 37 meV in Ref. [85]. We can also quantify the "lifetime" of the pinned state (that is, the time at which the skyrmion depins from the defect in the presence of fluctuations) using the Arrhenius

law $\tau = \tau_0 \exp(\Delta E/k_B T)$, where τ_0 is related to the attempt frequency $f_0 = 1/\tau_0$, ΔE is the energy barrier, k_B is the Boltzmann constant, and T is the temperature. In these estimates, the attempt frequencies are taken to be $f_0 = 10$ GHz as suggested in Ref. [84]. Fig. 4.13(b) reveals that the pinning lifetimes are in the nanosecond regime for room temperatures, as expected for monolayer skyrmions, but can be in the order of seconds at lower temperatures. While the pinned state for thin defects ($\leq 5\zeta$) can only survive milliseconds and at very low temperatures, seconds long lifetimes can be achieved at temperatures above 100 K when increasing the defect width (beyond 15ζ). Aside the parameter-dependent quantitative analysis, our findings clearly show that thermal stability of isolated skyrmions in racetrack memories can be significantly improved by pinning the skyrmion on linear defects, which can be also combined with recent proposal of advanced heterochiral racetracks with greatly increased barrier for detrimental skyrmion exit from the track [88,180], to reach the optimal conditions for skyrmion stability in applied systems with finite geometries [87]. Lastly, we note that very similar considerations can be applied to the linear defects (besides DMI ones) where off-center pinning of skyrmions is favorable - but then using two parallel linear defects that optimally pin the skyrmion on both sides off the center of its core, as a true “skyrmion on the rails”.

5 FROM SKYRMION LATTICES TO SPIN CYCLOIDS

So far, we have studied skyrmion stability in ferromagnetic cobalt or iron based structures. However, other spin configurations can compete with skyrmions when considering novel magnetic materials and substrates, and a proper understanding of how magnetic skyrmions transit to alternative non-trivial spin structures becomes crucial. In this Chapter[1] we revisit their stability by exploring such transitions in a Fe monolayer capped by Pd, on an Ir(111) surface, and reveal a previously unseen mechanism for collapse of skyrmions into cycloidal spin backgrounds. The transition is characterized by elongation of each skyrmion texture, followed by topological interconnection of domain walls and subsequent merger and dilation of 2D skyrmionic domains into a 1D spin cycloid. Our results reveal a non-trivial dependence of skyrmion stability on material parameters. We close off the study by reflections on the thermal stability of the skyrmion against two competing transition mechanisms, namely the collapse to either ferromagnetic or spin-cycloid order.

5.1 Introduction

Several groups have recently reported detailed descriptions regarding transitions from isolated metastable skyrmions into ferromagnetic ground states. Refs. [84, 85] were among the first in literature to analyze collapse mechanisms for isolated skyrmions in cobalt monolayers, which was later extended to racetrack memories [87] and room temperature skyrmions in few-monolayer heterostructures [88, 89]. Other works have focused on understanding transitions from other non-trivial spin configurations, such as spin cycloids [197,198], anti-ferromagnetic skyrmions [97], anti-skyrmions [95], and magnetic bobbers [92], into ferromagnetic ground states. Although isolated skyrmions remain the most promising candidates as potential information carriers in spintronics, little work has been done to analyze their possible transition to other non-collinear spin configurations. This can be partly attributed to the clear dominance of cobalt-based structures in literature, where the ground state is always ferromagnetic due to strong exchange interactions. However, other spin structures (for example, spin cycloids) can appear as metastable states, or even as ground-state configurations when considering other magnetic materials and substrates, such as Pd/Fe bilayers on the Ir surface [177]. Therefore, a proper understanding of how magnetic skyrmions transition to alternative spin configurations is necessary for the development and performance of spintronic devices.

To achieve this, we revisit the stability of magnetic skyrmions by considering the minimum energy paths for transitions between spin cycloids (SCy) and skyrmion lattices (SkX). We focus on a monolayer film of Pd and Fe on an Ir(111) substrate, where a spin cycloid ground state occurs and a skyrmion lattice dominates only under an applied magnetic field on the order of 1 T [48, 177]. We model the magnetic material

[1] The results of this Chapter are published in Ref. [94].

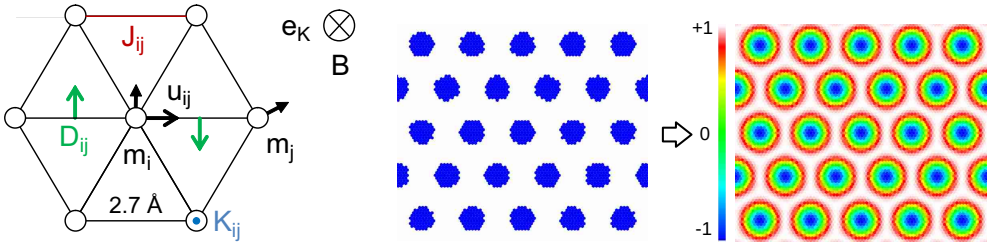

Figure 5.1 – Left: Illustration of a magnetic monolayer of classical spins (circles) on a hexagonal lattice within the Heisenberg model. The magnetic moments of sites i and j are indicated by black arrows. The in-plane projection of the DM vector $\boldsymbol{D}$ which couples spins on adjacent sites is given by green arrows. The exchange interaction J for pairs of nearest neighbors is given in red, and the uniaxial anisotropy is depicted by the point in blue. The direction of the magnetic field $\boldsymbol{B}$ and anisotropy orientation $\hat{\boldsymbol{e}}_K$ are also shown. Right: Top view of the magnetization m_z for an initial guess of a skyrmion lattice and the converged ground state after relaxing with steepest descent.

as a single monolayer of classical spins on a hexagonal lattice with fcc stacking and a lattice constant of $\zeta = 2.7$Å [47], as sketched in Fig. 5.1. The system can be characterized by Eq. (2.4) with material parameters retrieved from Ref. [104] and corresponding to results obtained from experiments [45, 48]. The considered sample is delimited by periodic boundary conditions, where the size of the unit cell (8 nm $\times$ 7 nm) is chosen such that the total energy per spin is not affected by the artificiality of the imposed periodicity, as opposed to simulating the entire sample. The exchange stiffness ($J = 7$ meV per bond), DM interaction ($D = 2.24$ meV per bond), and effective anisotropy ($K = 0.49$ meV per atom) are retrieved from Ref. [104] and correspond to results obtained from experiments [45,48]. Since the ground state of the system comprises either spin cycloids or skyrmion lattices, to find them the system is numerically relaxed with a steepest descent method after initializing a set of spins (in the shape of a rectangular strip for spin cycloids or a circle for skyrmion lattices) to point in the opposite direction of magnetization [65]. This hard domain ensures convergence to a ground state if the corresponding solution exists, as shown in Fig. 5.1. An external magnetic field $\boldsymbol{B}$ is applied in the perpendicular direction (parallel to the surface normal) and used to control the width of the cycloid or the skyrmion diameter.

We also consider the case of Fe bilayers epitaxially sandwiched between Ir and Rh/Pd layers with material parameters retrieved from DFT calculations [167]. The effective interlayer coupling, $J_\perp = 24.48$ meV, is very strong and favors FM alignment of magnetic moments between the two Fe layers. On the other hand, the effective exchange coupling within each Fe layer, $J_\parallel = 1.46$ meV, is much smaller and facilitates the formation of non-collinear states. The DMI arises with a contribution of 1.5 meV for Fe@Ir, -0.3 for Fe@Pd, and 0.1 meV between the two Fe layers. The uniaxial anisotropy is assumed 0.6 meV per Fe atom with an out-of-plane magnetization.

5.2 Analyzing the transitions

5.2.1 Path of minimum energy

Deciphering the mechanism by which a spin cycloid transitions into a skyrmion lattice implies a search for the easiest path that links the two states, which can be accomplished by minimum energy path calculations. Fig. 5.2 plots the total energy difference along the MEP between the skyrmion lattice and the spin cycloid configurations. The energy landscape is characterized by a local maximum (or energy barrier) between the SkX and SCy states that must be overcome in order to transition from one state to another. The activation energy for the collapse of the skyrmion is calculated to be 50 meV, but the activation energy for formation of skyrmion lattice from the spin cycloid state is 85 meV. This follows from the fact that the spin cycloid forms a ground state while the skyrmion lattice is an excited state in absence of an external magnetic field, which implies the latter is energetically closer to the saddle point in the energy landscape connecting the two states. Spin configurations in Fig. 5.2 reveal that the path involves local interconnection and subsequent merging of skyrmion textures before forming a spin cycloid. The interconnection occurs at the saddle point, after the initial elongation of the circular skyrmion texture followed by the formation of a topological knot and recombination of domain walls. Finally the formed spin cycloid dilates at interconnection points into a uniform domain. Obviously, the number of topological knots during the transition is one more than the number of skyrmions along the lattice dimension.

Fig. 5.3 plots the distribution of individual components of the magnetization as a skyrmion collapses into the spin cycloid ground state. The plots of m_x reveal that merger of skyrmions and dilation of a cycloid are associated with approach and fading of two oppositely polarized regions of spins, pointing in the $+x$ and $-x$ directions. In distribution of m_y one sees the spins are polarized along the domain wall of the elongated skyrmion texture in the $+y$ and $-y$ directions on the top and bottom domain wall respectively, which is also preserved during merger beyond the saddle point. m_z shows the transition most clearly: first lateral elongation of the skyrmion texture, followed by interconnection and recombination of the domain walls, and final dilation of the domain at expense of the cusp-like protrusions of opposite magnetization (see also Fig. 5.2), before the 1D spin-cycloid is fully formed. In other words, the non-collinear structure changes from having a row of singly connected, enclosed domain walls around skyrmions before the saddle point, to a single domain with two parallel domains walls after the saddle point.

Mapping the energy landscape of the transition provides a useful characterization of the minimum energy path. Fig. 5.4 plots spatial variations in the energy contributions per spin as a skyrmion texture collapses into the spin-cycloid ground state. Looking at the profile of normal component of magnetization, m_z, along the line connection the centers of neighboring skyrmions before the transition [Fig. 5.4(a)], we observe that the spin distribution changes from a uniformly magnetized state into a progressive rotation of the spins from $+\hat{\boldsymbol{n}}$ to $-\hat{\boldsymbol{n}}$ away from the center. Moreover, the spins actually exhibit two modes of slightly slanted spin orientations with respect to the surface normal, $\hat{\boldsymbol{n}}$, in the late stages of the transition. These modes decrease in height and move farther apart, with a shallower well between them, until they merge

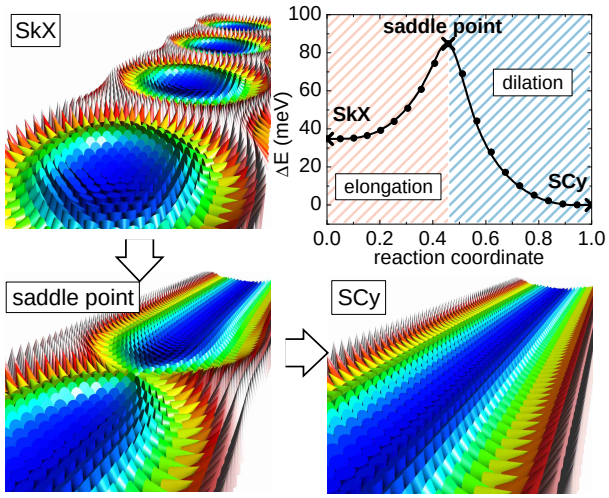

Figure 5.2 – Minimum energy path from skyrmion lattice (SkX) to spin cycloid (SCy) at zero external magnetic field. The energy of the system along the path is shown with respect to the spin cycloid ground state, where the skyrmion lattice represents an excited state. The striped regions represent the elongation (in red) and merger (in blue) of domains that characterize the transition. The reaction coordinate is defined as the normalized (geodesic) displacement along the formation path. The spatial configuration of spin magnetization is shown for the initial skyrmion lattice state, saddle point configuration (the topological knot), and the final spin-cycloid state. The color code represents the perpendicular spin component from blue (downward) to red and white (upward), via green (in plane).

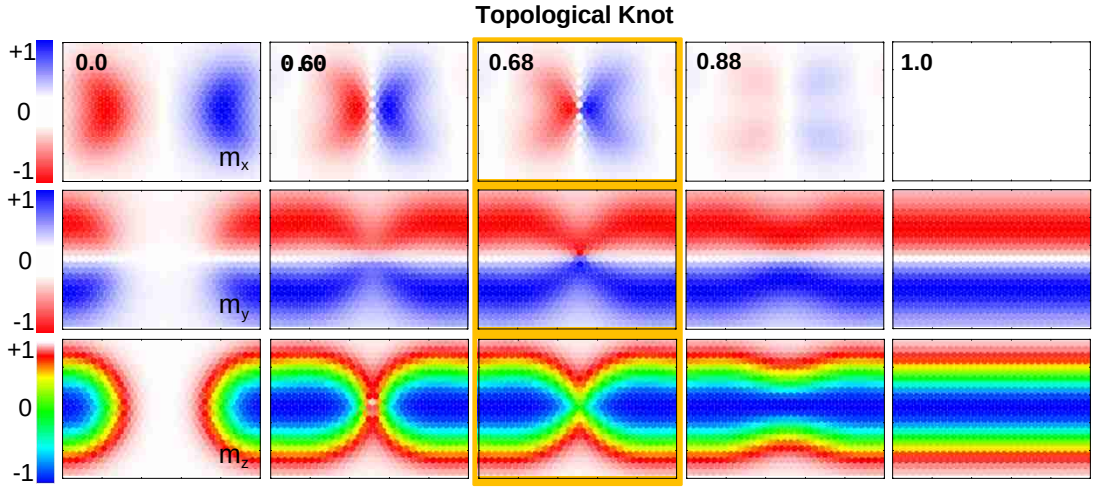

Figure 5.3 – Bird view of spatial distributions of x, y, and z components of magnetization $\boldsymbol{m}$, for several transitional images as the skyrmion lattice collapses into a spin cycloid in absence of an external magnetic field. The images are denoted by the reaction coordinate along the minimum energy path (cf. Fig. 5.2).

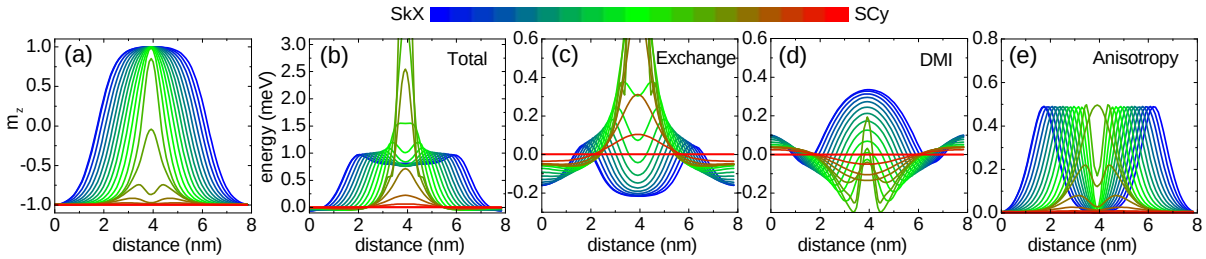

Figure 5.4 – Evolution of the line profile for (a) perpendicular spin component, and (b-e) energy contributions, along the SkX to SCy transition path at zero external magnetic field. ΔE is calculated with respect to the spin-cycloid ground state. The profile is composed of successive spins along x-direction, starting from the left edge of the simulation region, and centered in y-direction. The color code represents different images along the path from blue (SkX) to red (SCy) over green (saddle point) (see given color bar).

into a uniform distribution of spin orientations along z. The energy profiles also reveal some interesting properties of the transition. Fig. 5.4(b) shows the total energy represents a minimum in the initial configuration (SkX), since the skyrmion core is located at the periodic boundary, and approaches a discontinuity at the saddle point along the center of x. The finite discontinuity in total energy stems from the exchange contribution [see Fig. 5.4(c)], which suggests the saddle point can be described by a sharp reversal of magnetic moments such as those occurring in a Bloch point. The exchange energy landscape is characterized by two minima which correspond to the skyrmion core at the periodic boundary and the uniform ferromagnetic background at the center. Fig. 5.4(d) plots the distribution of DM energies and reveals a parabolic shape in the early stages of the transition. As skyrmionic domains approach during the transition, the parabola narrows between two approaching minima. At the saddle point the parabola becomes a sharp maximum, which further flattens into the uniform distribution as spin cycloid is formed. Fig. 5.4(e) shows that two maxima emerge for the anisotropic energy, centered at the domain walls, which move closer as transition progresses along the considered path.

5.2.2 Topological knot

Next we study the saddle point associated with the activation barrier that separates the skyrmion lattice and spin cycloid states. The corresponding magnetic configuration is shown in Fig. 5.5. There, two skyrmion cores meet (in blue), and their domain walls (in green) interconnect, to subsequently recombine and form two parallel domain walls with uniform yet opposite m_y spins. The main hurdle to untie this topological knot at the interconnection of two skyrmions is the a rotation of two central spins, denoted $\hat{\boldsymbol{m}}_1$ and $\hat{\boldsymbol{m}}_2$ in Fig. 5.5, that lie in the xy-plane and point towards each other. These magnetic moments are slightly slanted in the $-y$ direction because of the strong energy contribution coming from the exchange interactions favoring parallel alignment. The bond between them forms the base of adjacent lattice triangles (shaded in inset of Fig. 5.5), where the upper and lower spins, $\hat{\boldsymbol{m}}_3$ and $\hat{\boldsymbol{m}}_4$, are ori-

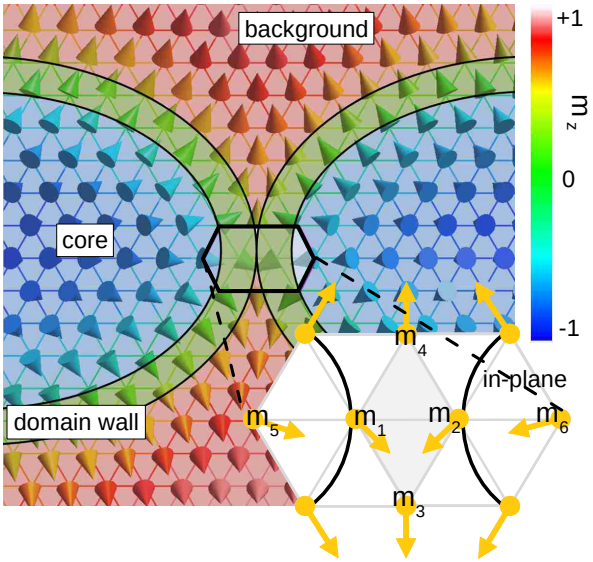

Figure 5.5 – Top view of magnetization distribution, m_z, of the saddle point (topological knot) as the skyrmion transitions into a spin cycloid. The color shaded regions represent the skyrmion core (in blue), domain walls (in green), and the uniform background (in red). The inset shows a magnified view of the spins in the vicinity of the Bloch point. Black lines denote domain walls where the orientation of spins is in-plane.

ented in the $+y$ and $-y$ directions, albeit with positive z orientations. Neighboring spins that are inside the skyrmion cores, $\hat{\boldsymbol{m}}_5$ and $\hat{\boldsymbol{m}}_6$, point along the same direction in the xy-plane as $\hat{\boldsymbol{m}}_1$ and $\hat{\boldsymbol{m}}_2$ respectively, but contain $-z$ component.

The broken vertical symmetry of the central magnetic moments suggests there might be other possible spin orientations at the saddle point. Conceivably, $\hat{\boldsymbol{m}}_1$ and $\hat{\boldsymbol{m}}_2$ can point either down and towards each other ($\searrow\swarrow$) or up and inwards ($\nearrow\nwarrow$), without any changes to the activation energy. The frustration arising from competing energy contributions suggests there are in fact two distinct realizations of magnetic moments. In both scenarios, the two spins $\hat{\boldsymbol{m}}_1$ and $\hat{\boldsymbol{m}}_2$ make an angle of 30 degrees with respect to the bond between them. An interesting question is how do these magnetic moments twist along the minimum energy path. Fig. 5.6 plots the evolution of spin orientations neighboring the Bloch-like point at the knot. We find that $\hat{\boldsymbol{m}}_1$ and $\hat{\boldsymbol{m}}_2$ progressively rotate away from the x-axis during the transition, while $\hat{\boldsymbol{m}}_5$ and $\hat{\boldsymbol{m}}_6$ experience a similar rotation along the azimuthal angle φ but at larger rate. $\hat{\boldsymbol{m}}_3$ and $\hat{\boldsymbol{m}}_4$ remain unchanged pointing along the $+y$ and $-y$ directions, respectively. However, rotations along the xy plane are quickly surpassed by motion in the polar direction, θ. $\hat{\boldsymbol{m}}_1$ and $\hat{\boldsymbol{m}}_2$ can then be interpreted as twisting from $-z$ to $+z$ with rotations along xy. $\hat{\boldsymbol{m}}_5$ and $\hat{\boldsymbol{m}}_6$ display a similar but less noticeable twisting behavior; they remain close to the x axis for most of the transition. $\hat{\boldsymbol{m}}_3$ and $\hat{\boldsymbol{m}}_4$ are aligned with the y axis and rotate only out of xy plane.

Let us also discuss the changes in the topological charge around the knot, to provide more quantitative description of the topological transition taking place at the saddle point of the transition from the skyrmion lattice to the spin cycloid. The observed unwinding of the topological knot of the magnetic texture during the transition

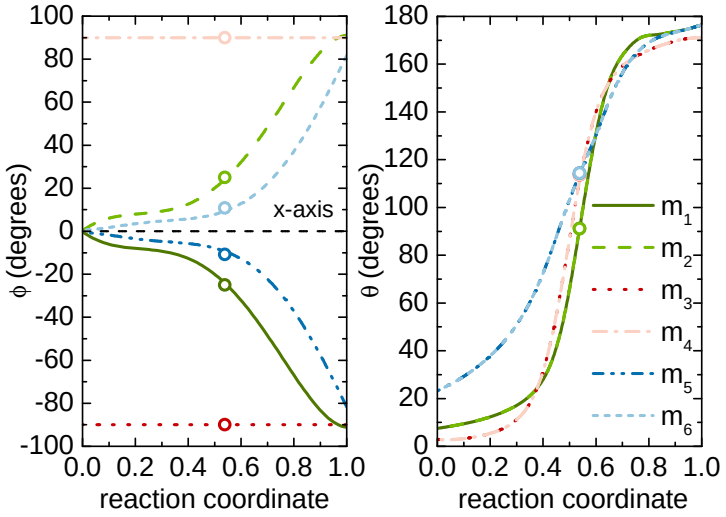

Figure 5.6 – Evolution of spin orientations in the xy-plane with respect to the x-axis, where the azimuthal angle is defined as $\varphi = \arctan(\hat{\boldsymbol{m}}_y/\hat{\boldsymbol{m}}_x)$, and with respect to the angle out of that plane, where the polar angle is defined as $\theta = \arccos(\hat{\boldsymbol{m}}_z)$. Open dots correspond to spin orientations at the saddle point.

should be accompanied by a distinct change in the topological charge, as shown in Fig. 5.7. This transition is continuous and involves a change from a positive topological number, where a skyrmion lattice exists, to a value of zero due to lack of topological wrapping in the spin cycloid. Spatial variations in the topological charge density (see Fig. 5.7) reveal a merger of the positive charge contributions Q_+, while negative charge contributions Q_- emerge in the upper and lower regions of where the skyrmions interconnect. The topological knot is characterized by protrusions of the negative charge into the region of positive charge until the latter is again separated into two distinct regions. The dilation of the spin cycloid proceeds with an enlargement of the region with negative charge, until the average charge becomes zero, after which the local charge gradually diminishes to zero in the entire structure.

Finally, we briefly consider the topological unwrapping of skyrmions into a spin cycloid in the case of a double atomic layer, with thus additional degree of freedom in the z direction. This is motivated by the fact that spin cycloids with periods in nanometer range were found particularly stable in Fe double layers, when grown or Ir(111) as experimentally studied in Ref. [199], or when epitaxially sandwiched between Ir and Rh/Pd layers as in Ref. [167], where material parameters were retrieved from DFT calculations. In the latter case the exchange interaction in adjacent Fe layers can be tuned by alloying Rh with Pd and therefore changing the 4d band filling (for Fe@Pd layer), while a strong DMI can be induced from the 5d TM Ir (for Fe@Ir layer). For the Rh/Pd/2Fe/2Ir multilayer, the effective interlayer coupling, $J_\perp = 24.48$ meV, is very strong and favors FM alignment of magnetic moments between the two Fe monolayers. On the other hand, the effective exchange coupling within each Fe monolayer, $J_\parallel = 1.46$ meV, is much smaller and facilitates the formation of non-collinear states. The DMI arises with a contribution of 1.5 meV for Fe@Ir, -0.3 for Fe@Pd, and 0.1 meV between the two Fe layers. The uniaxial anisotropy is assumed 0.6 meV per Fe atom

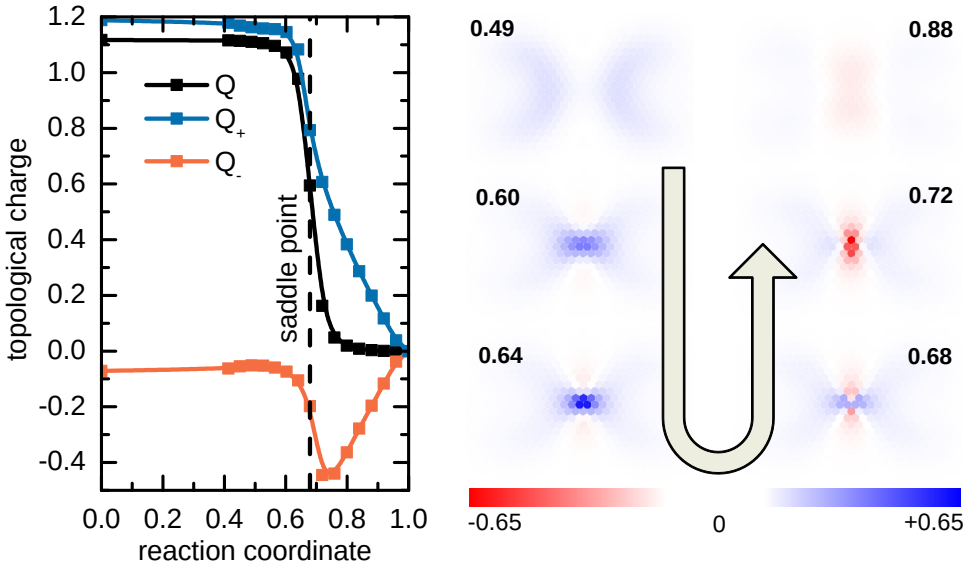

Figure 5.7 – Evolution of the topological charge Q and its positive and negative contributions, Q_+ and Q_-, as the skyrmion transitions into a spin cycloid in absence of an external magnetic field (the minimum energy path shown in Fig. 5.2). In the right panel, the spatial variation of the topological charge density $q(x, y)$ is shown for several transitional images, denoted by the reaction coordinate along the minimum energy path.

with an out-of-plane magnetization. These conditions are sufficient to create a spin spiral ground state [167] with a period of 2.25 nm at zero field.

We analyzed the collapse of skyrmions into spin cycloids in Fe double layers with parameters as above. The activation energy for collapse or nucleation of the skyrmion lattice to or from the spin cycloid state are calculated to be 33 meV or 42 meV, respectively. These barriers are lower than those found for the previously considered Pd/monoFe/Ir system because of weaker exchange interactions in the double layer system of Ref. [167]. Our simulations reveal that the minimal energy path involves a similar transition as in the Fe monolayer: elongation of the skyrmion core and dilation of the subsequently merged domain into a full spin cycloid. Moreover, we find that strong interlayer exchange interactions ensure the magnetic texture remains mostly the same in the two Fe monolayers.

The topological knot that separates the skyrmion lattice and spin cycloid states in Fe double layers is illustrated in Fig. 5.8. The main difference with respect to Pd/monoFe/Ir system discussed previously is in the central spins, where now degeneracy for the spin orientation of the nearest spins to the knot is lifted: $\hat{\boldsymbol{m}}_1^{\text{Fe@ir}}$ and $\hat{\boldsymbol{m}}_2^{\text{Fe@Ir}}$ point down and towards each other ($\searrow\swarrow$), while $\hat{\boldsymbol{m}}_1^{\text{Fe@Pd}}$ and $\hat{\boldsymbol{m}}_2^{\text{Fe@Pd}}$ point up and inwards ($\nearrow\nwarrow$). We also find that along the MEP, evolution of spins in the central line onnecting the skyrmions is mirror-symmetric in two Fe monolayers, throughout the entire transition. This very correlated behavior is caused by dominant interactions from the interlayer exchange coupling, $J_\perp$, compared to exchange interactions within an Fe layer, $J_\parallel$. As a result, near-ideal mirror-symmetric evolution of the topological knot between Fe layers is more energetically favorable since spins are aligned with those of the neighboring layer. For example, one finds from Fig. 5.8 that $\hat{\boldsymbol{m}}_1^{\text{Fe@Pd}}$ ex-

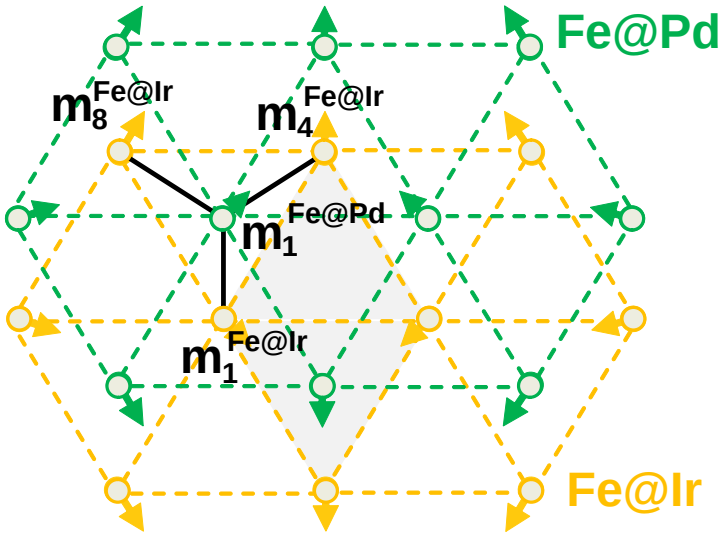

Figure 5.8 – Spins in the vicinity of the topological knot for the Fe@Ir and Fe@Pd layers in Rh/Pd/2Fe/2Ir system. Dashed lines indicate interactions within an Fe layer and solid lines represent interactions between Fe layers.

hibits partial alignment with $\hat{\boldsymbol{m}}_4^{\text{Fe@Ir}}$ and $\hat{\boldsymbol{m}}_8^{\text{Fe@Ir}}$, but would have been partially aligned only with $\hat{\boldsymbol{m}}_1^{\text{Fe@Ir}}$ if central spins in both Fe layers assumed $\searrow\swarrow$ or $\nearrow\nwarrow$ configurations.

5.3 Influencing the stability

Skyrmion lattices were shown to transition to spin cycloids through an activation barrier, and thus escape their topological protection. It is therefore of interest to study the influence of model parameters on skyrmion stability. In this section we consider three distinct parameters which can be exploited to induce particular stability of magnetic skyrmions. Needed variations can be achieved by either external influence or spatial engineering of relevant parameters.

5.3.1 Dependence on magnetic field

The external magnetic field plays an important role in Pd/Fe/Ir systems, mainly in manipulating transitions between spin cycloid, skyrmion lattice, and ferromagnetic phases. One can then expect variations in the activation energy for transitions between different states should also arise due to changes in the magnetic field. Fig. 5.9 plots the minimum energy paths as a function of external magnetic field, $\boldsymbol{B}$. At zero magnetic field, a spin cycloid state with a period of about 3 nm is energetically favorable as expected from literature [48,177]. A phase transition to a skyrmion lattice (marked by endpoints below the dashed line), which gains energy with respect to the spin cycloid state due to the Zeeman energy, occurs at a magnetic field of about 1.4 T. Thus, the critical fields in this system are on the order of experimental values [48], but smaller than those reported in Ref. [177]. Fig. 5.9 further reveals a dependence of the activation energy on the magnetic field. Nucleation of a skyrmion lattice is energetically less

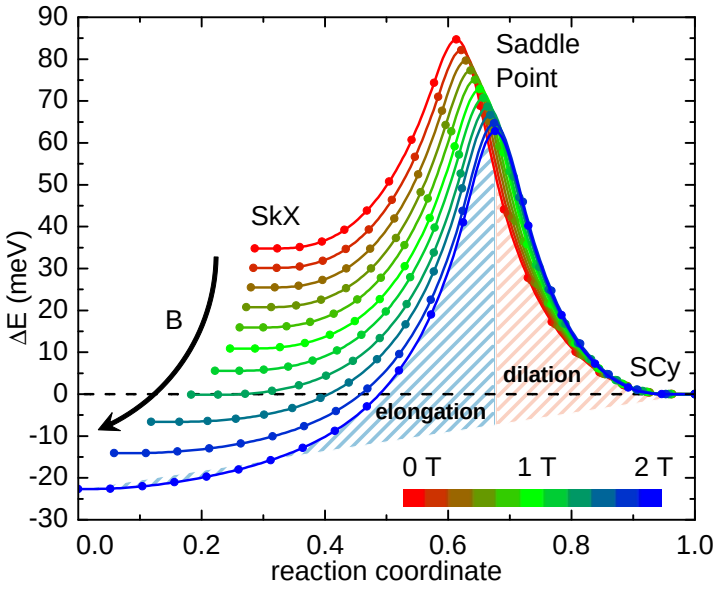

Figure 5.9 – Minimum energy paths from skyrmion lattices to spin cycloids for several external magnetic fields, $\boldsymbol{B}$. For each field, the energy difference (ΔE) with respect to the spin cycloid state is plotted. The stripped shaded regions represent the elongation and dilation processes that characterize the transition before and after the saddle point, respectively.

favorable at zero magnetic field, and increases in likelihood for stronger fields (from 63 meV at 0 T to 85 meV at 2 T). The inverse is true for collapse of a skyrmion, where the transition is more likely to occur at lower magnetic fields (from 88 meV at 2 T to 50 meV at 0 T). These contrasting relations can be explained by the magnetic phases, where one spin configuration has a lower-energy state than the other, which in turn induces a higher activation barrier.

We can analyze more closely the activation energies leading to the nucleation or annihilation of skyrmions with respect to the spin cycloid phase. Fig. 5.10 depicts the magnetic field dependence of the activation energy from either side of the transition. At low magnetic fields, the spin cycloid order has higher energy barrier than the skyrmion lattice, with ΔE almost twice in magnitude. In a sufficiently large field, however, the skyrmion lattice is more stable. We also find that the barrier for collapse of skyrmion lattices can be double that of spin cycloids for $B > 3$ T. While the activation barrier for spin cycloid states decreases linearly with the field, $\Delta E \propto -0.01B$, in skyrmion lattices the activation energy is characterized by two linear regimes: $\Delta E \propto 0.01B$ for $B < B_c$ and $\Delta E \propto 0.04B$ when $B > B_c$, where B_c is the critical field. The latter is more sensitive to field variations, which is likely related to regime changes in the minimum energy path that we observed earlier (namely, from elongation of the skyrmion core to dilation of the subsequently formed domain along the y direction; see Fig. 5.9). At the critical field B_c, a phase transition occurs from SCy to SkX ground states. The field-dependent energy landscape can be sketched as in Fig. 5.10. For $B < B_c$, the spin cycloid state is energetically more stable; for $B > B_c$, it is the skyrmion lattice state; and for $B = B_c$, the two states are energetically degenerate and their energy barriers can be overcome with equal probability. Therefore, the stability

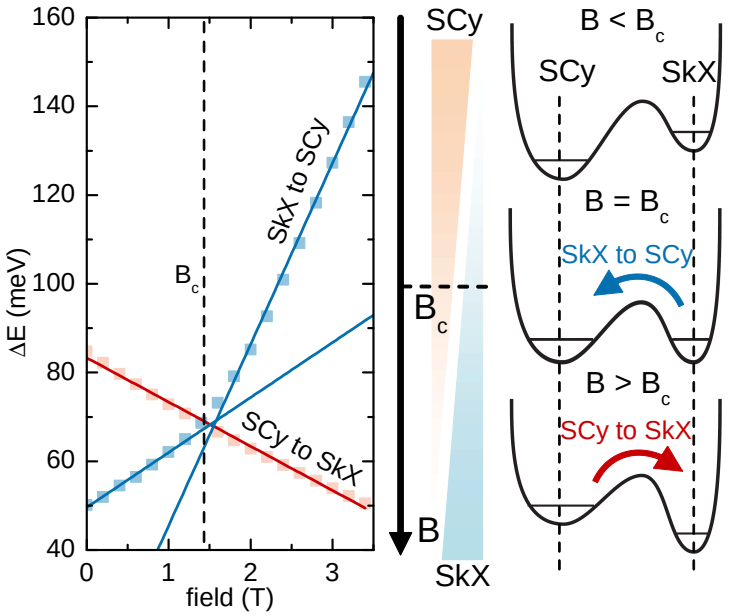

Figure 5.10 – Energy barriers for skyrmion lattice nucleation (in red) and annihilation (in blue) with respect to the spin cycloid state. An artistic illustration of the field-dependent energy landscape when transitioning between skyrmion lattices and spin cycloids is shown on the right.

of either spin cycloids or skyrmion lattices can be controlled through an externally applied magnetic field.

To clarify the asymmetric behavior of the activation barriers, particular attention has to be paid to the origin (energetically speaking) of the excitations leading to the transition between the two states. Fig. 5.11 plots energy contributions along the calculated minimum energy paths at three values of external magnetic field. In all cases the exchange energy dictates the profile of the total energy since it represents the dominating term in the Hamiltonian. Below the critical field, the anisotropy and Zeeman contributions are negligible, while the DM energy has a noticeable depression. At the critical field, the DM energy forms a very shallow potential well and the spin cycloid stability is decreased by a drop in exchange energy. The Zeeman energy already presents a significant contribution towards the end of the path, resulting in two energetically degenerate states. Above the critical field, the magnetic field induces a high contribution from the Zeeman energy, which moves the skyrmion lattice to the ground state and thus improves its stability. This implies that variations in the Zeeman term can explain the non-trivial dependence of stability of non-collinear states (spin cycloids or skyrmions) on the magnetic field.

5.3.2 Dependence on material parameters

The discussion is continued by considering variations in the magnetic material due to changes in DM interactions and magnetic anisotropy. Physically, local changes in the DM strength can be realized by increasing the interfacial spin-orbit coupling with two different materials below and above the film [49,50], and using lithographic techniques to change or remove the heavy-metal layer on top (see Refs. [88,180] for the-

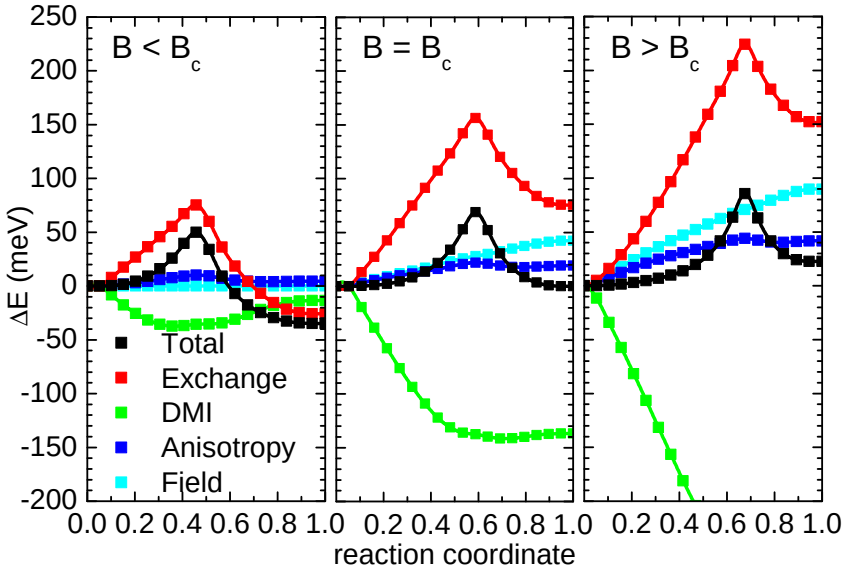

Figure 5.11 – Components of the energy along the considered minimum energy paths for different external magnetic field. Field values correspond to 0 T for $B < B_c$, 1.4 T for $B = B_c$, and 2 T for $B > B_c$.

ory, and references therein for experimental realization). The strength of the magnetic anisotropy can be varied by distortions in the underlying atomic lattice and from impurity sites [69,71]. Fig. 5.12 shows the effect of both the magnetic field and the respective material parameter (DM strength, D_{ij}, or anisotropy constant, K_i) on skyrmion stability (that is, the activation barrier for transitioning from SkX to SC states). Both plots reveal a parabolic dependence of the activation energy with respect to material parameters. Increasing the anisotropy improves skyrmion stability because the anisotropic contribution will move the skyrmion lattice to a lower-energy state and thus result in a higher energy barrier (cf. results in Fig. 5.11). The effect the anisotropy has on activation energies is highest at low magnetic fields ($B = 0$ T)

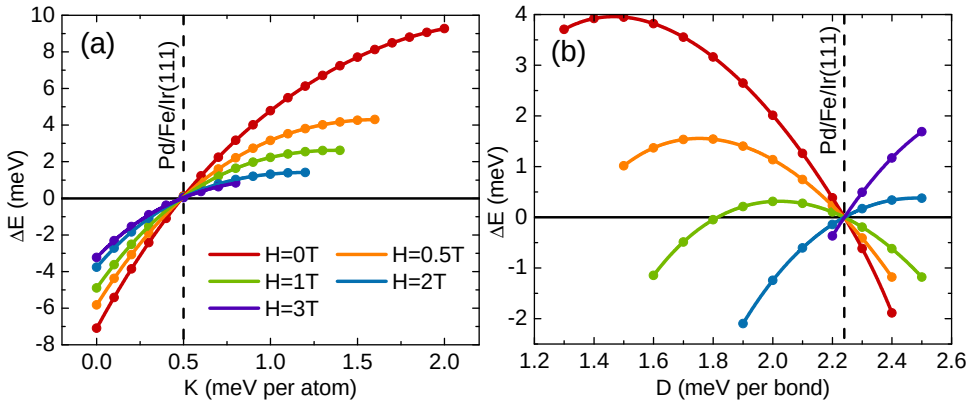

Figure 5.12 – Activation barriers for skyrmion collapse to spin cycloid as a function of (a) anisotropy constant and (b) DM strength for different external magnetic fields.

and decreases for larger fields. For changes in DM interactions, the activation barriers have an inverse relation with the DM strength at low magnetic fields ($B < B_c$). As B approaches the critical field B_c, the curves exhibit a more parabolic behavior, with a clear maximum in ΔE. For larger fields ($B > B_c$), the effect the DM strength has on activations is similar to the anisotropy case. Again, variations in ΔE become smaller for larger external fields. We can then conclude that changes in anisotropy and DM strength can have significant (but opposite) influences on skyrmion stability at low magnetic fields.

5.3.3 Effective energy landscape

Skyrmions can be nucleated or annihilated by overcoming the energy barrier separating the skyrmion configuration from other available states. Therefore, their stability will depend a lot on the spin configuration chosen for magnetic skyrmions to transition into. The relevant literature has mostly focused on skyrmion stability in ferromagnetic backgrounds with cobalt-based structures [84, 85, 87, 88]. In Pd/Fe/Ir(111), however, the ground state is spin cycloid or a skyrmion lattice, and becomes ferromagnetic only for sufficiently high magnetic fields [48, 177]. Apart from transitions with spin cycloids considered in this paper so far, skyrmion lattices can also collapse into a uniform ferromagnetic state. We therefore consider skyrmion stability with respect to both possible alternative configurations.

Fig. 5.13 depicts the energy surface (or the activation energy for skyrmion annihilation) in the parameter space of varying DM and anisotropy constants, at zero external magnetic field. Fig. 5.13(a) shows the energy barrier landscape when transitioning from skyrmion lattice to ferromagnetic ordering. We observe stronger skyrmion stability with increasing DM strength and decreasing anisotropy, as expected from previous works [88]. In Fig. 5.13(b), the activation energies for skyrmion collapse to spin cycloid are shown, where they appear to have an inverse relation with the DM strength and anisotropy compared to the previous case (see also Fig. 5.12). This reflection, along the diagonal, of energy landscapes for the two considered transitions can be interpreted as follows. In SkX to FM transitions, DM interactions favor canting of spins in skyrmions rather than parallel alignment in ferromagnetic ordering, which moves skyrmions to lower-energy states and as a result enhances the energy barriers. In SkX to SCy transitions, however, the same interactions will favor spin cycloid orders more than skyrmions, pushing the latter to higher-energy states, which results in lower barriers. A similar explanation can be made in terms of the anisotropy, where the anisotropic energy favors alignment of spins with the surface normal, $\hat{\boldsymbol{n}}$.

Fig. 5.13(c) plots the effective energy landscape, i.e. the lowest energy barrier between the two discussed transitions. The dashed line represents the cross-over between regimes where one collapse mechanism is favored over the other. While SkX-to-SCy transitions dominate skyrmion stability in regions above the shown line, SkX-to-FM transitions have lower ΔE in regions below the line. The energy landscape steeply changes around the cross-over: the inner-most band (in red-orange) has energy barriers between 65 meV and 85 meV; the following band (in green-yellow) has activation energies between 30 meV and 65 meV; and the broadest band (in teal-blue) has values below 30 meV. These results show there is a rather narrow range of material parame-

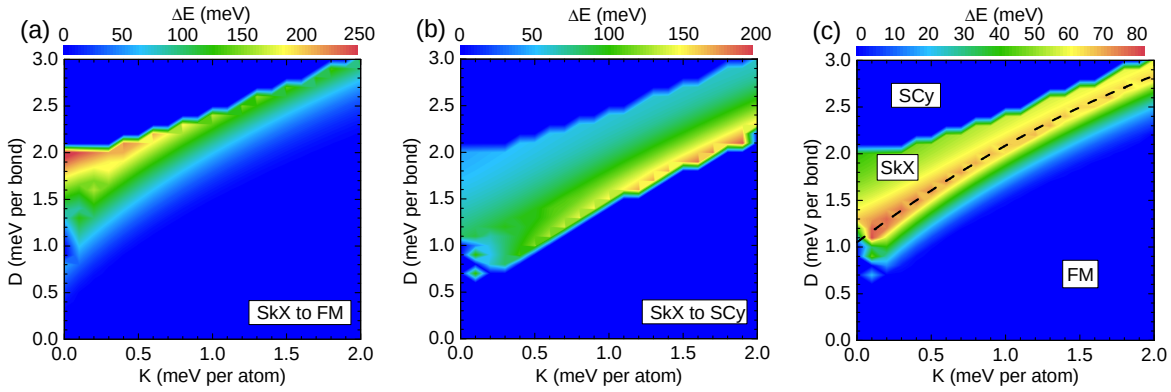

Figure 5.13 – Energy landscape, composed of activation barriers for varied material parameters, for SkX to FM transitions (a) and SkX to SCy transitions (b). (c) The effective energy landscape of only the lowest energy barrier of the two shown in (a)-(b). Dashed line represents the transition where one collapse mechanism dominates the other.

ters which will retain skyrmion stability in Pd/Fe/Ir(111) systems. For values above the critical field, $\boldsymbol{B} > \boldsymbol{B}_c$, there is a reversal of the energy landscape for SkX-to-SCy transitions since the skyrmion lattice becomes the ground state. The inverse behavior on material parameters can also be deduced from Fig. 5.12. Therefore, the effective energy landscape will look more like the SkX-to-FM transition depicted in Fig. 5.13(a), with significantly higher energy barriers that result in improved skyrmion stability.

6 HIGHER ORDER SKYRMIONS

In previous chapters we studied skyrmions with topological numbers of unity. However, in frustrated magnets skyrmions of higher order topologies can be found theoretically, but they remain elusive in experiments. In this Chapter[1] we explore the thermodynamic stability of higher order skyrmions in such systems. We discover the microscopic mechanisms for switching between skyrmions with different topological numbers. Namely, skyrmions transition to higher or lower topologies by absorbing a spin texture with topological number of $+1$ or -1. We also find that frustrated exchange couplings lead to attractive interactions between skyrmions of all types, but they are much weaker when $Q \neq 1$. Because of the attractive interaction, the skyrmions may be arranged into distinct topological clusters that are resistant against diffusion processes at finite temperature.

6.1 Introduction

The discovery of nontrivial topological particles has brought about much innovation in modern matter physics. A great deal of attention is being placed on metastable states characterized by high thermodynamic stability, which are able to persist for long periods of time. Among them, magnetic skyrmions have been of particular interest since they are expected to provide the means for electric control of magnetism.

So far, magnetic skyrmions with topological numbers of unity (see Section 2.1) have been extensively studied both in experiments and theory. Yet skyrmions with any topological number Q are possible as far as topological analysis is concerned. Such nontrivial topological particles are rather desirable as they can bring richer physics, such as a new topological Hall effect in anti-skyrmions [200], and may allow for more involved applications, such as n-ary bit representations of information. The literature indicates that research is heading toward this path, with recent developments in anti-skyrmions [55, 95, 200–202], bi-skyrmions [101, 203], and skyrmions with other topological charges [53, 54, 56–58, 204–206]. Relevant studies include mapping metastable spin textures with a broad range of topological charges [58, 206] and stabilizing skyrmion crystals with a high topological number of two in itinerant magnets [54]. Despite these efforts, the thermodynamic stability and underlying transition mechanisms for skyrmions with topological numbers higher than unity remains elusive, mainly because their increased Q costs additional energy making them harder to observe in experiments.

In order to explore higher order skyrmions, we consider a frustrated magnet composed of the $(Pt_{1-x}Ir_x)Fe$ bilayer on Pd(111) surface. The magnetic moments in the Fe layer are described by Eq. (2.4) using interactions beyond the nearest neighbor approximation (see Section. 2.3.2). In particular, we consider interaction coefficients between Fe spins taken to include up to 11 neighboring shells, or 72 nearest lattice sites, as illustrated in Fig. 2.6. The coupling coefficients J_{ij}, D_{ij} and the on-site anisotropy K_i

[1] The results of this Chapter are published in Ref. [98].

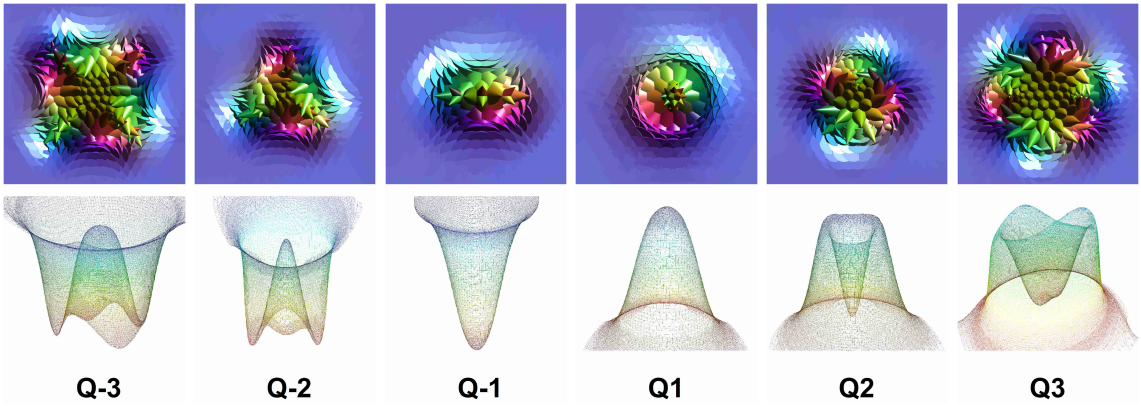

Figure 6.1 – Top: Spin orientations where individual components are mapped to an RGB color model, $(S_x, S_y, S_z) \rightarrow (R, G, B)$. Bottom: Topological charge density, $q = -(4\pi)^{-1}\boldsymbol{m} \cdot (\partial_x \boldsymbol{m} \times \partial_y \boldsymbol{m})dxdy$, plotted along the z axis and color coded from blue (high values) to red (low values).

are retrieved from *ab initio* calculations [58] for Ir concentrations of $x \geq 0.05$. Besides the Dzyaloshinskii-Moriya interaction, the presence of frustration in the isotropic exchange interaction is also responsible for stabilizing a diverse set of nontrivial topological spin textures [52]. The two-dimensional magnetization configuration $\hat{\boldsymbol{m}}(t)$ of a single topological particle is evolved in time according to Eq. (2.20).

6.2 Non-trivial properties

A plethora of nontrivial topological particles can be observed for $Q \neq 1$ [56]. With this in mind, we examine possible spin textures by direct minimization of Eq. (2.4), and ensure they are metastable by numerically solving Eq. (2.20) for sufficiently long times. Given small nonzero variations to the topological charge density, we obtain skyrmions that represent locally stable solutions for topological charges $Q \pm 1, \pm 2, \pm 3$, and they exhibit similar characteristics to those presented in the literature [58, 205]. We also discover a novel skyrmion texture with an unusually high topological number $Q = 3$ [56] that resembles the molecular form of two bound bi-skyrmions (or textures with $|Q| = 2$). Fig. 6.1 reveals that the studied skyrmions embody increasingly complex magnetizations, $\hat{\boldsymbol{m}}$, and charge density distributions, $q(x, y)$, for higher topologies. We can observe that the magnetic textures gain more complex representations for increasing magnitudes of Q. Similarly, the parabolic functions of the topological charge densities acquire multiple minima or maxima, as seen in Fig. 6.1.

Skyrmions with opposite topological charges become energetically degenerate [53, 57] under the application of large enough magnetic fields, which affect higher topologies more in size and energy [46]. Fig. 6.2 shows that higher order skyrmions possess higher energies, as expected, and there are significantly more spins that form the topological objects. Interestingly, there is a qualitative pattern to be followed when moving to higher topologies, namely the insertion of a unit charge to the current texture, which suggests that we can predict the spin orientations of particles with $|Q| > 3$ [56].

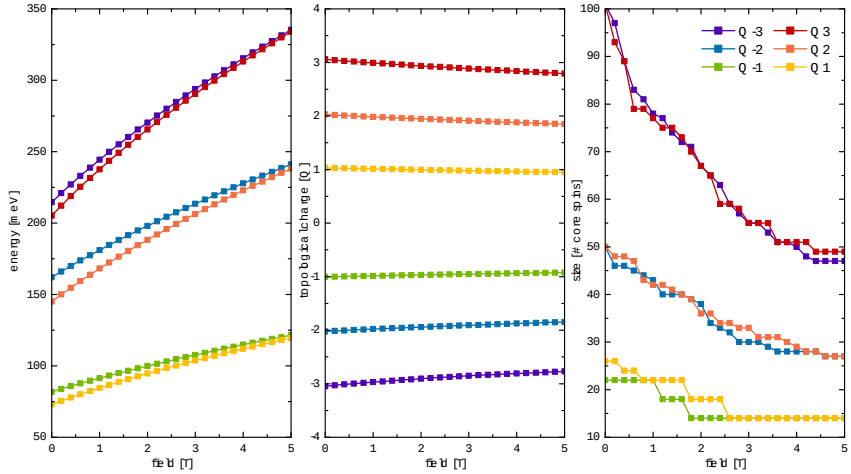

Figure 6.2 – Energy, topological charge, and size of considered topological objects as a function of external magnetic field.

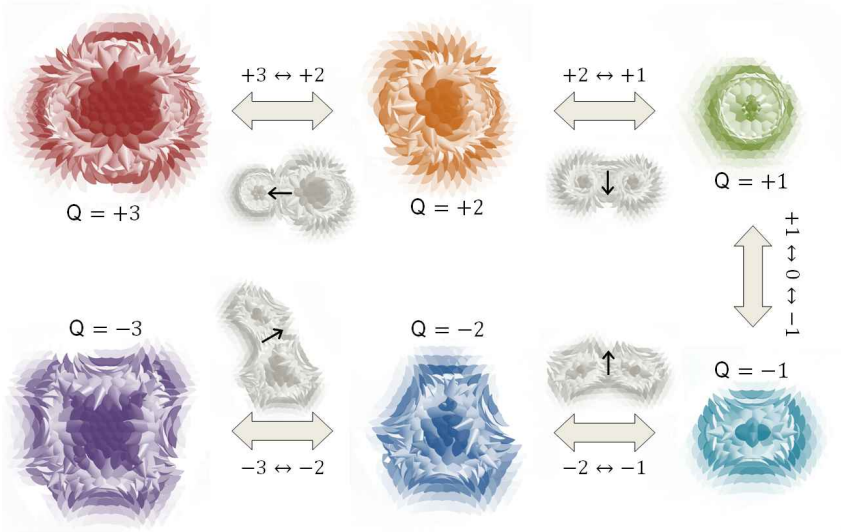

Figure 6.3 – Topological charge switching between skyrmions with successive topological numbers, namely $-3 \leftrightarrow -2 \leftrightarrow -1 \leftrightarrow 0 \leftrightarrow +1 \leftrightarrow +2 \leftrightarrow +3$. The magnetization distribution, $\hat{\boldsymbol{m}}$, is depicted by solid cones for locally stable solutions (in color) and transition mechanisms (in gray). Arrows indicate the direction of topological switching (big) and the orientation of in-plane spins (small).

6.3 Switching behavior

6.3.1 Same charged particles

Minimum energy path considerations reveal that the driving transition mechanism between skyrmions with neighboring integer topologies, denoted topological charge switching, involves combining or separating binary skyrmions ($|Q| = 1$) to the magnetic texture; see Fig. 6.3 for examples. Skyrmions with higher topological charges, denoted by points of local minima, represent more excited states and are thus more

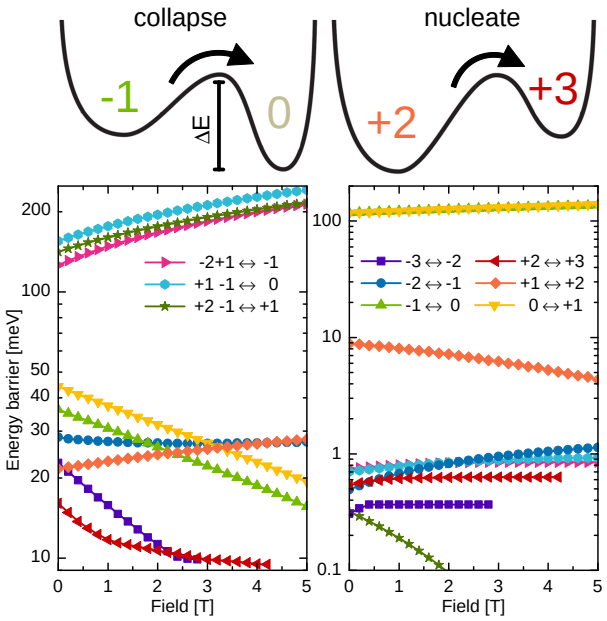

Figure 6.4 – Energy barriers for switching between skyrmions with different topological charges as a function of applied magnetic field. Left: Collapse barriers for transitions to lower topological numbers. Right: Nucleation barriers for switching to higher topologies.

likely to transition into other topologies, by acquiring or expelling a unit charge. This can be inferred from the collapse and nucleation energy barriers in Fig. 6.4, both of which decrease as $|Q| \to \infty$. For example, $+2 \leftrightarrow +3$ topological charge transitions have smaller energy barriers (0.1 meV and 16 meV for nucleation and collapse, respectively) than those found for $+1 \leftrightarrow +2$ transitions (9 meV and 22 meV), which in turn are much smaller than energy barriers for $0 \leftrightarrow +1$ topological switching (100 meV and 45 meV). The relations persist across different Ir concentrations ($x \geq 0.05$), so we can expect them to represent general physical properties of higher order skyrmions in frustrated magnets [58, 129, 205]. Fig. 6.4 illustrates the dependence of topological charge stability, which is determined by the energy barriers, on an applied magnetic field. The collapse barriers of unit charged particles decays quickly with the magnetic field, as expected from the impact of external fields on the size and shape of a skyrmion [46]. Bi-skyrmions become surprisingly more stable with increasing magnetic field and are thus less likely to collapse into textures of lower topology. This can be explained by the difference in spin orientations between distinct topological textures. For skyrmions with the same topological charge magnitude, $|Q|$, spins in opposing domain walls point in opposite directions along the surface and are thus not much affected by the perpendicular magnetic field. The same is not true for skyrmions with distinct $|Q|$, where domain wall spins point in the same direction and only differ in the normal component. Lastly, we find that the nucleation barriers decrease by an order of magnitude for each integer increase in the topological number, which means that merging unit charged particles to ones with higher topological numbers becomes dramatically easier. One can then argue there is a switching bias towards higher order topologies by merging same charged particles.

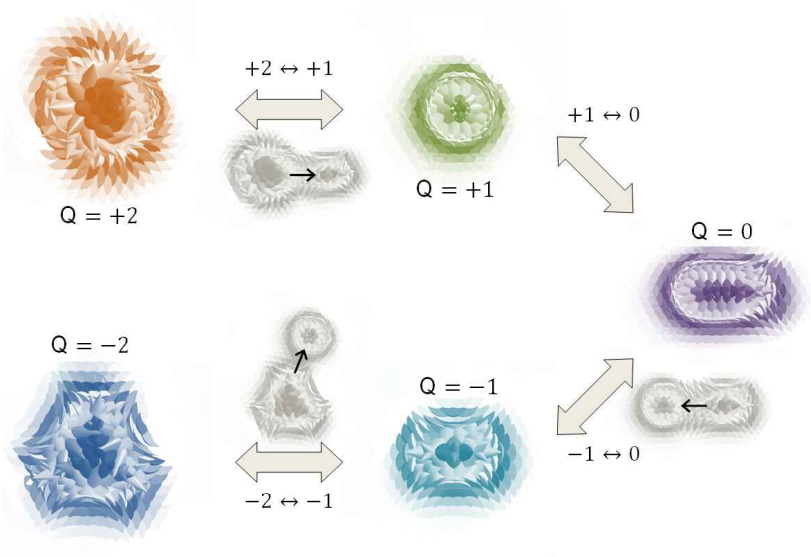

Figure 6.5 – Topological charge switching between skyrmions with successive topological numbers, namely $-2 \leftrightarrow -1 \leftrightarrow 0 \leftrightarrow +1 \leftrightarrow +2$. Here the transition mechanisms involve the interaction of skyrmion and anti-skyrmion pairs. The magnetization distribution, $\hat{\boldsymbol{m}}$, is depicted by solid cones for locally stable solutions (in color) and transition mechanisms (in gray). Arrows indicate the direction of topological switching (big) and the orientation of in-plane spins (small). Note that the in-plane spins are always parallel to the line connecting the skyrmion cores.

6.3.2 Pairs of opposite charges

Nontrivial topological textures can also emerge from the interactions of skyrmion and anti-skyrmion pairs. Illustrations for their transition mechanisms are presented in Fig. 6.5. The calculated energy barriers for combining pairs of opposite skyrmions [0.7 meV for $0 \leftarrow +1 - 1$ transitions] are an order of magnitude smaller than those encountered for same charged particles [10 meV for $+2 \leftarrow +1 + 1$ transitions], as shown in Fig. 6.4. The same holds true for merging binary particles into higher order skyrmions of opposite charge, while switching to higher topologies under the considered framework presents a significantly more difficult task (or higher energy barriers). This suggests that same charged particles prefer switching to higher topologies, while oppositely charged textures transition easier to lower ones. A plausible explanation is the partial alignment of spins between the respective textures along the in-plane orientation [56], which means that less energy is needed for spin rotations.

6.3.3 Nature of transitions

To better understand the nature of topological charge switching, we study their microscopic details from the minimum energy path perspective. The magnetization configurations, $\hat{\boldsymbol{m}}(t)$, reveal that a skyrmion or anti-skyrmion pair forms a magnetic texture with $Q = \pm 2$ by helicity-orbital coupling [56, 57], where the translational motion of a skyrmion is coupled with its helicity in frustrated magnets resulting in a rotational motion. The in-plane spins always align parallel or perpendicular to the line connect-

ing the skyrmion cores [see Fig. 6.3], and are then rotated into the $+z$ direction. This mechanism can also be used to describe switching processes of higher order topological particles, while transitions from binary skyrmions [or $-1 \leftrightarrow 0 \leftrightarrow +1$ switching] match the descriptions in previous works [84, 85, 95]. We can further confirm these transitions by finite-temperature spin dynamics simulations based on Eq. (2.20). Fig. 6.6 displays the evolution of the magnetization distribution, $\hat{\boldsymbol{m}}(t)$, on the onset, during, and at the end of a topological charge switch. Since the net topological charge does not change during the simulations, we drop the temperature from 50 K to 0 K so that we can observe the magnetic textures, which is similar to an infinitely rapid cooling process [57, 58] (note this is purely for visualization purposes). Our results shows that a pair of binary skyrmions switches into a bi-skyrmion after sufficiently long time. Similar switching behavior is found in Fig. 6.7 for the collapse of a skyrmion and anti-skyrmion pair into the ferromagnetic background.

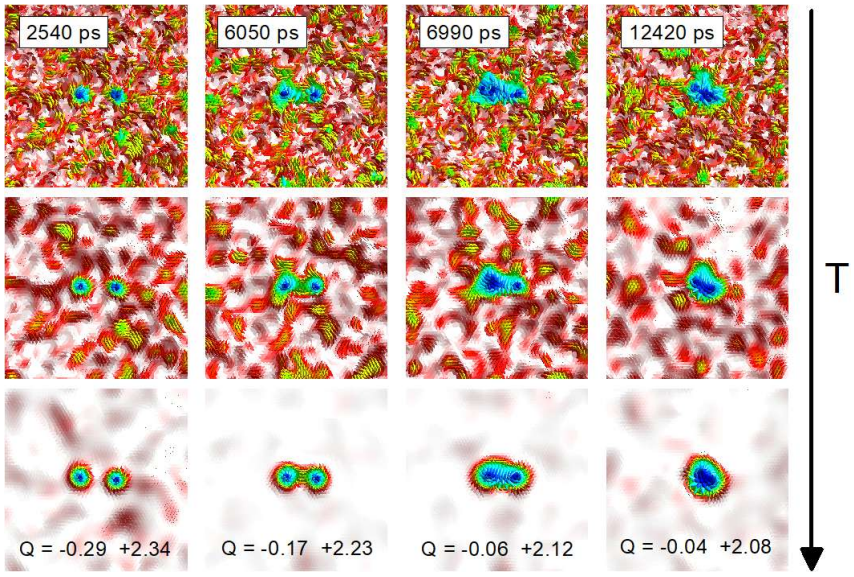

Figure 6.6 – Spin dynamics simulations of $+1 + 1 \rightarrow +2$ transitions. Evolution of the magnetization distribution, $\hat{\boldsymbol{m}}(t)$, on the onset, during, and at the end of a topological charge switch (from left to right). The temperature is lowered from 50 K (top) to 0 K (bottom) so we can observe the magnetic textures for visualization purposes. Numbers on the bottom indicate the sum of positive and negative topological charge densities, $q(t)$.

However, a more intuitive understanding of the switching mechanisms can be drawn from the evolution of the topological charge density, $q(t)$. Fig. 6.8 reveals that the charge density of binary particles are characterized by a single parabolic function, while higher order skyrmions consist of an irregular surface rim (for example, the rim is crescent shaped for textures with topological number of two) and a hole in charge density (parabolic in shape) located in the center. Note the surface rim becomes more complex and the number of holes increases as $|Q| \rightarrow \infty$. The switching mechanism for higher order topologies (namely, $|Q| > 1$) can then be explained through the insertion or deletion of holes in the topological charge densities of the textures, which also lead to the merging or splitting of rim surfaces. For binary switching mechanisms, a topological hole nucleates in the skyrmion core as a non-integer texture that holds

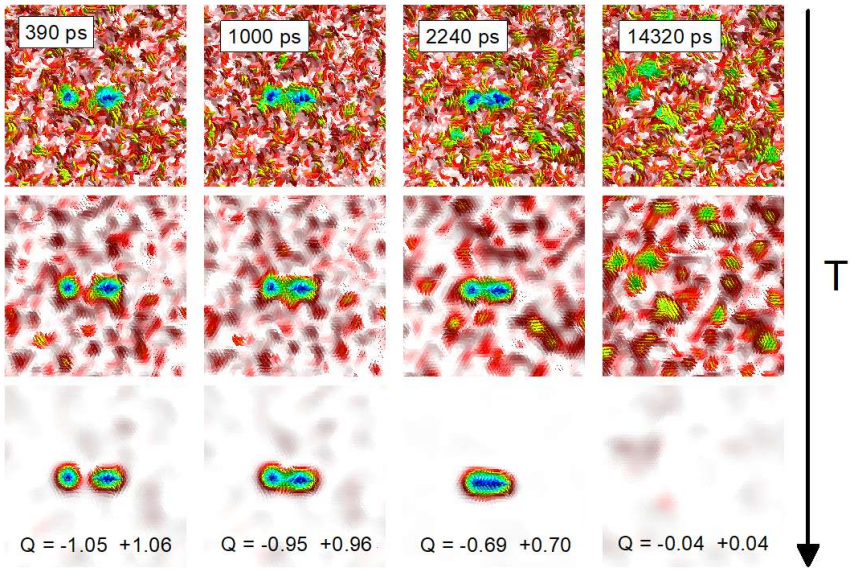

Figure 6.7 – Spin dynamics simulations of $-1+1 \rightarrow 0$ topological charge switching.

only a fraction of the skyrmion charge, which implies the existence of a fractional anti-skyrmion [207–209]. Such a microscopic description of the transition mechanisms has been eluded in previous studies [56, 57, 204].

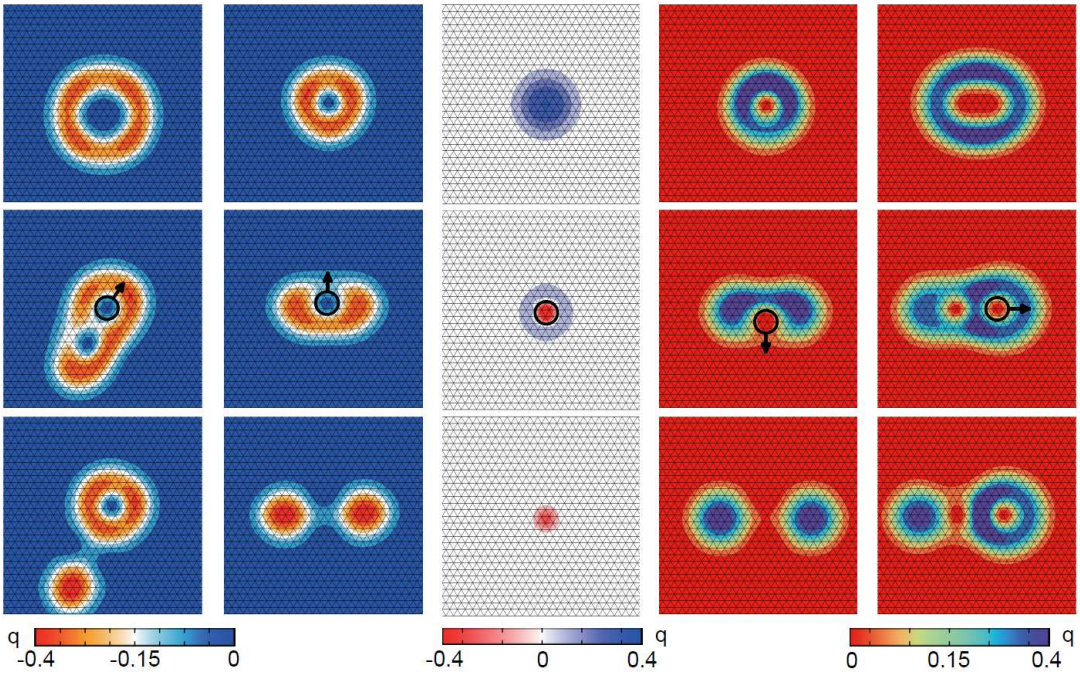

Figure 6.8 – Evolution of the topological charge density, $q(t)$, from top to bottom for (a) $-3 \leftrightarrow -2$, (b) $-2 \leftrightarrow -1$, (c) $0 \leftrightarrow +1$, (d) $+1 \leftrightarrow +2$, and (e) $+2 \leftrightarrow +3$ transitions. Circles specify positions of the topological holes while arrows indicate their directions.

6.4 Interactions

6.4.1 Attractive and repulsive

Frustrated exchange interactions play a prominent role in creating attractive interactions between binary skyrmions at short distances [125]. Here we analyze the interactions between skyrmions with various topological numbers, where the interaction energy between two such textures is calculated using minimum energy path considerations. Fig. 6.9 reveals that frustration in the exchange interactions lead to an oscillating interaction potential [125] for pairs of all types of skyrmions. Only the first local extrema are visible due to the exponential decay [53,57], while the first minimum indicates the presence of attractive interactions in the vicinity of energy barriers. Interestingly, we discover skyrmions exhibit much weaker attractive interactions (five to ten times) and at larger distances (up to $\sim 5a$ farther) when $Q \neq 1$. They also have no repulsive force before becoming attractive, as in the case of $Q = 1$. A plausible explanation is the partial alignment of spins between the respective textures along the in-plane orientation [56], which means that less energy is needed for spin rotations. Fig. 6.9 also shows that the strength of the interactions is proportional to the magnetic field, $\Delta E \propto B$, until saturation of the skyrmion texture.

6.4.2 Formation of clusters

This favors the formation of arbitrary skyrmion clusters that are resistant against diffusion processes at finite temperature. We can also expect that skyrmion clusters with an average topological number $\langle Q \rangle = 1$ will be much more stable than other topological clusters, since they possess stronger bonds than higher order skyrmions. Spin

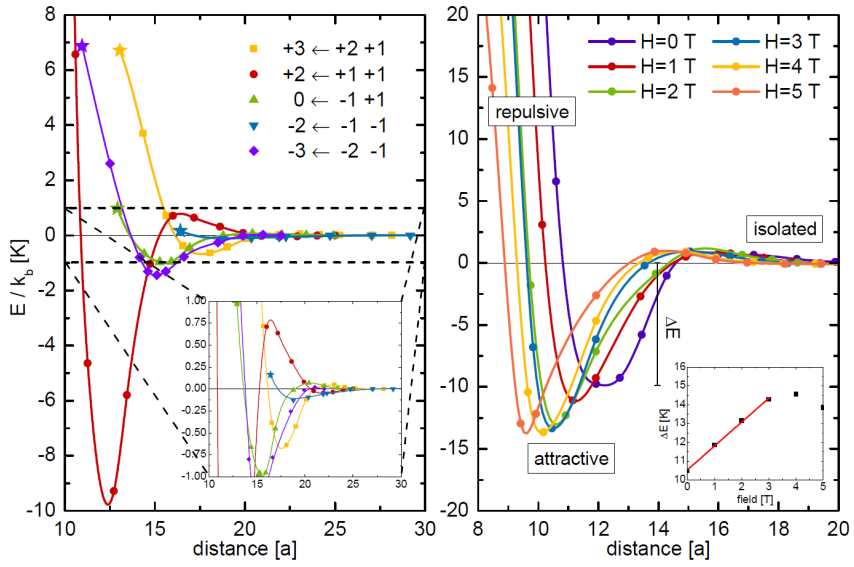

Figure 6.9 – Left: Interaction potentials between distinct skyrmion pairs for $B = 0$ T. Stars denote the energy barriers and inset is a magnified region. Right: Same considering only the case of binary skyrmions ($Q = 1$) for varying magnetic fields. Inset plots energy barriers as a function magnetic field.

dynamics simulations in Fig. 6.10 reveal that skyrmions with topological number of unity can form arbitrarily shaped clusters in situations where other skyrmion clusters are destroyed by thermal fluctuations, since they possess stronger bonds than higher order skyrmions. For example, while skyrmion clusters remain stable at 10 K, the anti-skyrmion structures are severely distorted because individual particles easily overcome their low attractive potentials and move apart or merge into higher order anti-skyrmions. This happens for all of the considered shapes: lines, triangles and dodecagons. An interesting concept involves exploiting the various stabilities of distinct topological clusters for spintronic applications.

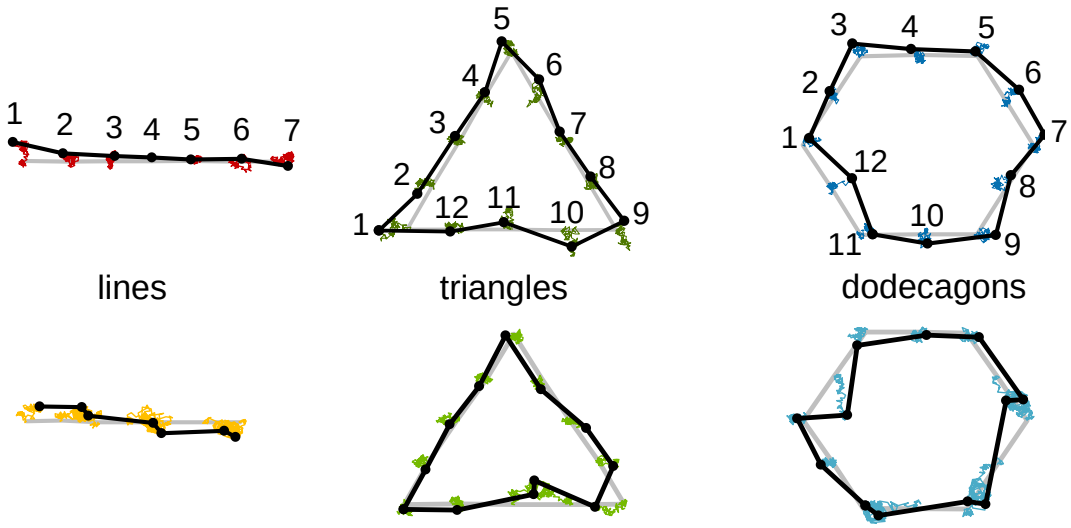

Figure 6.10 – Spin dynamics simulations of skyrmion (top) and anti-skyrmion (bottom) clusters arranged as lines, triangles, and dodecagons at 10 K. Evolutions of the skyrmion centroids (numbered) and bonds between them (solid lines) from zero to 10^5 ps.

7 NUMERICAL LIBRARY

In this Chapter[1] we discuss the numerical library which was developed along with this thesis to aid the numerical work. The library represents a culmination of the computational tools developed for each of the previous chapters. First, we present the interface of the library. We then focus on several numerical aspects used for conducting simulations of magnetic skyrmions. The goal is to provide the reader with the necessary tools for tackling the physics considered in this thesis. We conclude with a set of computer programs that describe how one could simulate some of the discussed problems.

7.1 Interface

The numerical library is written with the aim to be as user-friendly and flexible as possible. Under the hood, the C programming language [210] is used to accelerate demanding tasks and deliver high performance with low memory usage. The general workflow starts with the model definition. Three main parts are required to describe the model: (i) The lattice includes specification of a unit cell (of atomic spins and interactions) which can be user-defined or chosen from a repository of pre-made unit cells for several materials. (ii) The system geometry can be defined almost arbitrarily, and can be infinite through the use of periodic boundary conditions or it can be finite by specifying open boundaries. (iii) The material is defined by spatial maps representing exchange couplings, anisotropies, and applied fields on atomic sites. This allows for easy inclusion of defects considered in Chapter 4.

Once the model description is complete, the next step is to define the ansatz, or starting magnetic configuration. To that end, there are several possibilities: (i) A set of pre-defined routines for constructing the ansatz for distinct spin textures, e.g., Néel skyrmions, is provided. There are also several options for constructing the path ansatz used in minimum energy path calculations. (ii) Files storing magnetic states from previous simulations can be loaded into the library. (iii) The numerical library provides direct access to the magnetic vectors, which can then be used for custom definitions of the ansatz.

Lastly, we need to apply computations to describe the desired physics. This can be done in three ways: (i) The Hamiltonian energy is minimized with Monte Carlo or direct solvers, e.g., SD or QM. (ii) Transitions between different magnetic states are calculated using minimum energy paths calculations, e.g., GNEB. (iii) The time dependent dynamical behavior of the magnetic moments is simulated by LLG. The calculations can be performed on a terminal, or on a graphical interface that visualizes the numerical simulation in real-time. This way we can make changes to the simulation throughout its execution. After the main computation is complete, various utility functions are available for post-processing the results.

[1] The results of this Chapter are published in Ref. [99].

The library provides a structure that is used to define the model. For instance, one can specify the lattice dimensions or material parameters to be used. Properties which are not explicitly defined will take on default values when creating the model. Below is an example code which creates a hexagonal lattice for the Pt/Co monolayer:

```
#include <stdlib.h>
#include <numerical_library.h>
void main(){
  NL_TYPE nl;           // Library structure
  // Lattice
  nl.nx=100;            // Number of cells along x
  nl.ny=100;            // Number of cells along y
  nl.nz=1;              // Number of cells along z
  nl.a=2.51;            // Lattice constant
  nl.cell=HEXAGONAL;    // Unit cell
  // Material (Pt/Co)
  nl.mu=2.51;           // Magnetic moment
  nl.J[0]=29;           // Isotropic exchange coupling
  nl.D[0]=1.5;          // DM coupling
  nl.K[0]=0.293;        // Anisotropy constant
  // Create the model
  model(nl);
}
```

where `nl` is the library structure. To avoid repeating the material parameters, one can use the `fill` routine which automatically populates the parameter list:

```
#include <stdlib.h>
#include <numerical_library.h>
void main(){
  NL_TYPE nl;           // Library structure
  // Lattice
  nl.nx=100;            // Number of cells along x
  nl.ny=100;            // Number of cells along y
  nl.nz=1;              // Number of cells along z
  // Material (Pt/Co)
  fill(nl,"PtCo");
  // Create the model
  model(nl);
}
```

for several predefined materials that have been retrieved from literature. The routines from the library are included in the `numerical_library.h` header. We will go over the parts of the library in the following sections. In order to save space and not distract from the main point, some common and repetitive statements will be omitted (like includes and declarations).

7.2 Geometry

The geometry of the nanostructure is an essential part for modeling at the atomic scale. Due to symmetry, we can represent the lattice by a basis or unit cell, which is then translated along its dimensions. The cell specification is made in the library when creating the model. For example, a square lattice (denoted by `nl.cell=SQUARE`) can be

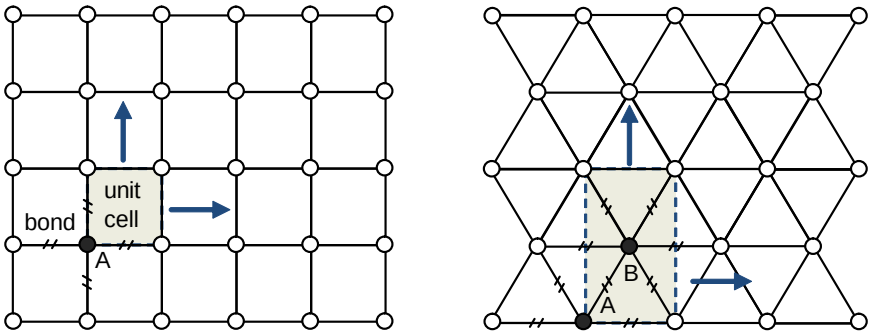

Figure 7.1 – Sketch of square lattice (left panel) and hexagonal lattice with fcc stacking (right panel). The unit cells are denoted by shaded region with dashed lines and consists of atomic sites A and B. Arrows indicate direction of translation when constructing the model.

described by a unit cell composed of a single atom with 4 interactions, as illustrated in Fig. 7.1. Similarly, the hexagonal lattice with fcc stacking, which is the lattice of choice in the thesis, utilizes a unit cell of 2 atoms and 12 interactions. This greatly simplifies the representation as one can easily model all of the common crystal structures: simple cubic (sc), face centered cubic (fcc), body centered cubic (bcc), and hexagonal close packed (hcp), as well as define new unit cells for specific nanostructures. Particularly, the few-atom thick ferromagnetic layer considered in Chapter 3 is modeled using a unit cell that describes the entire fcc stacking sequence composed of 6 atoms and 72 interactions.

The geometry is specified by an integer map (`nl.geometry`) that determines which basis cells are to be occupied with atoms. This way we can construct nanostructures of nearly arbitrary geometries. For instance, a circular structure with diameter that is half the lattice width (`nx`) can be created as follows:

```
// Create the geometry
for(j=0;j<nl.ny;j++)
for(i=0;i<nl.nx;i++){
  r=(i-nl.nx)*(i-nl.nx)+(j-nl.ny)*(j-nl.ny);
  nl.geometry[i+nl.nx*j]=(r<nl.nx*nl.nx/4)?1:0;
}
```

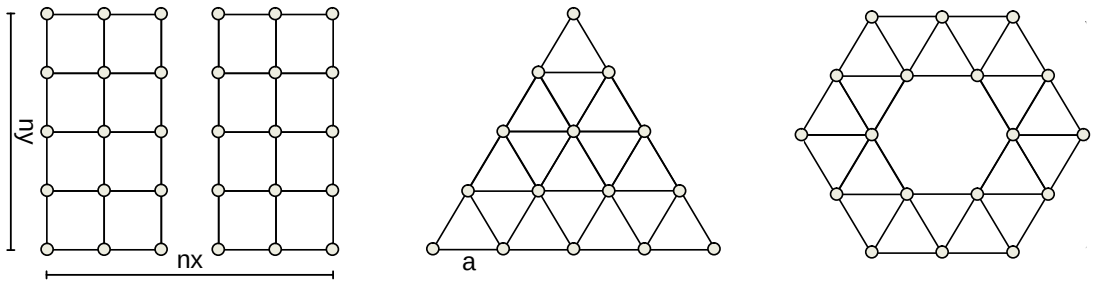

Figure 7.2 – Sketch of nanostructures with distinct exotic geometries from left to right: protrusion on square lattice, triangle on hexagonal lattice, and ring on hexagonal lattice.

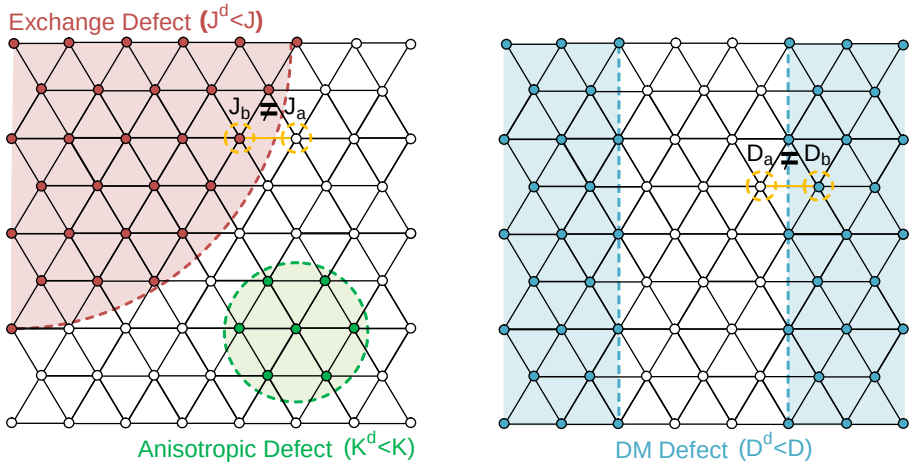

Figure 7.3 – Sketch of hexagonal lattice with circular anisotropic ($K^d < K$) and exchange ($J^d < J$) defects located in dashed regions (left panel). J_a and J_b denote exchange couplings at opposite sides of the interface. Same for a racetrack geometry with vertical DM-induced defects ($D^d < D$) (right panel).

where `1` indicates an occupied site and `0` an atomic vacancy. Several possible exotic geometries are illustrated in Fig. 7.2. Note that granularity of the geometry depends on the definition of the unit cell.

7.3 Material images

The material can be specified by floating-point maps (or images) which are created in the `model` routine. They provide spatial representations of the exchange couplings, anisotropies, and external fields by mapping their values onto lattice sites. This allows for the modeling of inhomogeneities in the material, e.g., material defects considered in Chapter 4. While initially set to a single homogeneous value, one can change the maps defined in the `nl` structure. For example, we can model circular regions of lower isotropic exchange and anisotropy as follows:

```
// Create circular defects
for(j=0;j<nl.ny;j++)
for(i=0;i<nl.nx;i++){
  r=(i-ax)*(i-ax)+(j-ay)*(j-ay);
  nl.Jmap[i+nl.nx*j]=(i*i+j*j<nl.nx*nl.nx/4)?J:J/2;
  nl.Kmap[i+nl.nx*j]=(r<nl.nx*nl.nx/16)?K:K/2;
}
```

which amounts to constructing an image map with different values for the background and inhomogeneity (see Fig. 7.3). The skyrmion racetrack with an extended film that lacks DMI considered in Chapter 3 can be modeled as:

```
// Create racetrack
for(j=0;j<nl.ny;j++)
for(i=0;i<nl.nx;i++){
```

```
  nl.Dmap[i+nl.nx*j]=((i<lx)||(i>rx))?0:D;
}
```

as illustrated in Fig. 7.3.

While mapping the inhomogeneous material is trivial for the anisotropy constants and applied fields, special considerations are required for the exchange couplings. The typical situation is when the exchange interactions are calculated on an interface, where neighboring spins have different values for the coupling constants since they are mapped to lattice sites (see Fig. 7.3). To ensure that the exchange couplings remain the same for a given pair of spins, the library internally performs a min or max operation on the coupling coefficients, J_a and J_b, for every pair of lattice sites a and b. For more realistic simulations, we also consider the average of the two, $(J_a + J_b)/2$, which provides a smoother transition from one coupling to the other.

7.4 The Hamiltonian

To construct the model, we execute the `model` routine:

```
// Create the model
model(nl);
```

which creates the lattice and allocates the internal memory. Parameters not specified are initialized to default values. The lattice geometry and material can be further modified through the `nl` structure as discussed above. Once the model description is complete, we need to consider the Hamiltonian defined in Eq. 2.4. The library evaluates the Hamiltonian numerically by separating into its individual parts: exchange interactions, anisotropy, applied fields, and dipole-dipole interactions. The breakdown is useful for optimizations as well as when only a subset of terms need to be evaluated, e.g., when integrating the spin dynamics. Rather than evaluating the Hamiltonian twice, the library calculates the derivatives, $\partial\mathcal{H}_i/\partial\hat{\boldsymbol{m}}_i$, which are used for minimization and LLG calculations, followed by the energetics, $\mathcal{H}_i$, for the ith Hamiltonian term. For anisotropy and applied fields the calculations are trivial as the contribution of every lattice site is considered (see Fig. 7.4). For exchange interactions, however,

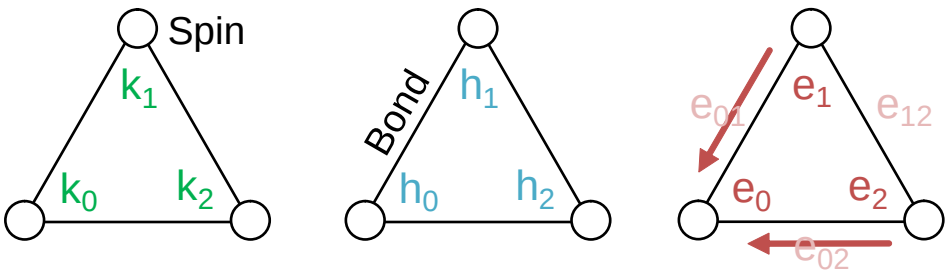

Figure 7.4 – From left to right: Sketch of hexagonal lattice with anisotropy, applied field, and exchange Hamiltonian contributions. Numbers represent lattice indices and arrows indicate the interactions that form the exchange contribution, e.g., $e_0 = e_{01} + e_{02}$.

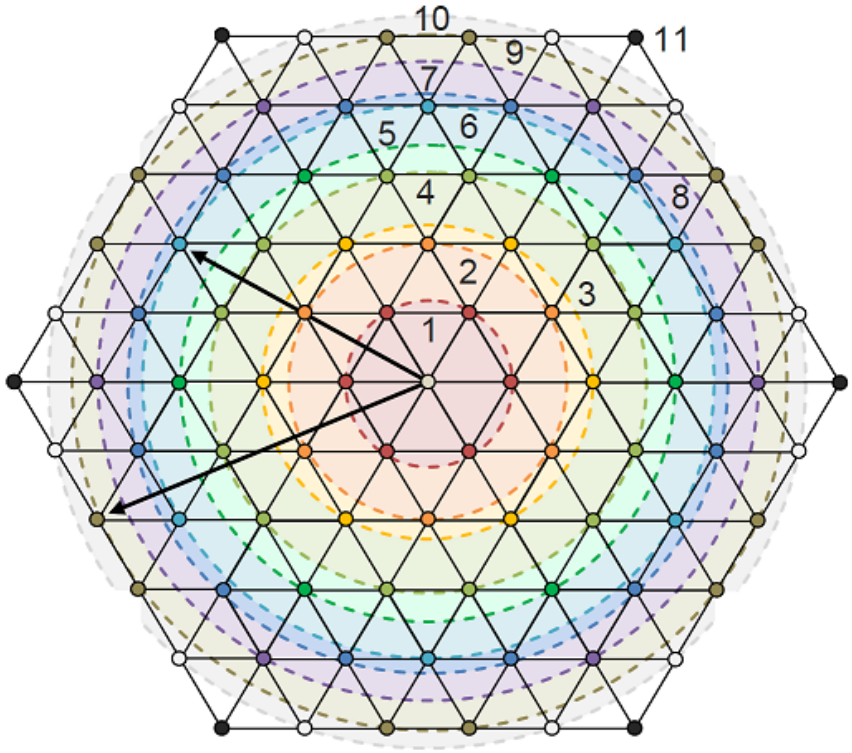

Figure 7.5 – Sketch of the eleven neighboring shells for Pd/Fe/Ir with exchange frustration, retrieved from ab initio calculations. The shells are numbered and colored with dashed regions.

the contributions depend on the exchange coupling which is specified for atomic spin pairs. Treating the Hamiltonian both by their spins and by their pairs makes storing in memory and numerical calculations more difficult. Instead, we can represent the exchange interactions for a given spin $\hat{\boldsymbol{m}}_i$ by summing over the contribution e_{ij} from every neighbor $\hat{\boldsymbol{m}}_j$, or $e_i = \sum_j e_{ij}$, as illustrated in Fig. 7.4. The exchange interactions will then be counted twice, $\hat{\boldsymbol{m}}_i \to \hat{\boldsymbol{m}}_j$ and $\hat{\boldsymbol{m}}_j \to \hat{\boldsymbol{m}}_i$, so we must halve the total sum as done in Eq. 2.13. This allows us to map inhomogeneities in the exchange interactions to lattice sites as mentioned earlier. The dipole-dipole interactions are handled separately, and will be discussed later in this Chapter.

7.5 Diffusion search

For exchange interactions beyond the nearest neighbor approximation, the model is created using neigborhood shells, or set of atomic sites with constant distance from the spin. However, the material parameters cannot be varied spatially as considered earlier. The exchange interactions are specified by floating-point lists:

```
float Jshell[]={23.06,-2.08,-5.78, 0.65,0.62, 0.05,-0.39,-0.37,-0.02,0.06, 0.23};
float Dshell[]={ 1.22,-0.05,-0.78,-0.16,0.32,-0.03, 0.07,-0.06,-0.03,0.02,-0.02};
memcpy(nl.J,Jshell,sizeof(Jshell));
memcpy(nl.D,Dshell,sizeof(Dshell));
```

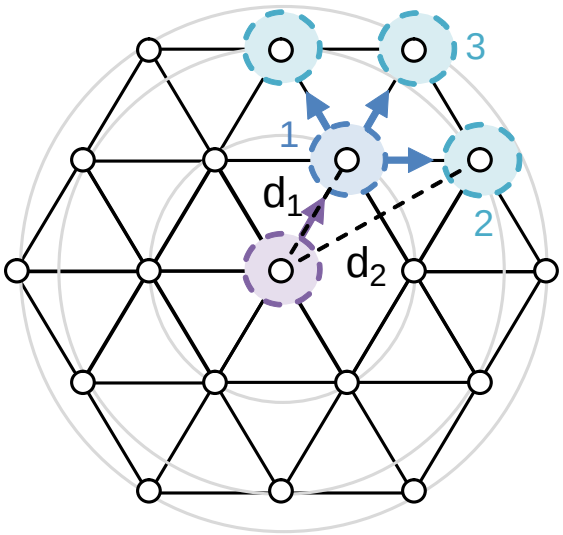

Figure 7.6 – Sketch of the diffusion search through a hexagonal lattice. Circles represent the visited sites, starting from the center, and arrows indicate the direction of the search. Labels correspond to the shells that the neighbors are stored in, given the distances $d_1 < d_2 < 2d_1$.

which represent the coupling values for each neighborhood shell, as illustrated in Fig. 7.5.

Calculations of the exchange interactions amounts to searching through a list that contains the neighboring spins for each lattice site. While constructing such neighborhood sets is feasible for common crystal structures, there is no trivial way to do this for arbitrary unit cells. Instead, we devise an algorithm that searches for neighboring shells and constructs the effective neighborhood for each spin. The basic idea is to treat the problem as a diffusion process, where the search collects information about the neighborhood as it expands from a localized point throughout the lattice, as shown in Fig. 7.6. The algorithm begins by choosing an atomic site and visiting its nearest neighbors, which we already have. The distance from each neighbor is calculated and possibly added to a list of unique distances ranked by magnitude. Each nearest neighbor is then added to the neighborhood shell numbered by the distance rank, i.e., closest neighbors are put in the first shell and farthest neighbors in the last shell. The algorithm repeats this process by visiting the nearest neighbors of each neighboring spin, in a recursive manner. The recursion only considers neighbors that are farther to the source from the point being considered. This way we guarantee that the search avoids repetitions and is always expanding outwards, like a diffusion process. We stop when the desired number of shells has been reached, which is determined by the coupling coefficients retrieved from ab initio calculations. The algorithm is repeated for each spin in the system, thereby constructing an effective neighborhood for each lattice site. The exchange Hamiltonian, $\mathcal{H}_{ex}$, is then trivial to calculate by summing up the contributions of the neighborhood shells for each spin. Particularly, in Chapter 6 we considered interaction coefficients between Fe spins taken to include up to 11 neighboring shells, or 72 nearest lattice sites (see Fig. 7.5).

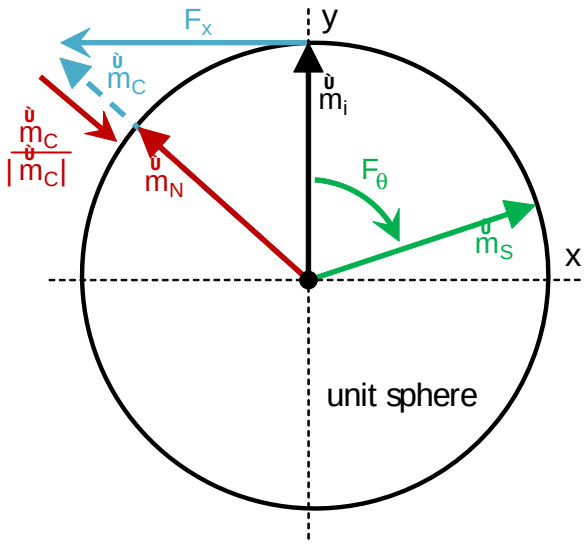

Figure 7.7 – Sketch of the steepest descent (SD) update on a unit sphere along the x and y dimensions. The spin $\hat{\boldsymbol{m}}_i$ is updated in spherical coordinates with the polar force $\boldsymbol{F}_\theta$ into $\hat{\boldsymbol{m}}_S$, or in Cartesian coordinates with the horizontal force $\boldsymbol{F}_x$ into $\hat{\boldsymbol{m}}_C$, which is then normalized to the unit sphere becoming $\hat{\boldsymbol{m}}_N$.

7.6 Minimization

To obtain stable skyrmions, we must find their local solutions in the Hamiltonian. One option is to solve the LLG equations with large damping, $\alpha \gg 1$, which is much like a steepest descent since the precession term is all but removed:

```
// Relax by LLG
nl.alpha=100;
nl.dt=1e-14;
nl.T=0;
while(de>epsilon){
  e=llg(nl,nl.M);
}
```

where LLG parameters are specified in the `nl` structure, and `nl.M` represents the magnetic configuration. Another consideration is Monte Carlo, which corresponds to a greedy search at zero temperature:

```
// Relax by Monte Carlo
nl.T=0;
while(de>epsilon){
  e=mc(nl,nl.M);
}
```

Although well-established in magnetism, both of these approaches are slow and require much computation. Instead, we can reduce the problem to that of minimization and solve it using direct techniques:

```
// Relax by direct minimization
nl.dt=1;
```

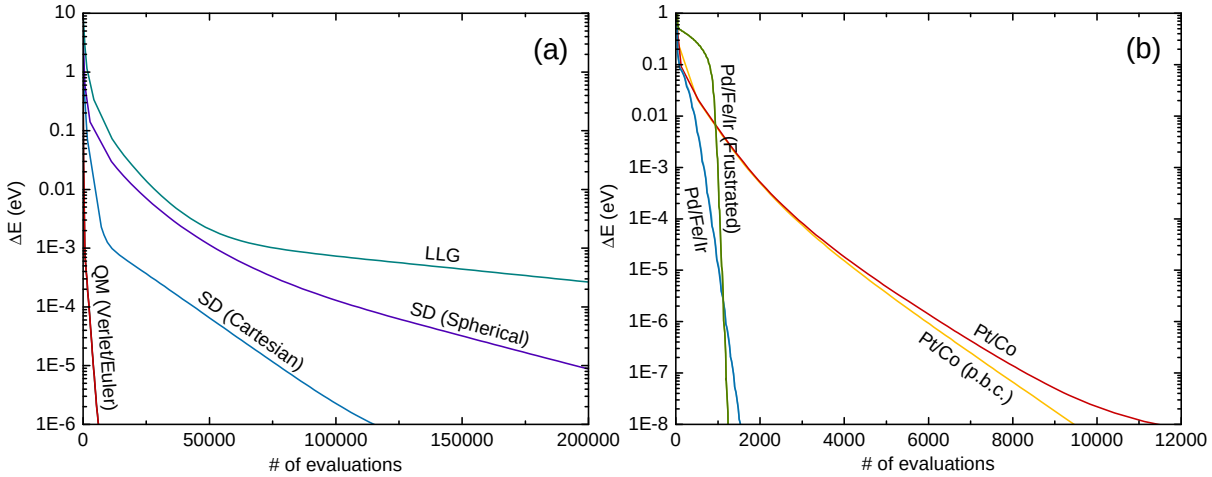

Figure 7.8 – Relaxation from a circular domain to a metastable skyrmion. (a) Evolution of the energy difference, ΔE, as a function of Hamiltonian evaluations for different minimization procedures on a Pt/Co monolayer. (b) Evolution of the energy difference for QM on different materials, with open or periodic boundary conditions (p.b.c.).

```
nl.method=SD;
while(de>epsilon){
  e=min(nl,nl.M);
}
```

Our focus is on approaches that rely only on the force, which we take to be the effective field, $\boldsymbol{H}_i^{\text{eff}}$, that is exerted on each spin (see Eq. 2.21). The simplest of these is SD, which follows the force vector (or field) until it becomes zero (see Section 2.5.3). Here we can consider either Cartesian or spherical coordinates for updating the spin orientations, as illustrated in Fig. 7.7. Cartesian coordinates are preferred since they avoid numerically costly trigonometric operations, but the spin can be moved outside of the unit sphere. Therefore, the spin must be normalized after every update to preserve its magnitude, which proves to be a good solution for most situations. To achieve faster minimization we can accelerate the search in the force direction by using QM (see Section 2.5.3). This approach damps the velocity by including only the component in the direction of the force, and can be coupled with Euler or Verlet integration.

Fig. 7.8 reveals that QM can find the skyrmion solution the fastest, but does not differ between Euler and Verlet. SD takes an order of magnitude longer to converge under Cartesian coordinates, and even longer for spherical ones. Lastly, LLG takes significantly longer times to obtain the skyrmion compared to direct minimization, since the Hamiltonian needs to be evaluated twice for the predictor-corrector integrator. We also consider how different materials affect the minimization. Fig. 7.8 shows that the skyrmion state is hardest to obtain on Co films, and is affected depending whether the boundary conditions are open or periodic. For PdFe bilayers the QM converges to the solution much faster, but takes longer to start in the presence of exchange frustration. Here, the minimization is not affected by the boundary conditions. Therefore, a plausible explanation for the slow convergence in Co-based systems is that strong

exchange interactions introduce some form of constraints which limit the search.

7.7 Ansatz

7.7.1 For magnetic states

Given a metastable state we want to achieve, e.g. a skyrmion, an important question is how can we obtain its magnetic configuration. In practice, the typical approach is to repeat many numerical simulations, by LLG or Monte Carlo, until the state in question is found. However, this can be a laborious task and does not always guarantee a result. A more trivial approach is to introduce an ansatz that the magnetic configuration,

$$\hat{\boldsymbol{m}}^{\text{ansatz}} = \{\hat{\boldsymbol{m}}_1, \hat{\boldsymbol{m}}_2, \hat{\boldsymbol{m}}_3, \dots\}, \tag{7.1}$$

is located in the basis of attraction of the desired state, which allows us to relax the system into the magnetic state we want to obtain (see Fig. 7.9). The choice of ansatz is important. Particularly, if we chose to start from a state that is not in the basis of attraction, then the steepest descent (by SD, QM, or LLG) will converge into a different local minima, or magnetic configuration, whereas a good choice will render the desired solution. The library provides a number of possibilities for ansatz definitions. For a Néel skyrmion with helicity $\gamma = 0$, a plausible ansatz is the circular domain that points in the skyrmion direction, $\hat{\boldsymbol{z}}$:

$$\hat{\boldsymbol{m}}_i^{\text{ansatz}} = \begin{cases} +\hat{\boldsymbol{z}}, & \text{if} \quad r_i \leq r, \\ -\hat{\boldsymbol{z}}, & \text{if} \quad r_i > r, \end{cases} \tag{7.2}$$

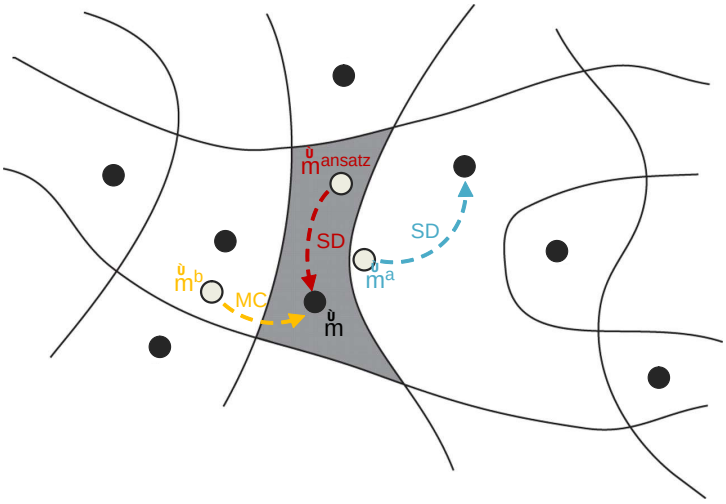

Figure 7.9 – Basins of attraction with simple boundaries, adapted from Ref. [211]. Dots denote local minima which correspond to stable magnetic states. The ansatz, $\hat{\boldsymbol{m}}^{\text{ansatz}}$, is taken to be inside the shaded basin and converges to the desired state, $\hat{\boldsymbol{m}}$, when minimized by steepest descent (SD). $\hat{\boldsymbol{m}}^{\text{a}}$ is located in a neighboring basin and therefore converges to a different magnetic state. Lastly, $\hat{\boldsymbol{m}}^{\text{b}}$ is located near the shaded basin and can move into it by Monte Carlo (MC) with high temperature.

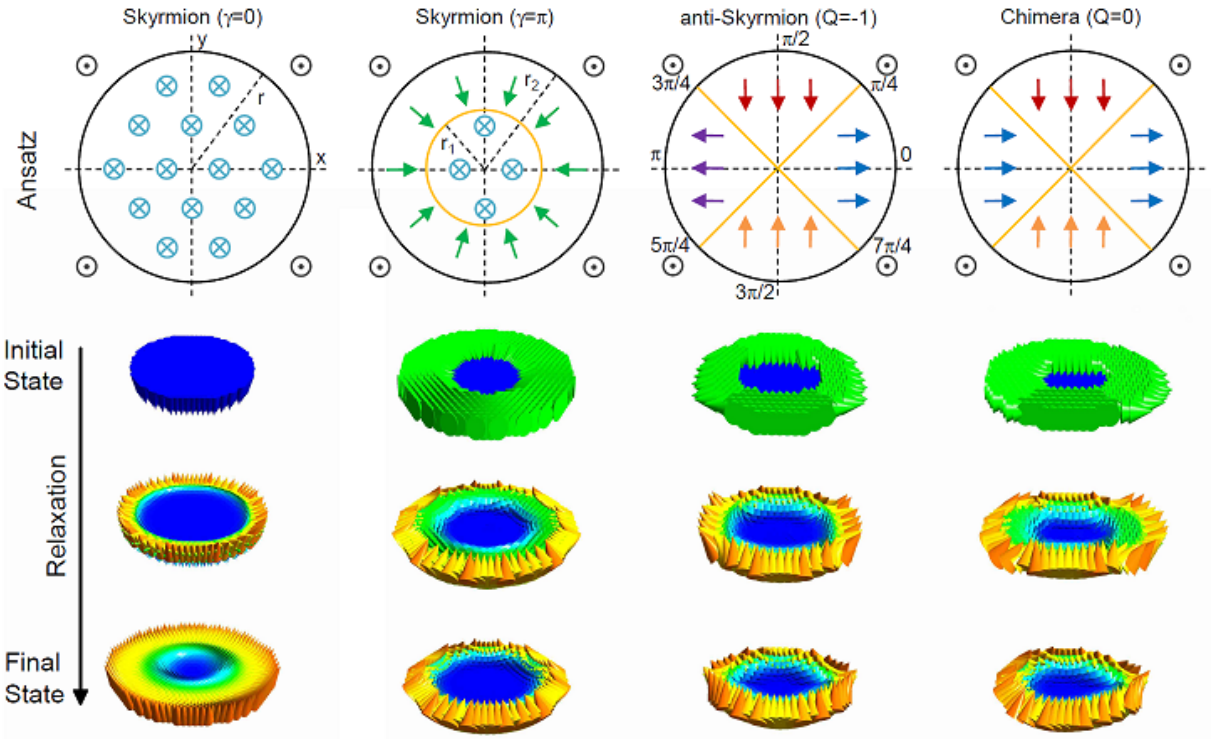

Figure 7.10 – Ansatz for skyrmions with $\gamma = 0, \pi$, an anti-skyrmion, and a chimera skyrmion (upper panel). Relaxation of the magnetic texture using the prescribed ansatz (lower panel).

where r_i is distance of site i from the skyrmion center, and r is the radius of the skyrmion. The anstaz can be defined using the numerical library as follows:

```
// Ansatz for Neel skyrmion
float pos[]={nl.nx/2,nl.ny/2,0};
float dir[]={0,0,+1};
ansatz_skyrmion(nl,nl.M,pos,r,dir);
```

Relaxing this state retrieves the desired magnetic configuration, as illustrated in Fig. 7.10, providing a quick way to obtain single skyrmions. For a skyrmion with helicity $\gamma = \pi$ caused by frustrated exchange interactions, we can define the ansatz as follows:

$$\hat{\boldsymbol{m}}_i^{\text{ansatz}} = \begin{cases} +\hat{\boldsymbol{z}}, & \text{if} \quad r_i \leq r_1, \\ -\hat{\boldsymbol{r}}_i, & \text{if} \quad r_1 < r_i \leq r_2, \\ -\hat{\boldsymbol{z}}, & \text{if} \quad r_i > r_2, \end{cases} \tag{7.3}$$

where $\hat{\boldsymbol{r}}_i$ is the unit position vector of the site i, and we point the in-plane spins in $r_1 < r_i \leq r_2$ inwards. The library routine for this ansatz becomes:

```
// Ansatz for Neel skyrmion with helicity
float pos[]={nl.nx/2,nl.ny/2,0};
float dir[]={0,0,+1};
ansatz_skyrmion_helicity(nl,nl.M,pos,r1,r2,dir);
```

The ansatz approach is vital for Chapter 6, where we need to determine magnetic configurations of skyrmions with topological integers, Q, different than unity [58]. Here,

we must take care in choosing the ansatz as the spin orientations are significantly more complex than those of a regular skyrmion. For an anti-skyrmion, or $Q = -1$, the ansatz can be chosen as:

$$\hat{\boldsymbol{m}}_i^{\text{ansatz}} = \begin{cases} +\hat{\boldsymbol{x}}, & \text{if} \quad r_i \leq r, \quad -\pi/4 \leq \theta < \pi/4, \\ -\hat{\boldsymbol{y}}, & \text{if} \quad r_i \leq r, \quad \pi/4 \leq \theta < 3\pi/4, \\ -\hat{\boldsymbol{x}}, & \text{if} \quad r_i \leq r, \quad 3\pi/4 \leq \theta < 5\pi/4, \\ +\hat{\boldsymbol{y}}, & \text{if} \quad r_i \leq r, \quad 5\pi/4 \leq \theta < 7\pi/4, \\ -\hat{\boldsymbol{z}}, & \text{if} \quad r_i > r \end{cases} \tag{7.4}$$

where θ is the counterclockwise angle of the spin orientation, $\hat{\boldsymbol{m}}_i$, from the x-axis, $\hat{\boldsymbol{x}}$, and spins outside the radius r are aligned to the ferromagnetic background, $-\hat{\boldsymbol{z}}$. Similarly, we can define the ansatz for a chimera skyrmion, or $Q = 0$, aligned in the x-axis by having the same orientations for spins along $-\pi/4 \leq \theta < \pi/4$ and $3\pi/4 \leq \theta < 5\pi/4$. For a bi-skyrmion, or $Q = 2$, we can construct an ansatz of two overlapping skyrmions of radius r along with vertical alignment of spins in their intersection,

$$\hat{\boldsymbol{m}}_i^{\text{ansatz}} = \begin{cases} +\hat{\boldsymbol{z}}, & \text{if} \quad r_{i1} \leq r, \quad r_{i2} \leq r, \quad -\pi/4 \leq \theta < \pi/4, \\ +\hat{\boldsymbol{y}} + \hat{\boldsymbol{z}}/(1 - r_i/r), & \text{if} \quad r_{i1} \leq r, \quad r_{i2} \leq r, \quad \pi/4 \leq \theta < 3\pi/4, \\ +\hat{\boldsymbol{z}}, & \text{if} \quad r_{i1} \leq r, \quad r_{i2} \leq r, \quad 3\pi/4 \leq \theta < 5\pi/4, \\ -\hat{\boldsymbol{x}} + \hat{\boldsymbol{z}}/(1 - r_i/r), & \text{if} \quad r_{i1} \leq r, \quad r_{i2} \leq r, \quad 5\pi/4 \leq \theta < 7\pi/4, \\ -\hat{\boldsymbol{z}}, & \text{if} \quad r_{i1} > r \quad \text{or} \quad r_{i2} > r \\ -\hat{\boldsymbol{z}}, & \text{if} \quad r_{i1} > r \quad \text{or} \quad r_{i2} > r, \end{cases} \tag{7.5}$$

where r_{i1} and r_{i2} are the distances from the skyrmion centers, $(a - r, b)$ and $(a + r, b)$, relative to a point (a, b). Their relaxations are illustrated in Fig. 7.10. Similar definitions can be made for skyrmions with other topological numbers. Another ansatz option is to load the magnetic configuration that was stored in an earlier simulation:

```
// Load from file
load(nl,nl.M,"skyrmion.dat");
```

and which is in the basin of attraction of the desired state. We also note that the ansatz conditions can be further relaxed to include magnetic configurations that are located near the basin of attraction, by using a Monte Carlo approach to the minimization, where sufficiently high temperatures allow the search to jump from one basin to another (see Fig. 7.9).

7.7.2 For magnetic paths

The same concept can be used for finding the MEP between two magnetic states. Here, we can define an ansatz that the set of magnetic configurations (or images),

$$\boldsymbol{M}^{\text{ansatz}} = \left\{ \boldsymbol{M}^1, \boldsymbol{M}^2, \boldsymbol{M}^3, \ldots \right\}, \tag{7.6}$$

is located in the basin of attraction of the MEP, which is obtained by relaxing the images as described in Section 2.5. The problem then becomes one of defining an

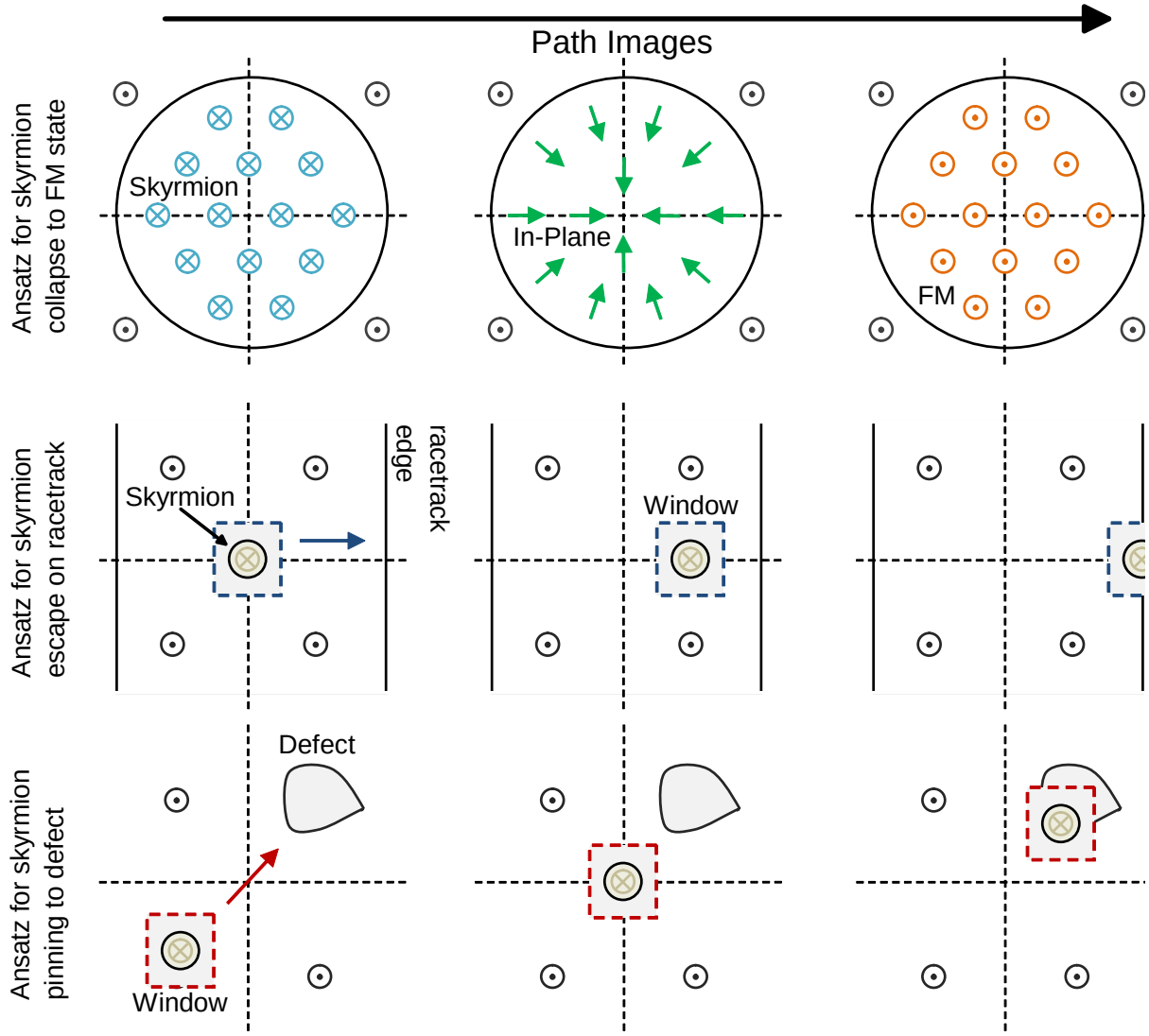

Figure 7.11 – Ansatz for skyrmions collapse to the ferromagnetic background (upper panel), escape on a racetrack edge (middle panel), and pinning to a defect (lower panel).

appropriate ansatz for a given MEP. Ref. [83] suggests an ansatz from the geodesic path formed by interpolating between the initial and final images, $\boldsymbol{M}^I$ and $\boldsymbol{M}^F$. A simple way to generate this interpolation is to rotate each magnetic moment from the initial orientation, $\hat{\boldsymbol{m}}_i^I$, to the final one, $\hat{\boldsymbol{m}}_i^F$, using Rodrigues' rotation formula:

$$\hat{\boldsymbol{m}}_i^v = \hat{\boldsymbol{m}}_i^I \cos w_i^v + (\hat{\boldsymbol{k}}_i \times \hat{\boldsymbol{m}}_i^I) \sin w_i^v, \tag{7.7}$$

where $\hat{\boldsymbol{m}}_i^v$ is the ith unit magnetic vector in the vth image, $\boldsymbol{M}^v = \{\hat{\boldsymbol{m}}_1^v, \ldots, \hat{\boldsymbol{m}}_N^v\}$, and $w_i^v = (v-1)\Delta w_i$ is an angle of rotation. For Q images in the chain, $\Delta w_i = w_i/(Q-1)$ where w_i is an angle between vectors $\hat{\boldsymbol{m}}_i^I$ and $\hat{\boldsymbol{m}}_i^F$. The unit vector $\hat{\boldsymbol{k}}_i$ describes the axis of rotation and is defined as $\hat{\boldsymbol{k}}_i = (\hat{\boldsymbol{m}}_i^I \times \hat{\boldsymbol{m}}_i^F)/|\hat{\boldsymbol{m}}_i^I \times \hat{\boldsymbol{m}}_i^F|$. This ansatz is very useful for finding the MEP of the nucleation or collapse of an isolated Néel skyrmion:

```
// Load from file
load(nl,initial,"skyrmion.dat");
```

```
load(nl,final,"ferromagnetic.dat");
// Initial path
ansatz_rotate(nl,nl.M,initial,final);
```

where `initial` and `final` are taken to be the skyrmion texture and the ferromagnetic background (see Fig. 7.11). However, we must resort to other definitions when dealing with more complex magnetic transitions. For MEPs involving the motion of spin textures, we can extract a window from the initial image, and choose an ansatz such that intermediate images are formed from spatial translations of the window, from the position of the texture in the initial image to its position in the final image. For example, the ansatz for skyrmion collapse at the edge of a racetrack is defined by translating the skyrmion from its center to the edge:

```
// Load from file
load(nl,initial,"skyrmion.dat");
load(nl,final,"ferromagnetic.dat");
// From center to edge of racetrack
float window[]={nl.nx/2-dx,nl.ny/2-dy,nl.nx/2+dx,nl.ny/2+dy}
float move[]={nl.nx/2,0};
ansatz_translate(nl,nl.M,initial,final,window,move);
```

while for pinning a skyrmion to a defect the ansatz involves moving the texture from a far away position to one in close proximity of the defect:

```
// Load from file
load(nl,initial,"free_skyrmion.dat");
load(nl,final,"pinned_skyrmion.dat");
// From unpinned to pinned on defect
float window[]={nl.nx/4-dx,nl.ny/4-dy,nl.nx/4+dx,nl.ny/4+dy}
float move[]={nl.nx/2,nl.ny/2};
ansatz_translate(nl,nl.M,initial,final,window,move);
```

as illustrated in Fig. 7.11. The translated windows can introduce artifacts to the path (e.g., interfaces of spins with different orientations) if they overlap or if the borders differ from the magnetic background, but the minimization procedure should smooth out such inconsistencies when approaching the MEP. However, in situations where the MEP appears susceptible to artifacts, we can instead define an ansatz with images that are taken directly from numerical simulations. This can be done by solving the LLG equations, with an applied current or field to induce a transition, or with direct minimization if the magnetic images are in the basin of attraction of the final state. For example, the ansatz for merging two skyrmions into a bi-skyrmion can be obtained by placing the skyrmions very close and then relaxing them:

```
// Load initial and final images
load(nl,nl.M,"two_close_skyrmions.dat");
load(nl,nl.M+(nl.images-1)*nl.size*3,"bi-skyrmion.dat");
// Construct the intermediate images
memcpy(tmp,nl.M,sizeof(float)*nl.size*3);
for(i=1;i<nl.images-1;i++){
  // Relax
  for(t=0;t<steps;t++){
    e=min(nl,tmp);
  }
```

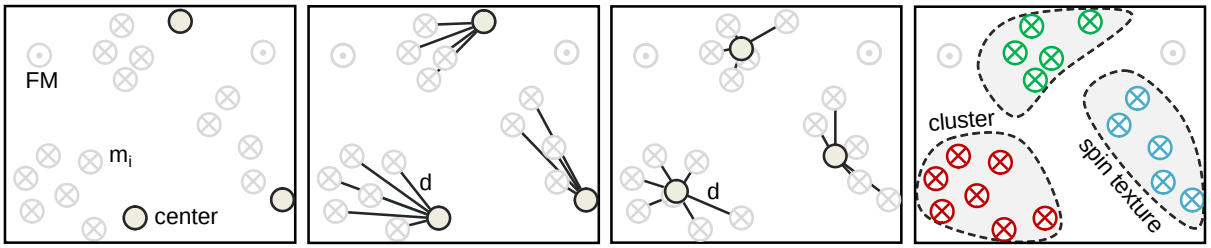

Figure 7.12 – Schematic for k-means clustering of magnetic textures. From left to right: Start with three random spins as centers by ignoring the ferromagnetic background. Assign each spin to the nearest cluster. Average the spin positions to obtain the new cluster centers. Repeat until the assignments are final, leaving with a clustering of the spin textures.

```
  memcpy(nl.M+i*nl.size*3,tmp,sizeof(float)*nl.size*3);
}
```

where the intermediate images are formed from magnetic configurations retrieved at specific points in time during the minimization. This ansatz combined with the sliding window approach allow us to study switching and interactions between higher order skyrmions in Chapter 6. Of course, one must experiment with different initial paths, e.g., by introducing noise to spin orientations, in order to fully explore all possible MEPs.

7.8 Dynamic spin clustering

When simulating the dynamics, we are often interested in properties of the spin textures, e.g. their position or size. For MEPs this is easy to obtain as we have a full microscopic description of the magnetic configurations along the path. For spin dynamics by LLG, however, storing the magnetic configurations at every time step for later processing is not possible, instead we need to collect the information dynamically. To achieve this, we develop a dynamic spin clustering approach using k-means clustering [212] to track each topological texture, e.g., single skyrmions, in the nanostructure as illustrated in Fig. 7.12. For the clustering, we consider the set of spins that are oriented in the same half-plane as the skyrmion direction, $\hat{\boldsymbol{z}}$:

$$\hat{\boldsymbol{m}}_{\text{set}} = \{\hat{\boldsymbol{m}}_i : \hat{\boldsymbol{m}}_i \cdot \hat{\boldsymbol{z}} > 0\}. \tag{7.8}$$

The number of clusters, k, is determined by visual inspection. The cluster centers are initially chosen randomly from the set of spins, $\hat{\boldsymbol{m}}_{\text{set}}$, and ensured they remain far apart to avoid having multiple clusters positioned in the same magnetic texture. We then calculate the distances from all considered spins to each cluster center, and assign each spin to the cluster with the closest center. The average of the spin positions in each cluster are calculated to obtain the k new cluster locations. These steps are repeated until cluster assignments do not change, or the maximum number of iterations is reached. The clustering is performed at each instance of the simulation, where rather than choosing the initial cluster centers randomly, we use the centers obtained from the previous time step. This ensures that the clustering remains robust against

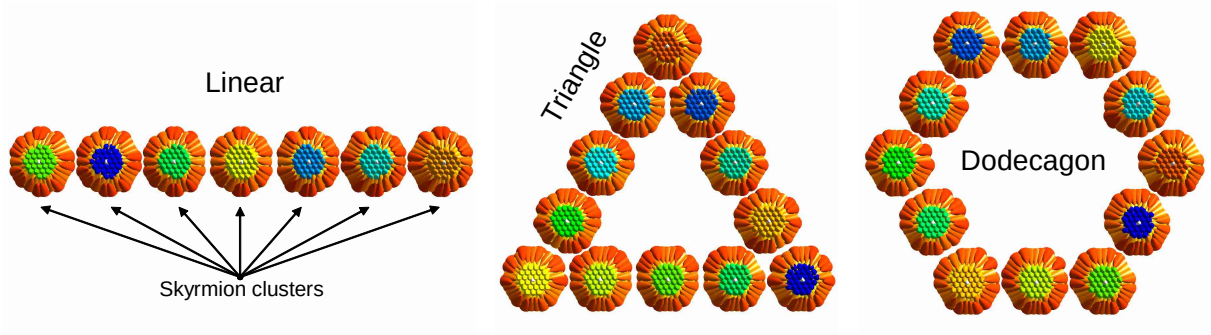

Figure 7.13 – Skyrmion clusters arranged as lines, triangles, and dodecagons in the Pd/Fe/Ir system at 10 K by solving LLG. Colors indicate distinct clusters. Spins with $\hat{\boldsymbol{m}} > 0.8$ are omitted.

magnetic moment oscillations over time, as well as provides an easy way to track specific spin textures. For example, we can use the numerical library to cluster skyrmions in different arrangements:

```
// Evolve by LLG
nl.clusters=12;
for(t=0;t<steps;t++){
  e=llg(nl,nl.M);
  clustering(nl,labels,nl.M)
}
```

as illustrated in Fig. 7.13. From the clustering information, we can obtain evolutions of properties such as positions, sizes, and topological charges of magnetic textures present in the nanostructure.

7.9 Optimizations

The computational demand of atomistic magnetic models grows linearly with the number of atomic spins, or quadratically with the area of the nanostructure. Simulations of large structures, e.g., magnetic multilayers at room temperature, will have a big impact on the computing resources needed. Therefore, we need to optimize the computational parts to be able to simulate such systems in realistic time frames. From a numerical aspect, the approach used in describing the physics plays a big role in performance. For example, simulating magnetic transitions with LLG will take orders of magnitude longer than using MEP. Similar arguments hold for finding a local magnetic solution, where distinct minimization procedures have different convergence rates, as discussed earlier. From a computational aspect, evaluation of the Hamiltonian is by far the most expensive calculation in the simulation. Finding the best numerical approach then becomes that of reducing the number of times the Hamiltonian needs to be evaluated for the chosen problem. Fig. 7.14(a) shows the total time it takes to evaluate the Hamiltonian for several cases. The breakdown of the computational time of Hamiltonian terms is illustrated in Fig. 7.14(b). The magnetic anisotropy, $\mathcal{H}_{ani}$, and applied field, $\mathcal{H}_{app}$, terms scale with the number of spins N in the nanostructure, or $O(N)$, since they are evaluated per lattice site. Exchange interactions, $\mathcal{H}_{ex}$, both

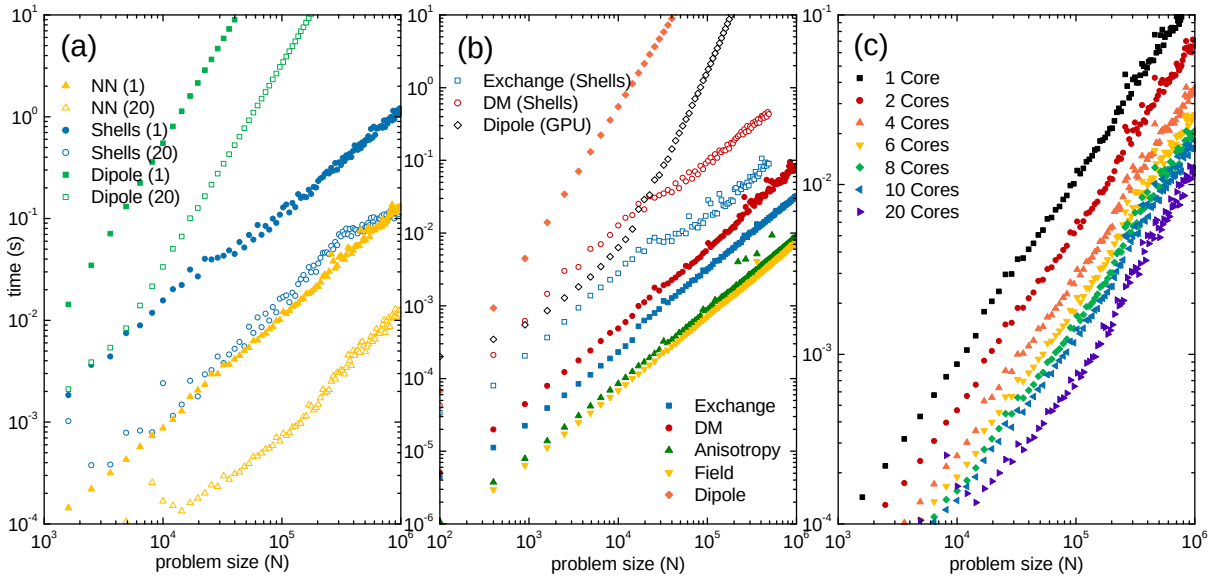

Figure 7.14 – Scaling behavior of time for computation with the number of spins, N. (a) Time it takes to evaluate the Hamiltonian with the effective nearest-neighbor exchange (NN), the 72-neighbor exchange (Shells), and including dipole-dipole interactions (Dipole), using either one (1) or twenty (20) CPU cores. (b) Times for individual terms of the Hamiltonian. (c) Times for calculation of the Hamiltonian by varying the usage of CPU cores.

of the isotropic and DM type, scale with $O(NM)$, where M is the number of neighbors being considered. Obviously, the nearest neighbor exchange considered in Pt/Co monolayers is calculated much faster than the 72-neighbor exchange (denoted shells) used for Pd/Fe/Ir layers. Lastly, dipole-dipole interactions scale quadratically with the size, $O(N^2)$, because they consider every possible pair of spins.

To speed up the simulation, we can optimize the calculations of the Hamiltonian. The common approach involves parallel processing, where computations are divided amongst virtual threads which map to physical cores on the central processing unit (CPU). Particularly, we can have each thread process the Hamiltonian terms for a unique set of spins in the lattice, and sum the obtained but partial results. The parallelism over threads is achieved using OpenMP, which is trivial to implement since all of the terms in the Hamiltonian are defined by the atomic spins. We find near linear scaling of the simulation time with the number of threads as illustrated in Fig. 7.14(c). Parallelism can be opted in the numerical library using:

```
// Define paralleism
nl.nthreads=12;
```

Dipole-dipole interactions are expensive to calculate even under the parallel approach because they scale quadratically with the problem size. An option to reduce the complexity involves truncating the neighborhood considered for each spin, however, this can introduce inaccuracies in the physics when long-range interactions are important. Instead, we evaluate the term on graphics processing units (GPUs), a massively parallel architecture consisting of thousands of smaller cores that are capable

of very fast calculations for certain problems. Much like the previous case, we partition computations of the dipole-dipole Hamiltonian amongst virtual threads, where each thread is mapped to a physical core that calculates the interactions of a single unique spin with the rest of the lattice. The difference being that we must deal with alignment of the data, memory hierarchies, thread divergence, and other architecture-specific constraints to ensure efficient utilization of the GPU. We start by copying the data (lattice sites and orientations) to the dedicated memory of the GPU, which can be time consuming. Then we issue a specific function, called a kernel, that is executed by each thread on the GPU. After all of the computation is completed, we retrieve the results from the GPU memory and sum them up to obtain the energetics. Despite our naïve GPU approach, we achieve an order of magnitude improvement in computation time over the optimized CPU approach (see Fig. 7.14(a)). We note that calculations of other terms in the Hamiltonian can benefit from a similar GPU approach.

7.10 Graphics

Being able to visualize numerical simulations is crucial for obtaining a proper understanding of the underlying phenomena. This gives us intuition on the behavior of the magnetic configuration for different geometries, materials parameters, and even numerical approaches. For instance, the magnetic field which stabilizes a skyrmion can be quickly determined by visual inspection. Similarly, a poor choice of time step for LLG or a bad initial path for MEP can be detected early in the simulation rather than observed later, or ignored completely. Therefore, instead of relying on inspection of results after the simulation, we develop a graphical tool for visualizing magnetic configurations in real-time. The graphical interface makes use of the Open Graphics Library (OpenGL) [213] for rendering magnetic configurations. We construct an orthogonal view which displays the distribution of a particular variable, e.g., components of the spin vector (see Fig. 5.3) or topological charge density (see Fig. 6.1), in two dimensions. This is useful for visualizing the evolution of certain magnetic properties over time, e.g., topological charge density of a collapsing skyrmion (see Fig. 6.8), or for simple magnetic simulations, e.g., the motion of an isolated spin texture (see Fig. 3.8). For more complex magnetic transitions, we construct a perspective view which describes the magnetic configuration in three dimensional space. The spins are characterized by cones which are oriented in the spin direction, while their positions are located along the lattice sites, as illustrated in Fig. 5.5. Such visual description is useful when describing spin orientations of complex spin textures, e.g., higher order skyrmions (see Fig. 6.3), and their interactions with other magnetic textures, e.g., collision of a skyrmion with an anti-skyrmion (see Fig. 6.7).

7.11 Computer programs

The problems in this thesis are diverse and hard to describe using a single code. Therefore, we used the library to construct separate computer programs for simulating different physics. In this section we describe how one could simulate some of these problems.

7.11.1 Obtain a single skyrmion

We start with an example code for relaxing a single Néel skyrmion on the Pt/Co system:

```
#include <stdlib.h>
#include <numerical_library.h>
void main(){
  NL_TYPE nl;
  float pos[3],dir[3],r;
  int i;
  // Lattice
  nl.nx=100; nl.ny=100; nl.nz=1;
  // Material (Pt/Co)
  fill(nl,"PtCo");
  // Create the model
  model(nl);
  // Ansatz for Neel skyrmion
  pos[0]=nl.nx/2; pos[1]=nl.ny/2; pos[2]=0;
  dir[0]=0; dir[1]=0; dir[2]=-1; r=10;
  ansatz_skyrmion(nl,nl.M,pos,r,dir);
  // Relax the magnetic texture
  nl.dt=1; nl.method=QM;
  for(i=0;i<1e5;i++){
    min(nl,nl.M);
  }
  save(nl,nl.M,"neel_skyrmion.dat");
}
```

The program first populates the `nl` structure with the `fill` routine and creates the model. Then it takes the ansatz for an isolated skyrmion and relaxes the magnetic texture. Once the skyrmion is stable, we can save the configuration for future simulations of the same nanostructure. This forms the basis for most of our calculations. One can easily include a sweep over the field by adding the code below:

```
// Sweep over field
for(h=0;h<1;h+=0.1){
  // Set applied field
  nl.H[2]=-h;
  // Get FM background
  ansatz_fm(nl,nl.M);
  for(i=0;i<1e3;i++){
    efm=min(nl,nl.M);
  }
  // Get Neel skyrmion
  load(nl,nl.M,"neel_skyrmion.dat");
  for(i=0;i<1e5;i++){
    esk=min(nl,nl.M);
  }
  // Print the skyrmion energy
  printf("%f\t%e\n",h,esk-efm);
}
```

where we first obtain the FM state, then the skyrmion state, and output their energy difference to the console, for every field value. Similar sweeps can be made for the other material parameters.

7.11.2 Collapse of a single skyrmion

Next, we consider an example code for the collapse mechanism of a single Néel skyrmion into the FM background:

```
#include <stdlib.h>
#include <numerical_library.h>
void main(){
  NL_TYPE nl;
  int i;
  nl.images=20;
  // Lattice
  nl.nx=100; nl.ny=100; nl.nz=1;
  // Material (Pt/Co)
  fill(nl,"PtCo");
  // Create the model
  model(nl);
  // Load from file
  load(nl,initial,"neel_skyrmion.dat");
  load(nl,final,"ferromagnetic.dat");
  // Initial path
  ansatz_rotate(nl,nl.M,initial,final);
  // MEP
  nl.dt=1; nl.k=0.1; nl.method=QM;
  for(i=0;i<1e5;i++){
    mep(nl,nl.M);
  }
}
```

Once the model has been created, the program loads the skyrmion and FM states and creates an initial path by interpolating between the two. The `mep` routine is then used to perform minimum energy path calculations. We can then add the following code to find the energy barrier from the saddle point:

```
// Find the saddle point
for(i=0;i<nl.images;i++){
  e=energetics(nl,nl.M[i*n.size*3]);
  emax=(e>emax)?e:emax;
  printf("%d\t%e\n",i,e);
}
// Print the energy barrier
esk=energetics(nl,nl.initial);
printf("Energy Barrier = %e\n",emax-esk);
```

7.11.3 Escape of racetrack skyrmion at boundary

Such computer programs allow us to study transitions between different magnetic states, which are crucial for this thesis. For example, to simulate the skyrmion racetrack we can use an example code as follows:

```
#include <stdlib.h>
#include <numerical_library.h>
void main(){
  NL_TYPE nl;
  float *initial,*final,window[4],move[2],dx=10,dy=10;
```

```
  int i,j;
  nl.images=20;
  // Lattice
  nl.nx=100; nl.ny=100; nl.nz=1;
  // Boundary conditions
  nl.pbcx=0; nl.pbcy=1;
  // Material (Pt/Co/Ir)
  fill(nl,"PtCoIr");
  // Create the model racetrack
  model(nl);
  // Get FM background
  final=malloc(nl.size*3,sizeof(float));
  ansatz_fm(nl,final);
  for(i=0;i<1e3;i++){
    min(nl,final);
  }
  // Get Neel skyrmion
  initial=malloc(nl.size*3,sizeof(float));
  load(nl,initial,"neel_skyrmion.dat");
  for(i=0;i<1e5;i++){
    min(nl,initial);
  }
  // From center to edge of racetrack
  window[0]=nl.nx/2-dx; window[1]=nl.ny/2-dy;
  window[2]=nl.nx/2+dx; window[3]=nl.ny/2+dy;
  move[0]=nl.nx/2; move[1]=0;
  ansatz_translate(nl,nl.M,initial,final,window,move);
  // MEP
  nl.dt=1; nl.k=0.1; nl.method=QM;
  for(i=0;i<1e5;i++){
    mep(nl,nl.M);
  }
  free(initial); free(final);
}
```

The program creates a racetrack by using periodic boundary conditions in the vertical dimension and open boundaries in the horizontal one. One could similarly extend the lattice along the vertical dimension. Then we obtain the skyrmion and FM states, construct a path ansatz by horizontal translation of a window of the skyrmion to the racetrack edge, and calculate the MEP. The energy barrier for escape through the edge is obtained from the energy difference of the saddle point and the skyrmion. One can also simulate the enhanced skyrmion racetrack proposed in Chapter 3 by introducing an interface of lower or zero DMI along the open boundaries:

```
// Create interface of zero DMI
for(j=0;j<nl.ny;j++)
for(i=0;i<nl.nx;i++){
  nl.Dmap[i+nl.nx*j]=((i<nl.nx/4)||(i>nl.nx-nl.nx/4))?0:nl.D[0];
}
```

which should significantly increase the energy barrier for skyrmion escape, and hence improve stability of an isolated skyrmion on the racetrack.

7.11.4 Pinning on a material defect

Next, we consider an example code for pinning the skyrmion on a material defect:

```
#include <stdlib.h>
#include <numerical_library.h>
void main(){
  NL_TYPE nl;
  float pos[3],dir[3],window[4],move[2];
  float *initial,*final,dx=10,dy=10,ax,ay,r;
  int i,j;
  nl.images=20;
  // Lattice
  nl.nx=100; nl.ny=100; nl.nz=1;
  // Material (Pt/Co)
  fill(nl,"PtCo");
  // Create the model
  model(nl);
  // Create circular defect
  ax=3*nl.nx/4; ay=3*nl.ny/4;
  for(j=0;j<nl.ny;j++)
  for(i=0;i<nl.nx;i++){
    r=(i-ax)*(i-ax)+(j-ay)*(j-ay);
    nl.Kmap[i+nx*j]=(r<nl.nx*nl.nx/32)?nl.K[0]:nl.K[0]/2;
  }
  // Get pinned skyrmion
  final=malloc(nl.size*3,sizeof(float));
  pos[0]=ax; pos[1]=ay; pos[2]=0;
  dir[0]=0; dir[1]=0; dir[2]=-1; r=10;
  ansatz_skyrmion(nl,final,pos,r,dir);
  for(i=0;i<1e5;i++){
    min(nl,final);
  }
  // Get unpinned skyrmion
  initial=malloc(nl.size*3,sizeof(float));
  load(nl,initial,"neel_skyrmion.dat");
  for(i=0;i<1e5;i++){
    min(nl,initial);
  }
  // From center to defect
  window[0]=nl.nx/2-dx; window[1]=nl.ny/2-dy;
  window[2]=nl.nx/2+dx; window[3]=nl.ny/2+dy;
  move[0]=nl.nx/4; move[1]=nl.ny/4;
  ansatz_translate(nl,nl.M,initial,final,window,move);
  // MEP
  nl.dt=1; nl.k=0.1; nl.method=QM;
  for(i=0;i<1e5;i++){
    mep(nl,nl.M);
  }
  free(initial); free(final);
}
```

The program prepares a circular anisotropic defect and relaxes a skyrmion on top. The path ansatz is constructed by moving a window enclosing the skyrmion from the center to the defect. Once the MEP is obtained, the energy barrier from the saddle point to the pinned state gives the activation energy for unpinning the skyrmion. We

can perform a sweep on the anisotropy, or take different material defects such as the exchange coupling:

```
// Create exchange defect
nl.defect_op=AVG;
ax=3*nl.nx/4; ay=3*nl.ny/4;
for(j=0;j<nl.ny;j++)
for(i=0;i<nl.nx;i++){
  nl.Jmap[i+nx*j]=((i<ax-dx)||(i>ax+dx)||(j<ay-dy)||(j>ay+dy))?nl.J[0]:nl.J[0]/2;
}
```

where the defect is squared and we take the average operation between coupling coefficients.

7.11.5 Spin dynamics of skyrmion clusters

Lastly, we consider an example code for simulating the spin dynamics of skyrmion clusters:

```
#include <stdlib.h>
#include <numerical_library.h>
void main(){
  NL_TYPE nl;
  float *labels,*centers,pos[3],dir[3];
  int i,k,steps=1e7;
  // Lattice
  nl.nx=100; nl.ny=100; nl.nz=1;
  // Material (Pd/Fe/Ir)
  fill(nl,"PtFeIr-shells");
  // Create the model
  model(nl);
  // Create the FM background
  ansatz_fm(nl,nl.M);
  // Create clusters of skyrmions
  nl.clusters=5; nl.ansatz_crop=1;
  for(k=0;k<nl.clusters;k++){
    pos[0]=nl.nx*rand(); pos[1]=nl.ny*rand(); pos[2]=0;
    dir[0]=0; dir[1]=0; dir[2]=-1; r=10;
    ansatz_skyrmion(nl,nl.M,pos,r,dir);
  }
  // Relax
  for(i=0;i<1e5;i++){
    min(nl,nl.M);
  }
  // Evolve by spin dynamics
  nl.alpha=1; nl.dt=1e-14; nl.T=20;
  labels=malloc(sizeof(float)*nl.size*nl.clusters);
  centers=malloc(sizeof(float)*nl.clusters*steps);
  for(i=0;i<steps;i++){
    llg(nl,nl.M);
    // Find clusters
    clustering(nl,labels,nl.M);
    center(nl,centers+i*nl.clusters,labels,nl.M);
    printf("\n%d",i);
    for(k=0;k<nl.clusters;k++){
```

```
      print("\t%f",centers[k+i*nl.clusters]);
    }
  }
  free(labels);free(centers);
}
```

The program creates clusters of skyrmions that are randomly distributed on the lattice. The spin dynamics is then obtained at finite temperature by evolving the LLG equations. For each time step, the dynamic spin clustering locates the individual clusters, and the cluster labels are used to determine their positions on the lattice. One can also use the cluster labels to extract other properties such as the size and topological number:

```
// Extract information about clusters
for(i=0;i<steps;i++){
  llg(nl,nl.M);
  clustering(nl,labels,nl.M);
  size(nl,sizes+i*nl.clusters,labels,nl.M);
  topology(nl,qs+i*nl.clusters,labels,nl.M);
}
```

Since the Pd/Fe/Ir system with neighborhood shells is used, which gives rise to exchange frustration, we can form clusters of different magnetic textures (e.g., anti-skyrmions) by changing the anstaz.

8 SUMMARY AND OUTLOOK

8.1 Summary

The discovery of skyrmions in magnetic materials has made them promising candidates for future consumer nanoelectronics. Recent advances in the field have provided all of the basic functions needed for storing and processing information. We can now stabilize small individual skyrmions at room temperature in multilayers. The current-induced motion of skyrmions can be controlled, and schemes for their controlled creation and detection have been proposed. However, some pending questions still need to be addressed before the realization of skyrmions in devices. For example, the size of skyrmions at room temperature needs to be reduced for applications (probably in the 10 nm range). A proper understanding of the role of defects and of the influence of inhomogeneities in the material is also needed for better control of the motion of skyrmions. In this thesis, we theoretically investigated the influence of different materials, geometric confinements, inhomogeneities, and interactions with other spin textures on the stability of isolated nanoscale skyrmions. We also explored ways of improving their stability and controlling their motion or size for use in practical devices.

These phenomena were investigated using atomistic models of magnetism, basically an extended Heisenberg spin model, where the parameters can be obtained from experiments or ab initio calculations. The multi-scale model was described in Chapter 2, together with important properties of skyrmions that emerge as a consequence of their magnetic structure. Minimum energy paths were extensively used in this thesis to describe magnetic transitions involving skyrmions, e.g., collapse to the ferromagnetic background, pinning on a defect, or interaction with other realizable spin textures. The LLG equations and Monte Carlo were also employed to simulate spin dynamics and search for stable magnetic configurations, respectively. In order to aid the numerical work, a numerical library was developed and is discussed in Chapter 7.

The results of our work were presented in Chapters 3 to 6. In Chapter 3 we studied the stability of isolated skyrmions in ultrathin ferromagnetic films with interfacially induced DMI - specifically three monolayers of Co on Pt, with or without a capping spin-orbit layer (MgO, Ir, Pt, or similar). We showed that such conditions give rise to more realistic but less stable skyrmion states than previously thought. Three possible mechanisms for skyrmion collapse in these realistic systems were discussed: isotropic rotation of the spins, collapse at the boundary of a laterally finite film, and collapse at the lateral interface where DMI changes. We found that the stability of skyrmions smaller than few nm is limited by the isotropic collapse, whereas larger ones are more likely to collapse at the boundary. The confined geometry in finite systems causes poor thermal stability and shorter lifetimes of the skyrmion, which severely limits their applicability at room temperature. We proposed a solution where the boundary was replaced by an interface with lower DMI, by e.g. having an extended Co film on Pt, but finite capping layer of MgO on top. This drastically increased the barrier for

skyrmion collapse at the DMI interface compared to the open boundary case. As a result, the lifetime of isolated skyrmions at room temperatures extended from few nanoseconds to few seconds, making skyrmions much more favorable for future data processing devices.

Chapter 4 reported fundamental properties of chiral ferromagnetic systems related to pinning of isolated skyrmions, taking Co monolayer on Pt as an exemplary system. Our results yield a more complete understanding of how magnetic skyrmions pin to defects. We found that pinning can occur at the skyrmion center, domain wall, or in-between the two, depending on the type of defect being used and the ratio of skyrmion to defect size. The effective pinning potentials have complex functional forms that cannot be described by parabolic shapes. Surprisingly, skyrmion collapse is strongly facilitated by the presence of atomic scale vacancies, which indicates a much weaker stability of skyrmions than previously anticipated. We proposed a solution to improve skyrmion stability by increasing the DMI (e.g. by a heavy-metal capping layer) in the vicinity of vacancies or holes in the magnetic material. The interaction of skyrmion with defects leads to a "breathing" behavior of the spin texture on its path to the pinning site, where prepattered ring-like defects can be broadly used to control the size of the skyrmion. Asymmetric and linearly extended defects were also discussed, further enabling our findings in the design of next-generation spintronic devices based on interaction with polarized light, tunable magnonic crystals, skyrmion ratchet systems, and racetrack memories.

Chapter 5 examined magnetic transitions dictating skyrmion stability in Pd/Fe/Ir systems. Rather than considering ferromagnetic backgrounds, the work yields understanding of how magnetic skyrmions transition to other non-trivial spin configurations. Our experiments reveal a different and often dominant transition mechanism between skyrmion lattice and spin cycloid states, characterized by formation of a 2D Bloch-like point at the saddle point of the transition, where domain walls of the skyrmions interconnect and recombine into parallel walls of the cycloid state, while the topological charge disappears due negative contributions to the charge density that emerge. Similar topological knot was characterized also in a Fe bilayer, epitaxially sandwiched between Ir and Rh/Pd layers (another system readily studied in literature), to capture some of the symmetry-breaking phenomena bound to arise with increasing thickness of the film. We also reported the effective energy landscapes of these competing mechanisms, as a function of magnetic field and other relevant parameters. Particularly, the activation energy for skyrmion collapse has an inverse relation on material parameters for transitions into spin cycloid and ferromagnetic orderings, resulting in a lower effective stability of a skyrmion lattice when all possible alternative spin configurations are considered. Although these conclusions based on the Pd/Fe/Ir system seem detrimental for applicability of skyrmions in devices based on ultrathin magnetic films, they do open a perspective on further fundamental studies of rich possible transitions between various possible skyrmionic and collinear states in e.g. antiferromagnetic films with chirality present as well as heterochiral systems.

In Chapter 6 we theoretically discovered the underlying switching mechanisms and interactions between skyrmions with distinct topological numbers. We found that skyrmions with higher topological charges are more likely to transition into

other topologies, either by absorbing or expelling a unit charge. While same charged skyrmions prefer switching to higher topologies, oppositely charged textures transition easier to lower ones. Our results on the thermodynamic stability (or energy barriers) of higher order skyrmions for various magnetic fields could provide valuable insight in future experimental studies. We also have found that skyrmions of different topological charges may be arranged into clusters because of the attractive interactions that arise in frustrated magnets. The topological charge switching behavior and the formation of distinct topological clusters may prove useful in potential applications.

In Chapter 7 we presented a numerical library to model the physics described in this thesis. This chapter represents a culmination of the computational effort made in each of the previous chapters. We focused on important numerical aspects for conducting simulations of magnetic skyrmions, and presented a set of examples on how one could simulate some of the discussed problems.

8.2 Outlook

Given the theoretical results of this thesis, there are several opportunities for future work, some of which are discussed below:

In Chapter 3 we examined the effects of monolayer-resolved DMI on the stability of isolated nanoscale skyrmions. It would be interesting to extend this consideration to variations in other material parameters within the magnetic layer. This would provide a more realistic atomistic model that can be later used for preparations of experiments. While the DMI interface was proposed to improve skyrmion stability in a racetrack, a full sweep of the DMI parameters was outside the scope of the work. Therefore, a theoretical investigation of skyrmion behavior as it crosses different interfaces (e.g., induced by variations in isotropic exchange and DM interactions, or magnetic anisotropy), could reveal more opportunities for stabilizing skyrmions in racetrack memories.

In Chapter 4 we investigated the pinning of magnetic skyrmions to defects. We observed that skyrmion collapse is strongly facilitated by the presence of atomic scale vacancies, using numerical simulations that took into account only nearest and next-nearest neighbor exchange interactions. However, farther interactions and exchange frustration could improve skyrmion stability. Future research should first analyze the effects of atomic vacancies around defects for neighbor-resolved exchange interactions retrieved from ab initio calculations, before moving on to experimental studies.

Chapter 5 considered transitions of magnetic skyrmions to other non-trivial spin configurations. The focus was on transition mechanisms between skyrmion lattices and spin cycloids. However, the analyzed scenario is reminiscent of the formation of magnetic skyrmion bubbles from a geometrical constriction (see Ref. [66]). Therefore, one could extend this work by searching for a similar blowing of magnetic skyrmions from geometrical constrictions on the nanoscale, and thus provide a possible scheme for creating skyrmions in nanoelectronics.

The topological spin textures investigated in Chapter 6 open a broad set of opportunities for theoretical research. Skyrmions of higher topological orders can be used to create more sophisticated ways to store and process information involving multi-

ple states, which correspond to their distinct topological numbers. While we analyzed their stability in ferromagnetic backgrounds, one can study the effects of open boundaries in racetrack memories on the lifetime of higher order skyrmions. Similarly, new work can be done in regards to pinning on material inhomogeneities in Chapter 4. The formation of clusters due to attractive interactions also brings opportunities for novel research into possible spintronic devices.

From the numerical standpoint, software for atomistic simulations of magnetism remains nearly non-existent. While a few libraries and packages can indeed be found on the internet, e.g., ASE [214] and FIDIMAG [215], they are by no means complete, much less for simulations of complex magnetic textures such as skyrmions. The ease of implementation, since the problem is classical (mostly) and discrete, has resulted in research groups developing their own custom software for internal use, which is never validated by the community. This is in sharp contrast to micromagnetics, where the apparent large demand has lead to the fruition of well-known frameworks, e.g., MuMax [216], OMNeS [217], and OOMMF [218], that are being constantly developed and verified by the users. However, the rapid interest in skyrmions, along with their promising applications, brings the necessity of practical and reliable ways to conduct their numerical simulations for a wide range of problems. Therefore, an important contribution to the area would be the development of an atomistic framework that can be eventually adopted as a standard by the community. One promising candidate is Spirit [219], which provides a framework for numerical optimizations and dynamics simulations of atomistic spin systems including skyrmions. Another potential option is the numerical library developed in this thesis, though the focus has been more on disseminating the numerical approaches for simulations of magnetic skyrmions.

REFERENCES

1 MOORE, G. E. Cramming more components onto integrated circuits. *Electronics*, v. 38, p. 114–117, 1965.

2 WALDROP, M. M. More than Moore. *Nature*, v. 530, p. 144–147, 2016.

3 SCHALLER, R. R. Moore's law: past, present and future. *IEEE Spectrum*, v. 34, n. 6, p. 52–59, 1997.

4 LUNDSTROM, M. Moore's law forever? *Science*, v. 299, n. 5604, p. 210–211, 2003.

5 MEDICUS, H. A. Fifty years of matter waves. *Physics Today*, v. 27, n. 2, p. 38–45, 1974.

6 TIWARI, S. Implications of scales in processing of information. *Proceedings of the IEEE*, v. 103, n. 8, p. 1250–1273, 2015.

7 SHALF, J. M.; LELAND, R. Computing beyond Moore's law. *Computer*, v. 48, n. 12, p. 14–23, 2015.

8 FEYNMAN, R. P. Simulating physics with computers. *International Journal of Theoretical Physics*, v. 21, n. 6, p. 467–488, 1982.

9 GIBNEY, E. Physics: Quantum computer quest. *Nature*, v. 512, p. 24–26, 2014.

10 MEAD, C. Neuromorphic electronic systems. *Proceedings of the IEEE*, v. 78, n. 10, p. 1629–1636, 1990.

11 MAHOWALD, M.; DOUGLAS, R. A sillicon neuron. *Nature*, v. 354, p. 515–518, 1991.

12 LUGT, A. V. Coherent optical processing. *Proceedings of the IEEE*, v. 62, n. 10, p. 1300–1319, 1974.

13 NOVOSELOV, K. S.; GEIM, A. K.; MOROZOV, S. V.; JIANG, D.; ZHANG, Y.; DUBONOS, S. V.; GRIGORIEVA, I. V.; FIRSOV, A. A. Electric field effect in atomically thin carbon films. *Science*, v. 306, n. 5696, p. 666–669, 2004.

14 GIBNEY, E. The super materials that could trump graphene. *Nature*, v. 522, p. 274–276, 2015.

15 HUSH, N. S. An overview of the first half-century of molecular electronics. *Annals of the New York Academy of Sciences*, v. 1006, n. 1, p. 1–20, 2003.

16 CHUA, L. Memristor - The missing circuit element. *IEEE Transactions on Circuit Theory*, v. 18, n. 5, p. 507–519, 1971.

17 AWSCHALOM, D. D.; FLATTÉ, M. E. Challenges for semiconductor spintronics. *Nature Physics*, v. 3, p. 153–159, 2007.

18 KANG, W.; HUANG, Y.; ZHANG, X.; ZHOU, Y.; ZHAO, W. Skyrmion-electronics: An overview and outlook. *Proceedings of the IEEE*, v. 104, n. 10, p. 2040–2061, 2016.

19 HEISENBERG, W. *Einführung in die einheitliche Feldtheorie der Elementarteilchen*. Stuttgart: Hirzel, 1967.

20 SKYRME, T. H. R. A non-linear field theory. *Proceedings of the Royal Society of London A: Mathematical, Physical and Engineering Sciences*, v. 260, n. 1300, p. 127–138, 1961.

21 SONDHI, S. L.; KARLHEDE, A.; KIVELSON, S. A.; REZAYI, E. H. Skyrmions and the crossover from the integer to fractional quantum Hall effect at small zeeman energies. *Phys. Rev. B*, v. 47, p. 16419–16426, 1993.

22 LEONOV, A. O.; DRAGUNOV, I. E.; RÖSSLER, U. K.; BOGDANOV, A. N. Theory of skyrmion states in liquid crystals. *Phys. Rev. E*, v. 90, p. 042502, 2014.

23 KHAWAJA, U. A.; STOOF, H. Skyrmions in a ferromagnetic Bose-Einstein condensate. *Nature*, v. 411, p. 918–920, 2001.

24 RÖSSLER, U. K.; BOGDANOV, A. N.; PFLEIDERER, C. Spontaneous skyrmion ground states in magnetic metals. *Nature*, v. 442, p. 797–801, 2006.

25 OU-YANG, T. Y.; SHU, G. J.; LIN, J.-Y.; HU, C. D.; CHOU, F. C. Mn vacancy defects, grain boundaries, and A-phase stability of helimagnet MnSi. *Journal of Physics: Condensed Matter*, v. 28, n. 2, p. 026004, 2016.

26 MÜHLBAUER, S.; BINZ, B.; JONIETZ, F.; PFLEIDERER, C.; ROSCH, A.; NEUBAUER, A.; GEORGII, R.; BÖNI, P. Skyrmion lattice in a chiral magnet. *Science*, v. 323, n. 5916, p. 915–919, 2009.

27 BOGDANOV, A. N.; YABLONSKII, D. Thermodynamically stable 'vortices' in magnetically ordered crystals. The mixed state of magnets. *J. Exp. Theor. Phys.*, v. 95, p. 178, 1989.

28 BOGDANOV, A.; HUBERT, A. Thermodynamically stable magnetic vortex states in magnetic crystals. *Journal of Magnetism and Magnetic Materials*, v. 138, n. 3, p. 255–269, 1994.

29 BOGDANOV, A. New localized solutions of the nonlinear field-equations. *JETP Lett.*, v. 62, p. 247–251, 1995.

30 BOGDANOV, A.; HUBERT, A. The stability of vortex-like structures in uniaxial ferromagnets. *Journal of Magnetism and Magnetic Materials*, v. 195, n. 1, p. 182–192, 1999.

31 NEUBAUER, A.; PFLEIDERER, C.; BINZ, B.; ROSCH, A.; RITZ, R.; NIKLOWITZ, P. G.; BÖNI, P. Topological Hall effect in the *a* phase of MnSi. *Phys. Rev. Lett.*, v. 102, p. 186602, 2009.

32 PAPPAS, C.; LELIÈVRE-BERNA, E.; FALUS, P.; BENTLEY, P. M.; MOSKVIN, E.; GRIGORIEV, S.; FOUQUET, P.; FARAGO, B. Chiral paramagnetic skyrmion-like phase in MnSi. *Phys. Rev. Lett.*, v. 102, p. 197202, 2009.

33 DZYALOSHINSKY, I. A thermodynamic theory of "weak" ferromagnetism of antiferromagnetics. *Journal of Physics and Chemistry of Solids*, v. 4, n. 4, p. 241–255, 1958.

34 MORIYA, T. Anisotropic superexchange interaction and weak ferromagnetism. *Phys. Rev.*, v. 120, p. 91–98, 1960.

35 NAGAOSA, N.; TOKURA, Y. Topological properties and dynamics of magnetic skyrmions. *Nature Nanotech.*, v. 8, p. 899–911, 2013.

36 YU, X. Z.; ONOSE, Y.; KANAZAWA, N.; PARK, J. H.; HAN, J. H.; MATSUI, Y.; NAGAOSA, N.; TOKURA, Y. Real-space observation of a two-dimensional skyrmion crystal. *Nature*, v. 465, p. 901–904, 2010.

37 YU, X. Z.; KANAZAWA, N.; ONOSE, Y.; KIMOTO, K.; ZHANG, W. Z.; ISHIWATA, S.; MATSUI, Y.; TOKURA, Y. Near room-temperature formation of a skyrmion crystal in thin-films of the helimagnet FeGe. *Nat. Mater.*, v. 10, p. 106–109, 2011.

38 HUANG, S. X.; CHIEN, C. L. Extended skyrmion phase in epitaxial FeGe(111) thin films. *Phys. Rev. Lett.*, v. 108, p. 267201, 2012.

39 SHIBATA, K.; YU, X. Z.; HARA, T.; MORIKAWA, D.; KANAZAWA, N.; KIMOTO, K.; ISHIWATA, S.; MATSUI, Y.; TOKURA, Y. Towards control of the size and helicity of skyrmions in helimagnetic alloys by spin–orbit coupling. *Nature Nanotech.*, v. 8, p. 723–728, 2013.

40 IWASAKI, J.; MOCHIZUKI, M.; NAGAOSA, N. Universal current-velocity relation of skyrmion motion in chiral magnets. *Nature Communications*, v. 4, n. 1463, 2013.

41 KARUBE, K.; WHITE, J. S.; REYNOLDS, N.; GAVILANO, J. L.; OIKE, H.; KIKKAWA, A.; KAGAWA, F.; TOKUNAGA, Y.; RONNOW, H. M.; TOKURA, Y.; TAGUCHI, Y. Robust metastable skyrmions and their triangular-square lattice structural transition in a high-temperature chiral magnet. *Nat. Mater.*, v. 15, p. 1237–1242, 2016.

42 TOKUNAGA, Y.; YU, X. Z.; WHITE, J. S.; RONNOW, H. M.; MORIKAWA, D.; TAGUCHI, Y.; TOKURA, Y. A new class of chiral materials hosting magnetic skyrmions beyond room temperature. *Nat. Comm.*, v. 6, p. 7638, 2015.

43 OIKE, H.; KIKKAWA, A.; KANAZAWA, N.; TAGUCHI, Y.; KAWASAKI, M.; TOKURA, Y.; KAGAWA, F. Interplay between topological and thermodynamic stability in a metastable magnetic skyrmion lattice. *Nature Physics*, v. 12, p. 62–66, 2015.

44 FERT, A.; REYREN, N.; CROS, V. Magnetic skyrmions: advances in physics and potential applications. *Nat. Rev. Mater.*, v. 2, p. 17031, 2017.

45 WIESENDANGER, R. Nanoscale magnetic skyrmions in metallic films and multilayers: a new twist for spintronics. *Nat. Mater.*, n. 16044, 2016.

46 ROMMING, N.; KUBETZKA, A.; HANNEKEN, C.; BERGMANN, K. von; WIESENDANGER, R. Field-dependent size and shape of single magnetic skyrmions. *Phys. Rev. Lett.*, v. 114, p. 177203, 2015.

47 HEINZE, S.; BERGMANN, K. von; MENZEL, M.; BREDE, J.; KUBETZKA, A.; WIESENDANGER, R.; BIHLMAYER, G.; BLÜGEL, S. Spontaneous atomic-scale magnetic skyrmion lattice in two dimensions. *Nature Physics*, v. 7, p. 713–718, 2011.

48 ROMMING, N.; HANNEKEN, C.; MENZEL, M.; BICKEL, J. E.; WOLTER, B.; BERGMANN, K. von; KUBETZKA, A.; WIESENDANGER, R. Writing and deleting single magnetic skyrmions. *Science*, v. 341, n. 6146, p. 636–639, 2013.

49 MOREAU-LUCHAIRE, C.; MOUTAFIS, C.; REYREN, N.; SAMPAIO, J.; VAZ, C. A. F.; HORNE, N. V.; BOUZEHOUANE, K.; GARCIA K. DERANLOT, C.; WARNICKE, P.; WOHLHüTER, P.; GEORGE, J.-M.; WEIGAND, M.; RAABE, J.; CROS, V.; FERT, A. Additive interfacial chiral interaction in multilayers for stabilization of small individual skyrmions at room temperature. *Nat. Nanotech.*, v. 11, p. 444–448, 2016.

50 BOULLE, O.; VOGEL, J.; YANG, H.; PIZZINI, S.; CHAVES, D. S. de S.; LOCATELLI, A.; MENTES, T. O.; SALA, A.; BUDA-PREJBEANU, L. D.; KLEIN, O.; BELMEGUENAI, M.; ROUSSIGNÉ, Y.; STASHKEVICH, Y. A.; CHÉRIF, S. M.; ABALLE, L.; FOERSTER, M.; CHSHIEV, M.; AUFFRET, S.; MIRON, I. M.; GAUDIN, G. Room-temperature chiral magnetic skyrmions in ultrathin magnetic nanostructures. *Nat. Nanotech.*, v. 11, p. 449–454, 2016.

51 WOO, S.; LITZIUS, K.; KRÜGER, B.; IM, M.-Y.; CARETTA, L.; RICHTER, K.; MANN, M.; KRONE, A.; REEVE, R. M.; WEIGAND, M.; AGRAWAL, P.; LEMESH, I.; MAWASS, M.-A.; FISCHER, P.; KLÄUI, M.; BEACH, G. S. D. Observation of room-temperature magnetic skyrmions and their current-driven dynamics in ultrathin metallic ferromagnets. *Nat. Mater.*, v. 15, p. 501–506, 2016.

52 OKUBO, T.; CHUNG, S.; KAWAMURA, H. Multiple-q states and the skyrmion lattice of the triangular-lattice Heisenberg antiferromagnet under magnetic fields. *Phys. Rev. Lett.*, v. 108, p. 017206, 2012.

53 LEONOV, A. O.; MOSTOVOY, M. Multiply periodic states and isolated skyrmions in an anisotropic frustrated magnet. *Nat. Comm.*, v. 6, p. 8275, 2015.

54 OZAWA, R.; HAYAMI, S.; MOTOME, Y. Zero-field skyrmions with a high topological number in itinerant magnets. *Phys. Rev. Lett.*, v. 118, p. 147205, 2017.

55 STIER, M.; HÄUSLER, W.; POSSKE, T.; GURSKI, G.; THORWART, M. Skyrmion-anti-skyrmion pair creation by in-plane currents. *Phys. Rev. Lett.*, v. 118, p. 267203, 2017.

56 ZHANG, X.; XIA, J.; ZHOU, Y.; LIU, X.; ZHANG, H.; EZAWA, M. Skyrmion dynamics in a frustrated ferromagnetic film and current-induced helicity locking-unlocking transition. *Nat. Comm.*, v. 8, p. 1717, 2017.

57 LIN, S.-Z.; HAYAMI, S. Ginzburg-Landau theory for skyrmions in inversion-symmetric magnets with competing interactions. *Phys. Rev. B*, v. 93, p. 064430, 2016.

58 RÓZSA, L.; PALOTÁS, K.; DEÁK, A.; SIMON, E.; YANES, R.; UDVARDI, L.; SZUNYOGH, L.; NOWAK, U. Formation and stability of metastable skyrmionic spin structures with various topologies in an ultrathin film. *Phys. Rev. B*, v. 95, p. 094423, 2017.

59 JONIETZ, F.; MÜHLBAUER, S.; PFLEIDERER, C.; NEUBAUER, A.; MÜNZER, W.; BAUER, A.; ADAMS, T.; GEORGII, R.; BÖNI, P.; DUINE, R. A.; EVERSCHOR, K.; GARST, M.; ROSCH, A. Spin transfer torques in MnSi at ultralow current densities. *Science*, v. 330, n. 6011, p. 1648–1651, 2010.

60 FERT, A.; CROS, V.; SAMPAIO, J. Skyrmions on the track. *Nature Nanotech.*, v. 8, p. 152–156, 2013.

61 HANNEKEN, C.; OTTE, F.; KUBETZKA, A.; DUPÉ, B.; ROMMING, N.; BERGMANN, K. von; WIESENDANGER, R.; HEINZE, S. Electrical detection of magnetic skyrmions by tunneling non-collinear magnetoresistance. *Nature Nanotech.*, v. 10, p. 1039–1042, 2015.

62 HAMAMOTO, K.; EZAWA, M.; NAGAOSA, N. Purely electrical detection of a skyrmion in constricted geometry. *Applied Physics Letters*, v. 108, n. 11, p. 112401, 2016.

63 NAGAOSA, N.; SINOVA, J.; ONODA, S.; MACDONALD, A. H.; ONG, N. P. Anomalous Hall effect. *Rev. Mod. Phys.*, v. 82, p. 1539–1592, 2010.

64 IWASAKI, J.; MOCHIZUKI, M.; NAGAOSA, N. Current-induced skyrmion dynamics in constricted geometries. *Nature Nanotech.*, v. 8, p. 742–747, 2013.

65 SAMPAIO, J.; CROS, V.; ROHART, S.; THIAVILLE, A.; FERT, A. Nucleation, stability and current-induced motion of isolated magnetic skyrmions in nanostructures. *Nature Nanotech.*, v. 8, p. 839–844, 2013.

66 JIANG, W.; UPADHYAYA, P.; ZHANG, W.; YU, G.; JUNGFLEISCH, M. B.; FRADIN, F. Y.; PEARSON, J. E.; TSERKOVNYAK, Y.; WANG, K. L.; HEINONEN, O.; VELTHUIS, S. G. E. te; HOFFMANN, A. Blowing magnetic skyrmion bubbles. *Science*, v. 349, n. 6245, p. 283–286, 2015.

67 HSU, P.-J.; KUBETZKA, A.; FINCO, A.; ROMMING, N.; BERGMANN, K. von; WIESENDANGER, R. Electric-field-driven switching of individual magnetic skyrmions. *Nature Nanotech.*, v. 12, p. 123–126, 2017.

68 YU, X. Z.; KANAZAWA, N.; ZHANG, W. Z.; NAGAI, T.; HARA, T.; KIMOTO, K.; MATSUI, Y.; ONOSE, Y.; TOKURA, Y. Skyrmion flow near room temperature in an ultralow current density. *Nature Comm.*, v. 3, p. 988.

69 SCHULZ, T.; RITZ, R.; BAUER, A.; HALDER, M.; WAGNER M. FRANZ, C.; PFLEIDERER, C.; EVERSCHOR K. GARST, M.; ROSCH, A. Emergent electrodynamics of skyrmions in a chiral magnet. *Nature Physics*, v. 8, p. 301–304, 2012.

70 THIELE, A. A. Steady-state motion of magnetic domains. *Phys. Rev. Lett.*, v. 30, p. 230–233, 1973.

71 EVERSCHOR, K.; GARST, M.; BINZ, B.; JONIETZ, F.; MÜHLBAUER, S.; PFLEIDERER, C.; ROSCH, A. Rotating skyrmion lattices by spin torques and field or temperature gradients. *Phys. Rev. B*, v. 86, p. 054432, 2012.

72 PARKIN, S. S. P.; HAYASHI, M.; THOMAS, L. Magnetic domain-wall racetrack memory. *Science*, v. 320, n. 5873, p. 190–194, 2008.

73 TOMASELLO, R.; MARTINEZ, E.; ZIVIERI, R.; TORRES, L.; CARPENTIERI, M.; FINOCCHIO, G. A strategy for the design of skyrmion racetrack memories. *Scientific Reports*, v. 4, p. 6784, 2014.

74 KANG, W.; HUANG, Y.; ZHENG, C.; LV, W.; LEI, N.; ZHANG, Y.; ZHANG, X.; ZHOU, Y.; ZHAO, W. Voltage controlled magnetic skyrmion motion for racetrack memory. *Scientific Reports*, v. 6, p. 23164, 2016.

75 ZHANG, X.; ZHAO, G. P.; FANGOHR, H.; LIU, J. P.; XIA, W. X.; XIA, J.; MORVAN, F. J. Skyrmion-skyrmion and skyrmion-edge repulsions in skyrmion-based racetrack memory. *Scientific Reports*, v. 5, p. 7643, 2015.

76 KISELEV, N. S.; BOGDANOV, A. N.; SCHÄFER, R.; RÖSSLER, U. K. Chiral skyrmions in thin magnetic films: new objects for magnetic storage technologies? *Journal of Physics D: Applied Physics*, v. 44, n. 39, p. 392001, 2011.

77 ZHANG, X.; ZHOU, Y.; EZAWA, M.; ZHAO, G. P.; ZHAO, W. Magnetic skyrmion transistor: skyrmion motion in a voltage-gated nanotrack. *Scientific Reports*, v. 5, p. 11369, 2015.

78 ZHANG, X.; EZAWA, M.; ZHOU, Y. Magnetic skyrmion logic gates: conversion, duplication and merging of skyrmions. *Scientific Reports*, v. 5, p. 9400, 2015.

79 MA, F.; ZHOU, Y.; BRAUN, H. B.; LEW, W. S. Skyrmion-based dynamic magnonic crystal. *Nano Letters*, v. 15, n. 6, p. 4029–4036, 2015.

80 MA, F.; REICHHARDT, C.; GAN, W.; REICHHARDT, C. J. O.; LEW, W. S. Emergent geometric frustration of artificial magnetic skyrmion crystals. *Phys. Rev. B*, v. 94, p. 144405, 2016.

81 CARPENTIERI, M.; TOMASELLO, R.; ZIVIERI, R.; FINOCCHIO, G. Topological, non-topological and instanton droplets driven by spin-transfer torque in materials with perpendicular magnetic anisotropy and Dzyaloshinskii–Moriya interaction. *Scientific Reports*, v. 5, p. 16184, 2015.

82 FINOCCHIO, G.; RICCI, M.; TOMASELLO, R.; GIORDANO, A.; LANUZZA, M.; PULIAFITO, V.; BURRASCANO, P.; AZZERBONI, B.; CARPENTIERI, M. Skyrmion based microwave detectors and harvesting. *Applied Physics Letters*, v. 107, n. 26, p. 262401, 2015.

83 BESSARAB, P. F.; UZDIN, V. M.; JÓNSSON, H. Method for finding mechanism and activation energy of magnetic transitions, applied to skyrmion and antivortex annihilation. *Computer Physics Communications*, v. 196, p. 335–347, 2015.

84 ROHART, S.; MILTAT, J.; THIAVILLE, A. Path to collapse for an isolated Néel skyrmion. *Phys. Rev. B*, v. 93, p. 214412, 2016.

85 LOBANOV, I. S.; JÓNSSON, H.; UZDIN, V. M. Mechanism and activation energy of magnetic skyrmion annihilation obtained from minimum energy path calculations. *Phys. Rev. B*, v. 94, p. 174418, 2016.

86 BESSARAB, P. F. Comment on "path to collapse for an isolated Néel skyrmion". *Phys. Rev. B*, v. 95, p. 136401, 2017.

87 CORTÉS-ORTUÑO, D.; WANG, W.; BEG, M.; PEPPER, R. A.; BISOTTI, M.-A.; CAREY, R.; VOUSDEN, M.; KLUYVER, T.; HOVORKA, O.; FANGOHR, H. Thermal stability and topological protection of skyrmions in nanotracks. *Scientific Reports*, v. 7, p. 4060, 2017.

88 STOSIC, D.; MULKERS, J.; WAEYENBERGE, B. V.; LUDERMIR, T. B.; MILOŠEVIĆ, M. V. Paths to collapse for isolated skyrmions in few-monolayer ferromagnetic films. *Phys. Rev. B*, v. 95, p. 214418, 2017.

89 BESSARAB, P. F.; MÜLLER, G. P.; LOBANOV, I. S.; RYBAKOV, F. N.; KISELEV, N. S.; JÓNSSON, H.; UZDIN, V. M.; BLÜGEL, S.; BERGQVIST, L.; DELIN, A. Lifetime of racetrack skyrmions. *Scientific Reports*, v. 8, n. 3433, 2018.

90 UZDIN, V.; POTKINA, M.; LOBANOV, I.; BESSARAB, P.; JÓNSSON, H. Energy surface and lifetime of magnetic skyrmions. *Journal of Magnetism and Magnetic Materials*, 2017.

91 UZDIN, V.; POTKINA, M.; LOBANOV, I.; BESSARAB, P.; JÓNSSON, H. The effect of confinement and defects on the thermal stability of skyrmions. *Physica B: Condensed Matter*, 2017.

92 RYBAKOV, F. N.; BORISOV, A. B.; BLÜGEL, S.; KISELEV, N. S. New type of stable particlelike states in chiral magnets. *Phys. Rev. Lett.*, v. 115, p. 117201, 2015.

93 STOSIC, D.; LUDERMIR, T. B.; MILOŠEVIĆ, M. V. Pinning of magnetic skyrmions in a monolayer Co film on Pt(111): Theoretical characterization and exemplified utilization. *Phys. Rev. B*, v. 96, p. 214403, 2017.

94 STOSIC, D.; MULKERS, J.; WAEYENBERGE, B. V.; LUDERMIR, T. B.; MILOŠEVIĆ, M. V. Collapse paths from skyrmion lattices to spin cycloids. *Prepared for submission to Phys. Rev. B*, 2018.

95 MALOTTKI, S. von; DUPÉ, B.; BESSARAB, P. F.; DELIN, A.; HEINZE, S. Enhanced skyrmion stability due to exchange frustration. *Scientific Reports*, v. 7, p. 12299, 2017.

96 WILD, J.; MEIER, T. N. G.; PÖLLATH, S.; KRONSEDER, M.; BAUER, A.; CHACON, A.; HALDER, M.; SCHOWALTER, M.; ROSENAUER, A.; ZWECK, J.; MÜLLER, J.; ROSCH, A.; PFLEIDERER, C.; BACK, C. H. Entropy-limited topological protection of skyrmions. *Science Advances*, v. 3, n. 9, 2017.

97 BESSARAB, P. F.; YUDIN, D.; GULEVICH, D. R.; WADLEY, P.; TITOV, M.; TRETIAKOV, O. A. Stability and lifetime of antiferromagnetic skyrmions.

98 STOSIC, D.; STOSIC, D.; LUDERMIR, T. B.; MILOŠEVIĆ, M. V. Switching and interactions between higher order skyrmions. *Prepared for submission to Phys. Rev. B*, 2018.

99 STOSIC, D.; STOSIC, D.; LUDERMIR, T. B.; MILOŠEVIĆ, M. V. Atomistic spin simulations of magnetic skyrmions. *In preparation for submission to J. Comput. Phys.*, 2018.

100 MOSKVIN, E.; GRIGORIEV, S.; DYADKIN, V.; ECKERLEBE, H.; BAENITZ, M.; SCHMIDT, M.; WILHELM, H. Complex chiral modulations in FeGe close to magnetic ordering. *Phys. Rev. Lett.*, v. 110, p. 077207, 2013.

101 YU, X. Z.; TOKUNAGA, Y.; KANEKO, Y.; ZHANG, W. Z.; KIMOTO, K.; MATSUI, Y.; TAGUCHI, Y.; TOKURA, Y. Biskyrmion states and their current-driven motion in a layered manganite. *Nat. Comm.*, v. 5, p. 4030, 2014.

102 RAJARAMAN, R. *Solitons and Instantons*. [S.l.]: Elsevier, 1987.

103 BRAUN, H.-B. Topological effects in nanomagnetism: from superparamagnetism to chiral quantum solitons. *Advances in Physics*, v. 61, n. 1, p. 1–116, 2012.

104 HAGEMEISTER, J.; ROMMING, N.; BERGMANN, K. von; VEDMEDENKO, E. Y.; WIESENDANGER, R. Stability of single skyrmionic bits. *Nature Communications*, v. 6, p. 8455, 2015.

105 SCHWARZ, K.; MOHN, P.; BLAHA, P.; KUBLER, J. Electronic and magnetic structure of BCC Fe-Co alloys from band theory. *Journal of Physics F: Metal Physics*, v. 14, n. 11, p. 2659, 1984.

106 ISING, E. Beitrag zur theorie des ferromagnetismus. *Zeitschrift für Physik*, v. 31, n. 1, p. 253–258, 1925.

107 WATSON, R. E.; BLUME, M.; VINEYARD, G. H. Spin motions in a classical ferromagnet. *Phys. Rev.*, v. 181, p. 811–823, 1969.

108 STANLEY, H. E. Dependence of critical properties on dimensionality of spins. *Phys. Rev. Lett.*, v. 20, p. 589–592, 1968.

109 EVANS, R.; FAN, W.; CHUREEMART, P.; OSTLER, T.; ELLIS, M.; CHANTRELL, R. Atomistic spin model simulations of magnetic nanomaterials. *Journal of Physics: Condensed Matter*, v. 26, n. 10, p. 103202, 2014.

110 JILES, D. *Introduction to Magnetism and Magnetic Materials*. London: Chapman and Hall, 1991.

111 UDVARDI, L.; SZUNYOGH, L.; PALOTÁS, K.; WEINBERGER, P. First-principles relativistic study of spin waves in thin magnetic films. *Phys. Rev. B*, v. 68, p. 104436, 2003.

112 MRYASOV, O. N.; NOWAK, U.; GUSLIENKO, K. Y.; CHANTRELL, R. W. Temperature-dependent magnetic properties of fept: Effective spin hamiltonian model. *EPL (Europhysics Letters)*, v. 69, n. 5, p. 805, 2005.

113 SZUNYOGH, L.; LAZAROVITS, B.; UDVARDI, L.; JACKSON, J.; NOWAK, U. Giant magnetic anisotropy of the bulk antiferromagnets IrMn and IrMn3 from first principles. *Phys. Rev. B*, v. 79, p. 020403, 2009.

114 FERT, A.; LEVY, P. M. Role of anisotropic exchange interactions in determining the properties of spin-glasses. *Phys. Rev. Lett.*, v. 44, p. 1538–1541, 1980.

115 BRUNO, P. Physical origins and theoretical models of magnetic anisotropy. In: DEDERICHS, P.; GRÜNBERG, P.; ZINN, W. (Ed.). *Magnetismus von Festkörpern und grenzflächen*. Jülich: Forschungszentrums Julich, 2006. v. 24.

116 HOHENBERG, P.; KOHN, W. Inhomogeneous electron gas. *Phys. Rev.*, v. 136, p. B864–B871, 1964.

117 BARTH, U. von; HEDIN, L. A local exchange-correlation potential for the spin polarized case. i. *Journal of Physics C: Solid State Physics*, v. 5, n. 13, p. 1629, 1972.

118 KRESSE, G.; FURTHMÜLLER, J. Efficient iterative schemes for ab initio total-energy calculations using a plane-wave basis set. *Phys. Rev. B*, v. 54, p. 11169–11186, 1996.

119 FLEUR: The Jülich FLAPW code family. <http://www.flapw.de/pm/index.php>.

120 KAZANTSEVA, N.; HINZKE, D.; NOWAK, U.; CHANTRELL, R. W.; ATXITIA, U.; CHUBYKALO-FESENKO, O. Towards multiscale modeling of magnetic materials: Simulations of FePt. *Phys. Rev. B*, v. 77, p. 184428, 2008.

121 ATXITIA, U.; HINZKE, D.; CHUBYKALO-FESENKO, O.; NOWAK, U.; KACHKACHI, H.; MRYASOV, O. N.; EVANS, R. F.; CHANTRELL, R. W. Multiscale modeling of magnetic materials: Temperature dependence of the exchange stiffness. *Phys. Rev. B*, v. 82, p. 134440, 2010.

122 JOURDAN, T.; MARTY, A.; LANCON, F. Multiscale method for Heisenberg spin simulations. *Phys. Rev. B*, v. 77, p. 224428, 2008.

123 LUCIA, A. D.; KRÜGER, B.; TRETIAKOV, O. A.; KLÄUI, M. Multiscale model approach for magnetization dynamics simulations. *Phys. Rev. B*, v. 94, p. 184415, 2016.

124 LUCIA, A. D.; LITZIUS, K.; KRÜGER, B.; TRETIAKOV, O. A.; KLÄUI, M. Multiscale simulations of topological transformations in magnetic-skyrmion spin structures. *Phys. Rev. B*, v. 96, p. 020405, 2017.

125 RÓZSA, L.; DEÁK, A.; SIMON, E.; YANES, R.; UDVARDI, L.; SZUNYOGH, L.; NOWAK, U. Skyrmions with attractive interactions in an ultrathin magnetic film. *Phys. Rev. Lett.*, v. 117, p. 157205, 2016.

126 SZUNYOGH, L.; UDVARDI, L.; JACKSON, J.; NOWAK, U.; CHANTRELL, R. Atomistic spin model based on a spin-cluster expansion technique: Application to the IrMn3/Co interface. *Phys. Rev. B*, v. 83, p. 024401, 2011.

127 CAMOSI, L.; ROHART, S.; FRUCHART, O.; PIZZINI, S.; BELMEGUENAI, M.; ROUSSIGNÉ, Y.; STASHKEVICH, A.; CHERIF, S. M.; RANNO, L.; SANTIS, M. de; VOGEL, J. Anisotropic Dzyaloshinskii-Moriya interaction in ultrathin epitaxial Au/Co/W(110). *Phys. Rev. B*, v. 95, p. 214422, 2017.

128 MEYER, S.; DUPÉ, B.; FERRIANI, P.; HEINZE, S. Dzyaloshinskii-Moriya interaction at an antiferromagnetic interface: First-principles study of Fe/Ir bilayers on Rh(001). *Phys. Rev. B*, v. 96, p. 094408, 2017.

129 RÓZSA, L.; UDVARDI, L.; SZUNYOGH, L.; SZABÓ, I. A. Magnetic phase diagram of an fe monolayer on W(110) and Ta(110) surfaces based on ab initio calculations. *Phys. Rev. B*, v. 91, p. 144424, 2015.

130 LIU, Y.-H.; LI, Y.-Q. A mechanism to pin skyrmions in chiral magnets. *J. Phys.: Condens. Matter*, v. 25, p. 076005, 2013.

131 ZANG, J.; MOSTOVOY, M.; HAN, J. H.; NAGAOSA, N. Dynamics of skyrmion crystals in metallic thin films. *Phys. Rev. Lett.*, v. 107, p. 136804, 2011.

132 KRAUSE, S.; WIESENDANGER, R. Skyrmionics gets hot. *Nat. Mater.*, v. 15, p. 493–494, 2016.

133 ABERT, C. *"Discrete Mathematical Concepts in Micromagnetic Computations*. Tese (Doutorado) — University of Hamburg, 2013.

134 LANDAU, L.; LIFSHITS, E. On the theory of the dispersion of magnetic permeability in ferromagnetic bodies. *Phys. Zeitsch. der Sow*, v. 8, p. 153–169, 1935.

135 GILBERT, T. A lagrangian formulation of the gyromagnetic equation of the magnetic field. *Phys. Rev.*, v. 100, p. 1243, 1955.

136 GILBERT, T. L. A phenomenological theory of damping in ferromagnetic materials. *IEEE Transactions on Magnetics*, v. 40, n. 6, p. 3443–3449, 2004.

137 HILLEBRANDS, B.; OUNADJELA, K. *Spin Dynamics in Confined Magnetic Structures I and II*. Berlin: Springer, 2003.

138 MATTIS, D. *Theory of Magnetism I: Statics and Dynamics*. Berlin: Springer, 1988.

139 STILES, M. D.; MILTAT, J. Spin-transfer torque and dynamics. In: HILLEBRANDS, B.; THIAVILLE, A. (Ed.). *Spin Dynamics in Confined Magnetic Structures III*. Berlin: Springer, 2006. p. 225–308.

140 BROWN, W. Thermal fluctuation of fine ferromagnetic particles. *IEEE Transactions on Magnetics*, v. 15, n. 5, p. 1196–1208, 1979.

141 GARCÍA-PALACIOS, J. L.; LÁZARO, F. J. Langevin-dynamics study of the dynamical properties of small magnetic particles. *Phys. Rev. B*, v. 58, p. 14937–14958, 1998.

142 BERKOV, D.; GORN, N. Thermally activated processes in magnetic systems consisting of rigid dipoles: equivalence of the ito and stratonovich stochastic calculus. *Journal of Physics: Condensed Matter*, v. 14, n. 13, p. L281, 2002.

143 ATKINSON, K. *An Introduction to Numerical Analysis*. [S.l.]: Wiley, 1989.

144 MARSAGLIA, G.; TSANG, W. W. The ziggurat method for generating random variables. *Journal of Statistical Software, Articles*, v. 5, n. 8, p. 1–7, 2000.

145 PAZ, E.; GARCIA-SANCHEZ, F.; CHUBYKALO-FESENKO, O. Numerical evaluation of energy barriers in nano-sized magnetic elements with lagrange multiplier technique. *Physica B: Condensed Matter*, v. 403, n. 2, p. 330–333, 2008.

146 JÓNSSON, H.; MILLS, G.; JACOBSEN, K. W. Nudged elastic band method for finding minimum energy paths of transitions. In: BERNE, B. J.; CICCOTTI, G.; COKER, D. F. (Ed.). *Classical and Quantum Dynamics in Condensed Phase Simulations*. [S.l.: s.n.], 1998. p. 385–404.

147 HENKELMAN, G.; JÓNSSON, H. Improved tangent estimate in the nudged elastic band method for finding minimum energy paths and saddle points. *The Journal of Chemical Physics*, v. 113, p. 9978, 2000.

148 E, W.; REN, W.; VANDEN-EIJNDEN, E. String method for the study of rare events. *Phys. Rev. B*, v. 66, p. 052301, 2002.

149 TRYGUBENKO, S. A.; WALES, D. J. A doubly nudged elastic band method for finding transition states. *The Journal of Chemical Physics*, v. 120, p. 2082, 2004.

150 SUESS, D.; SCHREFL, T.; SUESS, D.; FÄHLE, S.; KIRSCHNER, M.; HRKAC, G.; DORFBAUER, F.; FIDLER, J. Exchange spring media for perpendicular recording. *Applied Physics Letters*, v. 87, p. 012504, 2005.

151 DITTRICH, R.; SCHREFL, T.; SUESS, D.; SCHOLZ, W.; FORSTER, H.; FIDLER, J. A path method for finding energy barriers and minimum energy paths in complex micromagnetic systems. *J. Magn. Magn. Mater.*, v. 250, p. 12–19, 2002.

152 DITTRICH, R.; SCHREFL, T.; FORSTER, H.; SUESS, D.; SCHOLZ, W.; FIDLER, J. Energy barriers in magnetic random access memory elements. *IEEE Transactions on Magnetics*, v. 39, n. 5, p. 2839–2841, 2003.

153 BESSARAB, P. F.; UZDIN, V. M.; JÓNSSON, H. Harmonic transition-state theory of thermal spin transitions. *Phys. Rev. B*, v. 85, p. 184409, 2012.

154 RHEOMAN: Nudged Elastic Band. <http://umet.univ-lille1.fr/Projets/RheoMan/en/to-learn-more-about/nudged-elastic-band.php>.

155 ANTROPOV, V. P.; KATSNELSON, M. I.; HARMON, B. N.; SCHILFGAARDE, M. van; KUSNEZOV, D. Spin dynamics in magnets: Equation of motion and finite temperature effects. *Phys. Rev. B*, v. 54, p. 1019–1035, 1996.

156 KORN, G.; KORN, T. *Mathematical Handbook for Scientists and Engineers*. New York: Dover Publications, 2000. 891 p.

157 SHEPPARD, D.; TERRELL, R.; HENKELMAN, G. Optimization methods for finding minimum energy paths. *The Journal of Chemical Physics*, v. 128, p. 134106, 2008.

158 PRESS, W. H.; TEUKOLSKY, S. A.; VETTERLING, W. T.; FLANNERY, B. P. *Numerical Recipes in C: The Art of Scientific Computing. Second Edition*. Cambridge: Cambridge University Press, 1992.

159 VERLET, L. Computer "experiments" on classical fluids. i. thermodynamical properties of lennard-jones molecules. *Phys. Rev.*, v. 159, p. 98–103, 1967.

160 HENKELMAN, G.; UBERUAGA, B. P.; JÓNSSON, H. A climbing image nudged elastic band method for finding saddle points and minimum energy paths. *Journal of Chemical Physics*, v. 113, n. 22, p. 9901–9904, 2000.

161 METROPOLIS, N.; ULAM, S. The Monte Carlo method. *Journal of the American Statistical Association*, v. 44, n. 247, p. 335–341, 1949.

162 ROBERT, C.; CASELLA, G. *Monte Carlo Statistical Methods*. New York: Springer, 2004.

163 METROPOLIS, N. The beginning of the Monte Carlo method. *Los Alamos Science*, v. 15, p. 125–130, 1987.

164 METROPOLIS, N.; ROSENBLUTH, A. W.; ROSENBLUTH, M. N.; TELLER, A. H.; TELLER, E. Equation of state calculations by fast computing machines. *The Journal of Chemical Physics*, v. 21, n. 6, p. 1087–1092, 1953.

165 THOMSEN, J. S. Logical relations among the principles of statistical mechanics and thermodynamics. *Phys. Rev.*, v. 91, p. 1263–1266, 1953.

166 MARSAGLIA, G. Choosing a point from the surface of a sphere. *Ann. Math. Statist.*, v. 43, n. 2, p. 645–646, 1972.

167 DUPÉ, B.; BIHLMAYER, G.; BÖTTCHER, M.; BLÜGEL, S.; HEINZE, S. Engineering skyrmions in transition-metal multilayers for spintronics. *Nature Communications*, v. 7, p. 11779, 2016.

168 YANG, H.; THIAVILLE, A.; ROHART, S.; FERT, A.; CHSHIEV, M. Anatomy of Dzyaloshinskii-Moriya interaction at Co/Pt interfaces. *Phys. Rev. Lett.*, v. 115, p. 267210, 2015.

169 SU, C. W.; HO, H. Y.; SHERN, C. S.; H., C. R. Changes in the magnetic anisotropy of Co thin films on Pt(111) capped by Ag overlayers. *Chinese Journal of Physics*, v. 41, n. 5, p. 519–527, 2003.

170 LUNDGREN, E.; STANKA, B.; SCHMID, M.; VARGA, P. Thin films of Co on Pt(111): Strain relaxation and growth. *Phys. Rev. B*, v. 62, p. 2843–2851, 2000.

171 PUSTOGOWA, U.; ZABLOUDIL, J.; UIBERACKER, C.; BLAAS, C.; WEINBERGER, P.; SZUNYOGH, L.; SOMMERS, C. Magnetic properties of thin films of Co and of (CoPt) superstructures on P(100) and Pt(111). *Phys. Rev. B*, v. 60, n. 1, p. 414–421, 1999.

172 ROHART, S.; THIAVILLE, A. Skyrmion confinement in ultrathin film nanostructures in the presence of Dzyaloshinskii-Moriya interaction. *Phys. Rev. B*, v. 88, p. 184422, 2013.

173 GARCIA-SANCHEZ, F.; BORYS, P.; VANSTEENKISTE, A.; KIM, J.-V.; STAMPS, R. L. Nonreciprocal spin-wave channeling along textures driven by the Dzyaloshinskii-Moriya interaction. *Phys. Rev. B*, v. 89, p. 224408, 2014.

174 CHO, J.; KIM, N.-H.; LEE, S.; KIM, J.-S.; LAVRIJSEN, R.; SOLIGNAC, A.; YIN, Y.; HAN, D.-S.; HOOF, N. J. J. van; SWAGTEN, H. J. M.; KOOPMANS, B.; YOU, C.-Y. Thickness dependence of the interfacial Dzyaloshinskii-Moriya interaction in inversion symmetry broken systems. *Nature Communications*, v. 6, p. 7635, 2015.

175 NEMBACH, H. T.; SHAW, J. M.; WEILER, M.; JUÉ, E.; SILVA, T. J. Linear relation between Heisenberg exchange and interfacial Dzyaloshinskii–Moriya interaction in metal films. *Nature Physics*, v. 11, p. 825–829, 2014.

176 MULKERS, J.; MILOŠEVIĆ, M. V.; WAEYENBERGE, B. V. Cycloidal versus skyrmionic states in mesoscopic chiral magnets. *Phys. Rev. B*, v. 93, p. 214405, 2016.

177 DUPÉ, B.; HOFFMANN, M.; PAILLARD, C.; HEINZE, S. Tailoring magnetic skyrmions in ultra-thin transition metal films. *Nature Communications*, v. 5, p. 4030, 2014.

178 ABO, G. S.; HONG, Y. K.; PARK, J.; LEE, J.; LEE, W.; CHOI, B. C. Definition of magnetic exchange length. *IEEE Transactions on Magnetics*, v. 49, n. 8, p. 4937–4939, 2013.

179 RAMSTÖCK, K.; HARTUNG, W.; HUBERT, A. The phase diagram of domain walls in narrow magnetic strips. *physica status solidi (a)*, WILEY-VCH Verlag, v. 155, n. 2, p. 505–518, 1996.

180 MULKERS, J.; WAEYENBERGE, B. V.; MILOŠEVIĆ, M. V. Effects of spatially engineered Dzyaloshinskii-Moriya interaction in ferromagnetic films. *Phys. Rev. B*, v. 95, p. 144401, 2017.

181 LIN, S.-Z.; REICHHARDT, C.; BATISTA, C. D.; SAXENA, A. Particle model for skyrmions in metallic chiral magnets: Dynamics, pinning, and creep. *Phys. Rev. B*, v. 87, p. 214419, 2013.

182 MÜLLER, J.; ROSCH, A. Capturing of a magnetic skyrmion with a hole. *Phys. Rev. B*, v. 91, p. 054410, 2015.

183 KIM, J.-V.; YOO, M.-W. Current-driven skyrmion dynamics in disordered films. *Applied Physics Letters*, v. 110, p. 132404, 2017.

184 LEGRAND, W.; MACCARIELLO, D.; REYREN, N.; GARCIA, K.; MOUTAFIS, C.; MOREAU-LUCHAIRE, C.; COLLIN, S.; BOUZEHOUANE, K.; CROS, V.; FERT, A. Room-temperature current-induced generation and motion of sub-100 nm skyrmions. *Nano Letters*, v. 17, n. 4, p. 2703–2712, 2017.

185 HANNEKEN, C.; KUBETZKA A. VON BERGMANN, K.; WIESENDANGER, R. Pinning and movement of individual nanoscale magnetic skyrmions via defects. *New Journal of Physics*, v. 18, p. 055009, 2016.

186 REICHHARDT, C.; RAY, D.; REICHHARDT, C. J. O. Quantized transport for a skyrmion moving on a two-dimensional periodic substrate. *Phys. Rev. B*, v. 91, p. 104426, 2015.

187 REICHHARDT, C.; RAY, D.; REICHHARDT, C. J. O. Collective transport properties of driven skyrmions with random disorder. *Phys. Rev. Lett.*, v. 114, p. 217202, 2015.

188 DÍAZ, S. A.; REICHHARDT, C. J. O.; AROVAS, D. P.; SAXENA, A.; REICHHARDT, C. Fluctuations and noise signatures of driven magnetic skyrmions. *Phys. Rev. B*, v. 96, p. 085106, 2017.

189 CHUDNOVSKY, E. M.; GARANIN, D. A. Skyrmion glass in a disordered magnetic film.

190 MA, X.; REICHHARDT, C. J. O.; REICHHARDT, C. Reversible vector ratchets for skyrmion systems. *Phys. Rev. B*, v. 95, p. 104401, 2017.

191 REICHHARDT, C.; REICHHARDT, C. J. O. Shapiro spikes and negative mobility for skyrmion motion on quasi-one-dimensional periodic substrates. *Phys. Rev. B*, v. 95, p. 014412, 2017.

192 NAVAU, C.; DEL-VALLE, N.; SANCHEZ, A. Analytical trajectories of skyrmions in confined geometries: Skyrmionic racetracks and nano-oscillators. *Phys. Rev. B*, v. 94, p. 184104, 2016.

193 REICHHARDT, C.; REICHHARDT, C. J. O. Magnus-induced dynamics of driven skyrmions on a quasi-one-dimensional periodic substrate. *Phys. Rev. B*, v. 94, p. 094413, 2016.

194 REICHHARDT, C.; REICHHARDT, C. J. O. Shapiro steps for skyrmion motion on a washboard potential with longitudinal and transverse ac drives. *Phys. Rev. B*, v. 92, p. 224432, 2015.

195 OGAWA, N.; SEKI, S.; TOKURA, Y. Ultrafast optical excitation of magnetic skyrmions. *Scientific Reports*, v. 5, p. 9552, 2015.

196 REICHHARDT, C.; RAY, D.; REICHHARDT, C. J. O. Magnus-induced ratchet effects for skyrmions interacting with asymmetric substrates. *New Journal of Physics*, v. 17, n. 7, p. 073034, 2015.

197 SHIMADA, T.; OKUNO, J.; KITAMURA, T. Ab initio study of spin-spiral noncollinear magnetism in a free-standing Fe(110) monolayer under in-plane strain. *Phys. Rev. B*, v. 85, p. 134440, 2012.

198 ROMMING, N.; PRALOW, H.; KUBETZKA, A.; HOFFMANN, M.; MALOTTKI, S. von; MEYER, S.; DUPÉ, B.; WIESENDANGER, R.; BERGMANN, K. von; HEINZE, S. Competition of Dzyaloshinskii-Moriya and higher-order exchange interactions in Rh/Fe atomic bilayers on Ir(111). *Phys. Rev. Lett.*, v. 120, p. 207201, 2018.

199 HSU, P.-J.; FINCO, A.; SCHMIDT, L.; KUBETZKA, A.; BERGMANN, K. von; WIESENDANGER, R. Guiding spin spirals by local uniaxial strain relief. *Phys. Rev. Lett.*, v. 116, p. 017201, 2016.

200 HUANG, S.; ZHOU, C.; CHEN, G.; SHEN, H.; SCHMID, A. K.; LIU, K.; WU, Y. Stabilization and current-induced motion of antiskyrmion in the presence of anisotropic Dzyaloshinskii-Moriya interaction. *Phys. Rev. B*, v. 96, p. 144412, 2017.

201 KOSHIBAE, W.; NAGAOSA, N. Theory of antiskyrmions in magnets. *Nat. Comm.*, v. 7, p. 10542, 2016.

202 NAYAK, A. K.; KUMAR, V.; MA, T.; WERNER, P.; PIPPEL, E.; SAHOO, R.; DAMAY, F.; RöSSLER, U. K.; FELSER, C.; PARKIN, S. S. P. Magnetic antiskyrmions above room temperature in tetragonal heusler materials. *Nature*, v. 548, p. 561–566, 2017.

203 PENG, L.; ZHANG, Y.; HE, M.; DING, B.; WANG, W.; TIAN, H.; LI, J.; WANG, S.; CAI, J.; WU, G.; LIU, J. P.; KRAMER, M. J.; SHEN, B.-g. Generation of high-density biskyrmions by electric current. *Quan. Mat.*, v. 2, n. 30, p. 30, 2017.

204 ZHANG, X.; ZHOU, Y.; EZAWA, M. High-topological-number magnetic skyrmions and topologically protected dissipative structure. *Phys. Rev. B*, v. 93, p. 024415, 2016.

205 DUPé, B.; KRUSE, C. N.; DORNHEIM, T.; HEINZE, S. How to reveal metastable skyrmionic spin structures by spin-polarized scanning tunneling microscopy. *New Journal of Physics*, v. 18, n. 5, p. 055015, 2016.

206 PALOTÁS, K.; RÓZSA, L.; SIMON, E.; UDVARDI, L.; SZUNYOGH, L. Spin-polarized scanning tunneling microscopy characteristics of skyrmionic spin structures exhibiting various topologies. *Phys. Rev. B*, v. 96, p. 024410, 2017.

207 BALRAM, A. C.; WURSTBAUER, U.; WóJS, A.; PINCZUK, A.; JAIN, J. K. Fractionally charged skyrmions in fractional quantum Hall effect. *Nat. Comm.*, v. 6, p. 8981, 2015.

208 ZHANG, X.-H.; FAN, W.-J.; SHI, J.-W.; KOU, S.-P. Fractionalized topological defects in optical lattices. *New Journal of Physics*, v. 17, n. 10, p. 103019, 2015.

209 BAZEIA, D.; RAMOS, J.; RODRIGUES, E. Topological strength of magnetic skyrmions. *Journal of Magnetism and Magnetic Materials*, v. 423, p. 411–420, 2017.

210 KERNIGHAN, B.; RITCHIE, D. *The C Programming Language*. 2nd. ed. [S.l.]: Prentice Hall, 1988.

211 STEWART, I. Sources of uncertainty in deterministic dynamics: an informal overview. *Philosophical Transactions of the Royal Society of London A: Mathematical, Physical and Engineering Sciences*, v. 369, n. 1956, p. 4705–4729, 2011.

212 LLOYD, S. Least squares quantization in PCM. *IEEE Transactions on Information Theory*, v. 28, n. 2, p. 129–137, 1982.

213 SHREINER, D. *OpenGL Programming Guide: The Official Guide to Learning OpenGL*. 7th. ed. [S.l.]: Addison-Wesley, 2009.

214 ASE. <https://wiki.fysik.dtu.dk/ase/about.html>.

215 FIDIMAG. <http://computationalmodelling.github.io/fidimag/>.

216 MUMAX3: GPU-accelerated micromagnetism. <https://mumax.github.io/>.

217 OPEN Source Multiphysics Numerical Simulation Package (OMNeS). <https://www.omnes.uni-mainz.de/>.

218 THE Object Oriented MicroMagnetic Framework (OOMMF) project at ITL/NIST. <https://math.nist.gov/oommf/>.

219 SPIRIT – Atomistic Spin Code. <https://spirit-code.github.io/>.

APPENDIX A – PUBLICATIONS

1 STOSIC, D. et al. Foreign exchange rate entropy evolution during financial crises. *Physica A: Statistical Mechanics and its Applications*, v. 449, p. 233–239, 2016.

2 STOSIC, D. et al. Correlations of multiscale entropy in the FX market. *Physica A: Statistical Mechanics and its Applications*, v. 457, p. 52–61, 2016.

3 STOŠIĆ, D. et al. GPU-advanced 3D electromagnetic simulations of superconductors in the Ginzburg–Landau formalism. *J. Comput. Phys.*, v. 322, p. 183–198, 2016.

4 STOSIC, D. et al. Quantum factoring with CUDA. *Unpublished*, 2016.

5 STOSIC, D.; STOSIC, D.; LUDERMIR, T. Voting based q-generalized extreme learning machine. *Neurocomputing*, v. 174, p. 1021–1030, 2016.

6 STOSIC, D. et al. QRNN: *q*-generalized random neural network. *IEEE Trans. Neural Netw. Learn. Syst.*, v. 28, n. 2, p. 383–390, 2017.

7 STOSIC, D. et al. Paths to collapse for isolated skyrmions in few-monolayer ferromagnetic films. *Phys. Rev. B*, v. 95, p. 214418, 2017.

8 STOSIC, D.; LUDERMIR, T. B.; MILOŠEVIĆ, M. V. Pinning of magnetic skyrmions in a monolayer Co film on Pt(111): Theoretical characterization and exemplified utilization. *Phys. Rev. B*, v. 96, p. 214403, 2017.

9 STOSIC, D. et al. Nonextensive triplets in cryptocurrency exchanges. *Physica A: Statistical Mechanics and its Applications*, v. 505, p. 1069–1074, 2018.

10 STOSIC, D. et al. Collective behavior of cryptocurrency price changes. *Physica A: Statistical Mechanics and its Applications*, v. 507, p. 499–509, 2018.

11 STOSIC, D. et al. Exploring disorder and complexity in the cryptocurrency. *Under review in Physica A: Statistical Mechanics and its Applications*, 2018.

12 STOSIC, D. et al. Multifractal behavior of price and volume changes in the cryptocurrency market. *Submitted to Physica A: Statistical Mechanics and its Applications*, 2018.

13 STOSIC, D. et al. Multifractal characterization of Brazilian market sectors. *Submitted to Physica A: Statistical Mechanics and its Applications*, 2018.

14 STOSIC, D. et al. Distance metric learning through minimization of the free energy. *Submitted to IEEE Trans. Cybern.*, 2018.

15 STOSIC, D. et al. Natural image segmentation with non-extensive mixture models. *Prepared for submission to IEEE Trans. Image Process.*, 2018.

16 STOSIC, D. et al. Collapse paths from skyrmion lattices to spin cycloids. *Prepared for submission to Phys. Rev. B*, 2018.

17 STOSIC, D. et al. Switching and interactions between higher order skyrmions. *Prepared for submission to Phys. Rev. B*, 2018.

18 STOSIC, D. et al. Atomistic spin simulations of magnetic skyrmions. *In preparation for submission to J. Comput. Phys.*, 2018.